Ph.D.thesis

Antihydrogen production in cusp trap

カスプトラップ中での反水素の合成

東京大学大学院総合文化研究科

広域科学専攻

榎本　嘉範

February 13, 2011

Contents

List of Figures

List of Tables

Chapter 1

Introduction

We have been working on the production of antihydrogen atoms to test the CPT symmetry. In this chapter, the motivation and foregoing researches are described. In section 1.1, motivation of this research is described. In section 1.2, results of precise spectroscopy of the hydrogen atoms are presented. In section 1.3 foregoing researches of the production of the antihydrogen atoms by several groups are described.

1.1 Antimatter and symmetry

An epoch-making discovery in 1933 opened up doors to the antimatter science. Positrons were observed in cosmic ray by Anderson [1] shortly after the theoretical prediction by Dirac in 1931 [2, 3]. Since then, various antiparticles were found as listed in table 1.1. For example, antiprotons were observed in 1955 at Bevatron, Berkeley [4].

One of the motivation to search antimatter is to test the symmetry between matter and antimatter (CPT symmetry). It is known that if the CPT symmetry conserves, properties of antimatter, such as mass, absolute value of charge and magnetic moment, life time, are the same as those of the matter counterpart. Till now, experiments to test the CPT symmetry have been carried out. Some of them are summarized in table 1.2 [5]. The mass of the positron was determined to be the same as that of the electron within 8×10^{-9} precision by the measurement of the $1^3S_1 - 2^3S_1$ transition frequency of the Positronium for example [6]. The mass and the charge difference between the antiproton and the proton were determined by combining the results of spectroscopy of antiprotonic helium [7] and those of the cyclotron frequency of proton and antiproton [8]. On the other hand, the magnetic moment of antiproton was determined

only with 0.3 % precision by x-ray spectroscopy of heavy antiprotonic atom ($\bar{p}^{208}$Pb) in high Rydberg state [9].

Recently, the antihydrogen atom has been spotlighted as one of the best systems to test the CPT symmetry. Owing to various scientific and technical progresses, a large number of cold antihydrogen atoms was produced [10, 11, 12]. In addition to the simplicity of the system, the hydrogen atom (the matter counterpart) is the most precisely studied physical system. Thus the spectroscopy of the antihydrogen atoms is considered to be one of the most promising candidates to test the CPT symmetry.

year	achievement	finder	reference
1931	prediction of positron	Dirac	[2, 3]
1933	observation of positron	Anderson	[1]
1955	observation of antiproton	Chamberlain, Segre, Wiegand Ypsilantis	[4]
1995	observation of antihydrogen atoms in flight	PS210	[13]
2002	production of cold antihydrogen atoms in trap (uniform magnetic field)	ATHENA	[10]
2002	production of cold antihydrogen atoms in trap (uniform magnetic field)	ATRAP	[11, 12]
2008	production of cold antihydrogen atoms in trap (non-uniform magnetic field)	ATRAP	[14]
2010	production of cold antihydrogen atoms in trap (non-uniform magnetic field)	ALPHA	[15]
2010	production of cold antihydrogen atoms in trap (non-uniform magnetic field)	ASACUSA(this work)	[16]
2010	confinement of antihydrogen	ALPHA	[17]

Table 1.1: A list of important achievements related to antiparticles and antimatters.

$(m_{e^+} - m_{e^-})/m_{average}$	$< 8 \times 10^{-9}$
$(m_p - m_{\overline{p}})/m_{average}$	$< 2 \times 10^{-9}$
$\lvert q_p + q_{\overline{p}} \rvert / e$	$< 2 \times 10^{-9}$
$(\mu_p + \mu_{\overline{p}})/\mu_p$	$(-2.6 \pm 2.9) \times 10^{-3}$

Table 1.2: A list of some results of CPT tests.

1.2 Spectroscopy of hydrogen atom

Transition frequencies of hydrogen atom have been measured with extremely high precision. For example, the frequency of the ground state hyperfine splitting (ν_{HF}) was determined by maser technique [18, 19] to be

$$\nu_{HF} = 1\ 420\ 405\ 751.7667(9)\ \text{Hz} \tag{1.1}$$

On the other hand, theory can reproduce the value with a precision of 3.5×10^{-6} [20]. The reason of the uncertainty mainly originated from the uncertainty of the charge and magnetization distributions of proton.

The frequency of 1S-2S transition (ν_{1S-2S}) was determined by laser [21, 22, 23] to be

$$\nu_{1S-2S} = 2\ 466\ 061\ 413\ 187\ 074(34)\ \text{Hz} \tag{1.2}$$

The absolute uncertainty of 34 Hz (relative uncertainty of 1.4×10^{-14}) approaches its natural line width (1.3 Hz). In this case, theoretical uncertainty was 1×10^{-11} [24]. This originated from the uncertainty of the charge distributions of proton.

1.3 Production of antihydrogen atoms

Only several groups have succeeded to produce antihydrogen atoms. One of the difficulties was the fact that the energy range involved was quite broad, from GeV (during the antiproton production) to meV (antihydrogen production). To bridge these different energy regions, experimental techniques have been developed for many years. Some history of antiproton and antihydrogen atom can be found in several reviews [25, 26, 27, 28].

Figure 1.1 [26] is a schematic drawing of the experimental setup in which the first antihydrogen atoms were observed in 1995 at CERN [13]. Antiprotons of 2 GeV/c were circulating in a storage ring(Low Energy Antiproton Ring, LEAR) and xenon gas jet was injected into the ring perpendicular to the beam. A part of antiprotons virtually created positron-electron pair during passage through the gas jet, and captured the positron via the process

$$\bar{\mathrm{p}} + \mathrm{Z} \rightarrow \bar{\mathrm{p}} + (\mathrm{e}^+ + \mathrm{e}^-) + \mathrm{Z} \rightarrow \bar{\mathrm{H}} + \mathrm{e}^- + \mathrm{Z}. \tag{1.3}$$

Antihydrogen atom of 2 GeV/c so produced, which were electrically neutral, were not bent by the bending magnet in figure 1.1 and went straight to the detector located outside of the

ring. Then the antihydrogen atoms were stripped their positrons at the silicon counters. The positrons were stopped in the counters, annihilated at that point and emitted γ rays which were detected by the scintillation detectors surrounding the silicon counters (NaI). The antiprotons entered into a magnetic spectrometer (not shown in figure 1.1), and their momenta and time of flights were measured. This was an important experiment which demonstrated that the antihydrogen atom did exist and could be produced in the laboratory. Nevertheless, because the energy of the produced antihydrogen atoms was in a relativistic energy range and only 9 atoms were observed during whole experimental period of 15 hours, this method was not suitable for any precise spectroscopy of antihydrogen atoms.

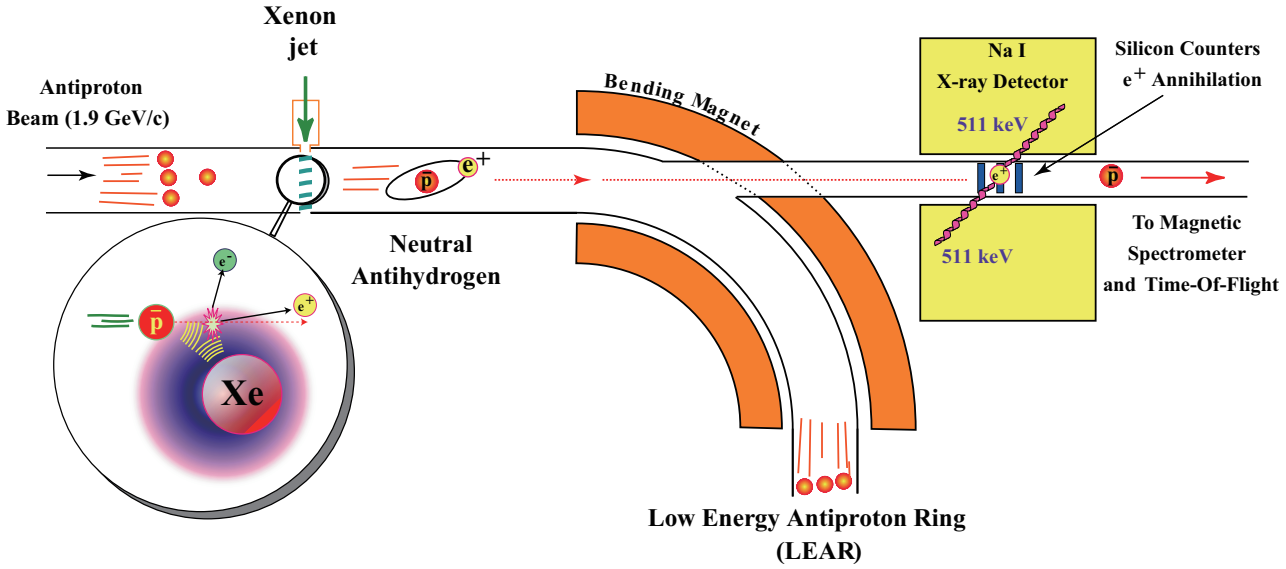

Figure 1.1: A schematic drawing of the experimental setup in which the first antihydrogen atoms were observed by PS210 collaboration.

Recently techniques for the production of cold antihydrogen atoms have progressed rapidly. Capture of antiprotons in the Penning trap [29] and cooling of them by electrons down to 100 meV [30] were demonstrated in 1980's. Electron cooling of proton (sympathetic cooling by trapped particles of opposite sign of charge) in the nested Penning trap [31] was also demonstrated. At the same time, trap based positron accumulator which can provide a large number of low energy positrons were developed [32]. In addition, theoretical aspect [33] and experimental aspect [34, 35] of recombination processes were intensively studied.

As a result of the series of developments, ATHENA [10] and ATRAP [11, 12] collaboration succeeded to produce antihydrogen atoms in the nested Penning trap at the antiproton

decelerator (AD) at CERN in 2002.

Figure 1.2 (a) is a schematic drawing of the experimental setup of the ATHENA experiment. It consists of an antiproton catching trap and a mixing trap placed in a superconducting solenoid of 3 T, a positron accumulator and detectors. Positrons from the accumulator were transported to the mixing trap. Antiprotons from the AD were captured and cooled in the antiproton capture trap then they were transported to the mixing trap. Figure 1.2 (b) schematically shows a cross sectional view of the mixing trap and figure 1.2 (c) shows the electric potential configuration used to mix antiprotons and positrons. Antiprotons were injected into positrons and eventually they recombined to antihydrogen atoms. The produced antihydrogen atoms, which were electrically neutral, flew away and annihilated on the trap electrodes (figure 1.2 (b)). The annihilation products of the positrons and the antiprotons were observed by cesium iodide (CsI) crystals and silicon strip detectors surrounding the trap respectively (figure 1.2(d)). Productions of antihydrogen atoms were identified by detecting antiprotons and positrons annihilations at the same time and at the same position. The maximum production rate of the experiment was several hundred antihydrogens per second [36].

ATRAP also succeeded to produce antihydrogen atoms [11]. The experimental setup was similar to that of ATHENA (figure 1.3 (a)) but the identification scheme of antihydrogen atoms was different. Figure 1.3 (b) shows the potential configuration and cross sectional view of the electrodes. A part of produced antihydrogen atoms drifting out the nested trap along the trap axis was re-ionized by the electric field at the ionization well and antiprotons originated from the ionized antihydrogen atoms were accumulated in the ionization well. After mixing operation, the ionization well was opened and escaping antiprotons were counted by detectors surrounding the trap. They reported 11 % of antiprotons in the nested trap formed antihydrogen atoms [11].

Both experiments demonstrated the production of a large number of cold antihydrogen atoms in the trap. However, the produced antihydrogen atoms freely flew away and it was difficult to use them for any precise measurements.

In 2010, ALPHA succeeded to confine 38 antihydrogen atoms in their trap using non-uniform magnetic field [17]. This success was an important step to the precise spectroscopy of the antihydrogen atoms.

In 2003, we have proposed and started to develop a so-called cusp trap, which can extract antihydrogen atoms as a beam, as an alternative antihydrogen source for the spectroscopy. In

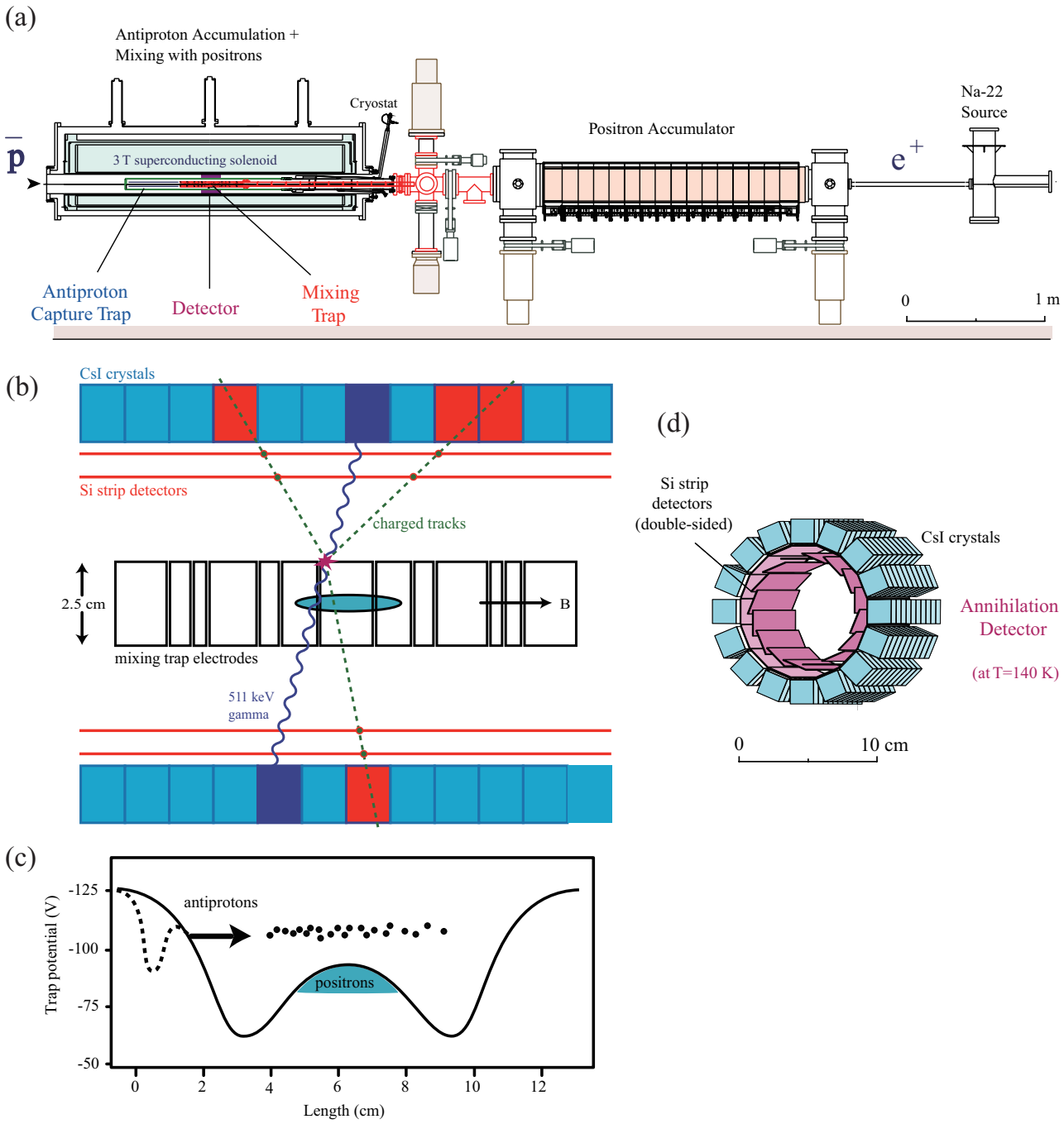

Figure 1.2: A schematic drawing of the experimental setup of the ATHENA experiment (a). A cross sectional view of the mixing trap (b). Potential configuration used to mix antiprotons and positrons (c). CsI crystals and Si strip detectors surrounding the mixing trap (d).

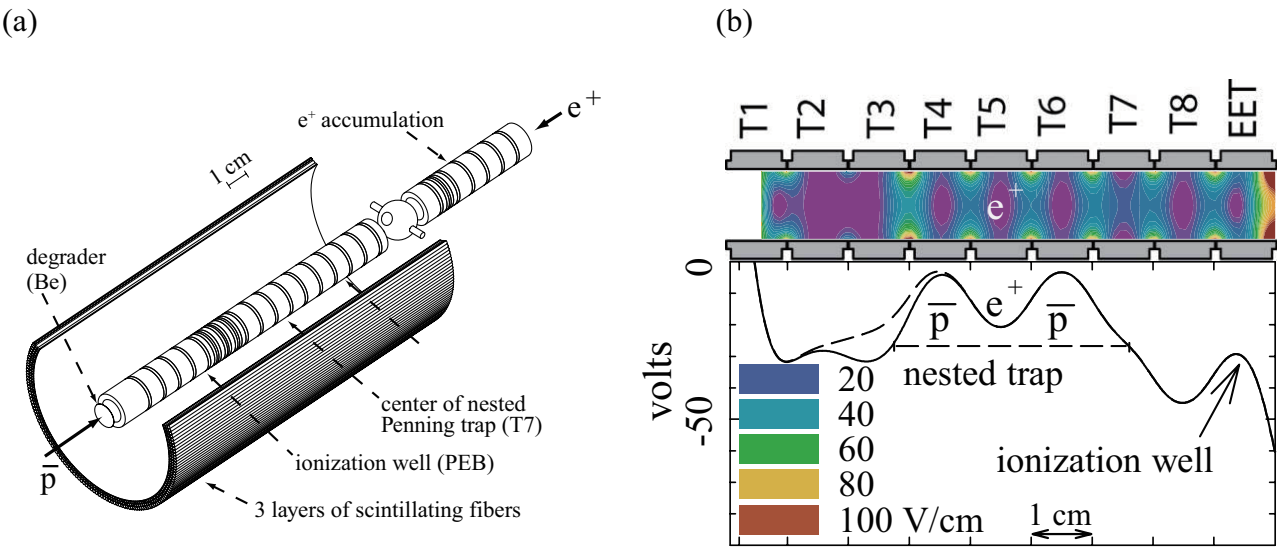

Figure 1.3: A schematic drawing of the experimental setup of the ATRAP experiment (a). A cross sectional view of the electrode with electric field strength and potential configuration of the trap (b). Antihydrogen atoms produced in the nested trap were re-ionized and accumulated in the ionization well.

chapter 2, our strategy for the spectroscopy of the antihydrogen atoms are described. Expected resolution of the measurement in our system are also discussed. In chapter 3, details of our apparatus are presented. The apparatus consist of several parts; an antiproton catching trap, a positron accumulator, the cusp trap, transport beamlines and detectors. We especially focus on the cusp trap, which is a key component for the production of the antihydrogen atoms. In chapter 4, transport of antiprotons to the cusp trap and confinement of antiprotons in the cusp trap are described. In chapter 5, transport of positrons to the cusp trap and the confinement of positrons in the cusp trap are described. In chapter 6, production of the antihydrogen atoms is described. We confirmed the production of the antihydrogen atoms by field-ionization method. We also measured the time evolution of the production rate of the antihydrogen atoms and estimated the principle quantum number of the produced antihydrogen atom. Finally in chapter 7, results are summarized.

Chapter 2

Our strategy - Cusp trap scheme

In this chapter, our strategy to test the CPT symmetry using the antihydrogen atoms is described. In section 2.1, we compare the 1S-2S transition and ground state hyperfine transition of the antihydrogen atoms discussing advantages and disadvantages for the CPT symmetry test. In section 2.2, we consider the method to measure hyperfine transition frequency. In section 2.3, an efficient way to produce and extract antihydrogen atoms for the precise measurement are discussed. In section 2.4, recombination processes to produce antihydrogen atoms are described. Finally, in section 2.5, the summary of our strategy and the expected precision of our experiment are described.

2.1 What should we measure?

We compare 1S-2S transition and ground state hyperfine transitions to consider which is suitable for the test of CPT symmetry. Our conclusion is that the measurement of the hyperfine transition (splitting) has several advantages over 1S-2S transition. The reasons are as follows.

1. It is not necessary to confine the antihydrogen atoms for the measurement of the hyperfine splitting by a classical beam method (see section 2.2). Expected precision of the measurement proposed by us is better than kHz order (see section 2.5). On the other hand, confinement of the produced antihydrogen atoms is necessary for the laser spectroscopy of the 1S-2S transition. Since the confinement of the electrically neutral antihydrogen atoms can be realized by non-uniform magnetic field, the energy levels of the atoms shift by the Zeeman effect and the amount of the shift is different depending on the position of the atoms in the trap. This non-uniform shift of the energy levels

causes broadening of the transition line. Figure 2.1 [37] shows the relation between the energy shift by the Zeeman effect and the strength of magnetic field to confine the atoms. The depth of the trapping potential U by magnetic field B is given by $U = 0.67B$ K/T for the ground state antihydrogen atoms. Thus to confine the atom of θ K, magnetic field of $\theta/0.67$ T is required. As can be seen, even if the temperature of antihydrogen atoms is 0.67 K (magnetic field is 1 T), the resolution cannot be better than 1 MHz.

2. The frequency of the ground state hyperfine splitting of (anti)hydrogen is given by

$$\nu_{HF} = \frac{16}{3}\left(\frac{m_p}{m_p + m_e}\right)^3 \frac{m_e}{m_p}\frac{\mu_p}{\mu_N}\alpha^2 cRy + \Delta \tag{2.1}$$

where m_p is the (anti)proton mass, m_e electron(positron) mass, μ_p magnetic moment of (anti)proton, μ_N nuclear magneton, c the speed of light, α the fine structure constant, Ry the Rydberg constant, and Δ correction terms. The frequency is proportional to the magnetic moment of the antiproton which is known only within 0.3 % precision [9], while other values are measured with better precisions (see table 1.2). Thus we can improve the precision of the magnetic moment of antiproton by three order of magnitude.

In addition, we note that the equation 2.1 can reproduce the experimental value within 0.1 % precision when $\Delta = 0$ for hydrogen atom. Including QED correction and non-relativistic magnetic size correction (Zemach correction), recent calculation of ν_{HF} agree with the experimental value of hydrogen atom within 3.5×10^{-6} precision [20]. Precision of the calculation is limited by the information on the magnetic and electric distribution of proton. Considering the expected precision of the measurement proposed by us ($\leq 10^{-6}$ see section 2.5), we can get ν_{HF} for antihydrogen atoms with a precision better than the theoretically predicted value for hydrogen atoms, i.e., the comparison of hyperfine splitting between antihydrogen and hydrogen atoms will allow us to explore a new physics regime which is not reachable by the present theory.

3. Kostelecky and his group proposed a theory [38], in which the Dirac equation was modified to include CPT violating terms in the Hamiltonian. They showed that the energy shift due to the CPT violating effect was not cancelled in hyperfine transitions whereas it was cancelled in the leading term in 1S-2S transition.

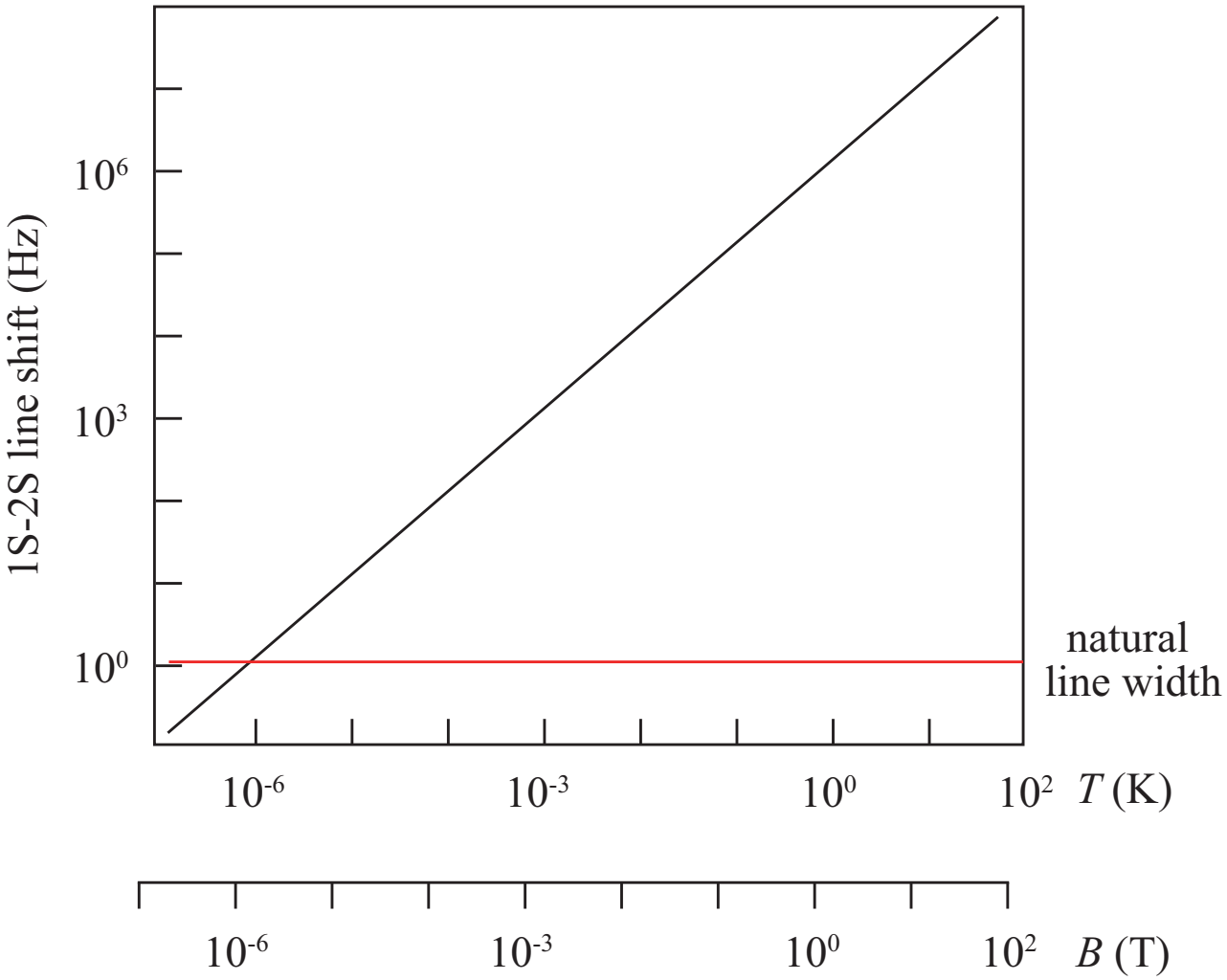

Figure 2.1: Shift of 1S-2S transition frequency of (anti)hydrogen atoms in the magnetic trap. The required magnetic field to confine (anti)hydrogen atoms is determined by their temperature.

2.2 How to measure the hyperfine splitting

The most precise measurement of the ground state hyperfine splitting of hydrogen atoms was accomplished by the maser technique [18]. However, this method can not be applied to the antihydrogen spectroscopy, since a large number of antihydrogen atoms has to be kept inside an RF cavity for a long time.

On the other hand, as early as 1930s, Rabi and his group measured the ground state hyperfine splitting of the hydrogen within 10 % precision by a simple Stern-Gerlach type experiment [39]. Figure 2.2 [39] is a schematic drawing of their experimental setup. The atomic hydrogen beam created left side was collimated and passed through the region where non-uniform magnetic field was applied. Then the beam split into two lines depending on their spin state. From the distance of the two lines, the transition energy was decided.

Figure 2.3 [40] shows an improved scheme. Hydrogen atoms from a source were selected at the A magnet depending on their spin state, then they passed through the R.F. Loop. When the RF frequency matched with the transition frequency of the atoms, the spin of the atoms flipped. The atoms were selected again at the B magnet and reached the detector (Pirani gauge). The transition frequency was determined by the change of the number of the atoms reached to the detector. By this method, Nafe and Nelson obtained $\nu_{HF} = 1420.410 \pm 0.006$ MHz in 1948 [41], and Kusch obtained $\nu_{HV} = 1420.40573 \pm 0.00005$ MHz in 1955 [42].

This method is compatible with our antihydrogen experiment. It is not necessary to confine antihydrogen atoms in the magnetic field, and the spectroscopy can be conducted at a distant place from the antihydrogen production trap where a strong magnetic field (~ 2 T) is applied.

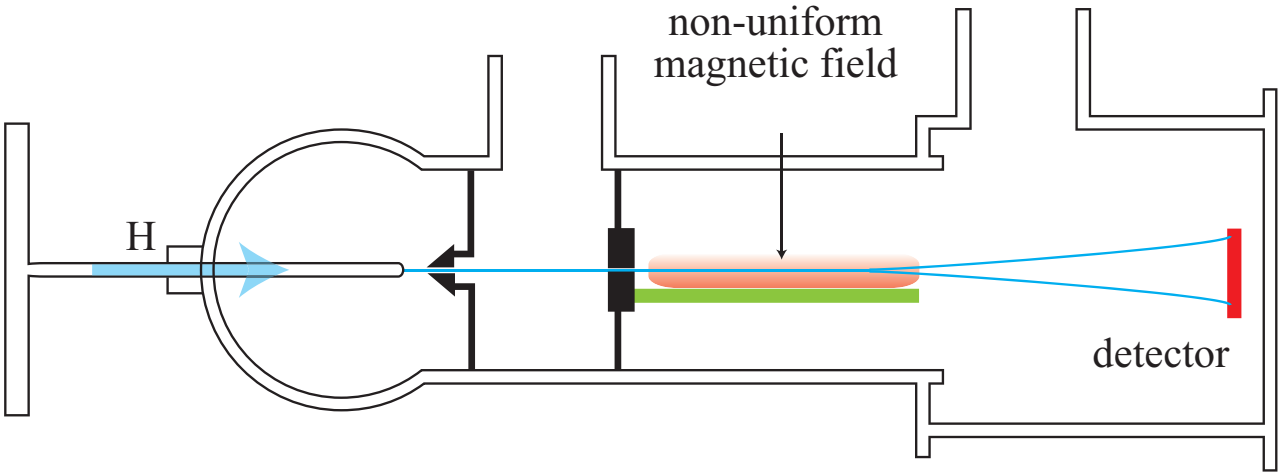

Figure 2.2: A schematic drawing of the experimental setup to measure hyperfine splitting of the hydrogen atoms in flight developed by Rabi.

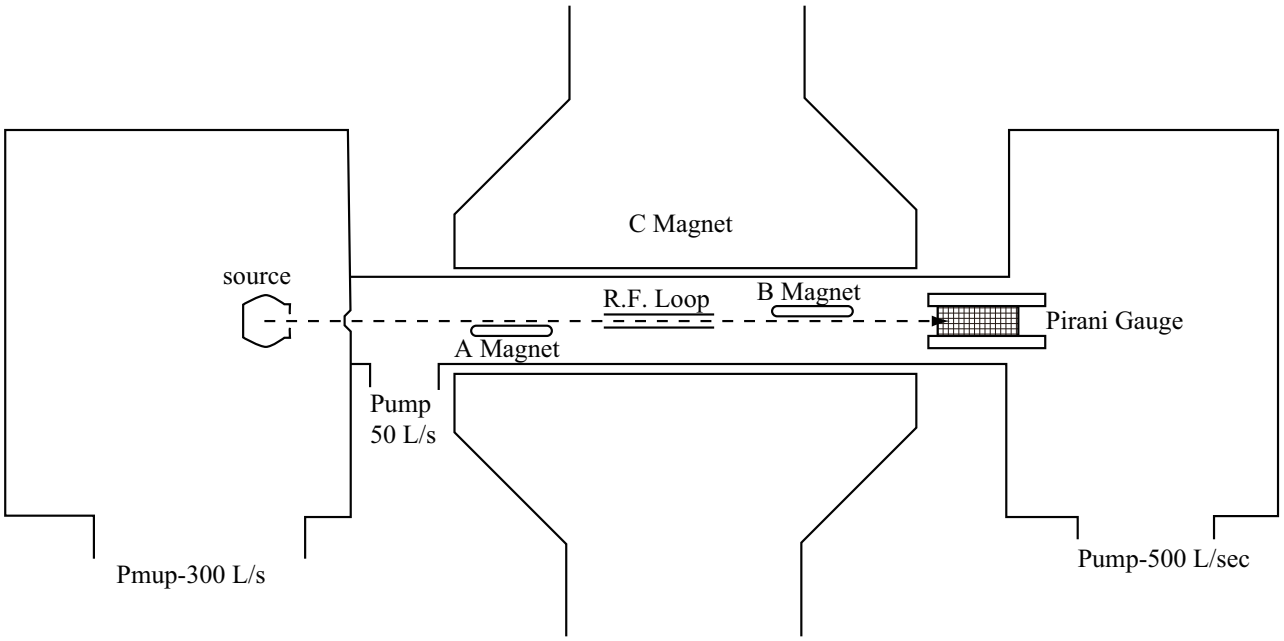

Figure 2.3: A schematic drawing of the experimental setup used by Prodell and Kusch for the measurement of the ground state hyperfine splitting of the hydrogen atoms.

2.3 How to make antihydrogen beam

Method to produce a large number of cold antihydrogen atoms is described in section 1.3 (i.e. confine positrons and antiprotons in the trap and recombine them.). Here, we consider how to extract antihydrogen atoms as a beam for the spectroscopy of ground state hyperfine splitting. We propose to use a cusp magnetic field whose magnetic field lines are shown schematically in figure 2.4. The magnetic field is created by two coils whose current direction is opposite as indicated by red arrows. There are two advantages in this magnetic field.

1. A spin polarized antihydrogen beam is extracted along the axis.

   Figure 2.5 shows the Breit-Rabi diagram, the energy levels of the antihydrogen atom in ground state as a function of the external magnetic field. Energy levels of the atom whose positron spin is antiparallel to the magnetic field increase with the magnetic field. In other words, it is attracted to a region where the magnetic field is lower than other places (Low Field Seeking state, LFS). On the other hand, the energy levels of the atom whose positron spin is parallel to the magnetic field decrease with magnetic field and it is attracted to a region where the magnetic field is higher than other places (High Field Seeking state, HFS).

   Figure 2.6 (a) shows a 2D map of the strength of the cusp magnetic field. Figures 2.6 (b) and (c) ((d) and (e)) show trajectories of antihydrogen atoms in LFS and HFS produced at $z = -0.14$ m[1], respectively. In this simulation, kinetic energy of the atoms is fixed. The values in the parentheses give corresponding temperature of antihydrogen atoms when their average kinetic energies match with the kinetic energies used for simulation. As can be seen from the figure, atoms in LFS are extracted to downstream side while those in HFS are not. Thus the extracted antihydrogen atoms are polarized automatically. Figure 2.7 (a) shows the enhancement factor of antihydrogen atoms transported 1.2 m downstream[2] from the center of the cusp trap ($z = 1.2$ m) as a function of kinetic energy. For example, when kinetic energy of the atoms is 0.26 meV (3 K), the number of the atoms in LFS reached $z = 1.2$ m is enhanced 50 times compared to the number expected from the solid angle while that in HFS is suppressed to 1/100. Figure 2.7 (b) shows the

[1] Antihydrogen atoms were produced around $z = -0.14$ m in the present experimental condition. See chapter 6.

[2] We plan to put a detector around here.

polarization[3] as a function of kinetic energy. When the kinetic energy of the atom is less than 0.86 meV (10 K), the polarization of the extracted beam is more than 80 %.

2. The axial symmetry of the magnetic field assures stable confinement of positrons and antiprotons.

   Since the antihydrogen atoms are produced through recombinations of positrons and antiproton in the trap, stable confinements of the charged particles are one of the most important properties required for the recombination trap. It is known that the equation of motion of charged particles in the trap whose magnetic field is uniform has a stable solution (see section 5.2). This is also true for non-uniform magnetic fields as long as the field is axially symmetric [43]. The stability analysis of the cusp trap was carried out [44] and a stable solution was found.

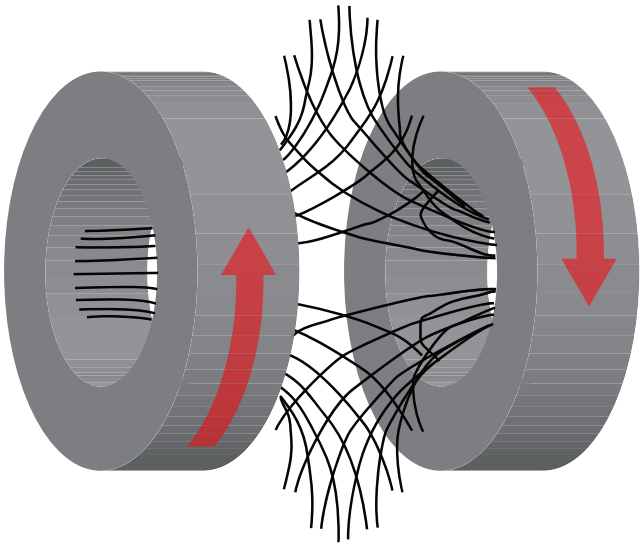

Figure 2.4: A schematic view of the coils to generate the cusp magnetic field with direction of the current and magnetic field lines.

[3]We define the polarization as $(n_{LFS} - n_{HFS})/(n_{LFS} + n_{HFS})$ where n_{LFS} and n_{HFS} are the number of antihydrogen atoms in LFS and HFS reached $z = 1.2$ m respectively.

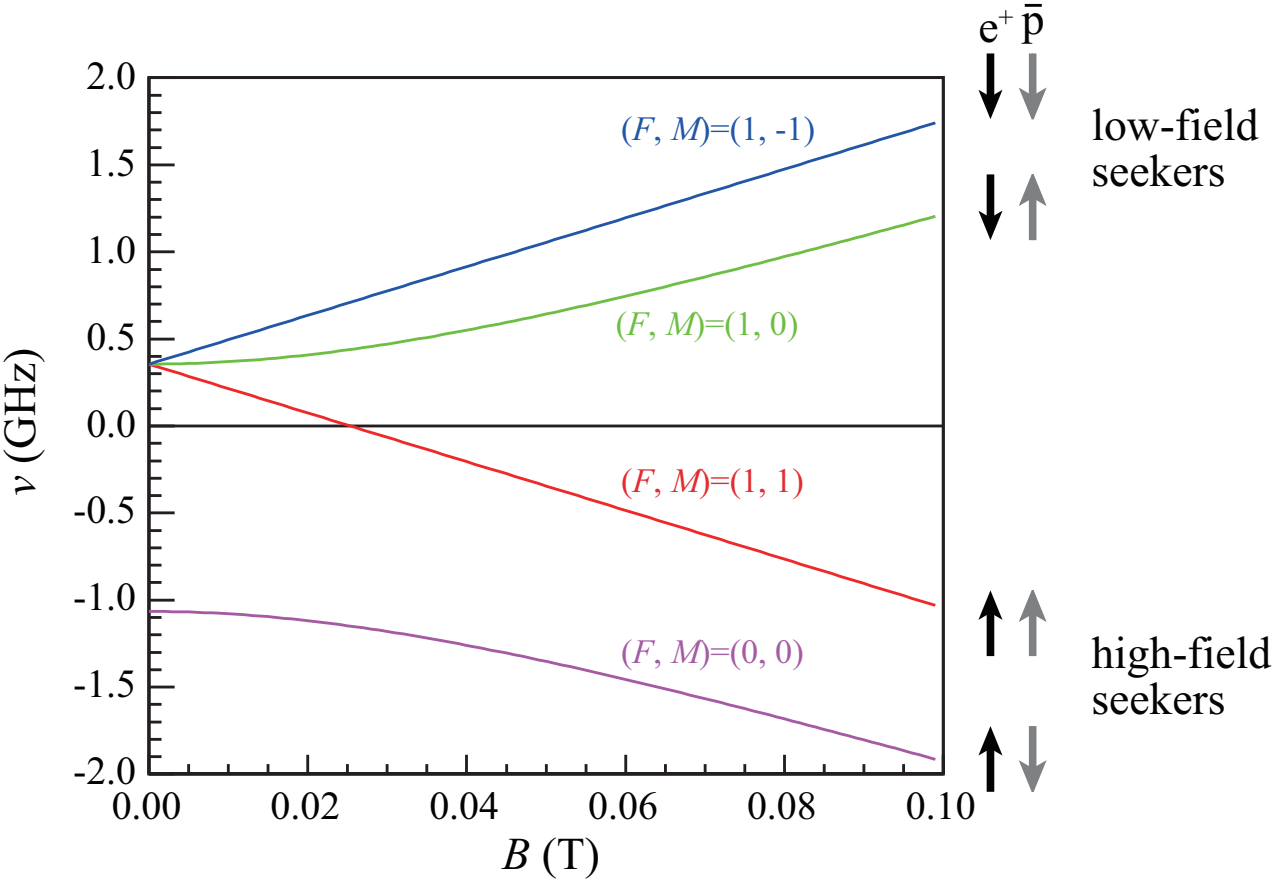

Figure 2.5: Energy levels of the antihydrogen atoms in ground state as a function of external magnetic field. The atom whose positron spin is anti-parallel to the magnetic field is called low-field seeker while whose positron spin is parallel to the magnetic field is called high-field seekers.

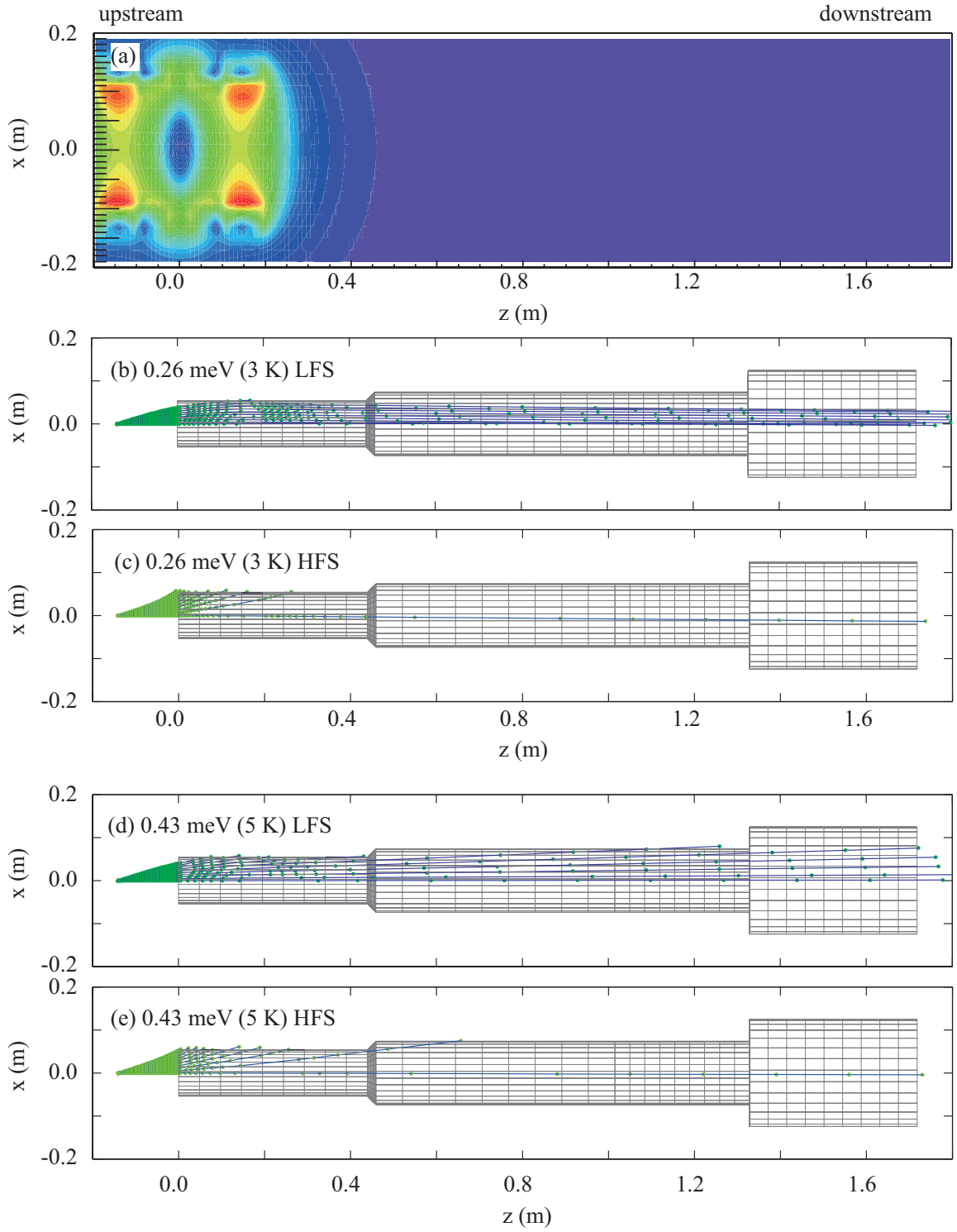

Figure 2.6: Results of trajectory simulation of the antihydrogen atoms produce in the cusp magnetic field at $z = -0.14$ m. A 2D map of the strength of the magnetic field (a). Trajectories of antihydrogen atoms of 0.26 meV (3 K) in LFS (b) and in HFS (c). Trajectories of antihydrogen atoms of 0.43 meV (5 K) in LFS (d) and in HFS (e).

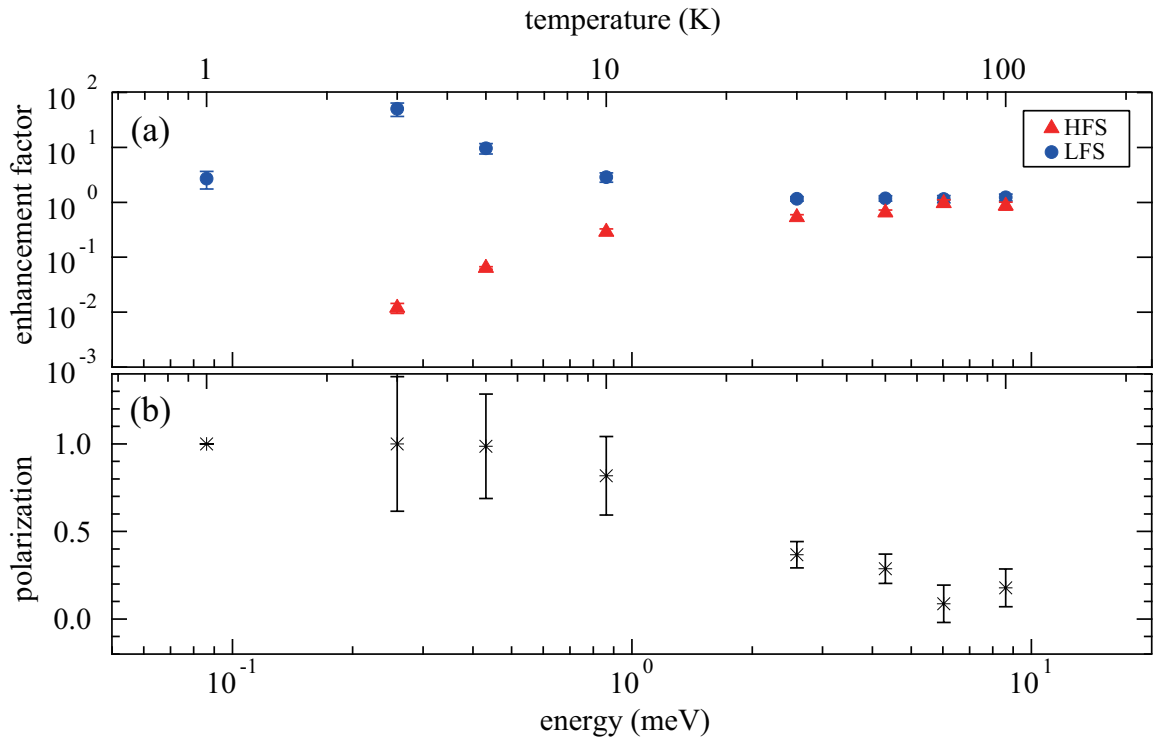

Figure 2.7: The enhancement factor of the antihydrogen atoms in LFS (blue) and in HFS (red) transported 1.2 m downstream from the center of the cusp trap as a function of kinetic energy of the atom (a). Polarization of the extracted antihydrogen beam as a function of kinetic energy of the atom (b).

2.4 Recombination process

The major recombination processes under no external fields are summarized here (in this section). More sophisticated treatments of the processes under external fields can be found in ref. [45, 46, 47, 48, 49, 50, 51].

2.4.1 Radiative recombination(RR)

The most simple reaction

$$\bar{\mathrm{p}} + \mathrm{e}^+ \rightarrow \bar{\mathrm{H}} \tag{2.2}$$

is not allowed because of the conservation of energy and momentum, and at least one more particle is necessary in the equation 2.2. One possibility is a radiative recombination(RR) process, which is the inverse process of photo-ionization, described as

$$\bar{\mathrm{p}} + \mathrm{e}^+ \rightarrow \bar{\mathrm{H}} + \mathrm{h}\nu, \tag{2.3}$$

where a photon takes care of the excess energy. The cross section of this reaction is given by [35]

$$\sigma_{RR}(n, E_{cm}) = 2.1 \times 10^{-22} \frac{E_0^2}{nE_{cm}(E_0 + n^2 E_{cm})} \ \mathrm{cm}^2, \tag{2.4}$$

where E_0 is 13.6eV, E_{cm} the relative energy in the positron-antiproton center-of-mass frame, n the principle quantum number of the produced antihydrogen atom. As can be seen from the formula, the antihydrogen atoms in low n states are preferably produced. More precisely, the cross section is proportional to n^{-1} when $E_0 \gg n^2 E_{cm}$ and n^{-3} when $E_0 \ll n^2 E_{cm}$. The n dependence of the cross section is shown in figure 2.8 for several different E_{cm}'s. The total cross section $\sigma_{RR}(E_{cm})$ can be obtained by summing up the $\sigma_{RR}(n, E_{cm})$ over n. However, in real experiments, the produced antihydrogen atoms collide with surrounding positrons and antiprotons and the atoms whose binding energy is smaller than the kinetic energy of the surrounding particles are re-ionized. Thus there exists maximum n (minimum binding energy) at which recombined atoms are not re-ionized and the summation should be taken from $n = 1$ to $n = n_{max}$.

$$\sigma_{RR}(E_{cm}) = \sum_{n=1}^{n_{max}} \sigma_{RR}(n, E_{cm}). \tag{2.5}$$

If the relative velocity distribution is spherically symmetric and we define the reaction coefficient α_{RR}, using the total cross section σ_{RR}, relative velocity v, and relative velocity

distribution $f(v)$, as

$$\alpha_{RR} = \int \sigma_{RR} v f(v) d^3v, \tag{2.6}$$

the reaction rate R of the recombination can be evaluated by

$$R = \int \alpha_{RR} \rho_e \rho_p d^3r, \tag{2.7}$$

where ρ_e is density of positrons, ρ_p density of antiprotons.

When $f(v)$ is the Maxwell distribution at temperature T, the reaction coefficient α_{RR} is given by Bell [52] as

$$\alpha_{RR} = 1.92 \times 10^{-13} \frac{1}{\sqrt{kT}} \left\{ \ln\left(\frac{5.66}{\sqrt{kT}}\right) + 0.196(kT)^{\frac{1}{3}} \right\} \text{ cm}^3/\text{s}, \tag{2.8}$$

where k is the Boltzmann constant. It is known that this equation can be approximated by

$$\alpha_{RR} = 3.79 \times 10^{-13} (kT)^{-0.678} \text{ cm}^3/\text{s} \tag{2.9}$$

within 1 % error if the kT[4] is between $0.07 < kT < 0.7$ and within 10 % error $0.01 < kT < 3$ [52].

2.4.2 Three body recombination(TBR)

The other process is three body recombination (TBR) process, which is the inverse process of positron impact ionization, described as

$$\bar{\text{p}} + \text{e}^+ + \text{e}^+ \rightarrow \bar{\text{H}} + \text{e}^+. \tag{2.10}$$

where the second positron takes care of the excess energy. The rate of this reaction can be written as

$$R = \sum_n^{n_{max}} \int \alpha_{TBR}(n, E_{cm}, \rho_e) \rho_e \rho_p d^3r, \tag{2.11}$$

where $\alpha_{TBR}(n, E_{cm}, \rho_e)$ is give [35] by

$$\alpha_{TBR}(n, E_{cm}, \rho_e) = 1.96 \times 10^{-29} \rho_e \frac{1}{kT} n^6 \text{ cm}^3/\text{s} \tag{2.12}$$

when $f(v)$ is the Maxwell distribution.

In contrast to α_{RR}, α_{TBR} increases with n. The total reaction coefficient $\alpha_{TBR}(E_{cm}, \rho_e)$ can be obtained by

$$\alpha_{TBR}(E_{cm}, \rho_e) = \sum_n^{n_{max}} \alpha_{TBR}(n, E_{cm}, \rho_e). \tag{2.13}$$

[4] In this section, the unit of kT is always eV.

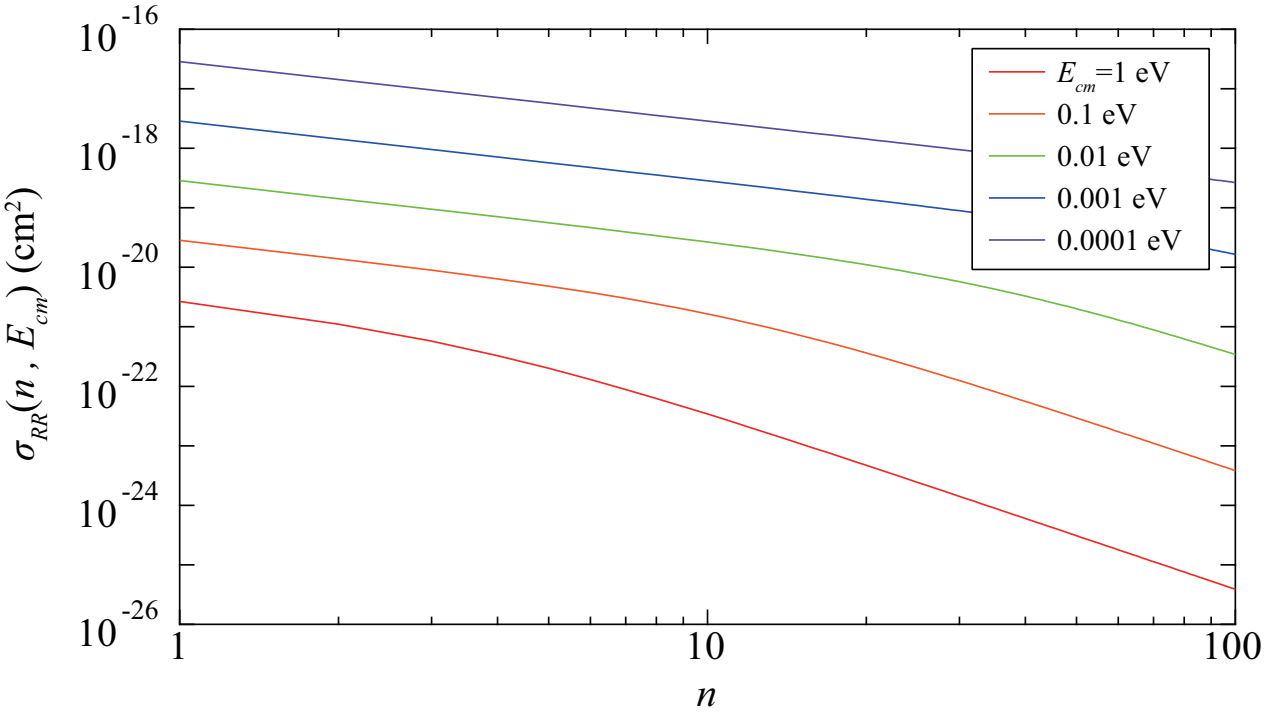

Figure 2.8: Cross sections of the radiative recombination process as a function of the principle quantum number of the produced antihydrogen atoms.

It is important to evaluate n_{max} correctly because $\alpha_{TBR}(n_{max}, E_{cm}, \rho_e)$ dominate the total reaction coefficient. Considering the binding energy of the antihydrogen atom is expressed as $E_n = 13.6/n^2$ eV, we assume the threshold as

$$\frac{13.6}{n_{max}^2} = akT, \tag{2.14}$$

where a is a tunable parameter close to unity. Replacing the sum with integral, $\alpha_{TBR}(E_{cm}, \rho_e)$ is given by

$$\alpha_{TBR}(E_{cm}, \rho_e) = 1.96 \times 10^{-29} \rho_e \frac{1}{kT} \int_1^{n_{max}} n^6 dn \text{ cm}^3/\text{s} \tag{2.15}$$

$$= 2.3 \times 10^{-27} \rho_e (kT)^{-4.5} \text{ cm}^3/\text{s} \tag{2.16}$$

when a=2 [35].

2.4.3 Summary of the reaction processes

The reaction coefficients of the radiative and the three body recombination processes are plotted as a function of the relative energy in figure 2.9. Since the α_{TBR} depend on the density of the positron, several curves for different ρ_e are drawn. As is seen from figure 2.9, α_{TBR} is

much larger than α_{RR} in the cryogenic temperature region for reasonably achievable positron densities.

Considering the temperature dependence of α_{TBR} including the external magnetic field is also proportional to $T^{-4.5}$ [33], the results shown here seem valid at least for the temperature dependence. The recent experimental result, however, revealed $\alpha \sim T^{-1.1\pm0.5}$ [53] which is not in accord with neither $\alpha_{RR} \propto T^{-0.678}$ nor $\alpha_{TBR} \propto T^{-4.5}$. Thus further experimental and theoretical studies are expected in this region.

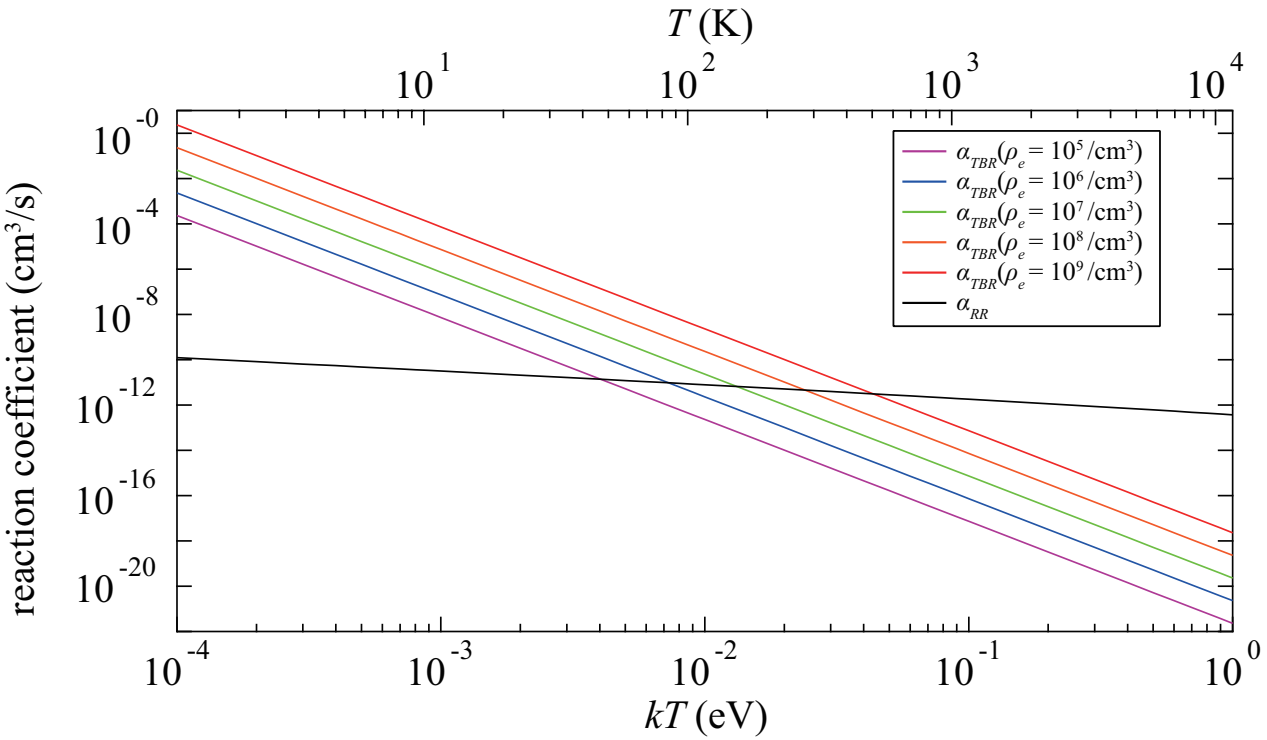

Figure 2.9: Reaction coefficients of the radiative recombination (black curve) and the three body recombination (colored curves) as a function of the relative energy.

2.5 The road to the spectroscopy

2.5.1 Summary of our strategy

We summarize our strategy to test the CPT symmetry according to above considerations.

1. The goal of the project is the spectroscopy of the ground state hyperfine splitting of antihydrogen atoms.

2. The atomic beam method originally developed by Rabi is adopted to measure the hyperfine splitting.

3. The cusp magnetic field is used to produce antihydrogen atoms and to extract spin polarized antihydrogen beam.

Figure 2.10 schematically shows our setup for the spectroscopy of the ground state hyperfine splitting of antihydrogen atoms. The produced antihydrogen atoms in low field seeking state are selectively focused and the spin polarised antihydrogen beam is extracted to the microwave cavity. When the frequency of the microwave matches with the transition frequency of the ground state hyperfine splitting, the spin of the antihydrogen atoms (positrons) flips and the atoms transit to the high field seeking state. They are defocused by the sextupole magnet (figure 2.10 (top)). On the other hand, when the frequency does not match with the transition frequency, the atoms remain in the low field seeking state. They are focused by the sextupole magnet (figure 2.10 (bottom)). Thus, resonance frequency can be determined as a dip in the count of the antihydrogen atoms on the detector as shown in the inset of figure 2.10.

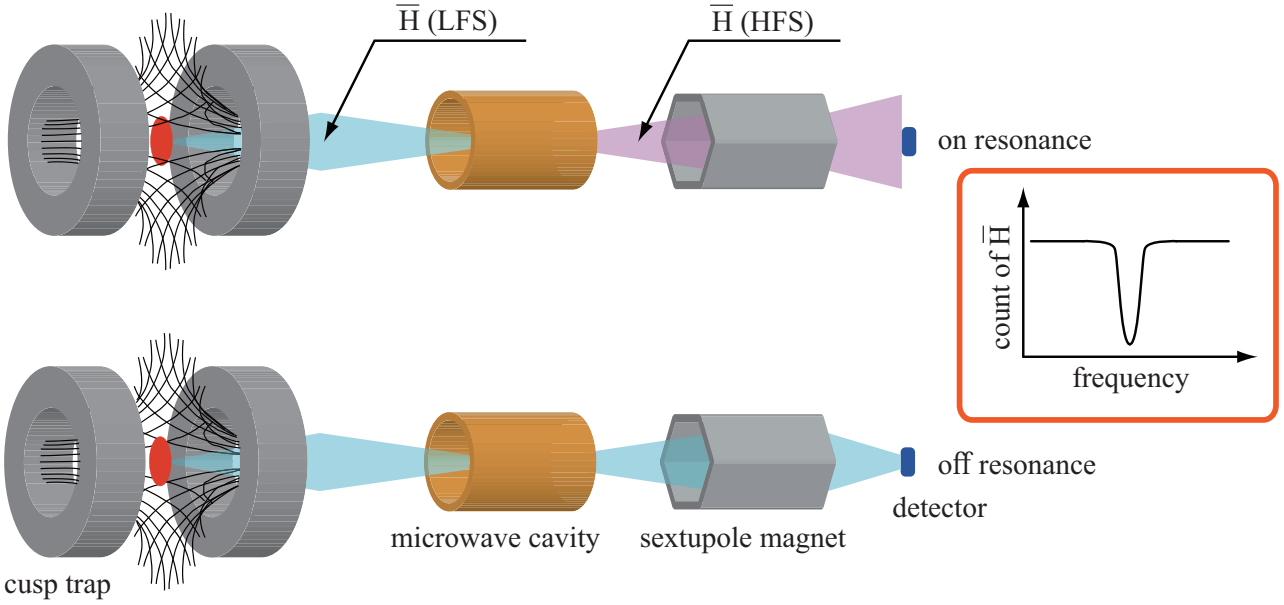

Figure 2.10: A conceptual drawing of our method to measure the ground state hyperfine splitting of antihydrogen atoms. When the frequency of the microwave in the cavity matches with the transition frequency of the hyperfine splitting of the atom, the atom transits to the HFS and is defocused by the sextupole magnet while it does not match with the transition frequency, the atom stays in the LFS and is focused on the detector. The transition frequency is determined from the dip position of the count of antihydrogen atoms as shown in the inset.

2.5.2 Expected precision

The achievable precision of this measurement is estimated as follows.

1. The oscillating magnetic field in the cavity $B(t) = B_0(e^{i\omega t} + e^{-i\omega t})$ induces transition between two of the hyperfine states of the antihydrogen atoms.

2. The transition probability of these states can be written as a function of time t by Rabi's formula [54].

$$P_{12}(t) = \frac{\gamma^2/\hbar^2}{\gamma^2/\hbar^2 + (\omega - \omega_{12})^2/4} \sin^2 \left\{ \sqrt{\frac{\gamma^2}{\hbar^2} + \frac{(\omega - \omega_{12})^2}{4}} t \right\}, \tag{2.17}$$

where $\hbar\omega_{12}$ is the energy difference of the states, ω frequency of the external field, $\hbar$ reduced Planck constant, and γ the coupling constant.

3. In this case, the coupling constant γ is given by

$$\gamma = \frac{e\hbar B_0}{2m_e}. \tag{2.18}$$

4. From the equation 2.17, amplitude of P_{12} reaches maximum when

$$\omega = \omega_{12}, \tag{2.19}$$

and the equation is reduced to

$$P_{12}(t) = \sin^2\left(\frac{\gamma}{\hbar}t\right). \tag{2.20}$$

P_{12} in equation 2.20 reaches its first maximum when

$$\frac{\gamma}{\hbar}t = \frac{\pi}{2}. \tag{2.21}$$

5. From the equation 2.21, the relation between required magnetic field amplitude B_0 and time t is given by

$$B_0 = \frac{m_e\pi}{te}. \tag{2.22}$$

6. We assume the distribution of the antihydrogen atoms is the Maxwell distribution at 15 K[5] whose most probable speed is 500 m/s. Because the length of the cavity is 20 cm which is a typical size for the 1.42 GHz microwave cavity, we obtain the values $t = 0.4$ ms and $B_0 = 4.5 \times 10^{-8}$ T (1.6×10^{-9} W).

7. One can find, from the equation 2.17, that the width (FWHM) of the resonance in frequency ($\delta\nu$) is given by

$$\delta\nu = \frac{4\gamma}{2\pi\hbar}. \tag{2.23}$$

8. Substituting all values, we obtain

$$\delta\nu = 2.5 \text{ kHz}. \tag{2.24}$$

9. Since the $\nu_{HF} = 1.42$ GHz, the relative resolution is expected to be $\delta\nu/\nu_{HF} = 1.8 \times 10^{-6}$.

Thus, with good enough statistics, the center of the resonance line can be determined with a relative precision of 10^{-6} or better [24].

[5]The environmental temperature of our trap is roughly 15 K

Chapter 3

Apparatus

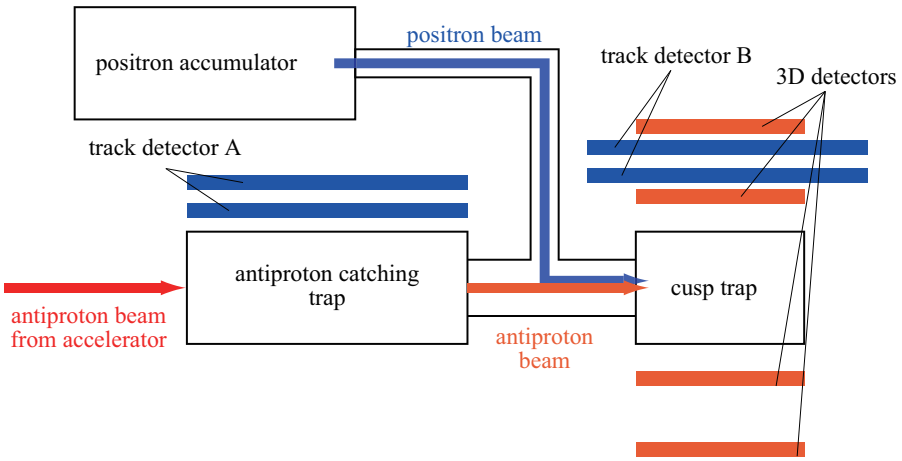

Figure 3.1: A schematic drawing of the apparatus. It consists of an antiproton catching trap, a positron accumulator, transport beamlines, a cusp trap and detectors.

In this chapter, details of apparatus to produce antihydrogen are described. Figure 3.1 shows the apparatus schematically. Also more realistic three dimensional isometric view of the apparatus is shown in figure 3.2. The apparatus consists of several parts;

1. an antiproton catching trap to capture, cool, and compress antiprotons to make an ultra-low energy pulsed antiproton beam (section 3.1).

2. a positron accumulator to make an ultra-low energy pulsed positron beam from radio isotope (section 3.2).

3. transport beamlines for the ultra-low energy antiproton and positron beam (section 3.3).

4. a cusp trap to produce antihydrogen atoms (section 3.4).

5. a 3D detector, track detectors, and MCPPS detectors to monitor the antihydrogen atoms and to diagnose antiprotons and positrons (section 3.5).

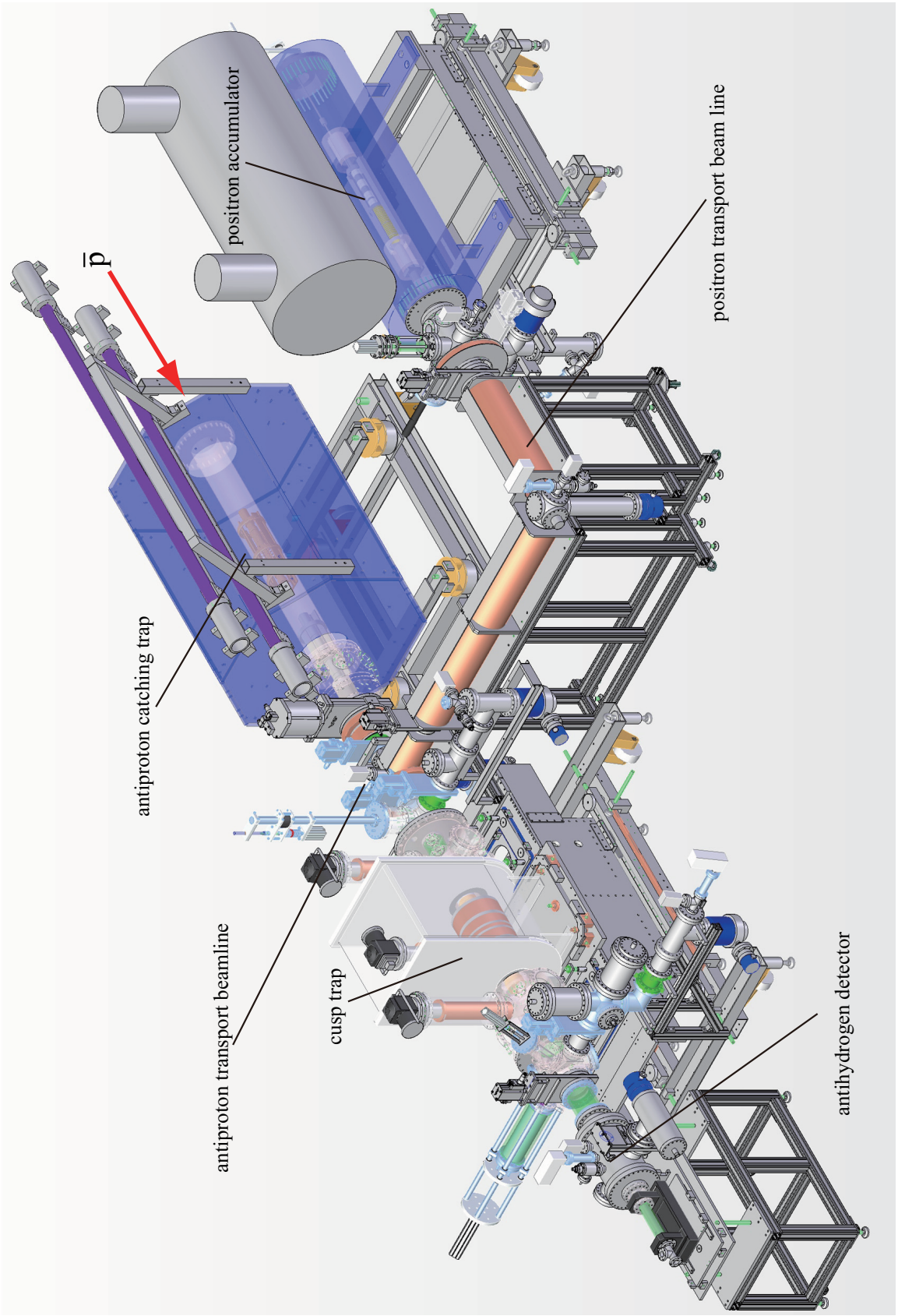

Figure 3.2: A three dimensional isometric view of the setup.

3.1 Antiproton catching trap

Figures 3.3 (a) and (b) are a cross sectional drawing of the antiproton catching trap and the magnetic field strength on axis respectively. The trap consists of a superconducting solenoid and a stack of multiple ring electrodes (MRE). At the entrance of the trap, PET foils are placed. Antiprotons from the antiproton decelerator (AD) via the radio frequency quadrupole decelerator (RFQD) (see appendix A) were first decelerated by the foils to ∼10 keV. Then they were captured in the MRE by the magnetic field and the electric potential. Inside the trap, antiprotons were cooled to sub eV by pre-loaded electrons. Next the electrons were selectively kicked out from the trap and the cloud of antiprotons was compressed by the so-called rotating wall technique. The compressed cloud was extracted as a DC or pulsed ultra-low energy (100 eV - 250 eV) beam by changing the voltages applied to the MRE. Extractor electrodes were placed downstream side of the MRE to focus the antiproton beam.

Details of components are described in the following sections.

3.1.1 Superconducting solenoid

The superconducting solenoid produces an uniform magnetic field up to 5 T, which confines charged particles radially. The uniformity of the field is better than 0.1 % in the volume of 635 mm×10 mmϕ around the center of the solenoid. The solenoid is surrounded by iron cage to shield the magnetic field outside the antiproton catching trap. The magnet is cooled by a GM refrigerator (Sumitomo SRDK-408D2-W71C) whose cooling capacity is 1.0 W at 4.2 K. A UHV bore tube whose inner diameter is 164 mm is inserted in the solenoid. The bore tube is cooled to 4-6 K by two GM refrigerators (Sumitomo SRDK-415D-W71C) whose cooling capacity is 1.5 W at 4.2 K to realize required vacuum condition; $\leq 10^{-12}$ Torr (see section 3.4.4). Details of magnetic and cooling properties such as typical cooling time of the magnet are described in ref. [55].

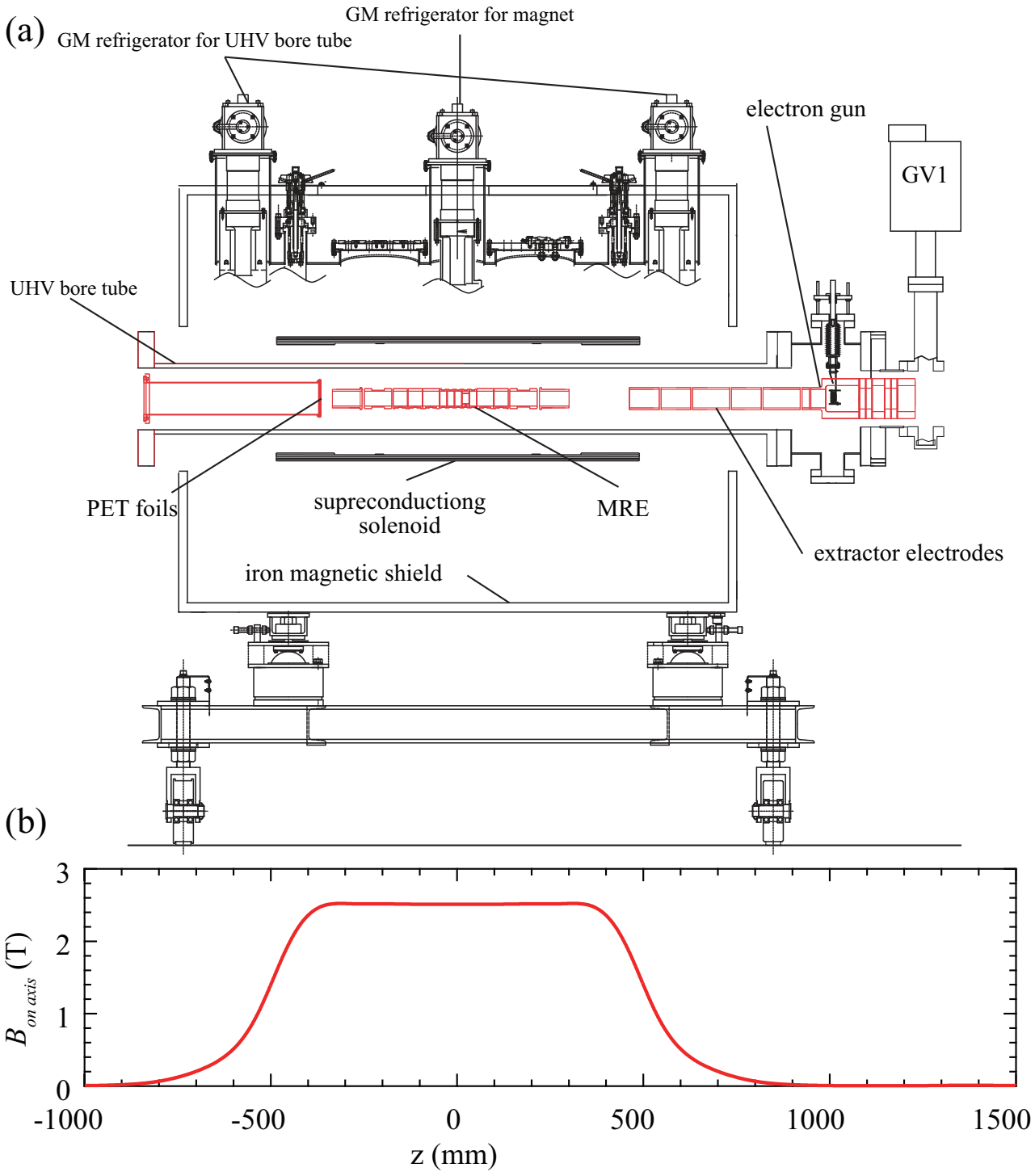

Figure 3.3: A cross sectional view of the antiproton catching trap which consists of an MRE, PET foils, extractor electrodes housed in a UHV bore tube, an electron gun and a superconducting solenoid (a). The solenoid and the UHV bore tube are cooled by GM refrigerators. Magnetic field on axis at 2.5 T (b)

3.1.2 PET foils

Double thin foils of 90 μg/cm^2 thickness made of PET (polyethylene terephtalate) (see figure 3.4 [56]) are installed at the entrance of the trap to separate vacuum between the trap ($\leq 10^{-12}$ Torr) and the upstream beamline (about 10^{-9} Torr). Since antiprotons injected into the trap lose their energy at the foils, the injection energy was adjusted to maximize the number of antiprotons captured in the trap by changing the bias voltage of the RFQD (see appendix A). Now the injection energy of antiprotons is 110 keV. On each foil, ten thin Ag strips of 50 nm (50 μg/cm^2) thickness and 940 μm width are printed(see figure 3.5 [56]) to monitor the profile of the antiproton beam by measuring secondary electrons emitted by passage of the antiprotons. The beam position is adjusted to the axial center of the MRE using the signal from the detector. Typical profile of the beam after tuning is shown in figure 3.6 [56].

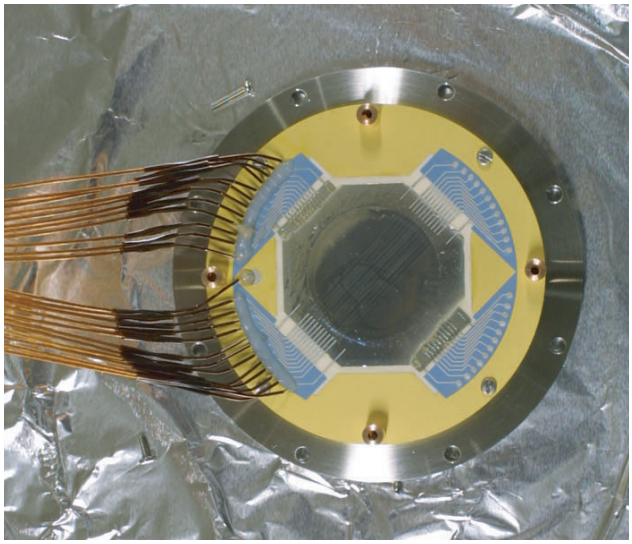

Figure 3.4: A photograph of the energy degrading foils with beam profile monitor.

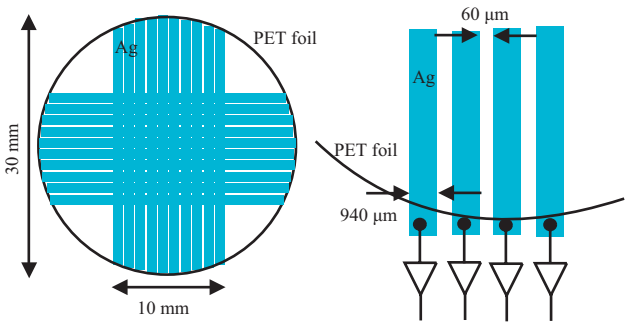

Figure 3.5: A schematic drawing of the beam profile monitor. Thin Ag strips are printed on the PET foils.

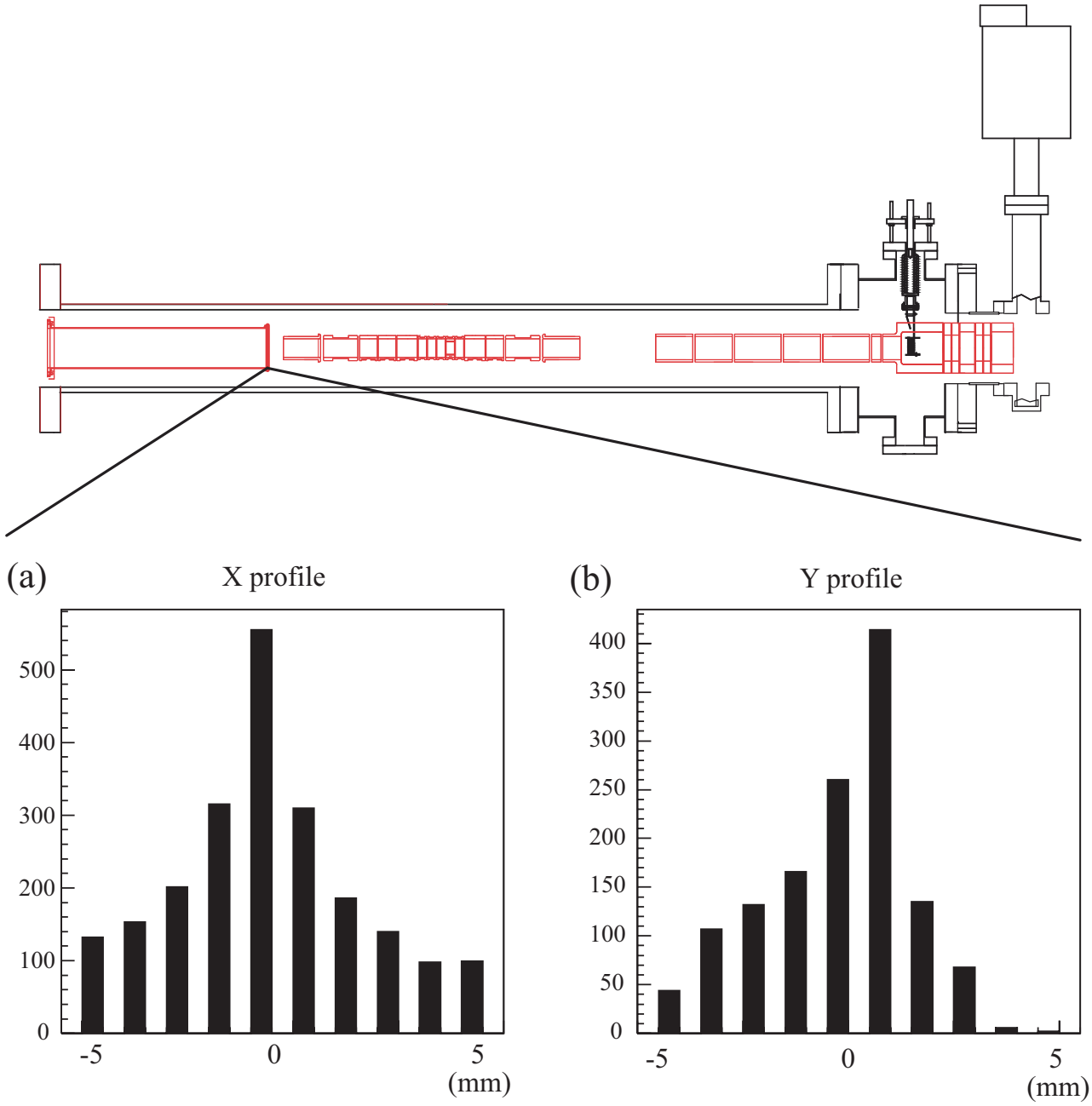

Figure 3.6: Typical beam profile measured by the beam profile monitor.

3.1.3 Multi ring electrodes (MRE)

Figure 3.7 is an isometric view of the MRE of the antiproton catching trap. The ring electrodes are aligned on a precisely machined plate[56] and the plate is connected to three outer rings which contact to the bore tube and hold the whole set. The MRE is cooled to around 10 K via thermal conduction with the UHV bore tube to realize the vacuum condition ($\leq 10^{-12}$ Torr). Figure 3.8 is a cross sectional drawing of the MRE. The MRE consists of 14 ring electrodes made of gold-plated oxygen free copper (C1020).

Figure 3.9 [56] shows potential configurations to capture and cool the energetic antiprotons. The upstream catching electrode (UCE) and downstream catching electrode (DCE) are used to capture and reflect energetic antiprotons. Before the injection of the energetic antiprotons a high voltage of about -13 kV is applied on the DCE. The injected antiprotons are reflected back by the potential wall made by the DCE. Then the UCE is biased about -13 kV before the antiprotons reach the UCE (figure 3.9 (a)). By this way energetic antiprotons are captured inside the MRE.

The five electrodes, FH2, FH1, BH1, S, and BH2 are used to make a harmonic potential. The captured energetic antiprotons are cooled by pre-loaded electrons and eventually settle down the bottom of the harmonic potential well. In this process, electrons and antiprotons are simultaneously trapped in the same potential well. Antiprotons undergo Coulomb scattering with electron and lose their energy. Energy of electrons are quickly (time constant of the cooling process is ~ 1 s [56]) disposed by synchrotron radiation in the strong magnetic field in the trap. After about 40 s from the injection of the energetic antiprotons, high voltages applied on the UCE and the DCE are changed to 0 V (figure 3.9 (b)).

The S electrode (azimuthally four-segmented electrode) are used to compress antiproton cloud by applying a rotating electric field [57] (see section 5.2 for the concept of this technique). Detailed considerations on the design of this MRE including material selection, heat contact with the bore tube, and machining are described in ref. [58].

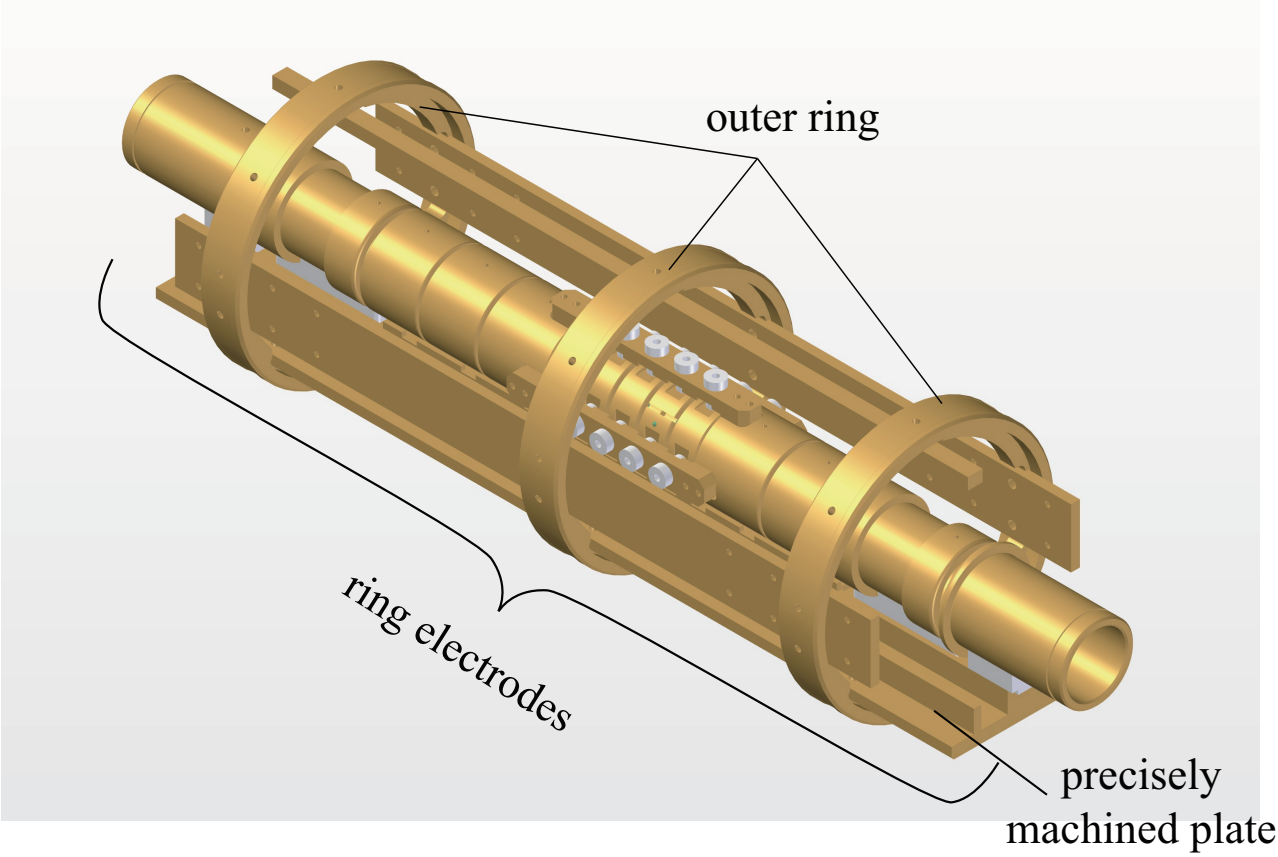

Figure 3.7: An isometric view of the MRE of the antiproton catching trap. The 14 ring electrodes, which are made of gold-plated oxygen free copper, are aligned on the precisely machined plate and the plate is connected to three outer rings which contact to the bore tube and hold the whole set.

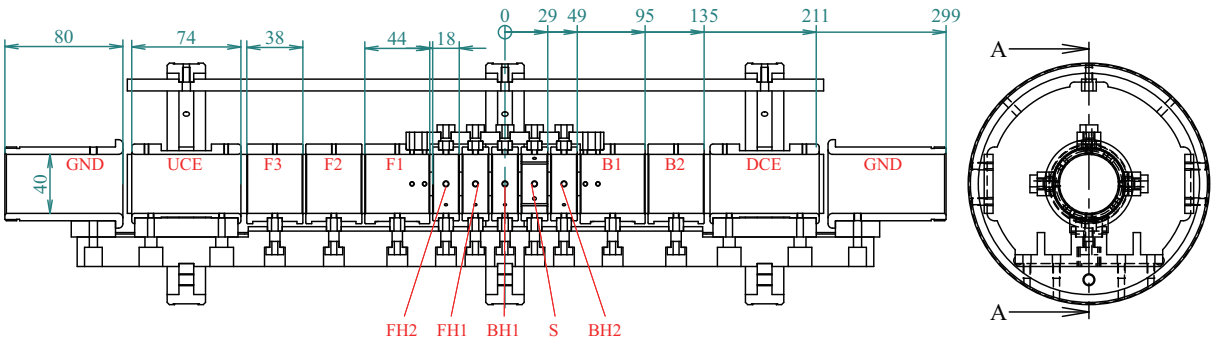

Figure 3.8: A cross sectional drawing of the MRE of the antiproton catching trap. The DCE and the UCE are used to capture energetic antiprotons by applying high voltage. The five electrodes, FH2, FH1, BH1, S, and BH2 are used to make a harmonic potential. The S electrode (azimuthally four-segmented electrode) are used to compress antiproton cloud by applying a rotating electric field.

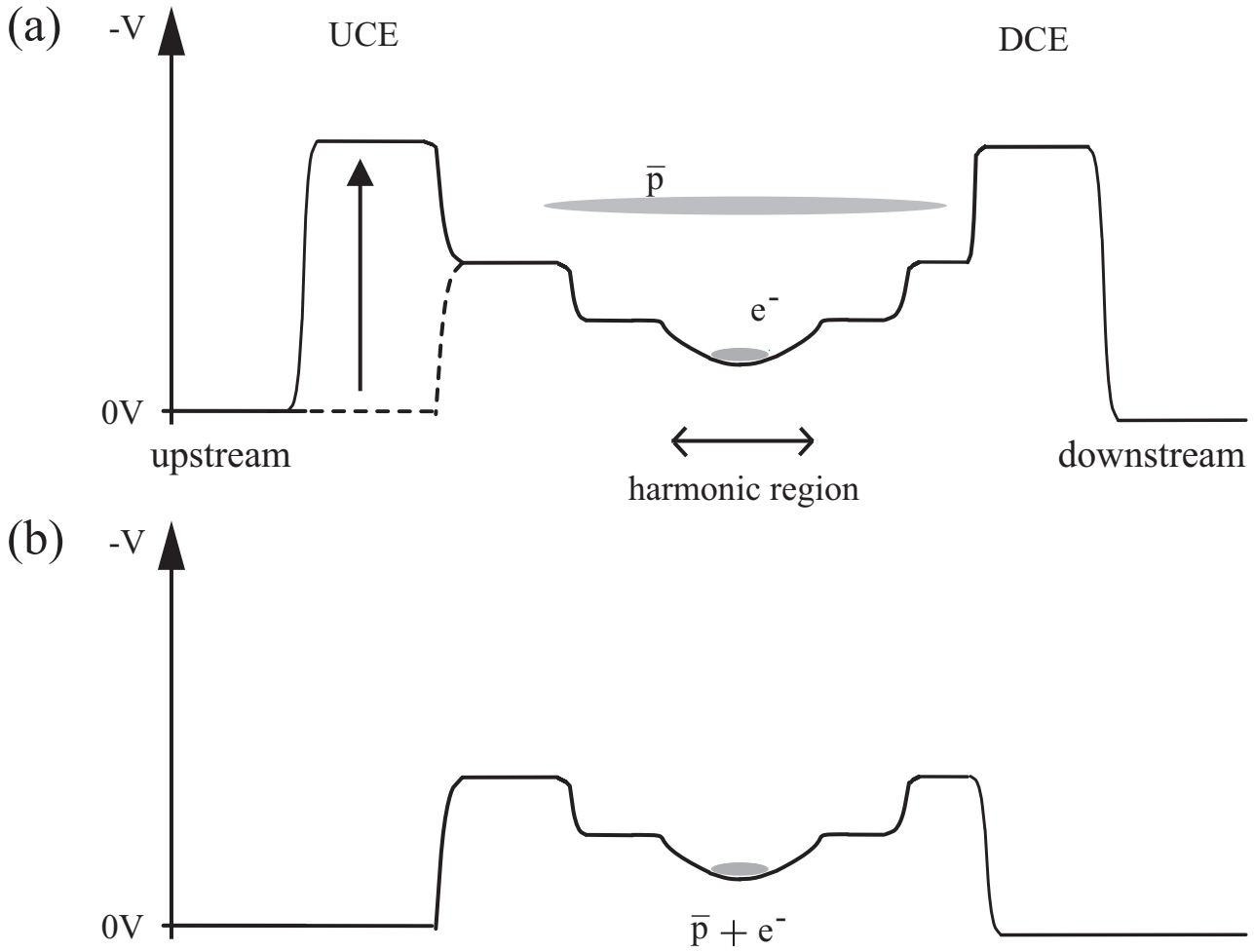

Figure 3.9: A schematic drawing of potential configurations for capture and cool the energetic antiprotons. The injected antiprotons are reflected back by the potential wall made by the DCE. Then the UCE is biased before the antiprotons reach the UCE and they are cooled by the pre-loaded electrons (a). After about 40 s from the injection of the energetic antiprotons, high voltages applied on the UCE and the DCE are changed to 0 V (b).

3.1.4 Extractor electrodes

Extraction of the ultra-low energy antiprotons from the trap where strong magnetic field is applied is difficult since the antiprotons tend to follow the field line, which diverge outside the solenoid. To suppress the divergence of the antiprotons by electrostatic lens, another stack of multiple ring electrodes (Extractor electrodes) is installed downstream side of the MRE. Figure 3.10 is an isometric view of the extractor electrodes which consist of six ring electrodes of aluminium alloy. Each electrode is aligned on a plate and the plate is connected to two outer rings which contact to the bore tube and hold the whole set. Figure 3.11 is a cross sectional view of the extractor. The inner diameter of the six electrodes are 50 mm. We carried out trajectory simulation of the extracted antiprotons with changing the voltage applied on the electrodes. The optimized trajectories are shown in figure 4.2.

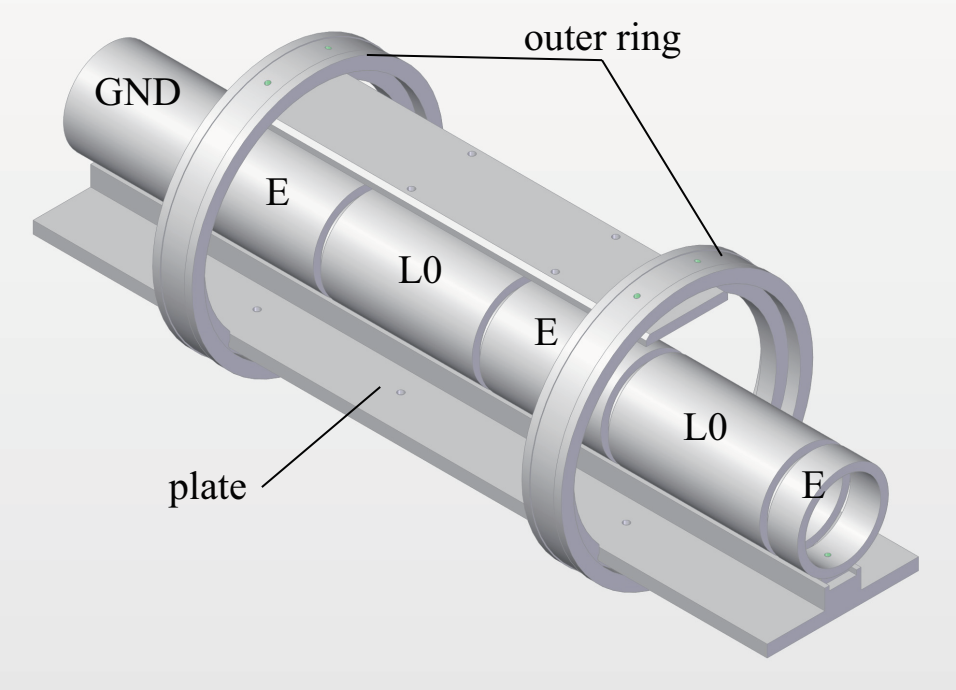

Figure 3.10: An isometric view of the extractor electrodes of the antiproton catching trap, which consist of six ring electrodes of aluminium alloy. Each electrode is aligned on a plate and the plate is connected to two outer rings which contact to the bore tube and hold the whole set.

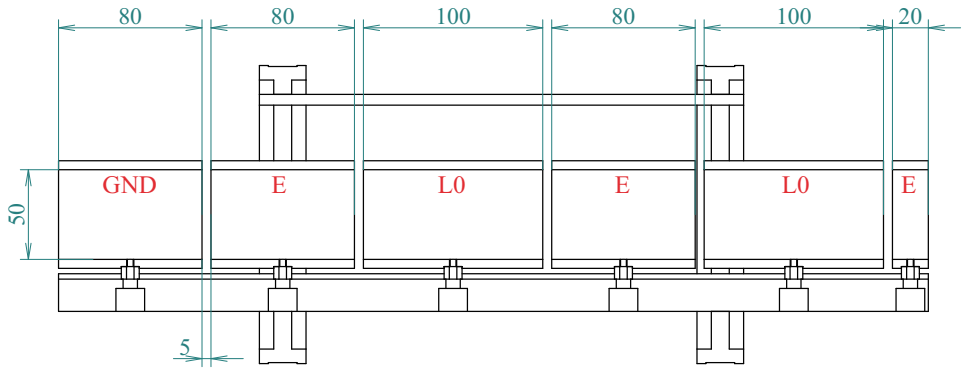

Figure 3.11: A cross sectional drawing of the extractor electrodes of the antiproton catching trap. The inner diameter of the six electrodes are 50 mm.

3.1.5 Electron gun

As is explained, the energetic antiprotons captured in the catching trap are cooled by electrons. To prepare electron cloud in the catching trap, an electron gun is attached as shown in figure 3.12 (a). Figure 3.12 (b) shows the structure of the electron gun. It consists of following parts,

1. a barium sintered cathode,
2. an electrode A to negatively bias the cathode,
3. an electrode B which works as anode,
4. an electrode C which is in the ground potential to fix electric field around the cathode,
5. an electrode D to cover the whole to insert the gun.

The gun is mounted on a movable mechanism and actuated by an air cylinder. It is inserted only when electrons are injected into the trap. The electrode D covers the hole to insert the gun so that the stray electric field from the gun does not affect the trajectory of the extracted antiprotons (see figure 3.12 (c)). Details of this electron gun are described in [55].

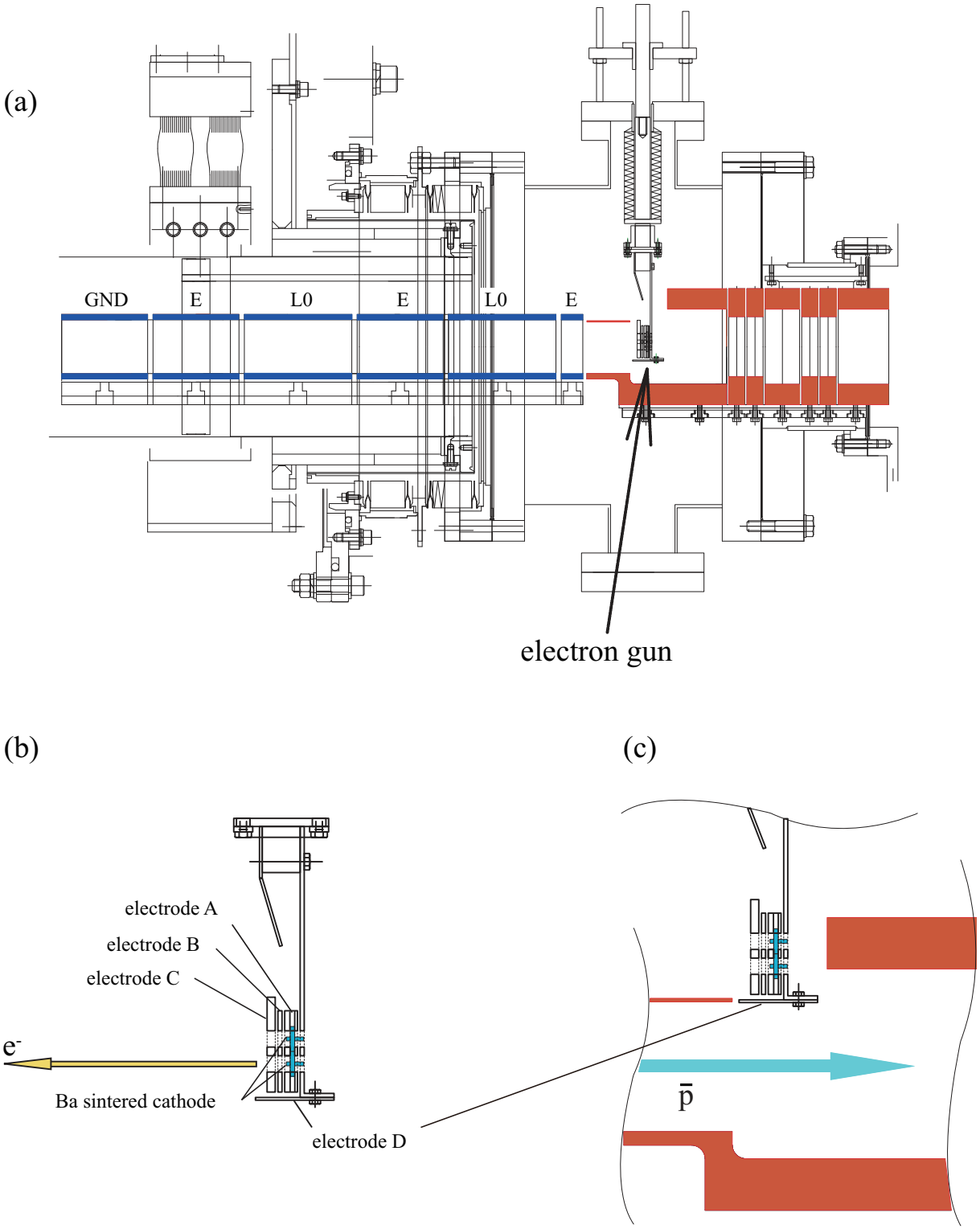

Figure 3.12: A cross sectional drawing of the electron gun and its circumference (a). Structure of the electron gun which consists of barium sintered cathode and several electrodes (b). The position of the electron gun when it is moved to off-axis for the extraction of the antiproton beam (c).

3.1.6 Performance of the antiproton catching trap

The number of antiprotons in the catching trap were measured by extracting them slowly. Figure 3.13 shows integrated annihilation number of the antiprotons as a function of time. The left axis represents the count of the track detector A and the right axis represents the total annihilation number taking into account the efficiency of the detector (0.5 %). At the first jump of the annihilation count in the figure, antiprotons were injected from the AD. Then antiprotons were cooled by the pre-loaded electrons. About 40 s after the injection, the high voltages applied on the DCE and UCE were changed to 0 V. Some of antiprotons which were not cooled in the trap annihilated at that time and made a second jump. Finally, about 60 s after the injection, antiprotons were extracted to the PET foils[1] by slowly decreasing the depth of the harmonic potential well as shown in figure 3.14. Typically 1-2 $\times 10^6$ antiprotons were trapped and cooled per one injection from the AD (one AD shot).

In addition, we were able to successively accumulate AD shots resulting in the increase of the number of the antiprotons. We call this operation as "stacking". Figure 3.15 shows the annihilation signal of antiproton when the number of stacking operation is twelve. The arrows in the figure indicate the timings of the injection of antiprotons. As can be seen from the figure, 1×10^7 antiprotons were trapped and cooled. This is the largest number of the antiprotons confined in a Penning trap. We are in a position of advantage with respect to the number of the antiprotons.

[1]Since the detection efficiency of the detector changes when the annihilation position of the antiproton changes, we extract them to the PET foils to fix the annihilation position.

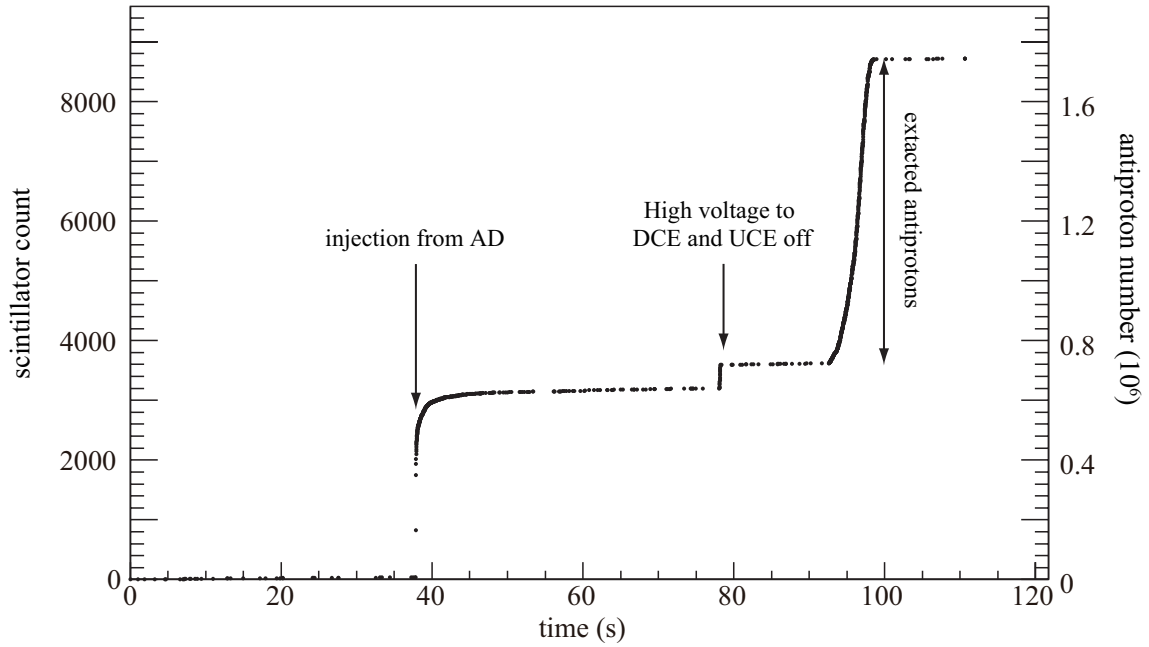

Figure 3.13: Typical annihilation count of the antiprotons. Integrated count of the annihilation signal is drawn as a function of time. Left axis shows the number of annihilation signal counted by the detector and right axis shows the number of annihilated antiprotons which is derived taking into account the detection efficiency of the detector. First and second jump of the count correspond to the timing when the antiprotons were injected from the AD and when the high voltages applied to the DCE and the UCE were changed to 0 V respectively. Third jump corresponds to the timing when the antiprotons in the trap were extracted slowly to count them.

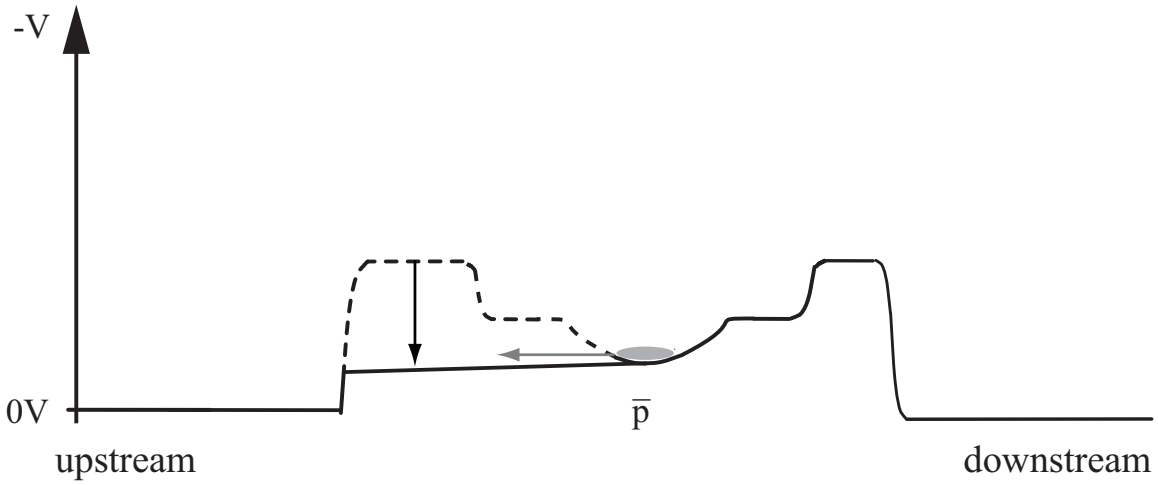

Figure 3.14: Potential configuration to extract antiprotons to the PET foils.

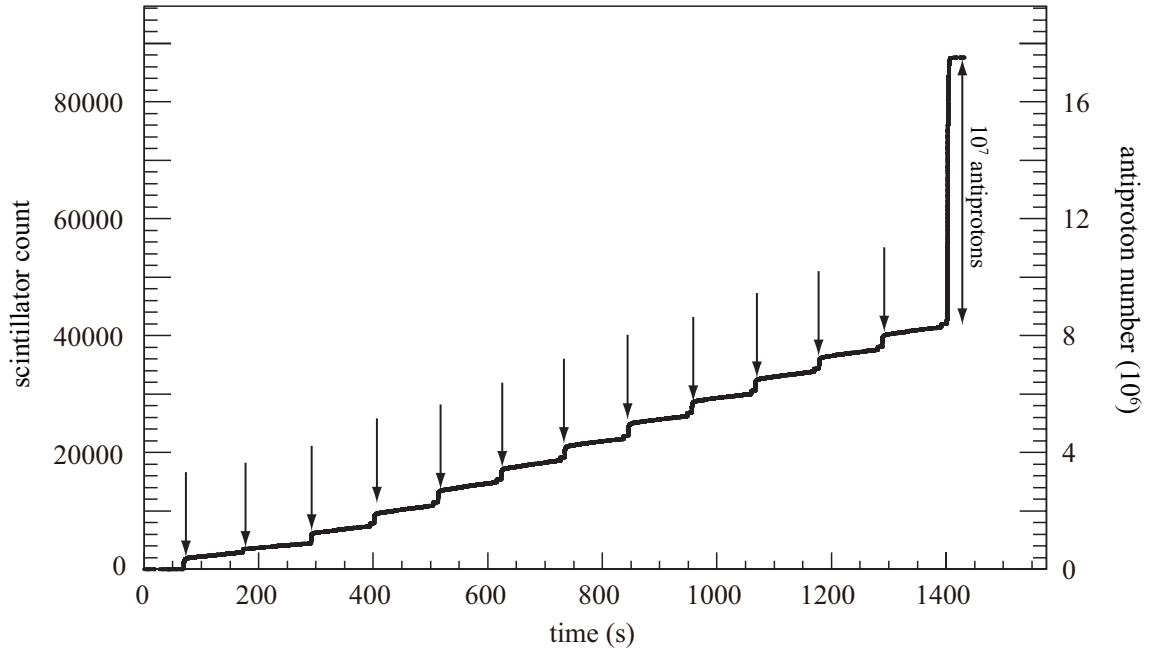

Figure 3.15: Integrated count of the annihilation signal is drawn as a function of time. In this case, the number of stacking operation is twelve. Arrows in the figure indicate the timings of the injection of antiprotons.

3.2 Positron accumulator

A compact positron accumulator is developed to provide a large number of positrons into the cusp trap[59, 60, 61]. Since the production rate of the antihydrogen atoms depend on the density of the positron as described in section 2.4, development of the efficient positron accumulator is one of the important issue. Figure 3.16 shows the principle of the accumulation of positrons. The positrons are emitted from a radio isotope source located inside the radiation shield. A part of them are captured in the transmission moderator of tungsten polycrystal then they are thermalized in the moderator and re-emitted from the other side of the surface. The energy of the re-emitted positrons is determined by the bias voltage of the moderator and the energy spread of them are typically 0.3 eV [62]. Rest of the positrons are captured and thermalized in the reflection moderator as well and re-emitted from the same surface. The re-emitted positrons gradually lose their energy via collisions with the nitrogen buffer gas introduced in to the gas cell. Finally they are accumulated in the bottom of the potential well created by the MRE.

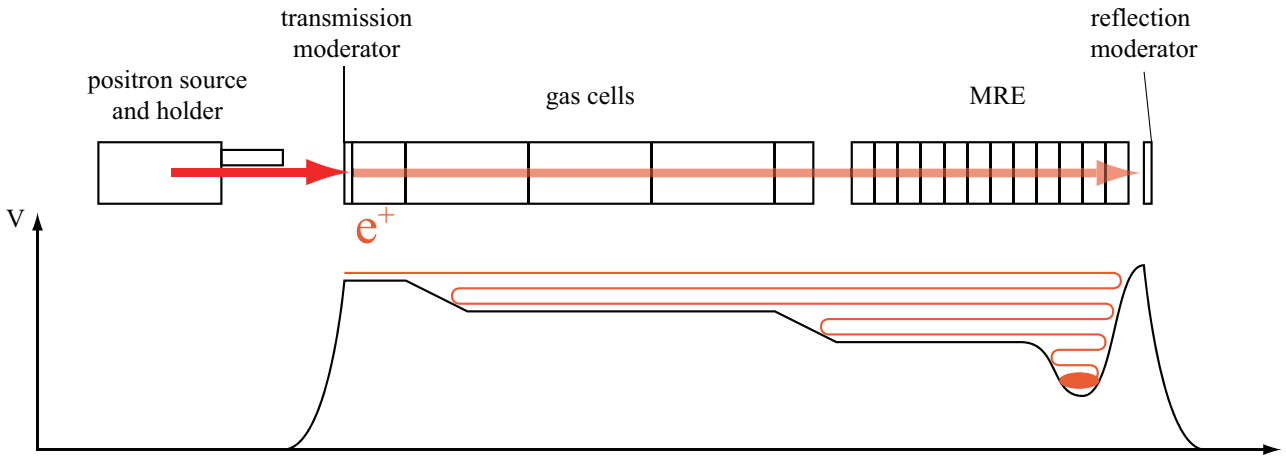

Figure 3.16: A schematic drawing of the positron accumulator and an electric potential. Positrons from the source are thermalized by the moderators and accumulated in the potential well made by the MRE via collisions with nitrogen buffer gas.

Figure 3.18 is an isometric view of the accumulator. One of the important feature of the accumulator is that whole system (the positron source, the gas cell, the MRE, the moderators) is in the superconducting magnet which enable efficient use of the positrons isotropically emitted from the source, since most of the positrons are captured by the strong magnetic field and guided to the moderators (see figure 3.25 for the relation between the configuration and the

magnetic field strength). At the exit of the accumulator a detector which is a combination of a micro channel plate (MCP) and a phospher screen (PS) is attached to monitor the extracted positron beam.

Figure 3.18 shows the structure inside the magnet. The positron source is surrounded by tungsten and stainless steel radiation shields. The gas cell for the buffer gas cooling of the positrons and the MRE are placed in between the transmission moderator and the reflection moderator. All components are aligned on the axis of the magnetic field. Details of each component are described following section.

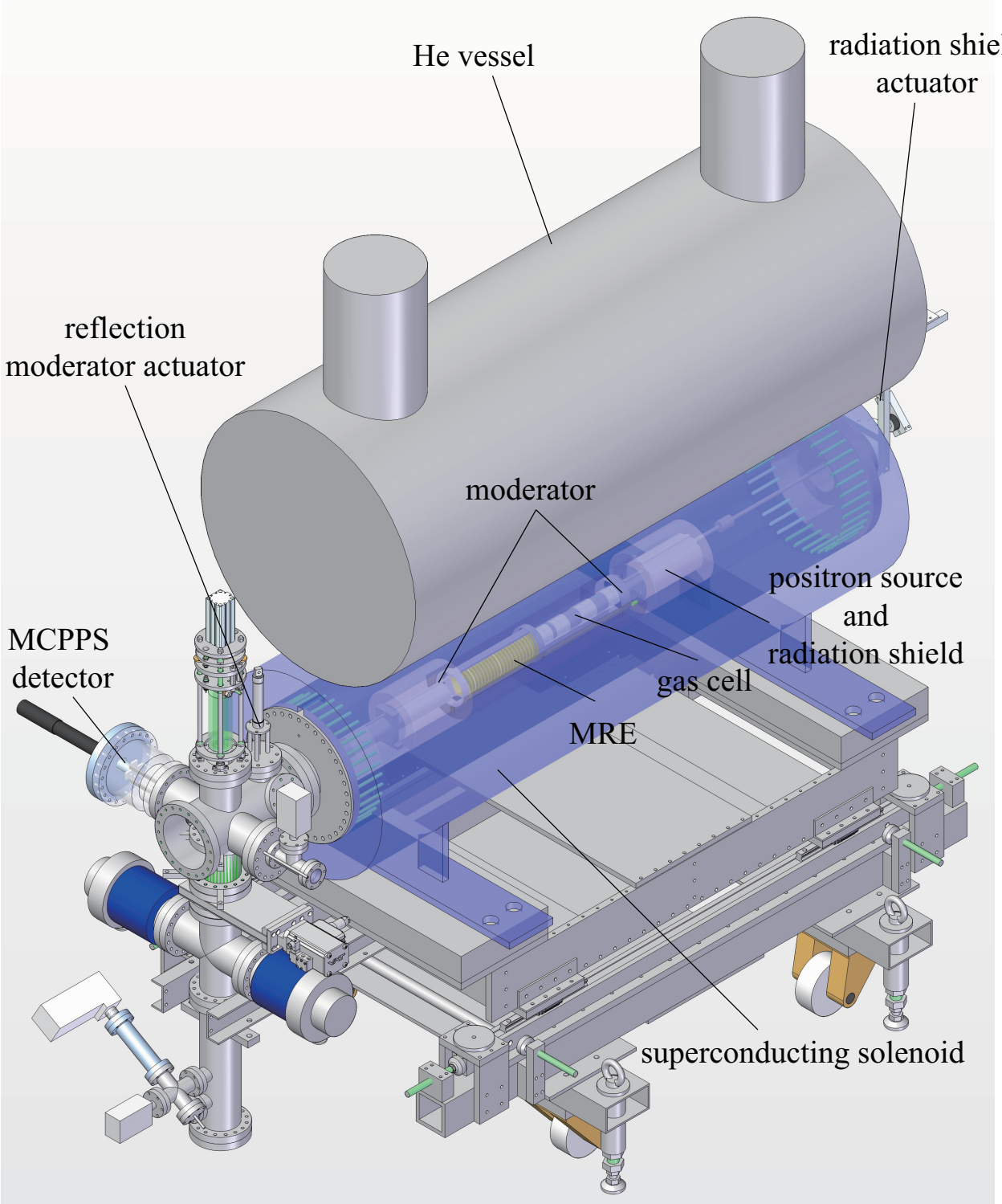

Figure 3.17: An isometric view of the positron accumulator. The source, the MRE, the gas cell and the moderators are housed in the superconducting solenoid. An MCPPS detector is attached downstream side of the solenoid to monitor extracted positrons.

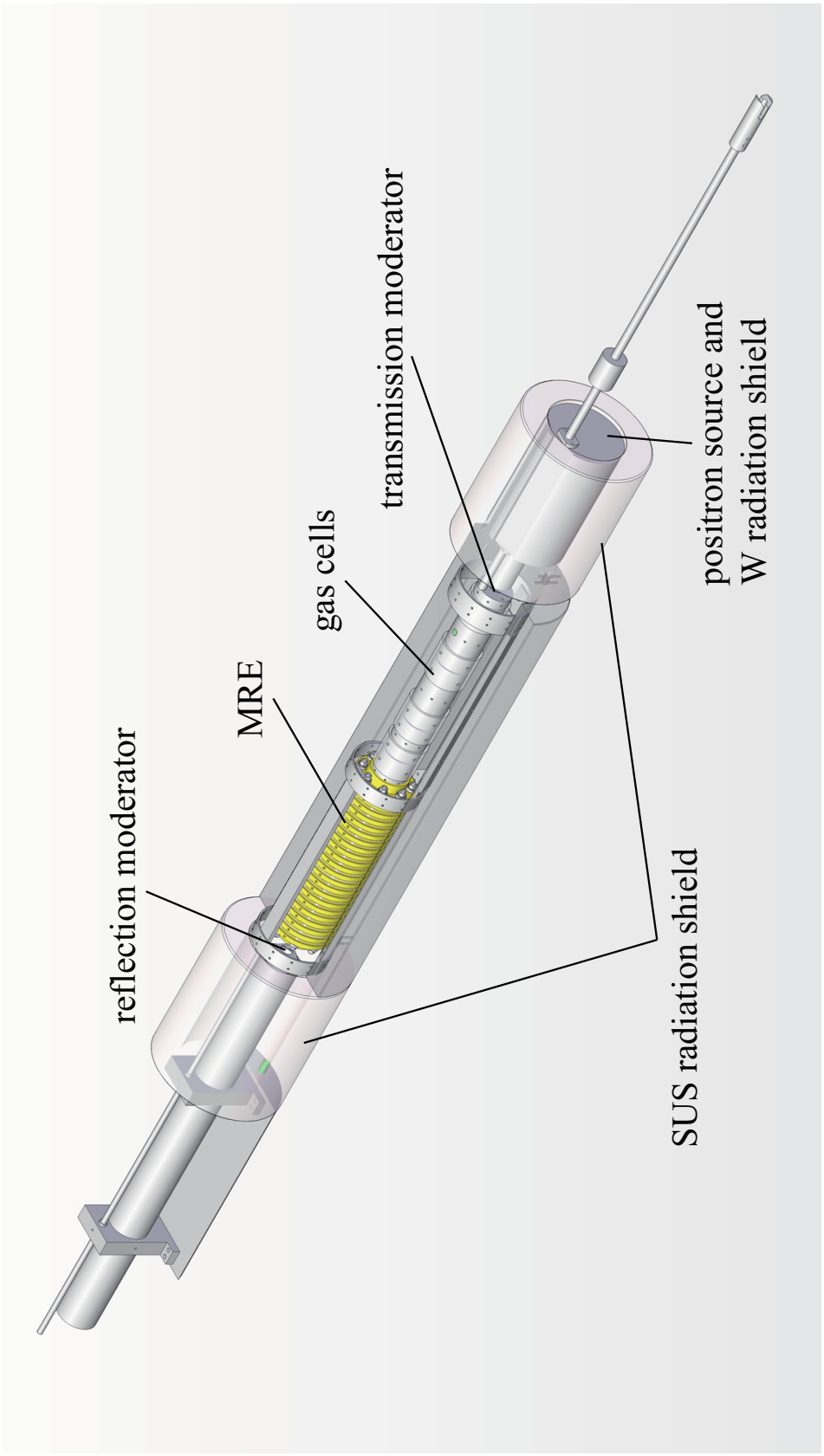

Figure 3.18: An isometric view of the positron accumulator (inside the solenoid).

3.2.1 superconducting solenoid

A superconducting solenoid magnet is used to confine positrons radially. Specifications of the magnet is summarized in table 3.1 and cross sectional drawing is shown in figure 3.19. The magnet is cooled by liquid helium. A UHV bore of 164.5 mm inner diameter is built in the magnet and also can be cooled by the liquid helium. An important feature of the magnet is its rapid sweep speed of the magnetic field. In the present work, positron accumulator is operated at 2.5 T, which means it takes only 150 s for ramping up or down of the magnetic field. The magnet is de-energized every time after positron stacking in the cusp trap is completed to avoid undesired effect on the trajectory of the antiproton beam.

manufacturer	Oxford
maximum central magnetic field	5 T
cooled by	Liquid He
volume of liquid helium vessel	330 l
magnetic shield	iron
homogeneity of the magnetic field	$\pm$0.5 % (1100 mm $\times$ 10 mm ϕ)
inner diameter of the UHV bore tube	164.5 mm ϕ
sweep speed of magnetic field	1 T/min

Table 3.1: Specifications of the superconducting magnet used in the positron accumulator.

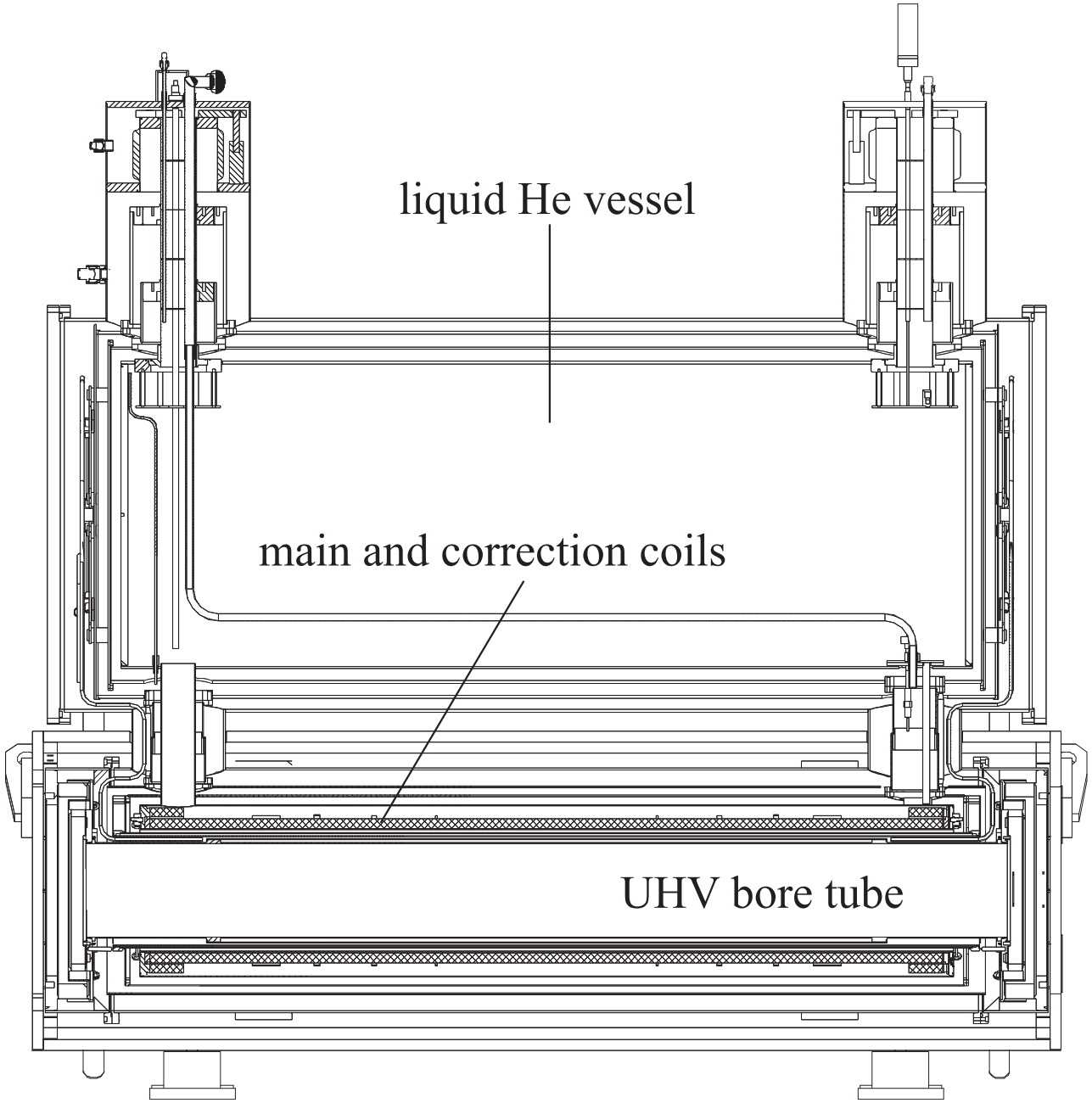

Figure 3.19: A cross sectional drawing of the superconducting magnet used in the positron accumulator. The UHV bore tube is inserted in the solenoid. The solenoid and the bore tube are cooled by liquid He.

3.2.2 positron source

As a positron source, $^{22}Na(Na_2CO_3)$ is adopted. Figure 3.20 is a decay diagram of the ^{22}Na. This radio isotope decay to ^{22}Ne by the electron capture process with the life time of 2.6 year. Considering the period of the experiment is several years to ten years, this intermediate life time of the isotope is suitable for our experiment. The activity of the source used in the present work is 1.87 GBq ± 30 % on 1 June 2007.

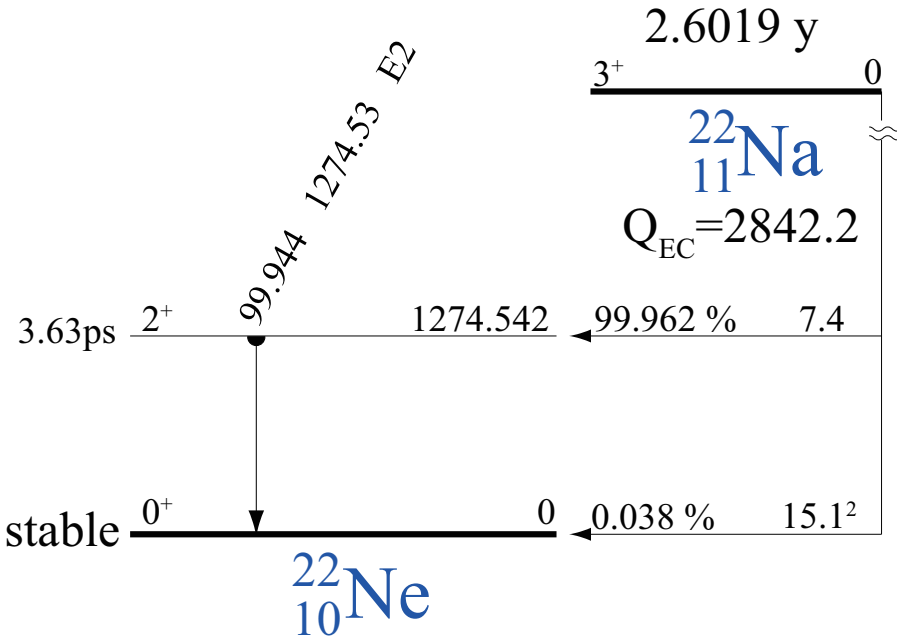

Figure 3.20: Decay diagram of ^{22}Na.

The source is stored in a holder made of tungsten alloy. Figure 3.21 is a photograph of the holder and figure 3.22 is a cross sectional drawing of the holder and stainless steel ring for further shielding of the radiation. The source is placed in the middle of the holder. In front of the source, a hole of 6 mm ϕ is drilled for the extraction of the positrons, which is covered by a shutter also made of tungsten alloy. The shutter is opened only during the positron accumulation process by the rod connected to the rotary motion feedthrough, which is actuated by an air cylinder(see figure 3.23).

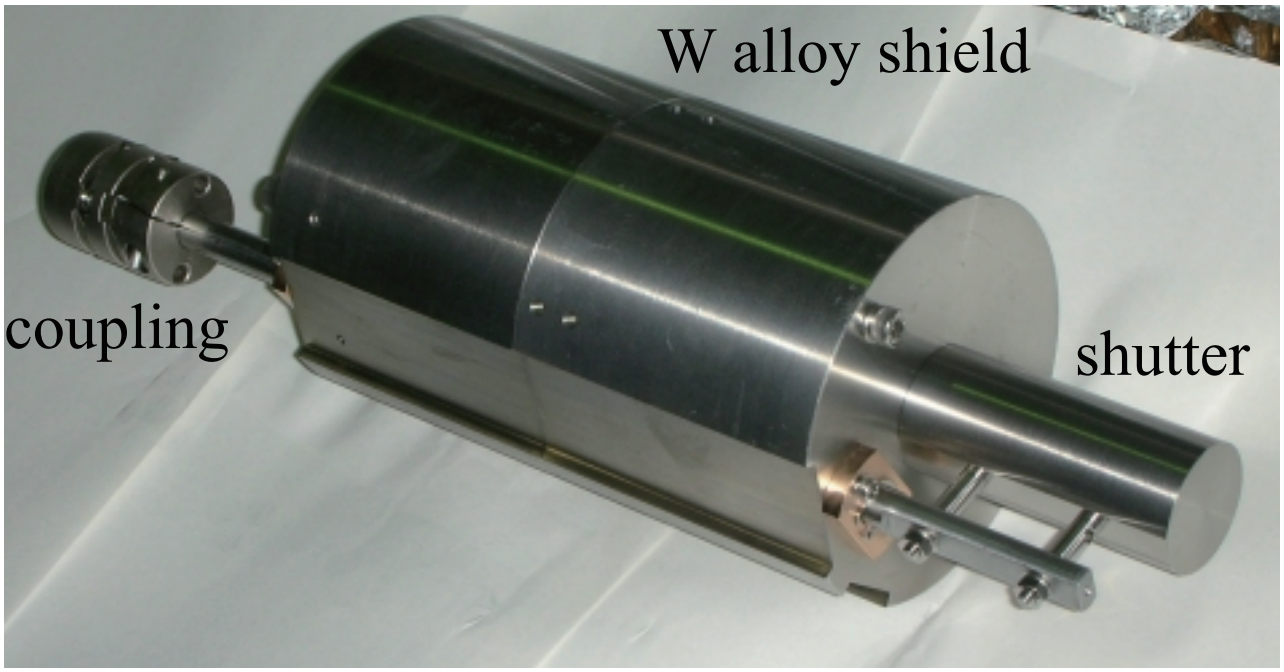

Figure 3.21: A photograph of the holder of the positron source.

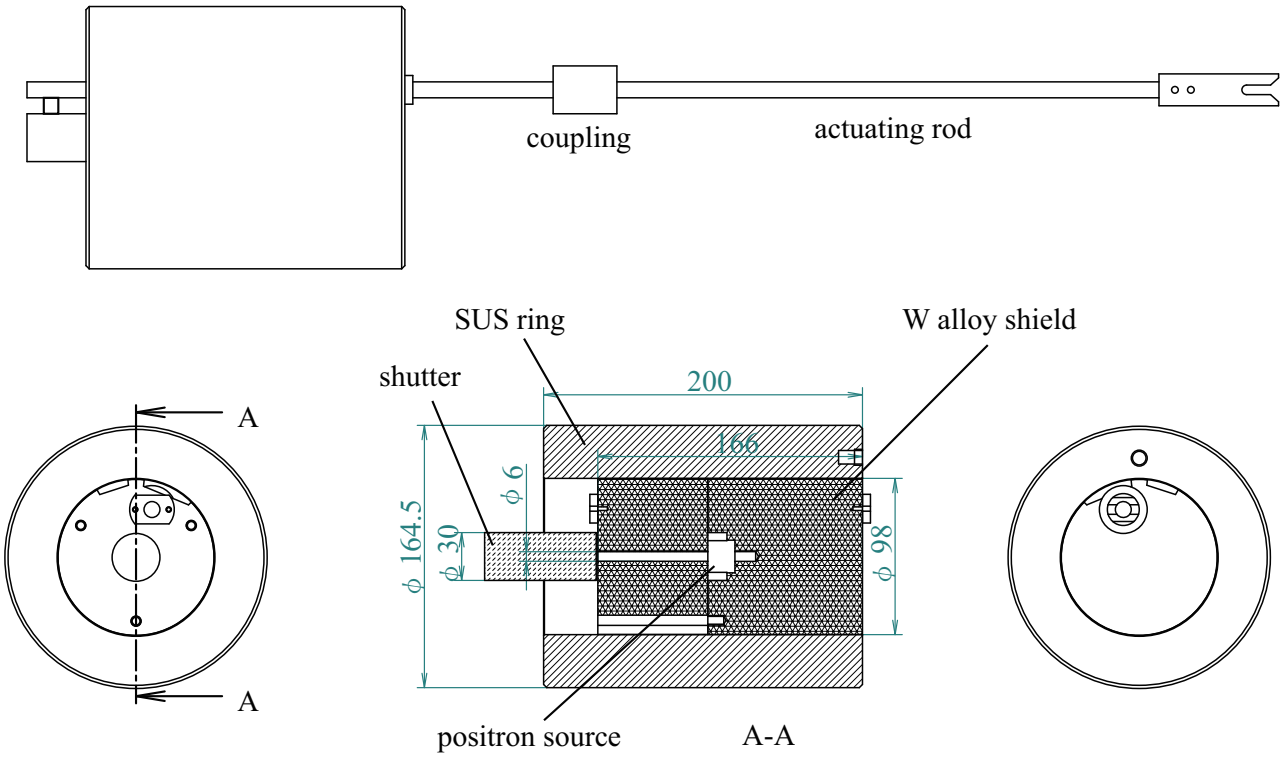

Figure 3.22: A cross sectional drawing of the holder. The shutter in front of the source is actuated by the rod.

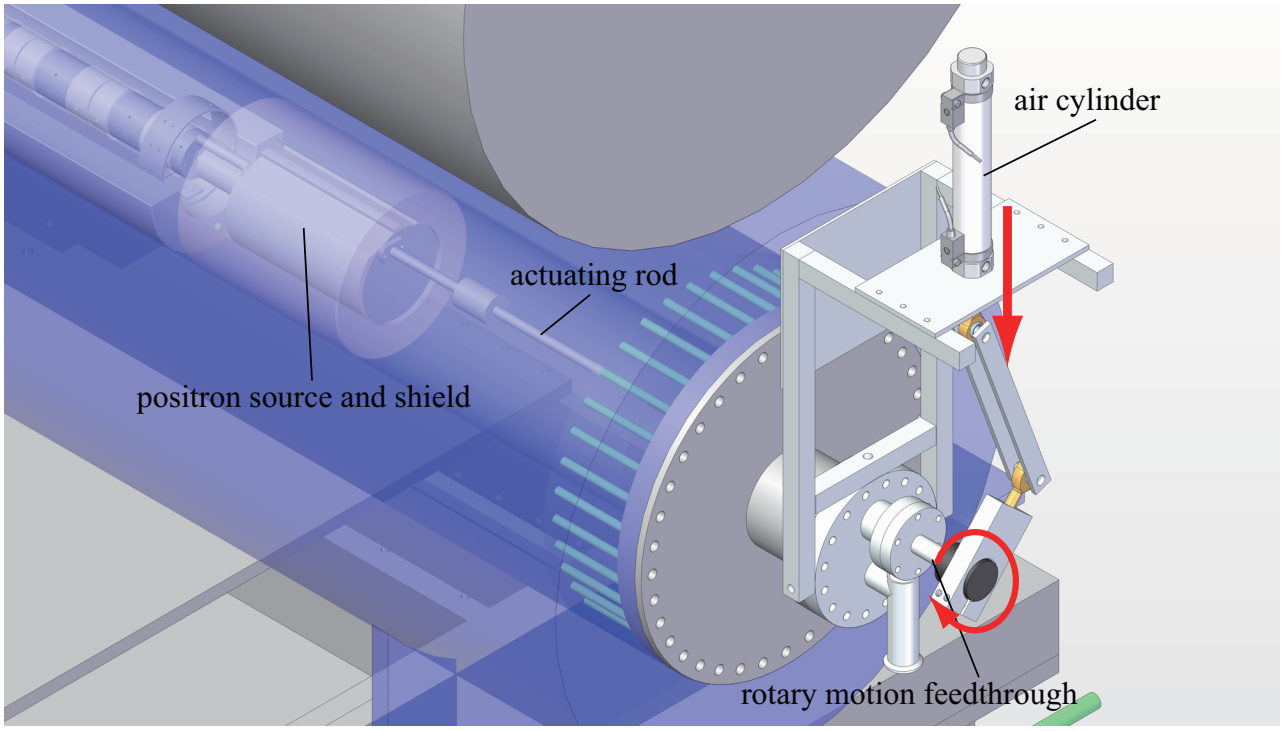

Figure 3.23: Actuating mechanism of the shutter of the positron source holder. The rod, connected to the shutter, is actuated by the air cylinder via rotary motion feedthrough.

3.2.3 moderators

Two polycrystalline tungsten moderators are used to convert the energetic positrons from the source to the monoenergetic beam. It is known that the positrons injected into material are thermalized and re-emitted from the surface as if the work function of the material is negative. For the configuration of the moderator, both transmission type(positrons are injected from one side of the moderator and re-emitted from the other side) and reflection type (positrons are injected from one side of the moderator and re-emitted from the same side) can be used. In the present work, one transmission and one reflection moderators are used to increased the conversion efficiency of the energetic positron from the source to monoenergetic beam.

Figure 3.24 shows photographs of the moderators along with the cross sectional drawing of the accumulator. The transmission moderator of 4μm thickness is located at the entrance of the buffer gas cell and the reflection moderator of 25μm thickness is located at the exit of the MRE. A part of the positrons from the source is converted to monoenergetic beam by the transmission moderator and rest are converted by the reflection moderator. Both of them are electrically isolated from the ground potential. Thus by applying voltage, energy of the positrons re-emitted from the moderators can be changed. The reflection moderator is mounted on a rotatable holder. During the positron accumulation phase, the moderator is on axis, before the extraction of positrons, the holder is rotated by the actuator and the hole get on axis.

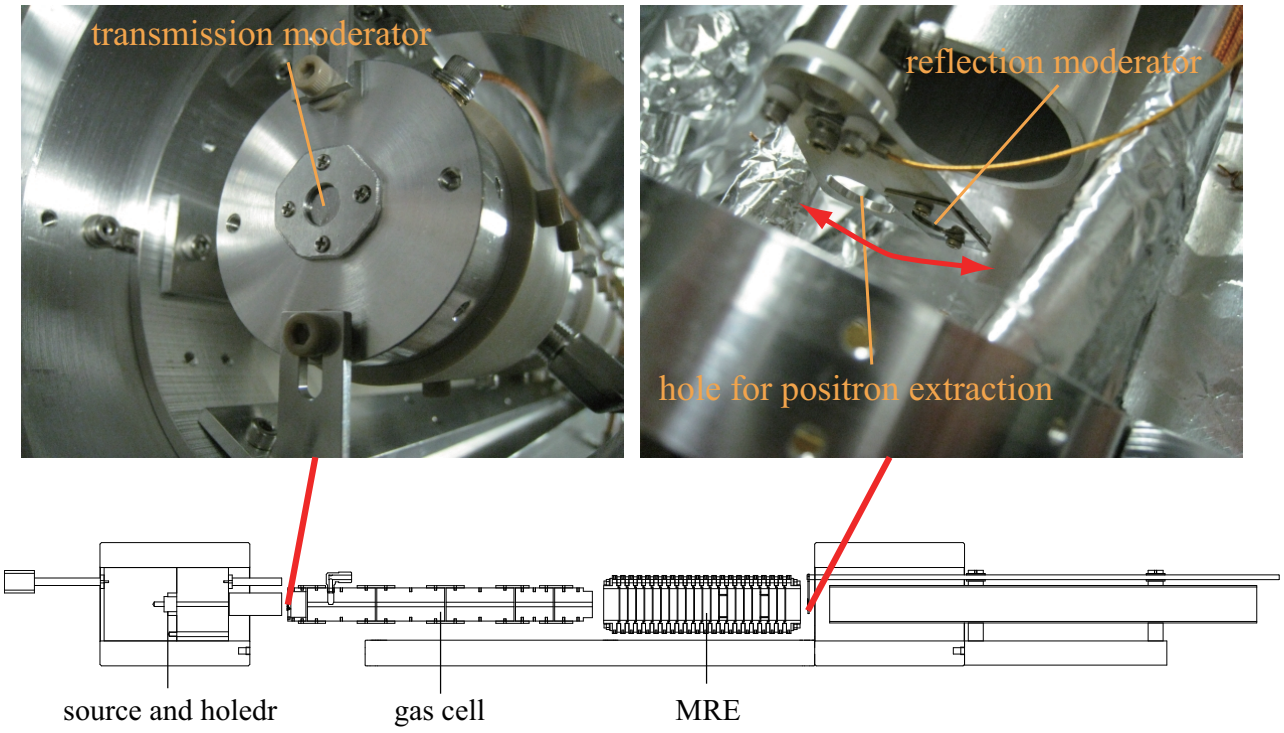

Figure 3.24: Photographs of the transmission and the reflection moderators.

3.2.4 MRE and gas cell

Figure 3.25 is a cross sectional drawing of the MRE and the gas cell along with the magnetic field. The gas cell consist of six ring electrodes made of aluminium alloy. The nitrogen buffer gas is introduced at the hole in G2 electrode pointed by red allow. The monoenergetic positron emitted from the moderators gradually lose their energy via collisions with the gas and finally they are accumulated in the potential well created by the MRE. The MRE consist of 22 ring electrodes made of gold plated aluminium alloy, some of them are connected electrically inside the vacuum(see figure 3.25) because of the limited number of the electric feedthrough.

For efficient deceleration of positron, dense buffer gas is required, on the other hand confinement time in the MRE region is limited by the pressure of the residual gas which cause expansion of confined positrons via collisions [63]. To fulfil these contradicting request, strong differential pumping is a key issue. Thus taking into account the beam size of the energetic positron which is mainly determined by the size of the source itself(6 mm ϕ), the inner diameter of the gas cell is determined to 6 mm ϕ. Also the length of the gas cell is maximized under the geometrical restriction. Because if the length of the gas cell is too long, the source have to be placed far from the region where the magnetic field is strong, and some of the energetic positrons will be lost inside the hole of the tungsten alloy holder since the cyclotron radius of the positron got too large[2].

Finally the conductance of the gas cell under above mentioned condition is calculated to be 0.07 l/s. Considering the nominal pumping speed (roughly 100 l/s), the pressure difference between inlet and outlet of the gas cell can be about 1:1400. Specifications of the MRE and the gas cell are summarized in table 3.2 and 3.3.

[2]The cyclotron radius r_c of the charged particle whose mass is m , charge is q, and kinetic energy perpendicular to the magnetic field is E_0 eV in the magnetic field B is given by $r_c = \frac{\sqrt{2mE_0}}{qB}$. Substituting values for the positron, we obtain $r_c = 3.37\sqrt{E_0/B^2}\mu$m.

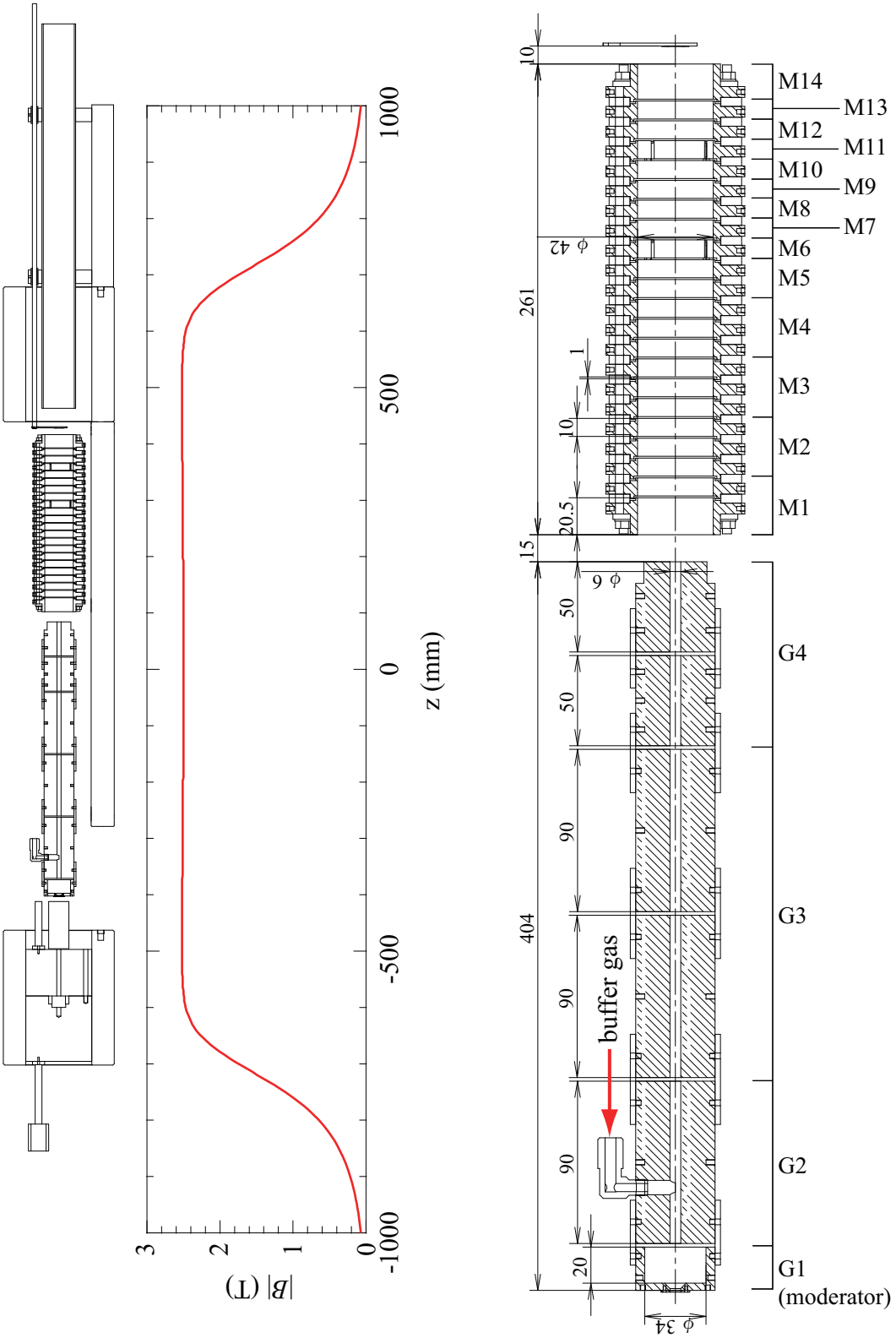

Figure 3.25: A cross sectional drawing inside the UHV bore tube of the positron accumulator with magnetic field strength (left). A cross sectional drawing of the MRE and the gas cell (right). Buffer gas is introduced at the position pointed by the red arrow.

number of electrodes	22
inner diameter of electrodes	42 mm
distance between electrodes	1 mm
width of electrodes (end electrodes)	20.5 mm
width of electrodes (others)	10 mm
material of electrodes	Al alloy (gold plated)
material of insulators	PEEK

Table 3.2: Specifications of the MRE.

number of cells	6
inner diameter of cells (G2-G4)	6 mm
inner diameter of cell (G1)	34 mm
width of cells	see figure 3.25
material of cells	Al alloy
material of insulators	PEEK
total conductance	0.07 l/s

Table 3.3: Specifications of the gas cells.

3.2.5 Vacuum and gas handling system

Because the positrons re-emitted from the moderators lose their energy through collisions with nitrogen buffer gas, the pressure control of the buffer gas is a key issue for this type of positron accumulators. In addition, it is known that the annihilation cross section of the positron get much large with heavy molecules such as hydro-carbon molecules. Thus the oil-free vacuum system is required for the positron accumulator.

Figure 3.26 schematically shows the nitrogen buffer gas handling system and vacuum system of the positron accumulator. The accumulator is evacuated by two turbo molecular pumps (TMPs) (Varian, V551) and one TMP (Varian V70) whose outlet is connected to a scroll pump (Varian, Triscroll300) to realize oil free evacuation system. In addition to those pumps, the bore tube of the accumulator is cooled down to about 100 K, some portion of the residual gases especially whose vapor pressure is low at low temperature like heavy molecules can be evacuated by sticking to the wall of the bore. By this means, the base pressure of the accumulator is achieved to be as low as 10^{-9} Torr order and the major component of the residual gas is hydrogen.

For the fine control of the pressure of the nitrogen buffer gas, a buffer gas reservoir is introduced in between the accumulator and the gas bottle. The reservoir is evacuated before in use by a combination of a TMP (Varian V70) and a scroll pump (Varian, Triscroll300) then the gate valve between the TMP and the reservoir is closed. The nitrogen gas is introduced from the gas bottle to the reservoir with monitoring the pressure of the reservoir by a Pirani gauge. When the pressure reaches the desired value[3], valves between the gas bottle accumulator and the reservoir are opened and the the gas is introduced into the accumulator.

[3]Typically the pressure of the reservoir is 1×10^{-2} Torr

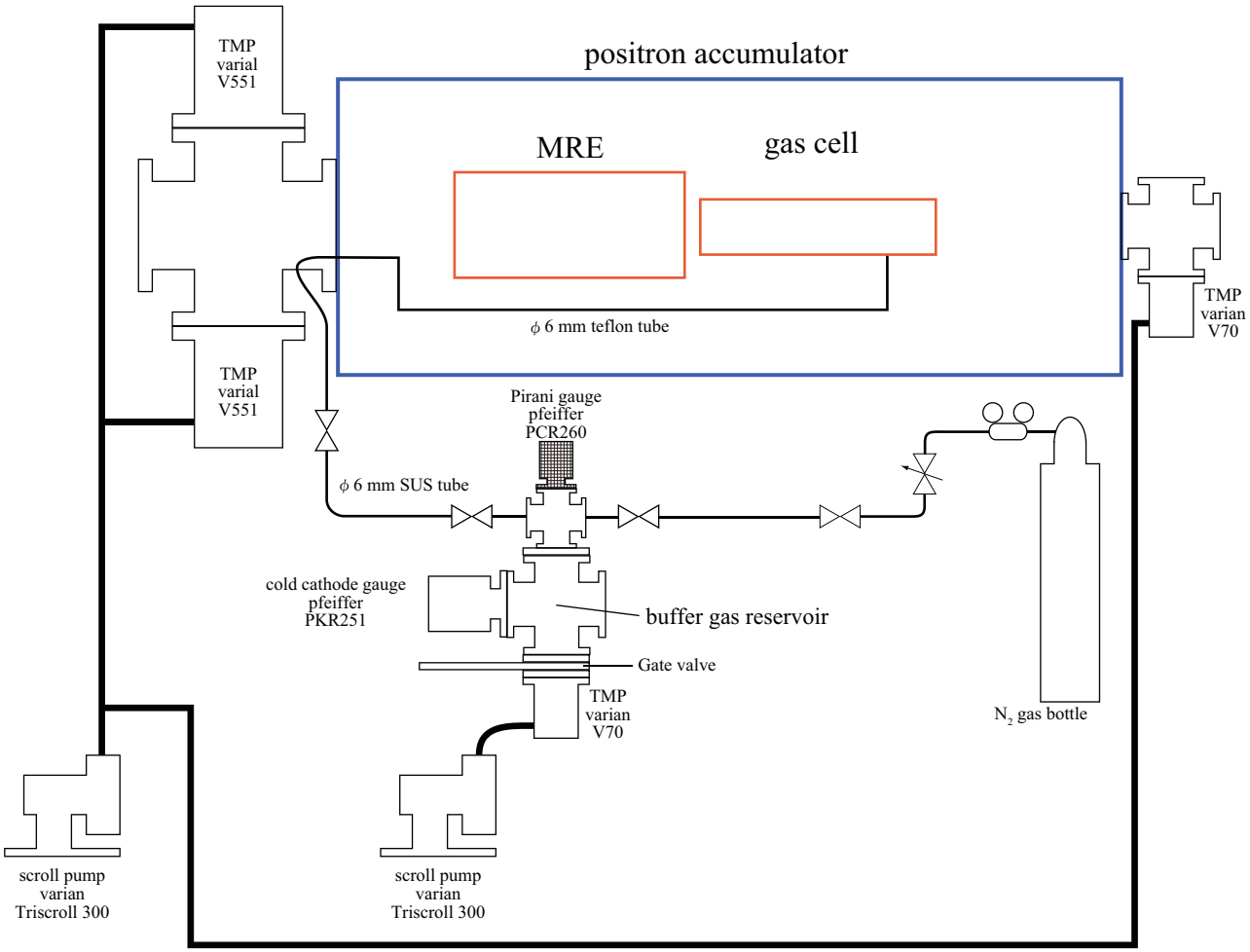

Figure 3.26: Schematic drawing of the buffer gas handling system and the vacuum system of the positron accumulator. The accumulator is evacuated by three TMPs, whose outlets are connected to a scroll pump. Nitrogen buffer gas is introduced in the gas cell via buffer gas reservoir. The reservoir is evacuated by the combination of a TMP and a scroll pump before in use. Then a gate valve between the TMP and the reservoir is closed and nitrogen gas is introduced. The pressure of the reservoir is monitored by the cold cathode gauge and the Pirani gauge.

3.2.6 Voltage control system

The voltage of the MRE, gas cell, moderators are controlled by a PC for the flexible operation. A PXI based system was adopted because of its expandability, availability, and uniformity with the control system of the cusp trap, which is also PXI based system and developed earlier.

Figure 3.27 is a block diagram of the components used to control the voltage. The PXI modules and the PC is connected via interface cards (National Instrument, PXI-8336 and PCI-8336) and optical fiber. Three 8 channel[4] digital to analogue converter (DAC) modules (National Instruments, PXI-6733) output voltages from -10 V to 10 V in 16 bit resolution. Then each signal is amplified about 160 times by the power amplifier (matsusad, OPTON-1PC). Four channels are connected to the gas cell and the transmission moderator, 14 channels are connected to the MRE, and 1 channel is connected to the reflection moderator. We note that one channel in the 14 channels connected to the MRE, is not directly connected to the MRE. To superimpose high speed high voltage pulse for the pulse extraction of the positron (see figure 3.91), a signal mixer consists of resisters and capacitors (RC signal mixer) is inserted in between the output of the power amplifier and the MRE. The control system of the pulse signal is described in section 3.4.6. The specifications of the system are summarized in table 3.4.

output range	0 to 1000 V
resolution	50 mV
power supply voltage	15 V
DC offset	adjustable by program
ripple	5 mV_{pp}
slew rate	1 mV/μs

Table 3.4: Specifications of the voltage control system used in the positron accumulator.

[4]There are 24 independent channels.

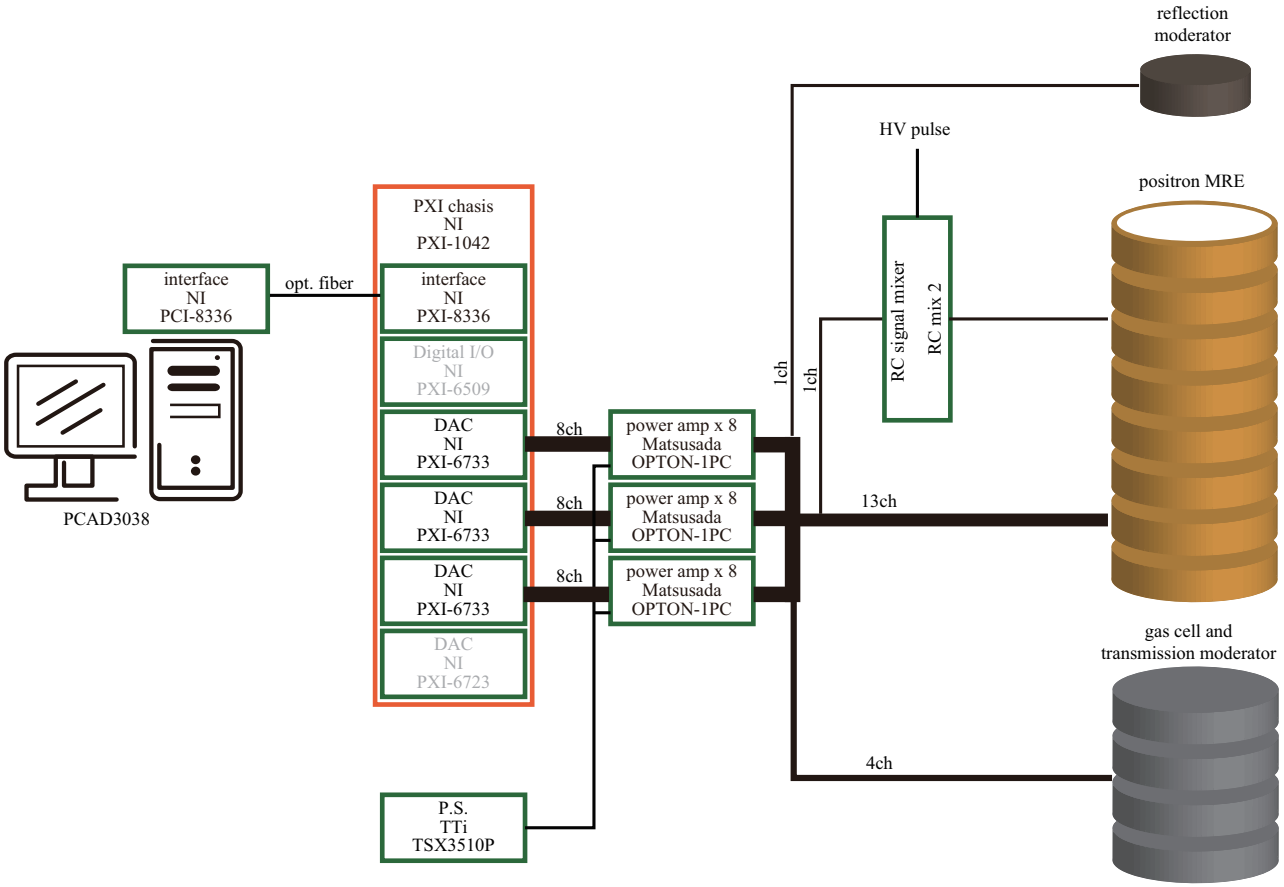

Figure 3.27: A connection diagram of components related to the control of the MRE and the gas cell.

3.2.7 Performance of the positron accumulator

Figure 3.28(top) shows the dependence of the accumulated positron number and its rate as a function of the accumulation time which is the duration when the cover of the source is open. The accumulated positron number increase with the accumulation time however, the rate decrease as the accumulation time decrease. A possible reason is that the accumulated positrons in the potential well created by the MRE gradually expand and lost via collisions with nitrogen buffer gas. Figure 3.28 (bottom) shows the corrected accumulation rate. Since there exist about 20 s extra time for the operation like opening and closing of the cover of the radiation shield, the effective number of positrons which can be used for transport to the cusp trap should be evaluated by the corrected accumulation rate which takes into account the extra operation time. As can be seen from the figure, the corrected accumulation rate reach maximum $\sim$ 20 s/ 30 s. Thus, typically we operate the accumulator with 30 s accumulation time (50 s for one cycle). In this condition, 2×10^6 positrons were extracted from the accumulator.

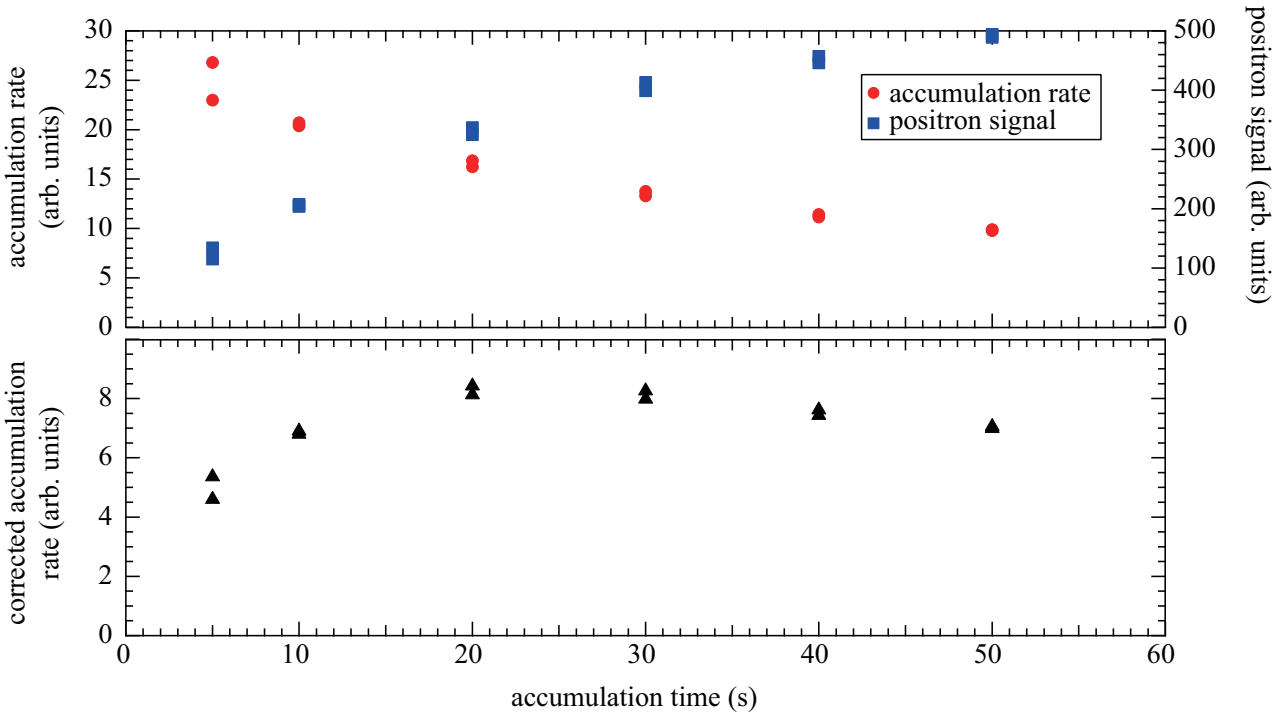

Figure 3.28: Dependence of the accumulated positron number and accumulation rate on the accumulation time (top). Corrected accumulation rate, which takes into account the 20 s extra operation time, is shown as a function of the accumulation time (bottom).

3.3 Transport beamline for low energy antiproton and positron beam

Ultra-low energy antiproton and positron beams were transported into the cusp trap guided by magnetic fields. Figure 3.29 shows the configuration of the transport coils. Two coils (coil A, coil B) were used for the transport of the antiproton beam and 6 coils (pos coil 1-5, coil B) and 2 steering coils(pos coil st 1-2) were used for the transport of the positron beam.

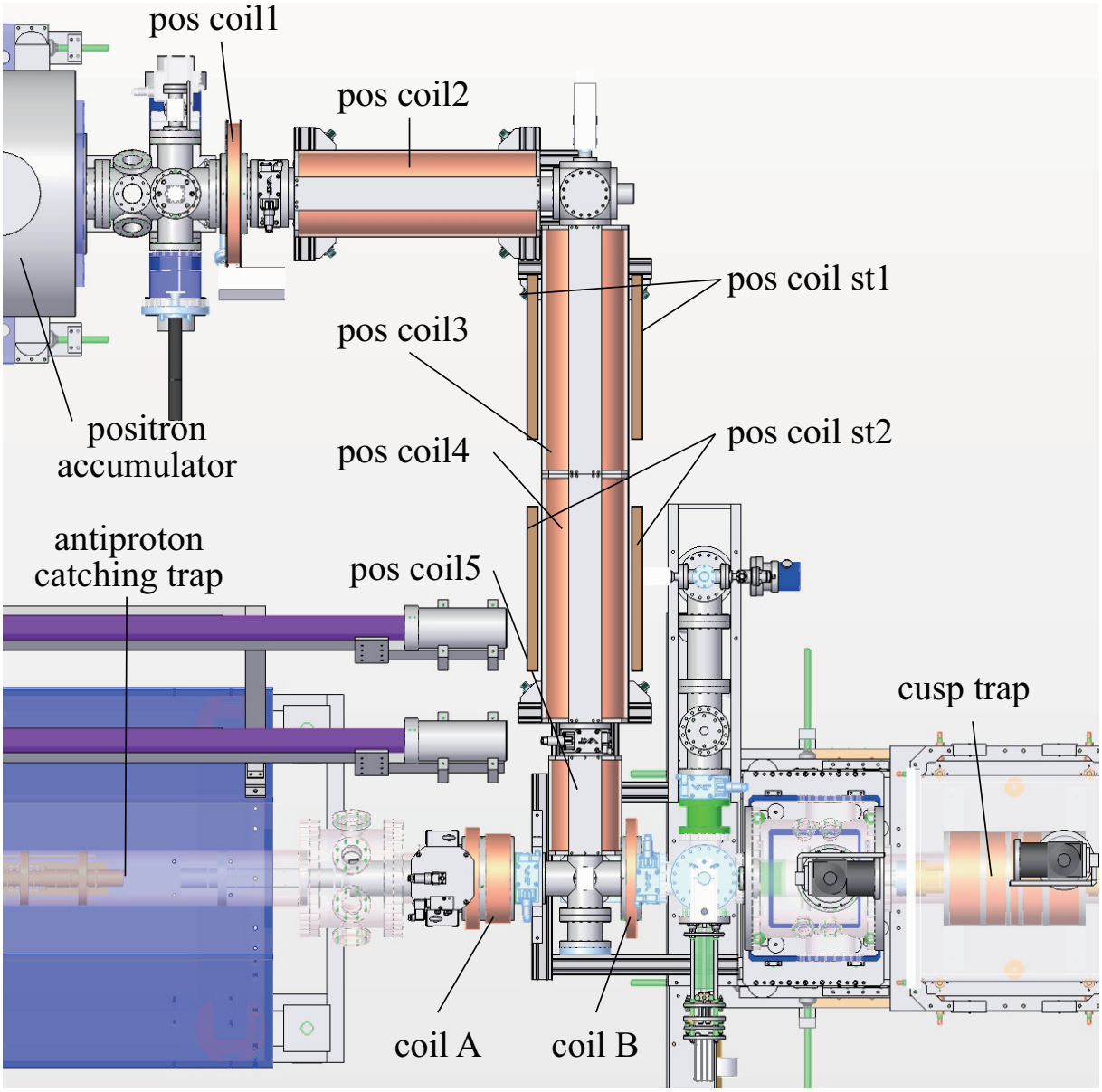

Figure 3.29: Configuration of the coils for the transport of the ultra-low energy antiproton and positron beams.

3.3.1 Antiproton transport line

Figure 3.30 is a photograph and a cross sectional drawing of the coils used for the transport of antiproton beam. The inner diameter of the coils is 240 mm and mounted directly on the vacuum pipe. Figure 3.31 shows the control diagram of the coils. These coils are energized by power supplies (Matsusada, PRk30-53) whose current are controlled by the voltages of another power supply (Agilent, E3648A) which has GPIB interface and controlled by a PC. They are energized only for a few seconds synchronous to the extraction of the ultra-low energy antiproton beam from the antiproton catching trap. Figure 3.32 shows the coil current and the maximum magnetic field on axis generated by each coil as a function of the control voltage. The coils can generate magnetic field up to 0.035 T.

The section between the antiproton trap and the cusp trap is evacuated by one TMP (Shimadzu, TMP-303). The base pressure is around 10^{-9} Torr.

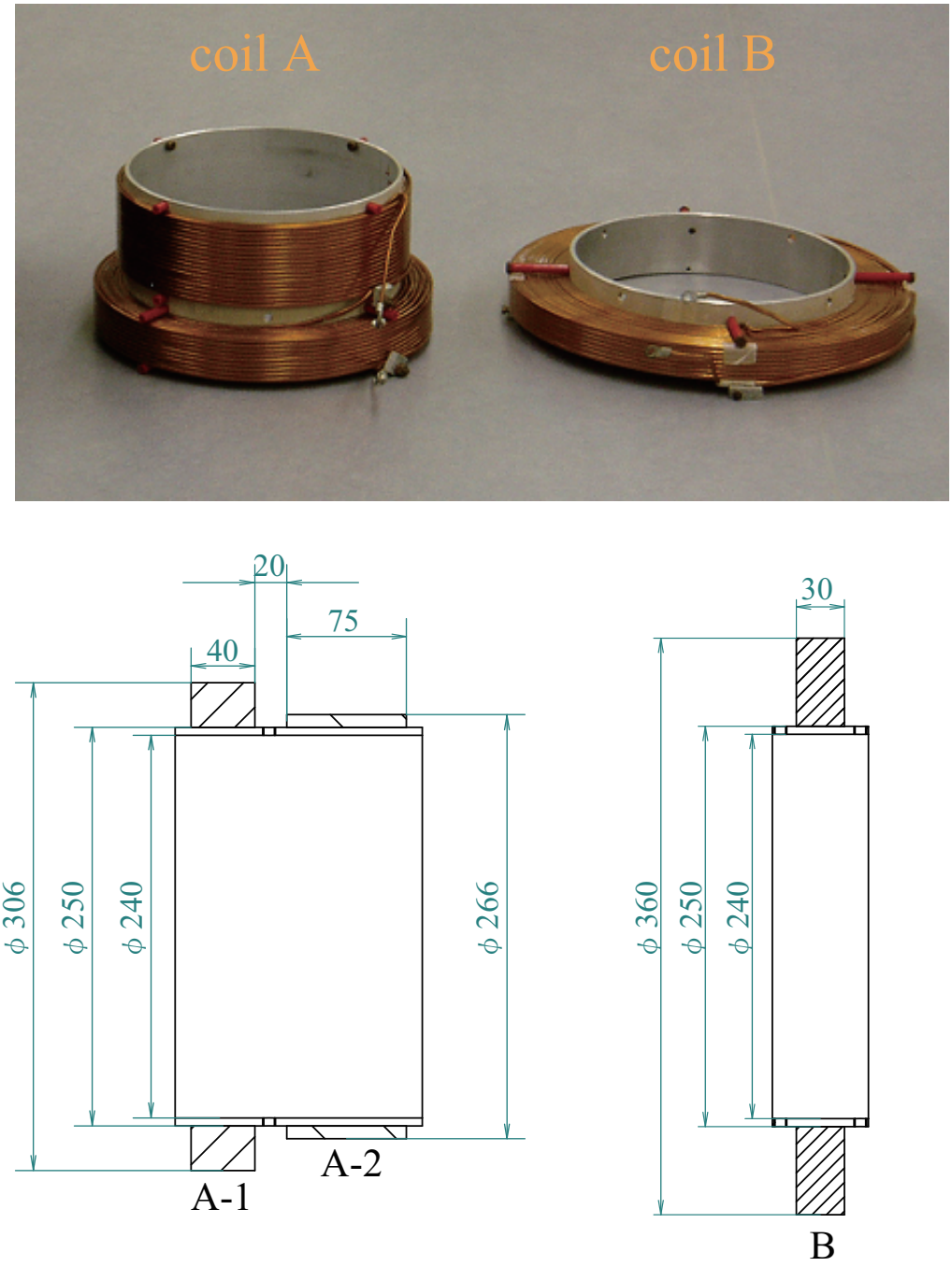

Figure 3.30: A photograph (top) and a cross sectional drawing (bottom) of the coils for the antiproton beam transport.

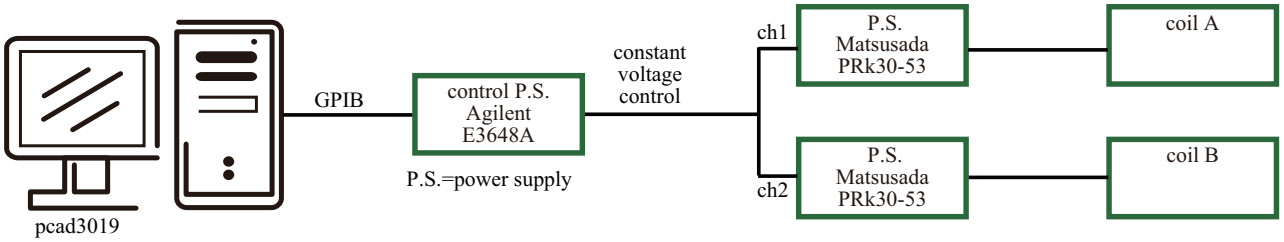

Figure 3.31: A control diagram of the antiproton beam transport coils. Coils are energized by power supplies (Matsusada, PRk30-53) whose current are controlled by the voltages of another power supply (Agilent, E3648A) which has GPIB interface and controlled by a PC

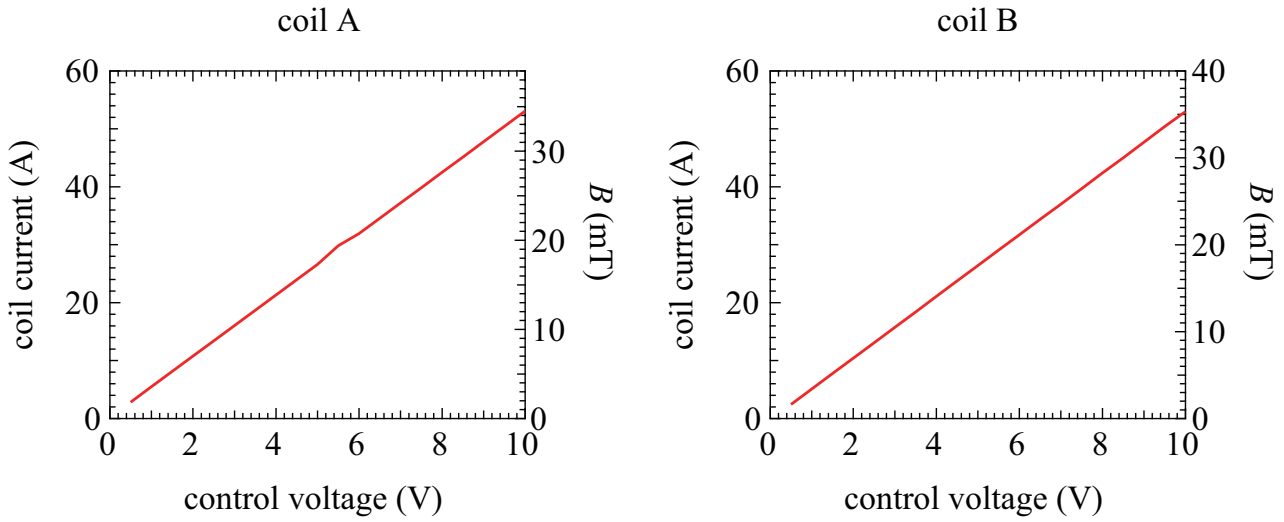

Figure 3.32: Coil current and maximum magnetic field on axis generated by each coil as a function of the control voltage.

3.3.2 Positron transport line

Figure 3.33 is cross sectional drawings of the coils used for the positron transport. For the positron transport, coil pos 1-coil pos 5 and coil B are used, at the same time pos st 1-2 are also used to deflect the beam. Figure 3.34 shows a control diagram of the coils. These coils are energized by power supplies whose current is controlled by the external voltage as well as antiproton transport coils[5]. These coils are also energized only for a few seconds synchronous to the extraction of the ultra-low energy positron beam from the positron accumulator. Figure 3.35 shows the coil current and the maximum magnetic field on axis generated by each coil as a function of the control voltage.

The section between the positron accumulator and the cusp trap is evacuated by one TMP (Varian, V301). The base pressure is around 10^{-8} Torr, however the positron accumulator uses nitrogen gas for the cooling of positrons and the pressure in the accumulator is as high as 1×10^{-6} Torr as described in section 3.2.5. To reduce the gas inflow from the positron accumulator into the cusp trap at the time of positron beam extraction[6], a special gasket whose inner diameter is 60 mm (see figure 3.36) is used at the flange under the pos coil 1. The conductance of this gasket is 300 l/s, on the other hand that of a normal CF203 gasket is 2000 l/s.

[5]The control voltages are supplied by a DAC module (National Instruments PXI-6723).

[6]The gate valve between the positron accumulator and the positron transport line is opened only when the positron beam are transported.

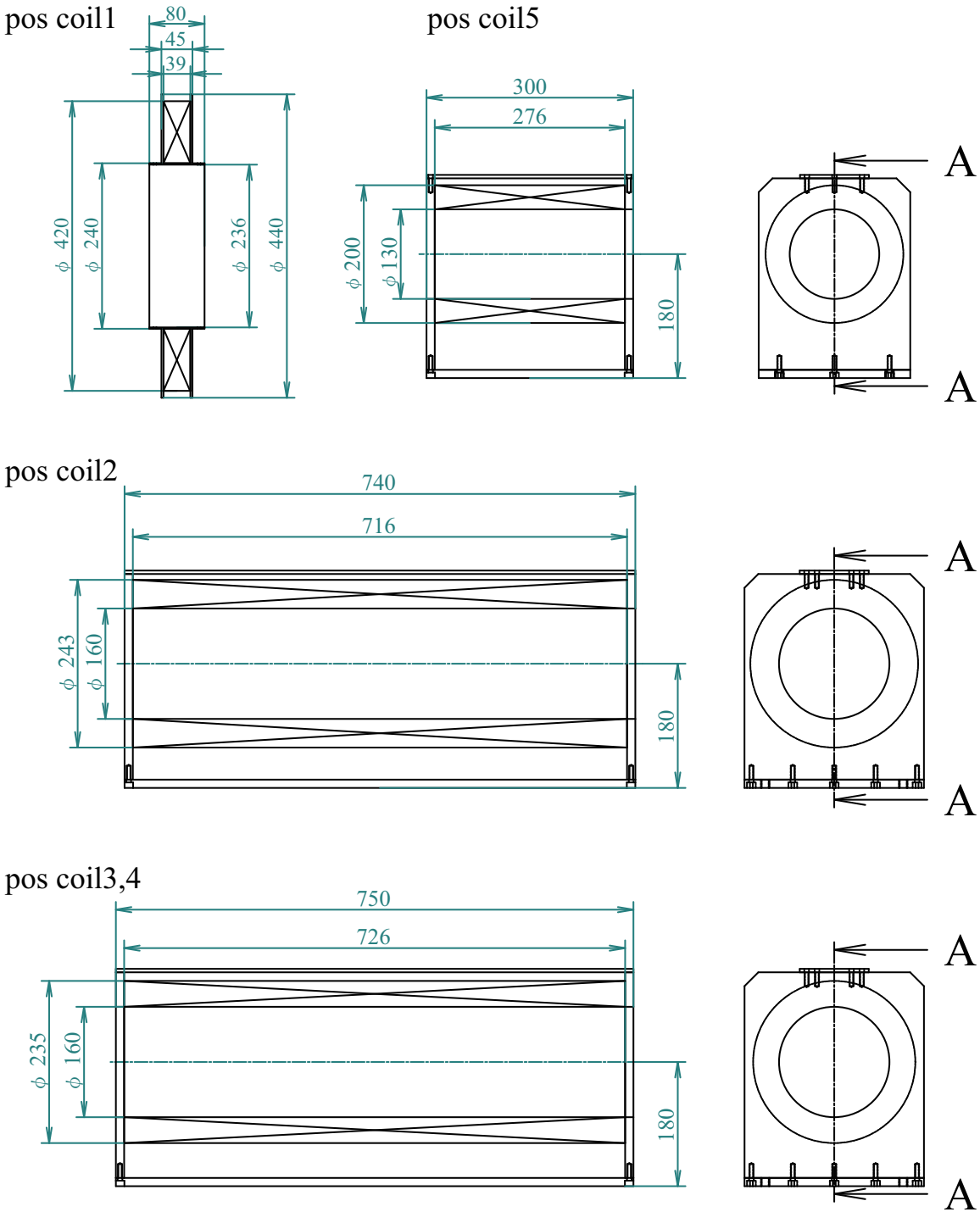

Figure 3.33: Cross sectional drawings of the coils for the positron transport.

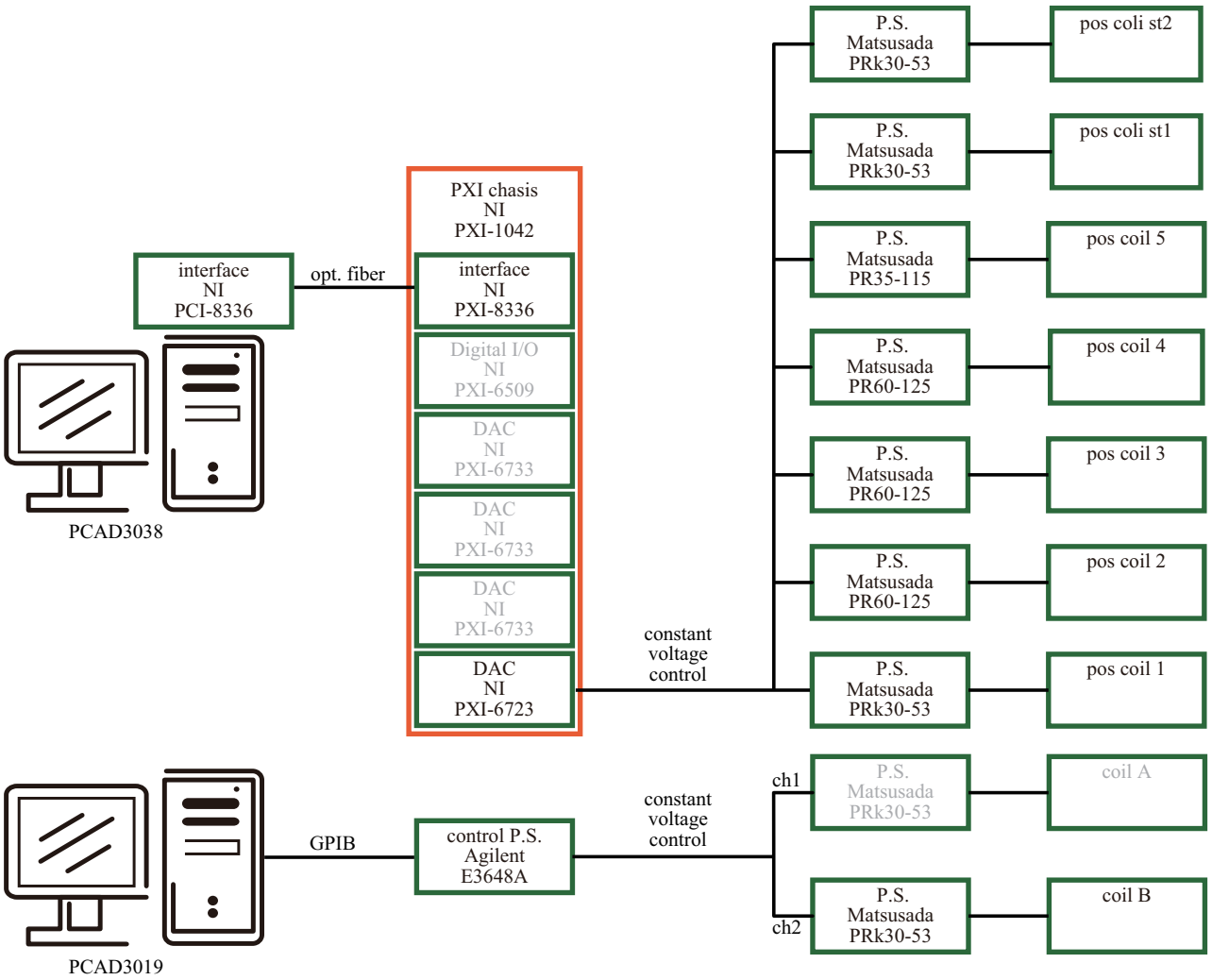

Figure 3.34: A control diagram of the positron transport coils. Coils are energized by power supplies whose current are controlled by the voltages of a DAC (National Instruments, PXI-6723).

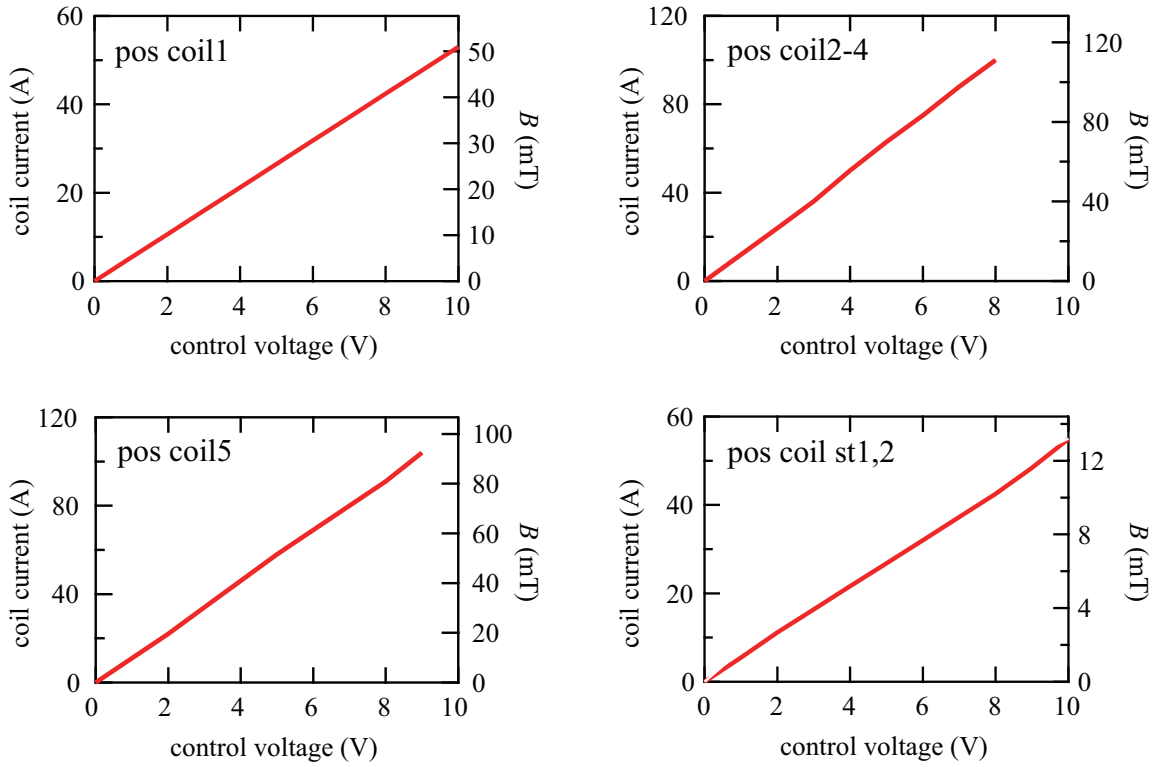

Figure 3.35: Coil current and maximum magnetic field on axis generated by each coil as a function of the control voltage.

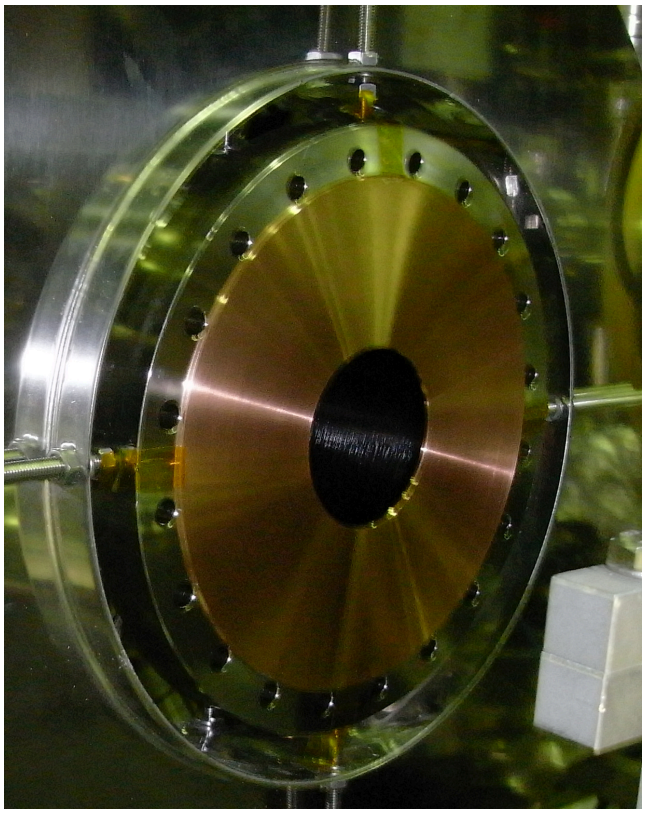

Figure 3.36: A photograph of the special CF203 gasket whose inner diameter is 60 mm. The gasket is used at the flange under the pos coil 1 to reduce the gas inflow from the positron accumulator into the cusp trap.

3.4 Cusp trap

A cusp trap is designed and constructed to produce antihydrogen. Figure 3.37 and figure 3.38 shows an outline view and isometric view inside the magnet of the cusp trap respectively. It major components are a superconducting magnet and an MRE housed in a cryogenic temperature UHV bore tube. Positrons and antiprotons are confided by magnetic field radially and electric potential created by the MRE axially. The trap is evacuated by two TMPs and three non evaporative getter (NEG) pumps. The vacuum of the trap is monitored by ion gauges and a quadrupole mass analyser. A MCPPS detector, which is described in section 3.5 is attached at a port of upstream side to monitor the charged particles in the trap. An electron gun is attached also at a port of upstream side to test the confinement of charged particles. The system is fixed on a base which enables the position of the trap to be adjusted finely. An upstream and a downstream thermal shield are installed to reduce the heat load and inflow of residual gases to the cryogenic bore tube and the MRE. The downstream thermal shield can be opened by the actuator located at a port of downstream side when we extract produced antihydrogen atoms. In this section, components of the cusp trap are described in detail.

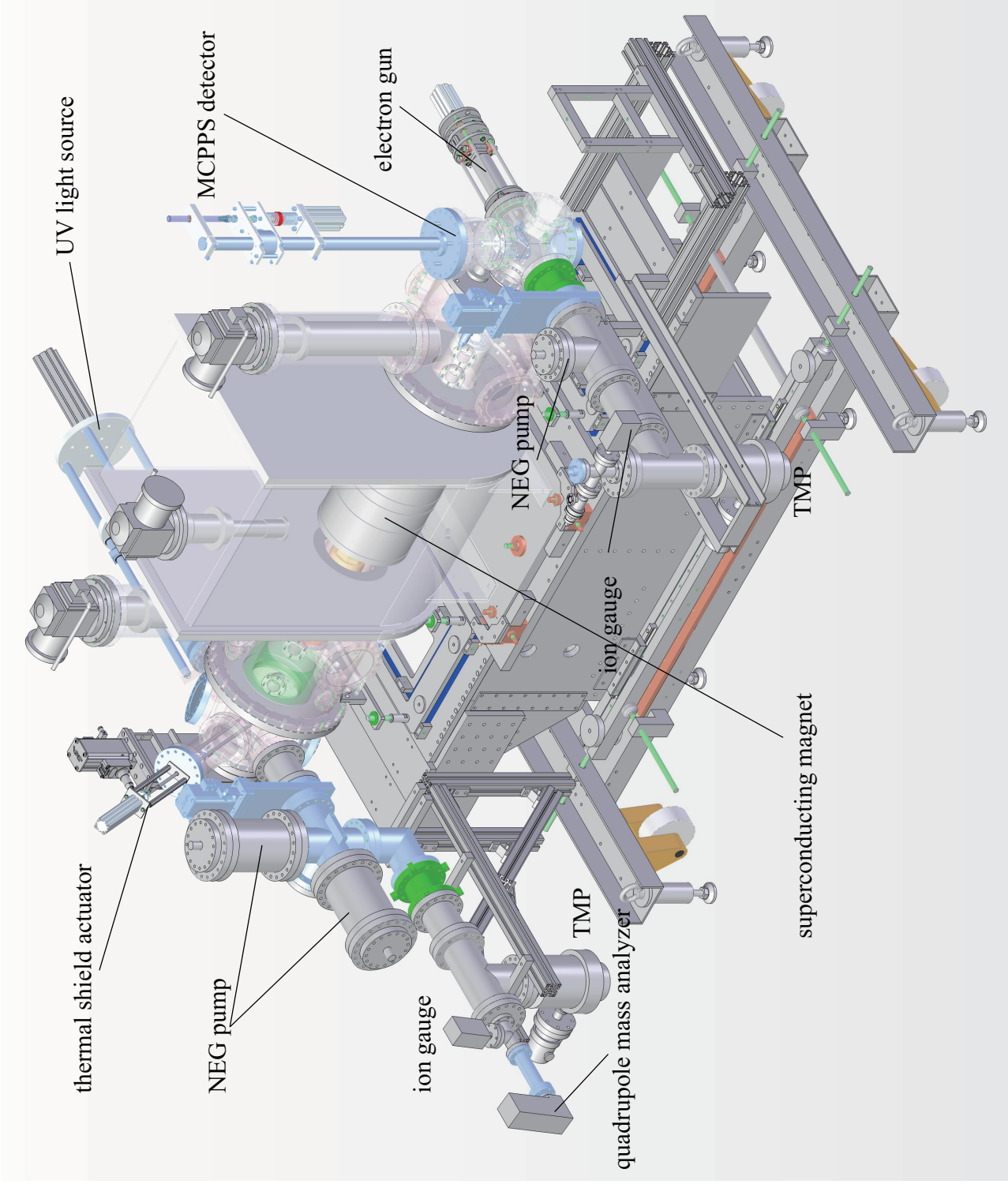

Figure 3.37: An isometric outline view of the cusp trap.

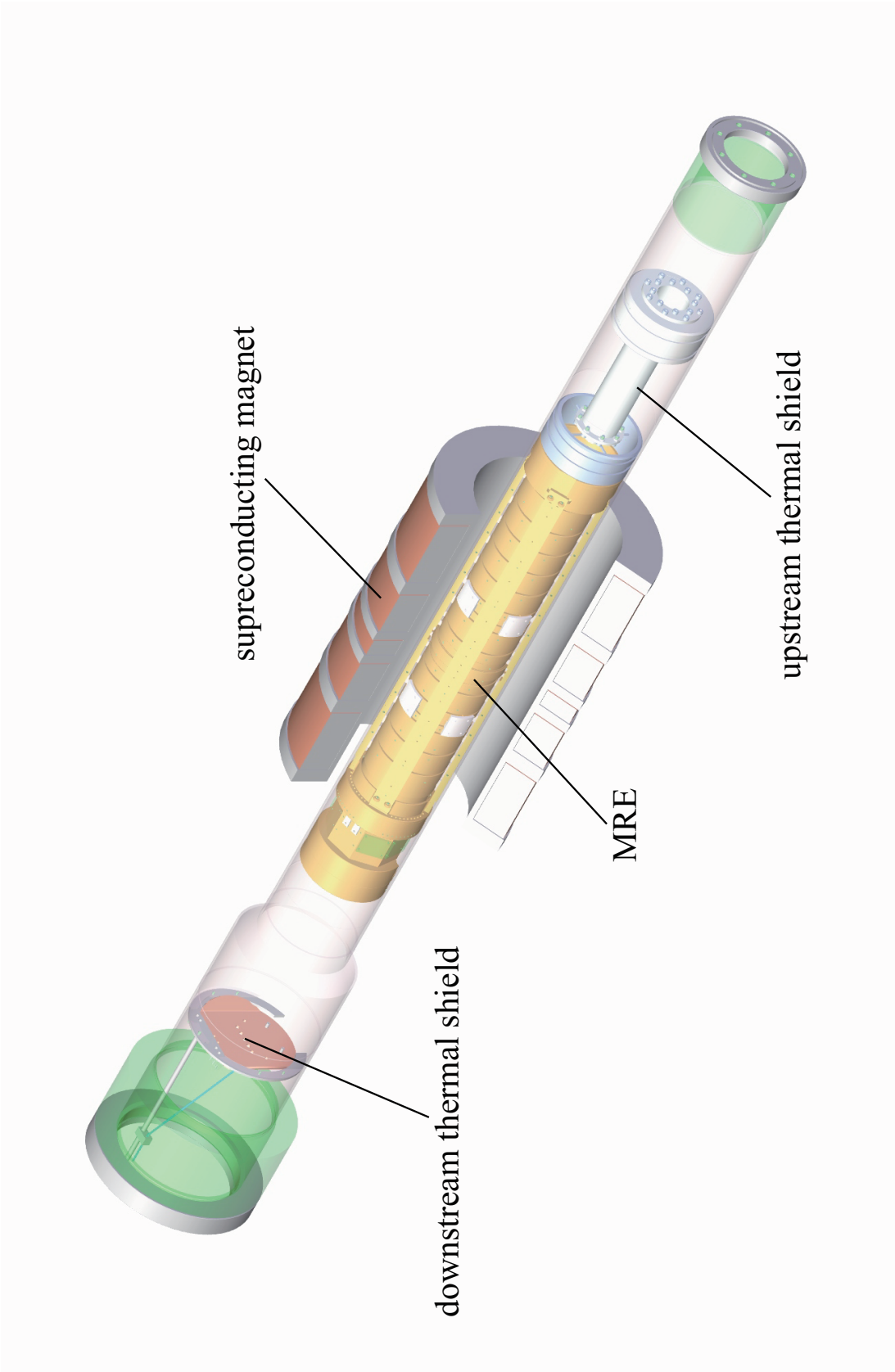

Figure 3.38: An isometric view of inner components of the cusp trap. Radiation shields and MRE are housed in a UHV bore tube. The tube is inserted in the superconducting magnet.

3.4.1 Superconducting magnet

outline and specification

Figure3.39 is a cross sectional drawing of the superconducting magnet of the cusp trap and figure 3.40 is its photograph. The magnet to generate the cusp magnetic field has inner diameter of 200 mm and consists of 5 coils made of NbTi. Each coil can be energized independently, which makes it possible to generate various magnetic field such as uniform, mirror, and cusp magnetic field. The current settings to generate those magnetic field are shown in table 3.5. Table 3.6 summarizes some important specifications of the magnet. The maximum magnetic field on axis in cusp magnetic field distribution is 3.4 T at $I = 101$ A. The magnet can be energized when the temperature of the coils are below 6 K. The maximum sweep speed of the current is 6 A/min.

magnetic field property

Figure 3.41 shows the magnetic properties of the magnet when $I = 80$ A[7]. Figure 3.41 (a) and (b) are $(\mathrm{grad}\boldsymbol{B})_z$ and magnetic field on axis as a function of axial position z. Figure 3.41 (c) shows the magnetic field lines and figure 3.41 (d) is a two dimensional distribution of the magnetic field strength. The advantage of the cusp magnetic field is its axial symmetry, which adjures the stable confinement of charged particles (see ref. [43, 64]) and enables the extraction of antihydrogen atoms along the axis. Figure 3.42 is a two dimensional distribution of the magnetic field strength in a larger region than that shown in figure 3.41 (d). Although the magnet does not have magnetic shield, the cusp magnetic field decrease more rapidly

coil No.	3L	2L	1	2R	3R
cusp	I	I	0	$-I$	$-I$
uniform	$0.66I$	$0.55I$	I	$0.55I$	$0.66I$
mirror	I	0	0	0	I

Table 3.5: Current settings to generate cusp, uniform, and mirror magnetic fields. To generate cusp magnetic field, coils 3L and 2L are energized by a certain amount of current while coils 3R and 2R are energized by the same amount but opposite direction of current.

[7]Most of the experiments were carried out at this current setting

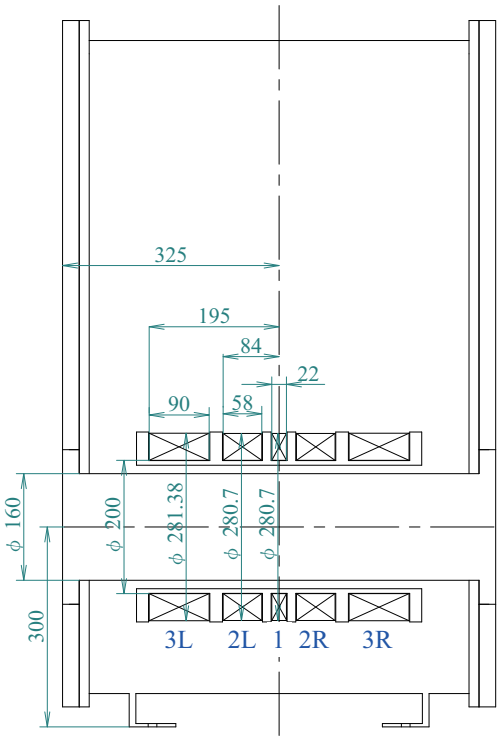

Figure 3.39: A cross sectional drawing of the superconducting magnet of the cusp trap. The magnet consists of five coils whose inner diameter is 200 mm.

Figure 3.40: A photograph of the superconducting magnet of the cusp trap.

Manufacturer	JASTEC(Japan Superconductor Technology, Inc.)
type	JMTD-C160
max. current	101 A
max. magnetic field on axis (cusp)	3.4 T
max. temp to energize magnet	6.0 K
max. current sweep speed	6 A/min
refrigerator	Sumitomo, SRDK-408D2-W71C
temp sensor	Scientific Instruments, RO105
temp sensor controller	Scientific Instruments, Model 1900
power supply	Oxford, IPS125-9
bore diameter	160 mm

Table 3.6: Specifications of the superconducting magnet of the cusp trap.

than uniform magnetic field outside the coils since the field generated by the coils 3L and 2L counteract that generated by the coils 3R and 2R.

cooling mechanism

The magnet is cooled by a GM refrigerator (Sumitomo, SRDK-408D2-W71C) down to around 4 K. The temperature is monitored by a Ruthenium oxide temperature sensor (Scientific Instrument, RO105). Figure 3.43 shows a typical cooling curve of the magnet. It takes about 75 hours to cool down the magnet from room temperature.

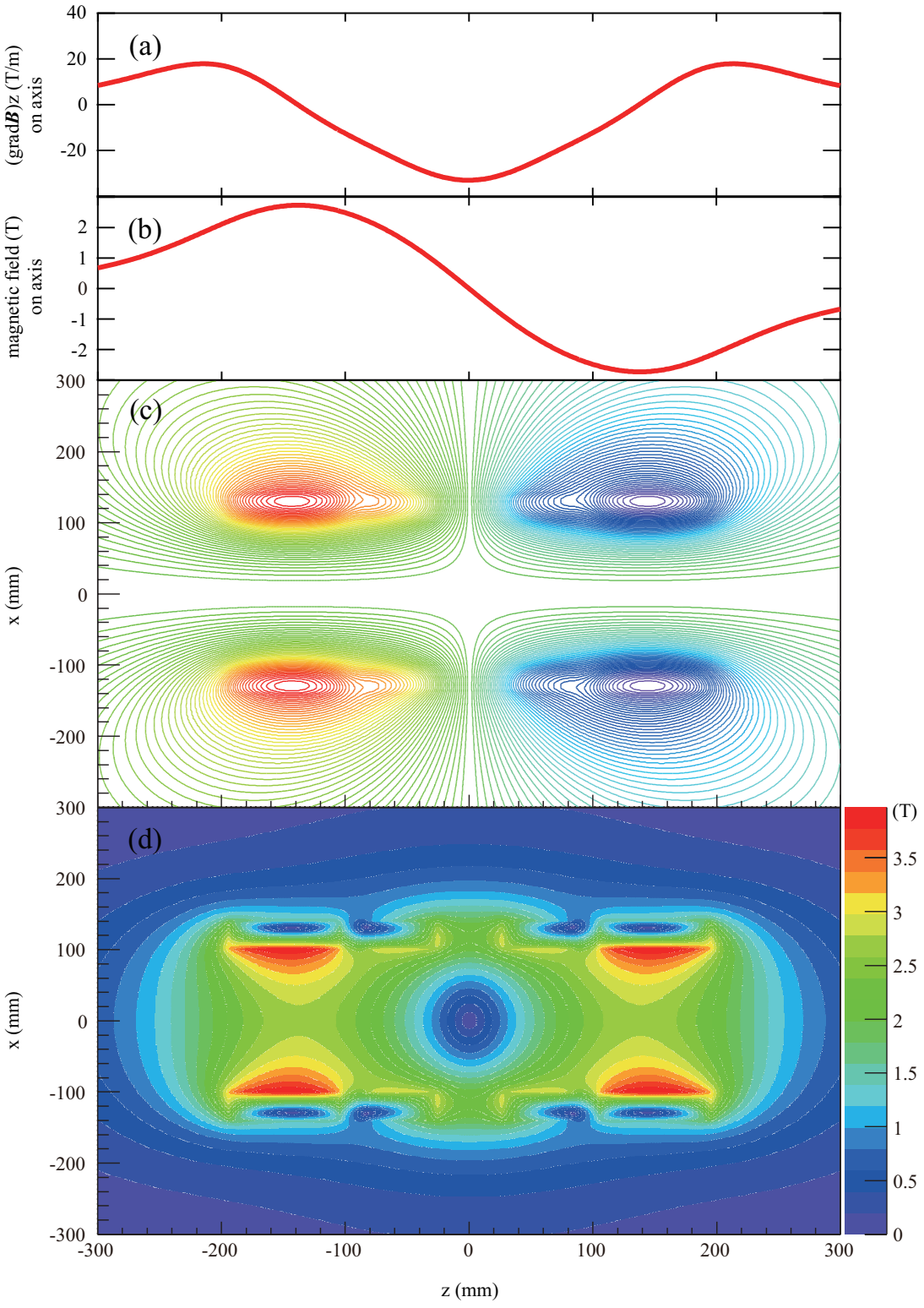

Figure 3.41: Magnetic properties of the cusp magnet; $(\mathrm{grad}\boldsymbol{B})_z$ on axis (a), magnetic field on axis (b), magnetic field lines (c), two dimensional distribution of magnetic field strength (d). Maximum gradient and strength of the magnetic field on axis is about 20 T/m and 2.7 T respectively. Magnetic field is zero at the central position ($z = r = 0$ mm).

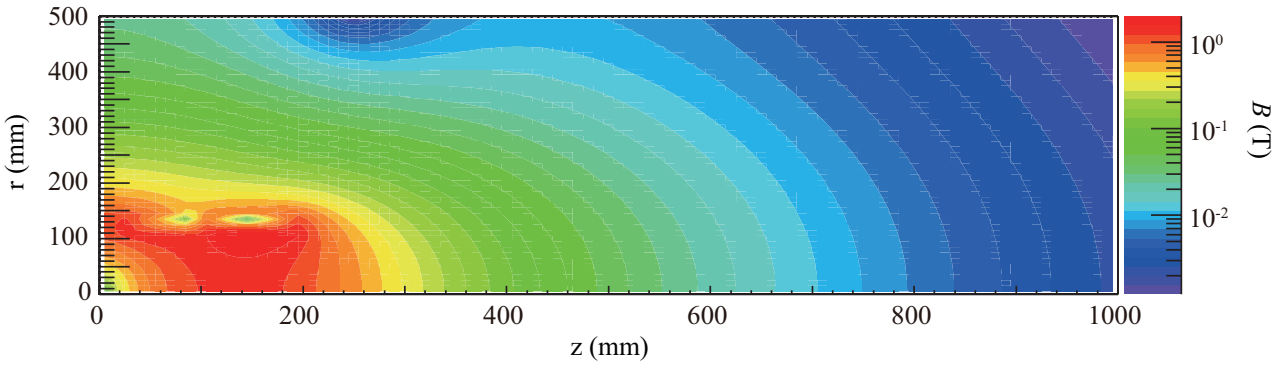

Figure 3.42: Two dimensional distribution of magnetic field strength. The cusp magnetic field decrease rapidly since the field generated by the coils 3L and 2L counteract that generated by the coils 3R and 2R.

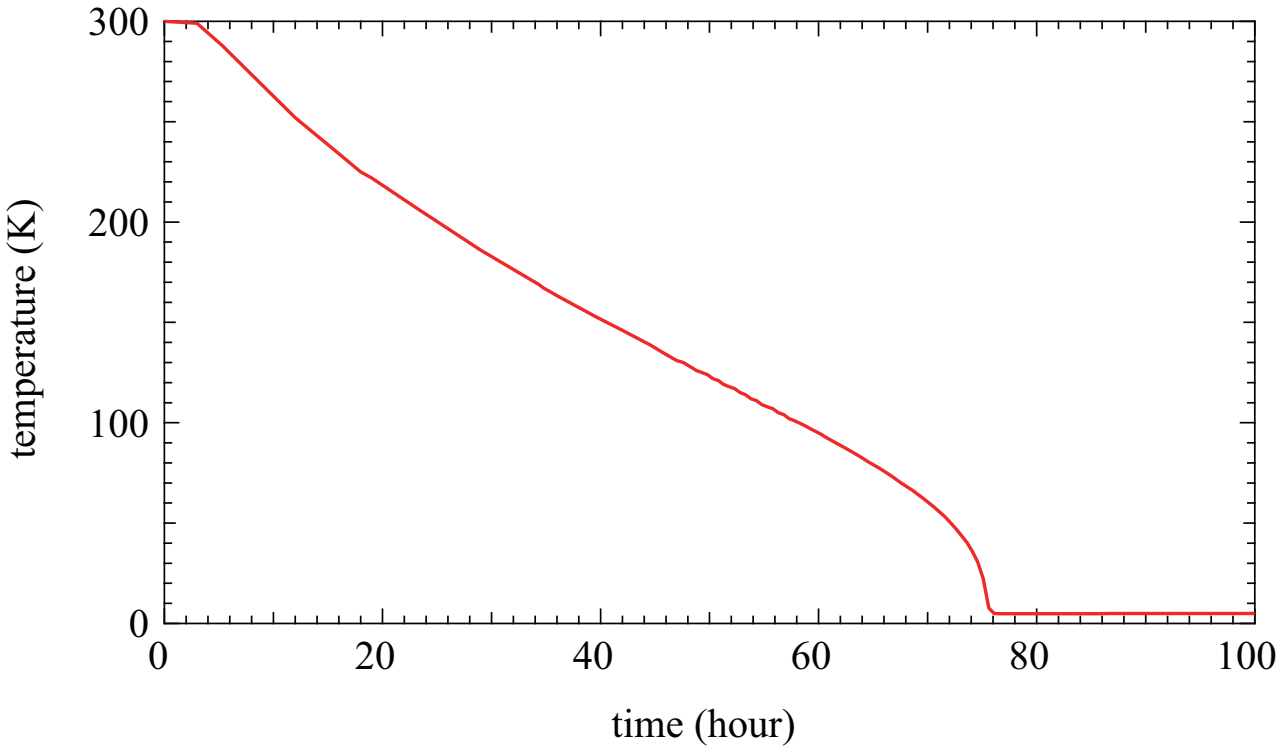

Figure 3.43: Typical cooling curve of the magnet. It takes about 75 hours to cool down the magnet from room temperature.

3.4.2 Multi ring electrode (MRE)

outline and specification

For the efficient extraction of antihydrogen atoms, an MRE whose inner diameter (80 mm) is larger than other MREs (antiproton catching trap (40 mm) and positron accumulator (42 mm)) is designed and constructed. Figure figure 3.44 is a cross sectional and outline view of the MRE of the cusp trap and figure 3.45 is its photograph. The MRE consists of 17 ring electrodes made of Al alloy (A7075) and 2 of them are segmented into four azimuthally for radial compression of charged particle cloud by rotating wall technique. The electrodes are supported by insulators and four support rods which are connected to the upstream support ring (USR) and downstream support ring (DSR) at each end. An aperture of 16 mm inner diameter is attached to the U9 electrode to restrict the inflow of the residual gases from the room temperature section to the MRE, which is placed in the cryogenic region. The aperture is electrically isolated from ground potential and directly mounted on the U9 electrode, it is always in the same potential as that of the U9 electrode. Table 3.7 is a summary of the dimension and materials of the MRE. Material of the insulators to support the electrode is aluminium nitride (AlN) whose thermal conductivity is 230 W/mK to keep good thermal conductivity between the support rods and ring electrodes.

number of electrodes	17
number of segmented electrodes	2 (U4, D4)
inner diameter of electrodes	80 mm
inner diameter of electrodes(CE)	89 mm
width of electrodes (U9, D7)	80 mm
width of electrodes (U8-U3, D3-D6)	30 mm
width of electrodes (U2,D2)	14 mm
width of electrodes (U1, D1)	12 mm
width of electrodes (CE)	14 mm
distance between electrodes	2 mm
material of electrodes	A7075 (gold plated)
material of insulators	AlN

Table 3.7: Summary of the dimension and materials of the MRE.

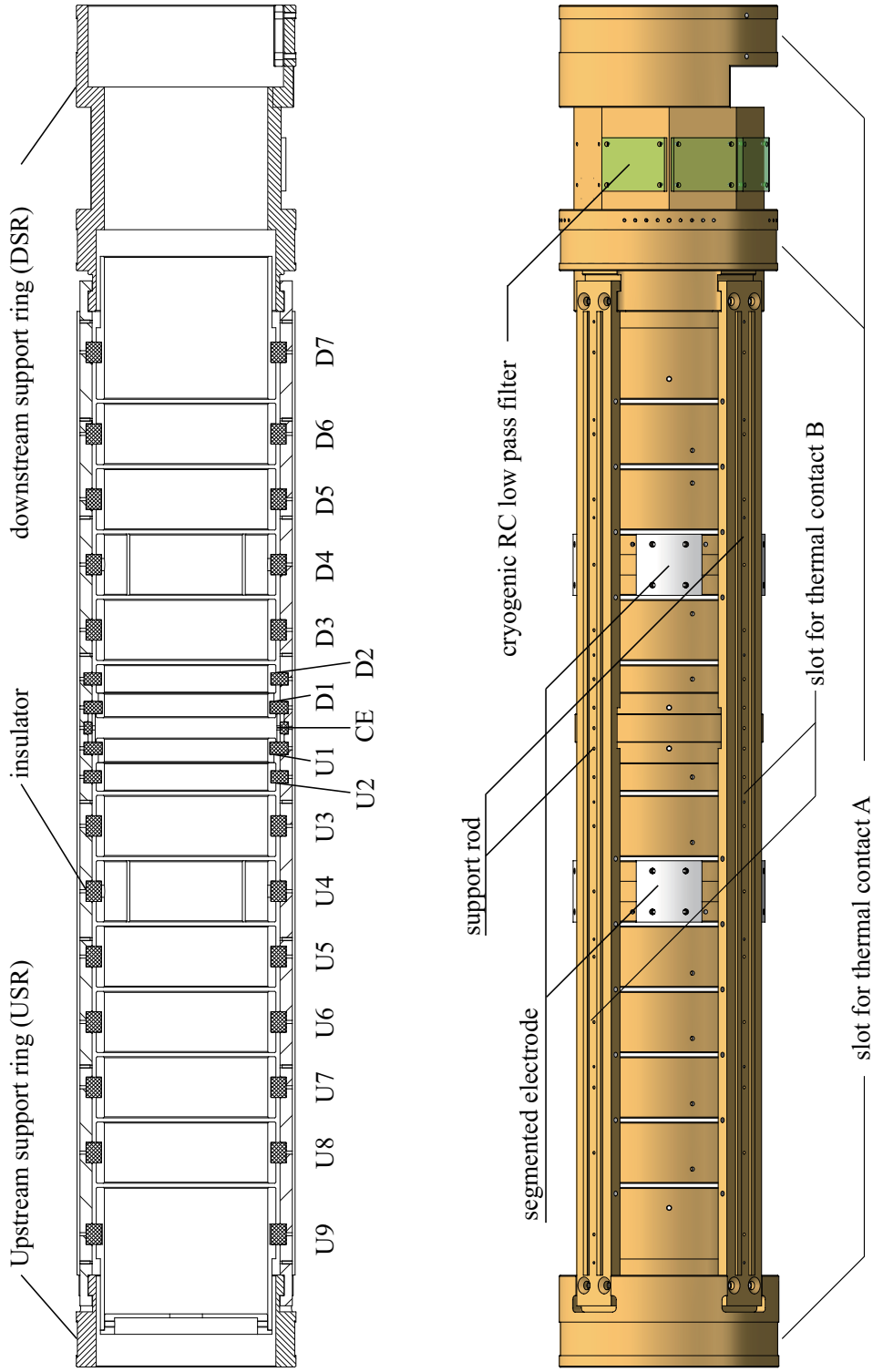

Figure 3.44: A cross sectional and an outline view of the MRE. The MRE consists of 17 ring electrodes and two of them are segmented by four azimuthally. The electrodes are supported by insulators and four support rods which are connected to the upstream support ring (USR) and downstream support ring (DSR) at each end. Slots are used to fix thermal contacts. Cryogenic RC low pass filters are attached at the DSR.

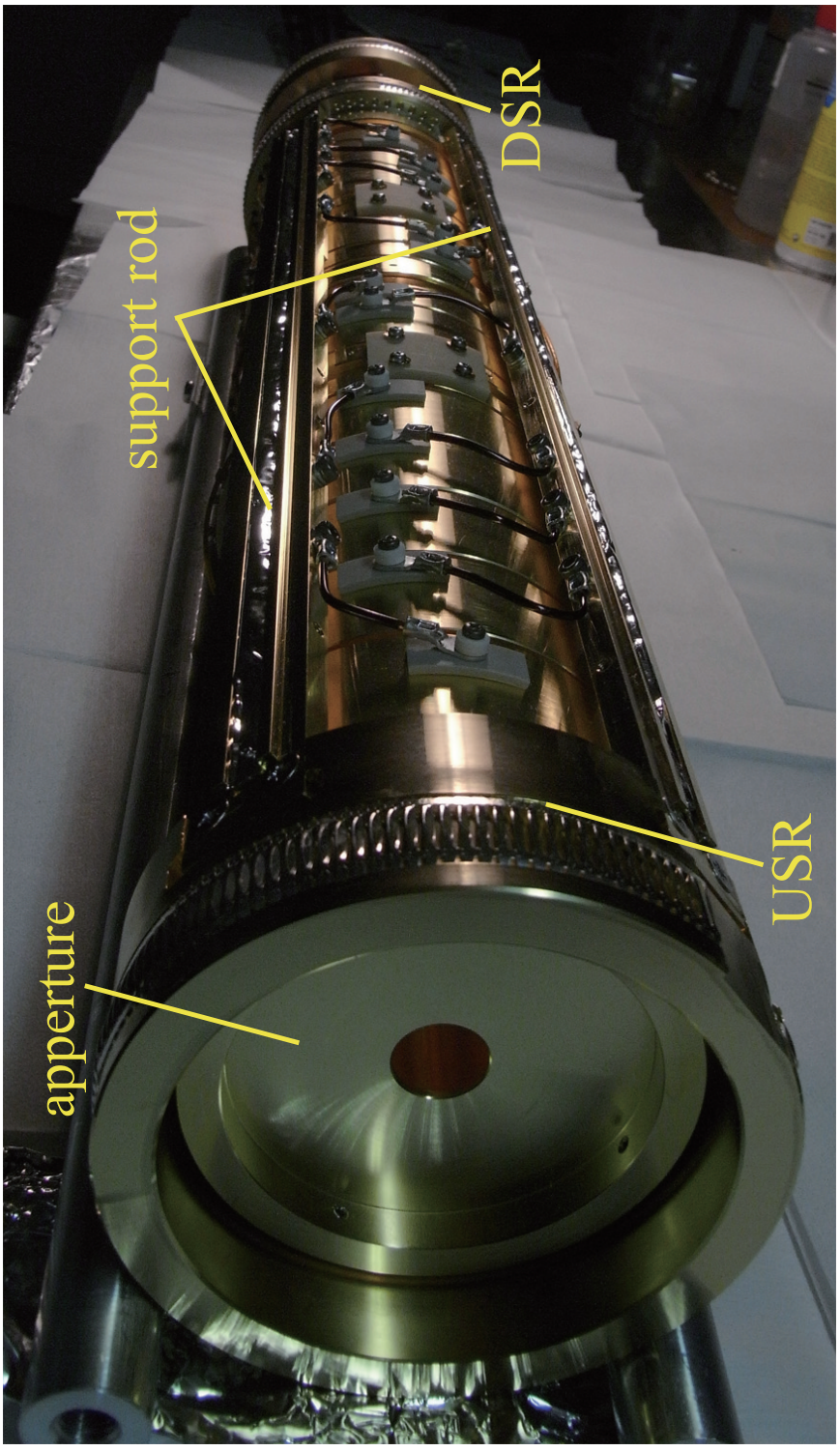

Figure 3.45: A photograph of the MRE. The aperture of 16 mm inner diameter is attached to the U9 electrode to restrict the inflow of the residual gases from the room temperature section to the MRE, which is placed in the cryogenic region.

wiring

In the present work, requirements for the wiring of the MRE of the cusp trap are as follows.

1. Vacuum around the MRE must be good (see section 3.4.4) for the long time confinement of antiprotons. Thus the outgassing rate of the material especially for the insulator should be low.

2. To achieve the vacuum condition, the UHV bore tube and the MRE are cooled down to cryogenic temperature (see section 3.4.5). Thus thermal resistance of the cable between cryogenic region and room temperature region must be high.

3. Each cable must be shielded to avoid cross talk.

4. Cables should be made of non-magnetic material to avoid disturbing the magnetic field.

5. Connectors to the feedthrough must have enough durability.

Figure 3.46 shows an overview of the wiring of the MRE. UHV compatible Kapton insulated coaxial copper cables (allectra[65], 311-KAPM-060-COAX) are used between cryogenic filter and ring electrodes (see figure 3.47 (a)). The cables are connected by normal solder to the cryogenic filter (see figure 3.47 (c)) and by crimp terminal to the ring electrodes (see figure 3.47 (d)). SUS 316L wires of 0.2 mm diameter are used between feedthrough and cryogenic filter to reduce heat inflow. Each wire is insulated by double polyimide tube and shielded by annealed SUS 316L thin tube (see figure 3.47 (b) and 3.48). Thermal property of the cable is described in detail in section 3.4.5. The wires are connected to the cryogenic filter by solder using flux and ultrasonic soldering iron. Structure of the connector to the feedthrough is shown in figure 3.49. The connector and wire are bridged by Cu tube. The polyimide tubes are extended inside the Cu tube to avoid kink of the core SUS wire (see figure 3.49).

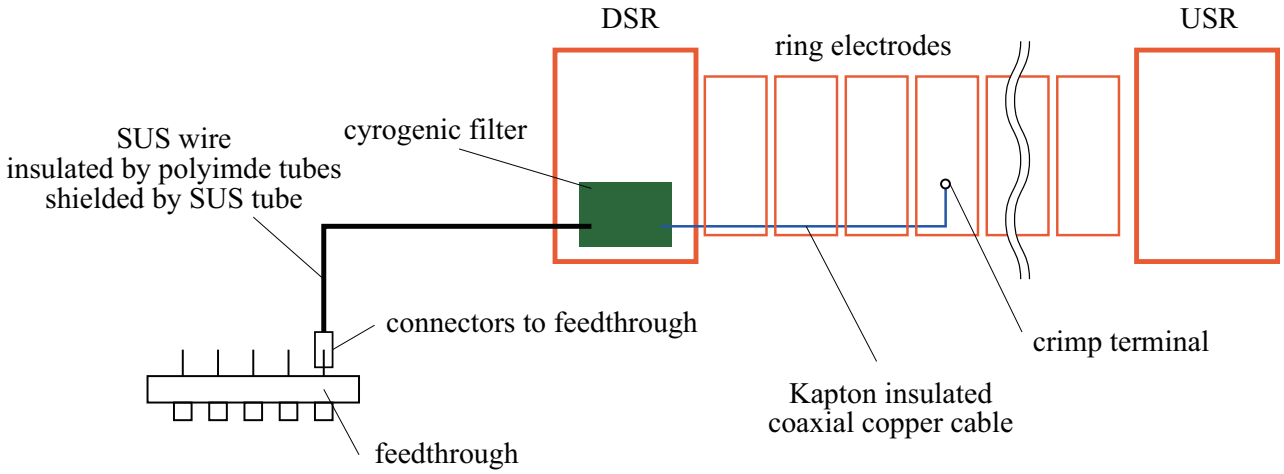

Figure 3.46: An overview of the wiring of the MRE. Kapton insulated coaxial copper cables are used between ring electrodes and cryogenic filters. SUS wires insulated by polyimde tubes and shielded by SUS tubes are used between feedthrough and the cryogenic filters

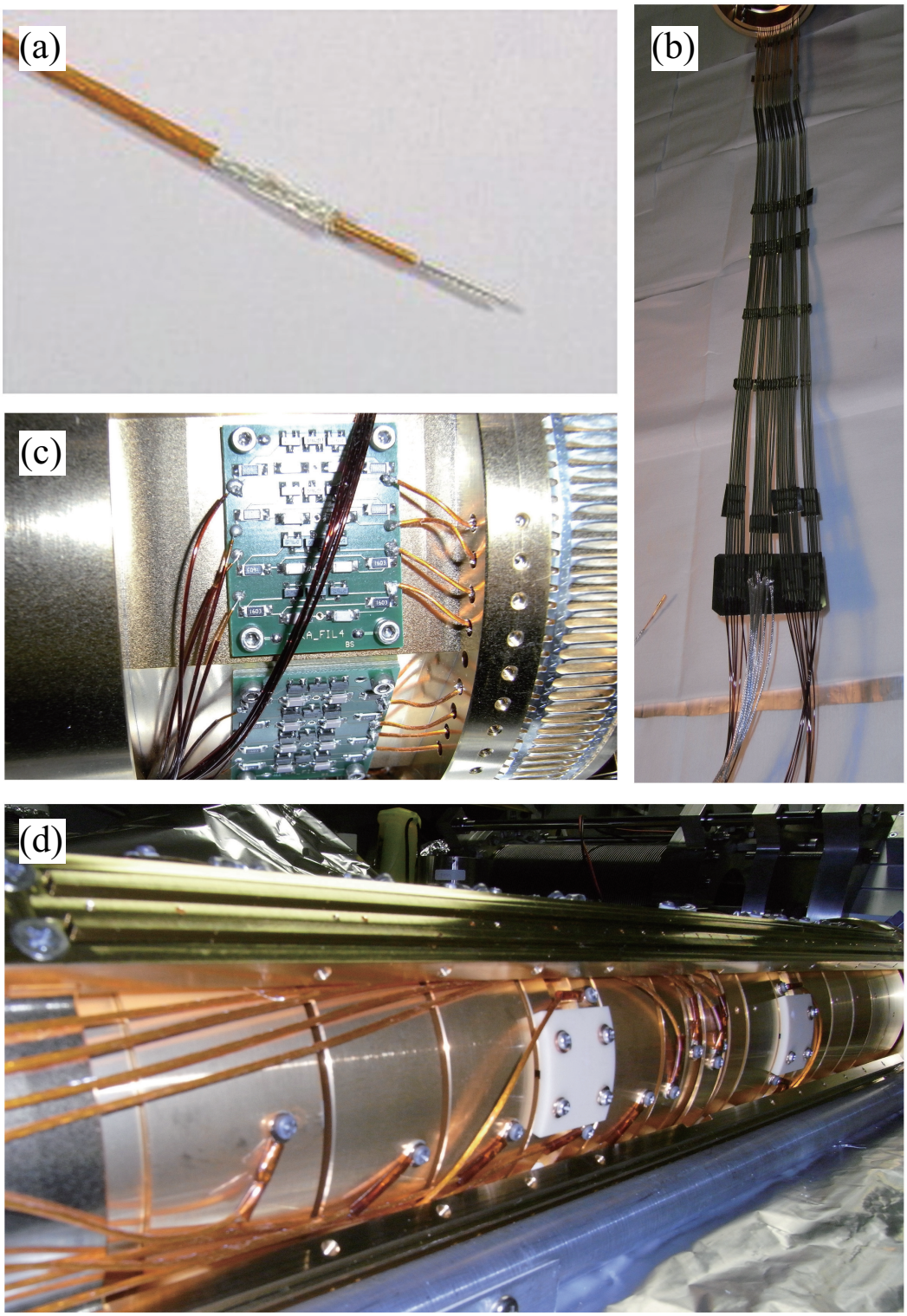

Figure 3.47: Photographs on wiring of the MRE of the cusp trap. Kapton insulated coaxial cables used between the ring electrodes and the cryogenic filter (a). Cables between the feedthrough and the cryogenic filter (b). Connection at the cryogenic filter, each cable is soldered to the filter (c). Connection at the ring electrodes, each cable is attached to the electrode via crimp terminal (d).

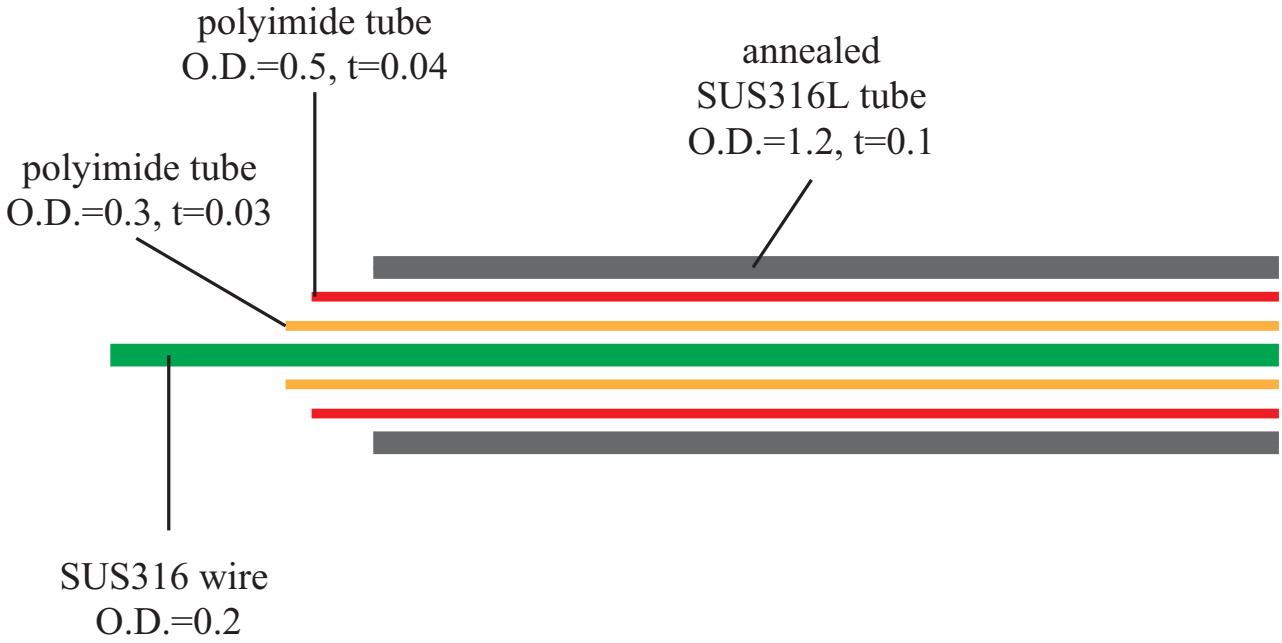

Figure 3.48: A schematic drawing of the cable between the feedthrough and the cryogenic filter. A SUS wire is insulated by double polyimide tube and shielded by a SUS tube.

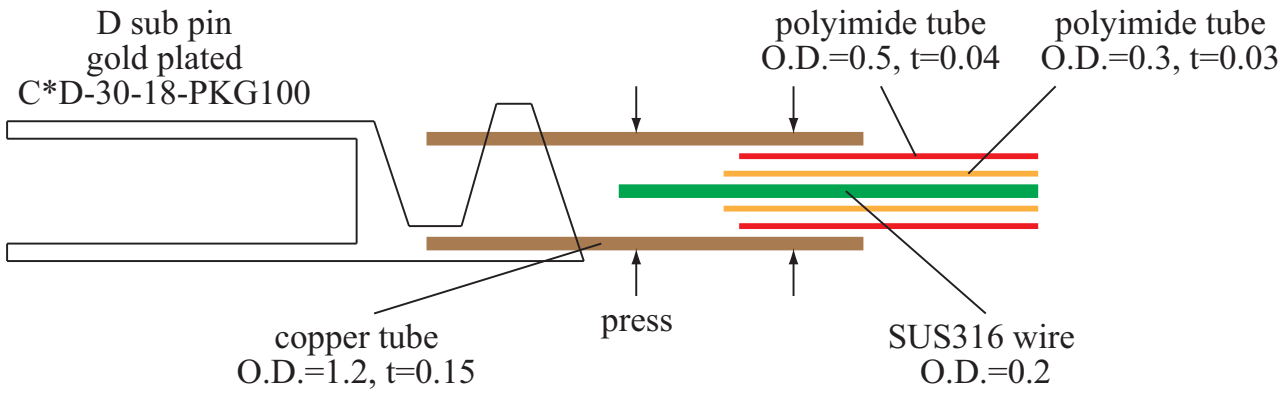

Figure 3.49: A schematic drawing of the connector to the feedthrough. The connector and the wire are bridged by a copper tube. The polyimide tubes are extended inside the copper tube to avoid kink of the core SUS wire.

Cryogenic low pass filter

Cryogenic low pass filters are inserted in between each ring electrode (except for segmented electrodes, U4 and D4) and feedthrough to reduce electric noise, which can heat up charged particles. Table 3.8 summarizes technical specifications of the filter. The filter is 2nd order RC passive low pass filter, but its input and output are connected by two oppositely directed Schottky barrier diode (SBD) to bypass fast and large ($\gtrsim$ 3 V) pulse signal like the pules to capture charged particle beams (see figure 3.50). The corner frequency of the filter is 4 kHz at 4 K, which is well below the characteristic frequencies [8] of charged particles in the cusp trap. The filters are fixed on the DSR (see figure 3.44) and cooled down to around 15 K to reduce thermal noise.

We measured the frequency response of the filter. Figure 3.51 shows the connection to measured the response. A Sine wave is generated by a function generator (NF, WF1974). The electric signal is divided into two and one is sent to the oscilloscope as a reference, the other is sent to an electrode through the cryogenic filter. Output signal is monitored by another cable connected on the same electrode but without the filter.

The results are shown in figure 3.52. For large amplitude signals (red curve, 10 V), frequency response is almost flat up to MHz region. This is because the SBD bypasses the signal. Decrease of the gain in higher frequency region seems due to stray capacitance of the cable. On the other hand, for small amplitude signal (blue curve, 0.1 V), the filter works and the gain decrease from kHz region.

manufacturer	Stahl-Electronics [66]
type	KA-FIL4
corner frequency	4 kHz at 4 K
composition	2nd order RC passive low pass filter
maximum DC voltage	350 V
dimension	33.2 mm × 26.1 mm × 3.04 mm

Table 3.8: Specifications of the cryogenic RC low pass filter.

[8] For example, cyclotron frequency of positrons and antiprotons are a few tens GHz and a few tens MHz, bounce frequency of them in the electric potential well are a few tens MHz and a few hundred kHz respectively.

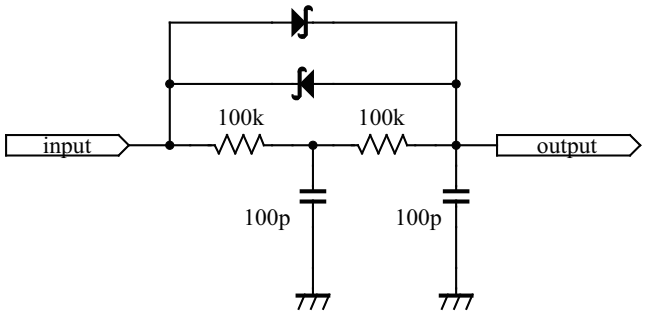

Figure 3.50: A circuit drawing of the cryogenic filter. The filter is 2nd order RC passive low pass filter. Input and output are connected by Schottky barrier diodes to bypass fast and large pulse signal.

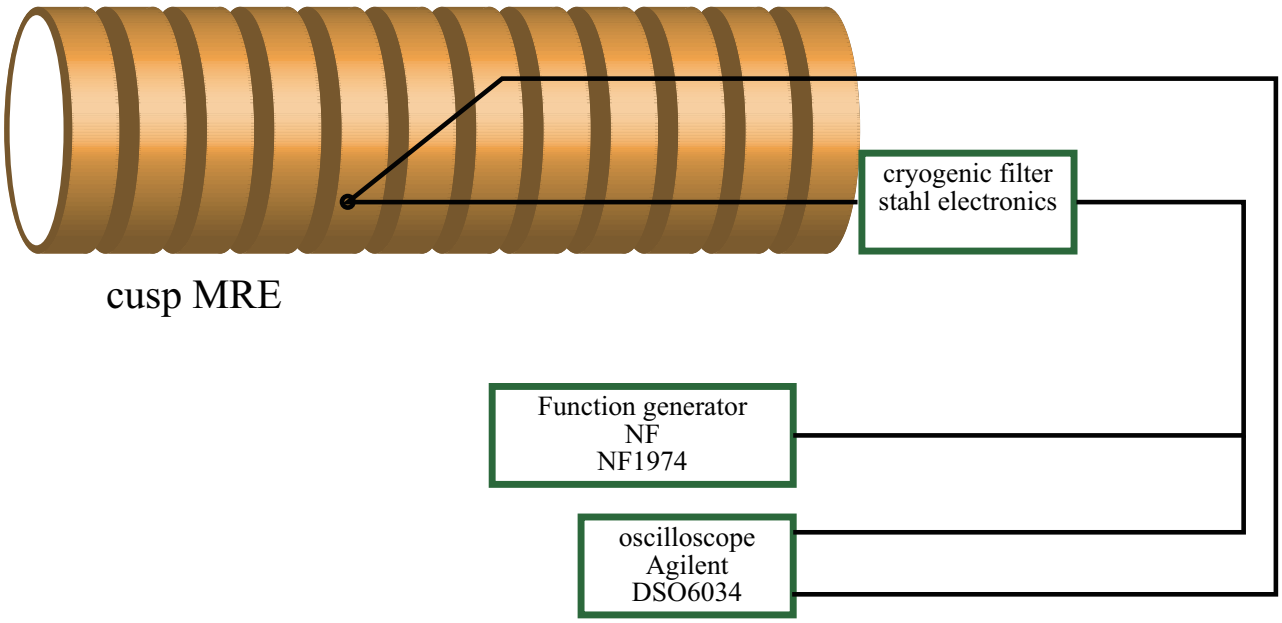

Figure 3.51: A schematic drawing to measure the frequency response of the cryogenic filter. A Sine wave is generated by a function generator (NF, WF1974). The electric signal is divided into two and one is sent to the oscilloscope as a reference, the other is sent to an electrode through the cryogenic filter. Output signal is monitored by another cable connected on the same electrode but without the filter.

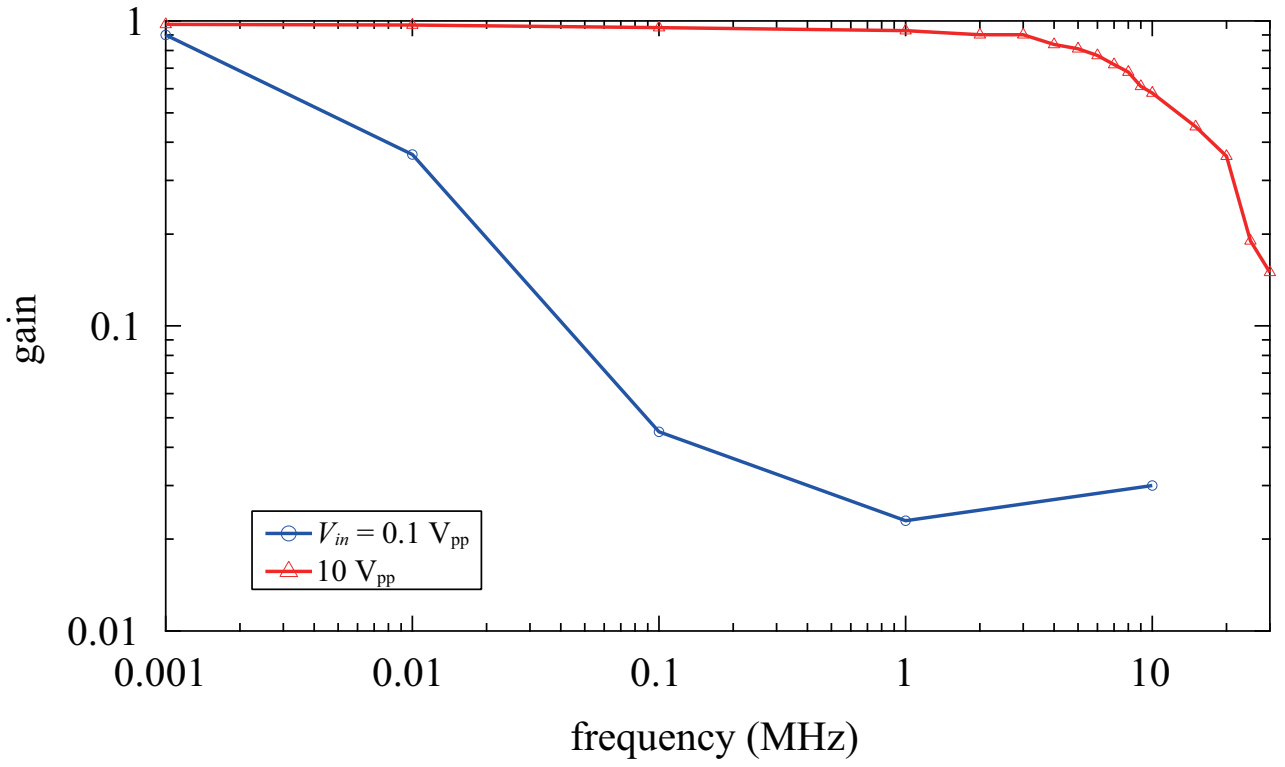

Figure 3.52: Frequency response of the cryogenic filter for small (blue curve, 0.1 V) and large (red curve, 10 V) input signal amplitude. The gain is almost flat up to MHz region for large input signal while it decrease from kHz region for small amplitude signal.

3.4.3 Extraction coil

A detector which consists of an MCP and a phospher screen (MCPPS detector, see section 3.5.3) is attached to observe charged particles in the cusp trap. However, due to the geometrical restriction, the detector is placed 1 m away from the center of the cusp trap where the magnetic field is 1/300 of the trapping region. This means that the diameter of the cloud of positrons at the detector is $\sqrt{300}$ times larger than that in the trap. Considering the diameter of the active area of the MCP (47 mm, see table 3.18), the detector can monitor positrons whose radial position is less than 2.7 mm in the cusp trap. Thus we introduce a coil (extraction coil) near the detector to suppress the expansion.

Figure 3.53 (a) is a cross sectional view of the cusp trap, the MCPPS detector and the extraction coil. Considering the geometrical restriction, we attached the coil at the position indicated by red rectangles in the figure. Blue curve and red curve in figure 3.53 (b) shows magnetic field on without the extraction coil and with the extraction coil. In this case, the extraction coil generate magnetic field of 0.18 T at the center of the coil. Figure 3.53 (c) and (d) shows magnetic field lines without the extraction coil and with extraction coil respectively. Since the trajectory of low-energy charged particles follow the magnetic field line, figure 3.53 (c) and (d) represent the trajectory of them. The magnetic field at the position of the detector is 0.007 T without the extraction coil and 0.038 T with the extraction coil. Thus the diameter of the cloud of charged particles at the position of the detector is compressed 2.3 times.

Figure 3.54 is a photograph of the extraction coil and table 3.9 shows its specifications. A rectangular copper wire (2 mm $\times$ 4 mm in cross section) is wound directly on the vacuum tube and the inner diameter of the coil is 104 mm. Figure 3.55 shows the circuit to energized the coil. Current to the coil is supplied from a capacitor which is charged by a power supply to supply high current ($\sim$ 1000 A) in a short time ($\sim$ a few ms). Figure 3.56 is a connection diagram to trigger the coil and figure 3.57 shows the relation between trigger pulse and coil current. Since it takes 1.2 ms for the coil current to reach 90 % of the maximum value and positrons are extracted to the detector within a few hundred nano seconds from the extraction trigger, the coil have to be energized before the extraction of positrons. Typical operation to extract charged particles in the cusp trap using the coil is as follows.

1. A digital I/O module (National instruments, PXI-6509) send a start pulse (trigger in) to the controller of the extraction coil (extraction coil controller, see figure D.10 for the

circuit drawing) via Trig controller 1[9].

2. A thyristor in the extraction coil controller is triggered and the coil is energized.

3. When the coil current reached to the pre-set value I_{ex}, a pulse (trigger out) from the controller is sent to the high voltage switch connected to the MRE, then positrons are extracted.

The pre-set value I_{ex} can be varied by the dial of the controller. The coil current can be monitored by an oscilloscope. By this procedure, every time the same magnetic field determined by I_{ex} is applied when charged particles are extracted.

Figure 3.58 shows magnetic field on axis at the coil and at the detector as a function of the value of the dial of the controller and I_{ex}. When we set the dial at 1.0, I_{ex} is 520 A and magnetic field at the detector is 0.023 T, for example.

Effect of the coil is tested using electrons. Figure 3.59 shows images of electron cloud confined in and extracted from the cusp trap when magnetic field at the MCPPS detector is 0.035 T (a), 0.023 T (b), 0.015 T (c). As increasing the magnetic field, the images on the detector shrinks.

[9]Here, the Trig controller just relays the signal. Its function is explained in section 3.4.6 in detail.

coil inner diameter	104 mm
coil width	32 mm
coil outer diameter	108 mm
configuration	8 turn per layer, 2 layer
wire dimension	2 mm × 4 mm
rise time (10 to 90 %)	1.2 ms
fall time (90 to 10 %)	3.0 ms

Table 3.9: Specifications of the extraction coil.

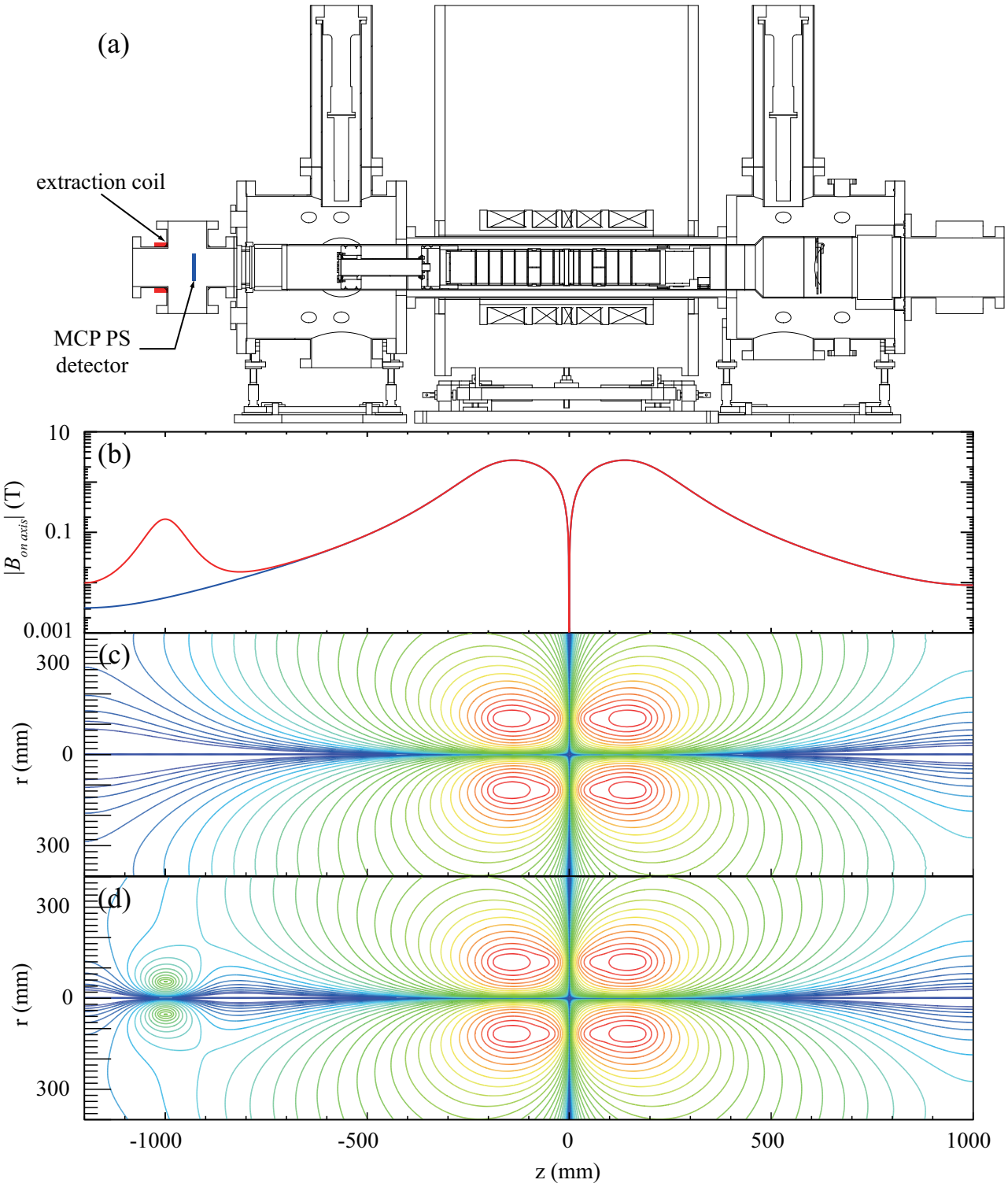

Figure 3.53: A cross sectional view of the cusp trap, the MCPPS detector and the extraction coil (a). Magnetic field on axis with (red curve) and without (blue curve) extraction coil (b). Configuration of the magnetic field lines without (c) and with (d) extraction coil.

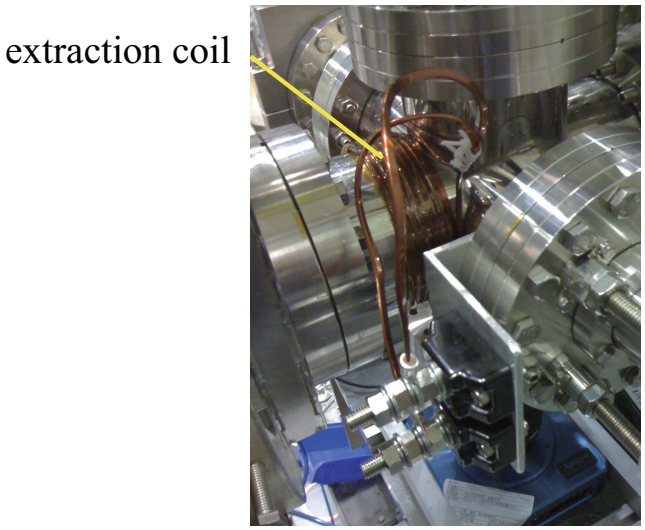

Figure 3.54: A photograph of the extraction coil. The magnet wire is wound directly on the vacuum pipe.

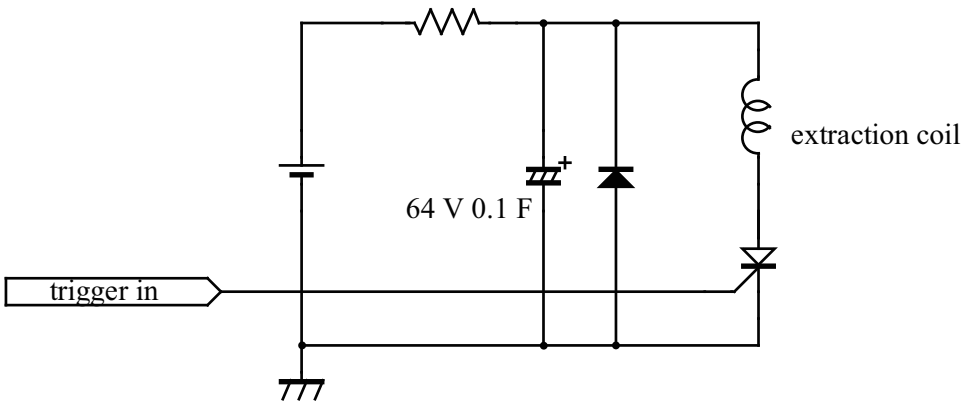

Figure 3.55: A circuit drawing to energize the extraction coil. Current to the coil is supplied from a capacitor which is charged by a power supply to supply high current ($\sim$ 1000 A) in a short time ($\sim$ a few ms).

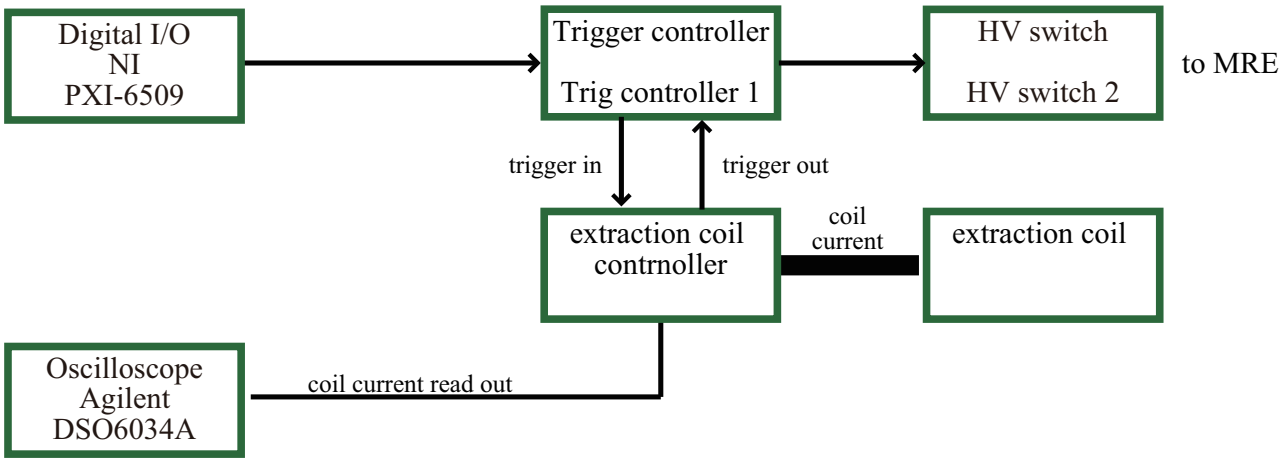

Figure 3.56: A connection diagram to trigger the extraction coil. A start pulse (trigger in) from a digital I/O module (National instruments, PXI-6509) is sent to the extraction coil controller via Trigger controller and the extraction coil is energized. When the coil current reached to the pre-set value, a pulse (trigger out) from the extraction coil controller is sent to the high voltage switch connected to the MRE, then positrons are extracted. Coil current can be monitored by an oscilloscope.

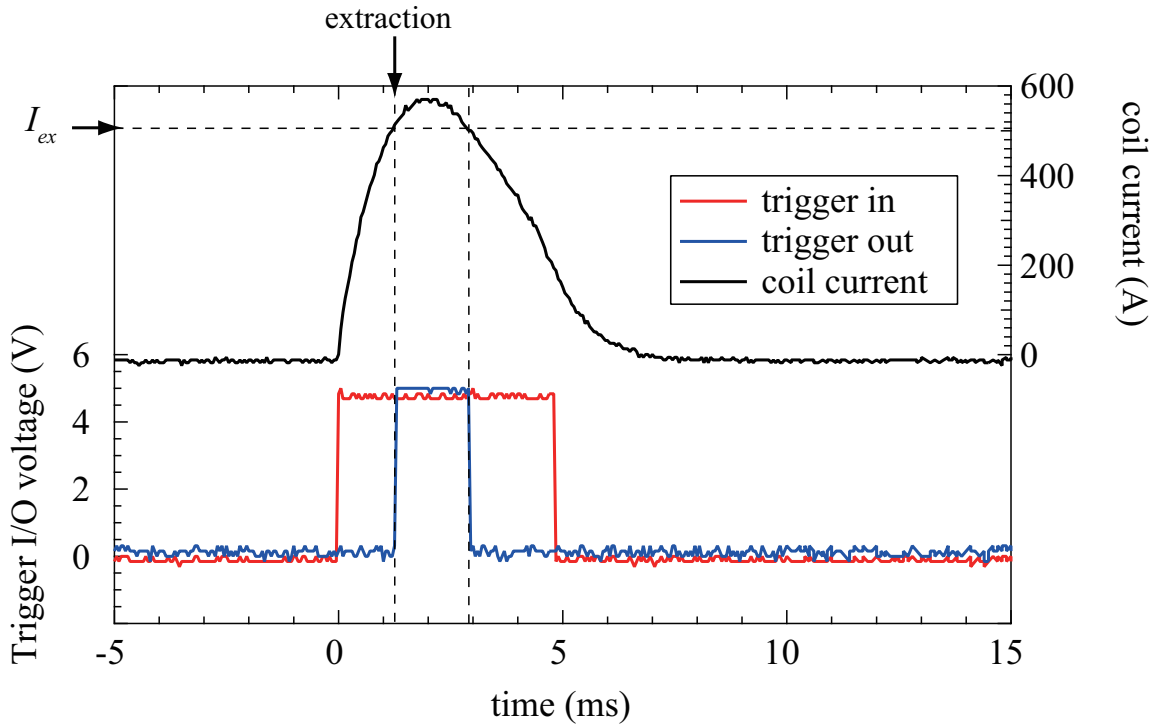

Figure 3.57: Relation between trigger timing and coil current. The current start flowing to the coil when the trigger in pulse comes. The trigger out signal is high during the current is higher than pre-set value (I_{ex}).

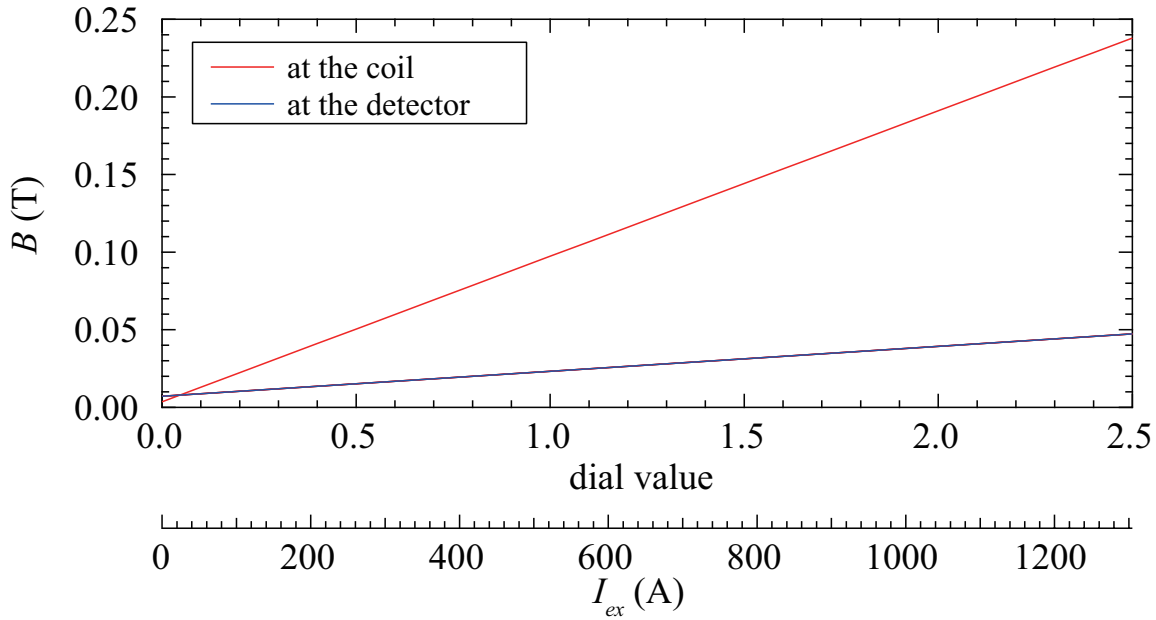

Figure 3.58: Magnetic filed on axis at the coil and at the MCPPS detector as a function of the dial value and I_{ex}.

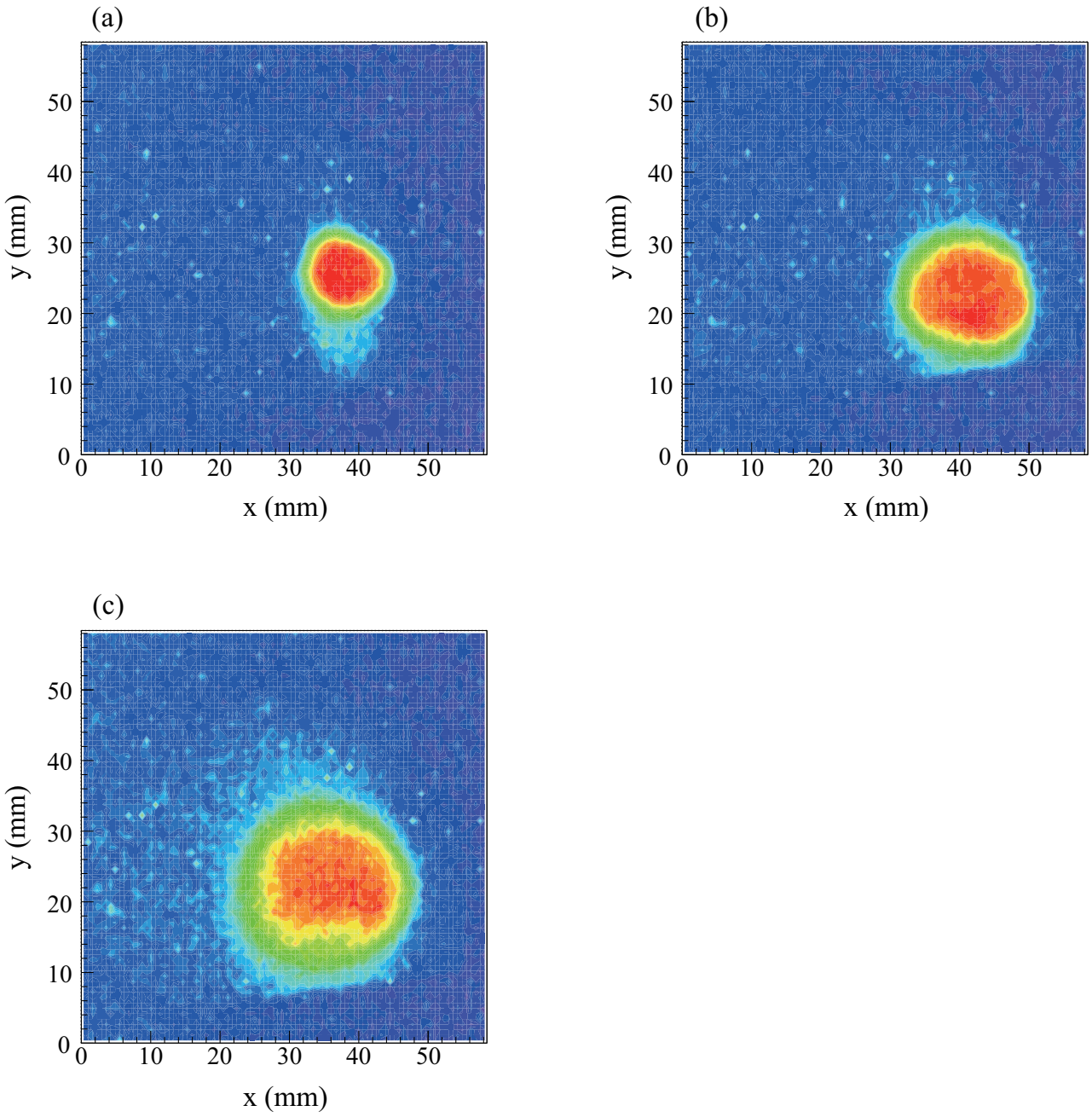

Figure 3.59: Images of electron cloud confined in and extracted from the cusp trap when magnetic field at the MCPPS detector is 0.035 T (a), 0.023 T (b), and 0.015 T (c). As increasing the magnetic field, the images on the detector shrinks.

3.4.4 Vacuum system

requirement and strategy

Antiproton itself is a stable particle in vacuum, however it can annihilate with ordinary matter like residual gas in vacuum chamber. Because it takes several tens of seconds to produce antihydrogen in our condition and the annihilation signal of antiproton with residual gas is one of background source for the detection of antihydrogen, vacuum in the cusp trap should be as high as possible.

Figure 3.60[58] shows a relation between temperature and vapor pressure of various gases. The figure indicates that the vapor pressure of most of the gases can be reduced by cooling the apparatus down to about 10 K. From the figure, candidates for the residual gas below 10 K are helium, hydrogen and neon. For helium and neon, there is no source of them and can be evacuated by TMPs. On the other hand, hydrogen is absorbed in stainless steel, which is major material of the vacuum chamber, and released to the vacuum for a long time. Consequently, evacuation of hydrogen is a key issue for the long time confinement of antiproton.

Here, we estimate required vacuum. Figure 3.61 [67] shows the cross section of hydrogen molecule and antiproton (σ_{H_2}) as a function of relative energy in the center of mass frame $E_{c.m.}$. The collision frequency of them (ν_{H_2}) can be calculated by

$$\nu_{H_2} = \sigma_{H_2} v n (/\mathrm{s}), \tag{3.1}$$

where v is relative velocity, n number density of the hydrogen molecules.

Figure 3.62 shows mean free time ($1/\nu_{H_2}$) of antiproton for several different hydrogen pressures[10]. Since recombination rate of antihydrogen atoms increases when the relative energy of positrons and antiprotons is low as described in section 2.4, we focus on the low energy region of the figure 3.62 where $1/\nu_{H_2}$ is almost independent of $E_{c.m.}$[11]. Considering typical operation period for the production of antihydrogen atoms in the present work is 100 s[12], pressure of hydrogen gas should be kept under 1×10^{-12} Torr.

To achieve this requirement, our strategy is as follows.

1. Use TMPs as roughing pump and evacuate the chamber down to 10^{-10} Torr.

[10] We assumed the temperature of hydrogen as 15 K in this calculation to convert number density to pressure.

[11] It is known that in the low energy ion-neutral atom collision process, the cross section is proportional to $1/v$ (Langevin cross section) and the collision frequency is independent from the relative energy.

[12] See chapter 6

2. Cool the bore tube down to 4 K to freeze all residual gases but hydrogen.

3. Use NEG pumps, which has large pumping speed for hydrogen, to evacuate hydrogen.

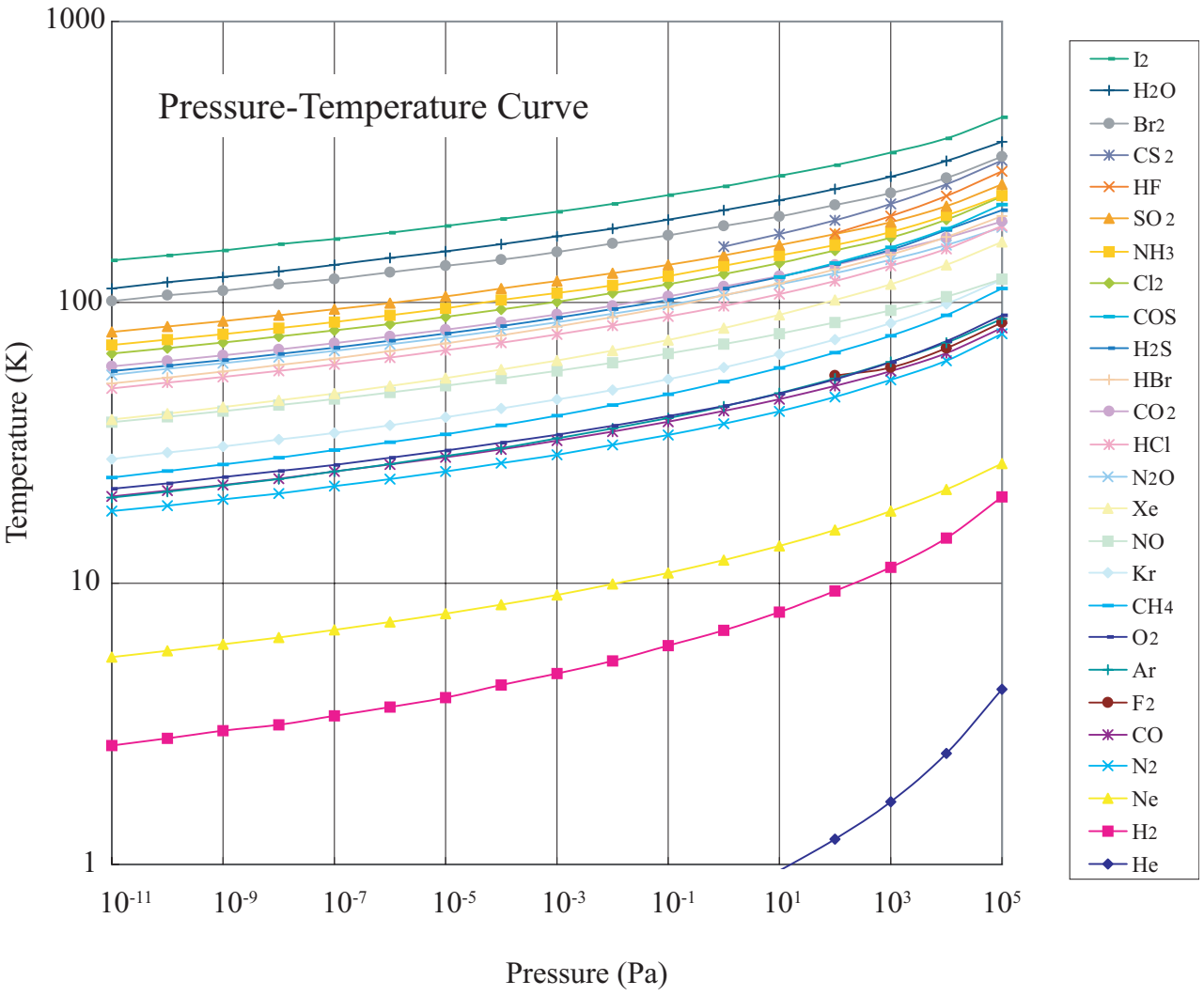

Figure 3.60: Relation between temperature and vapor pressure of various gases.

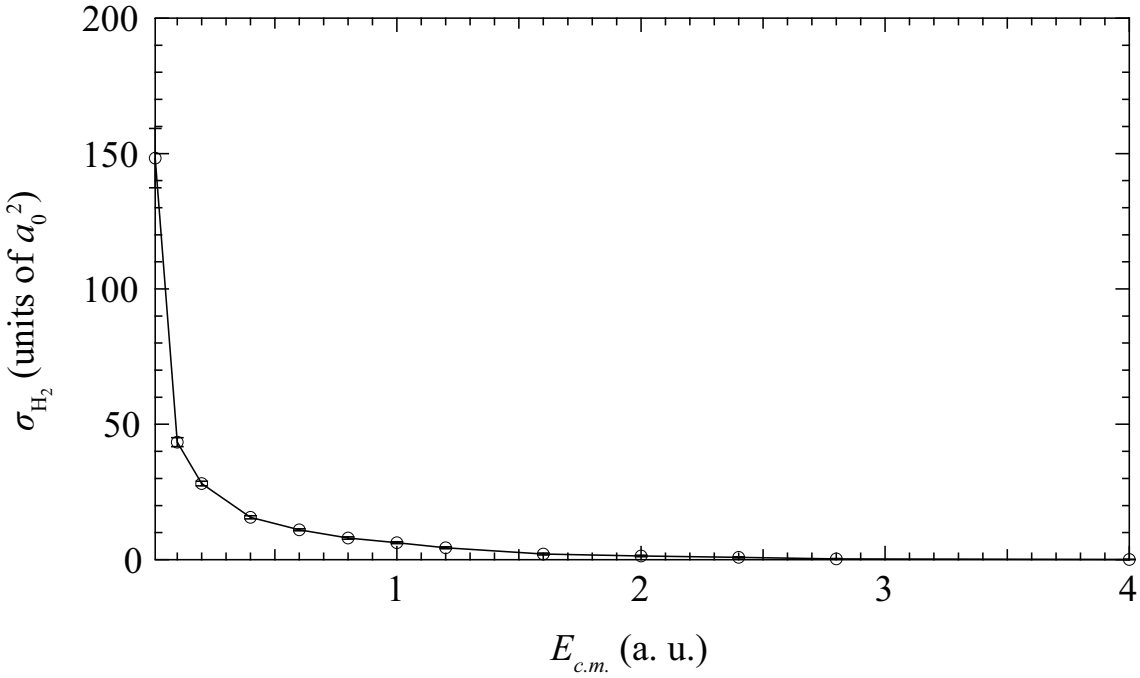

Figure 3.61: Cross section of hydrogen molecule and antiproton as a function of relative energy in the center of mass frame.

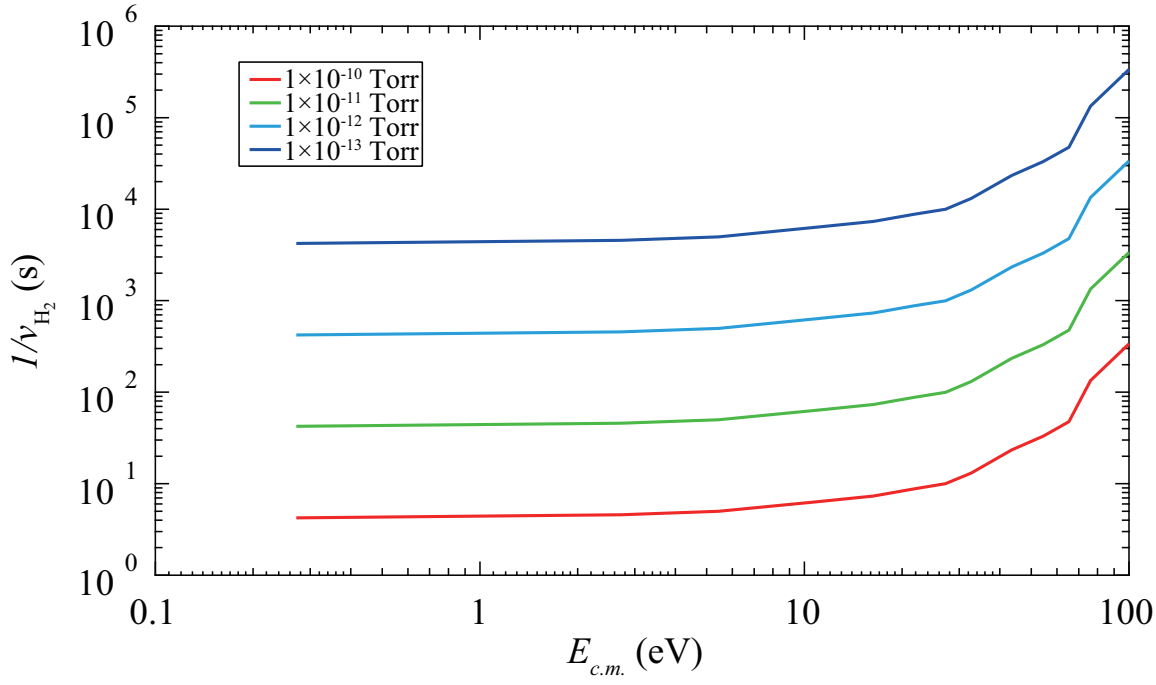

Figure 3.62: Mean free time ($1/\nu_{H_2}$) as a function of relative energy under various hydrogen gas pressures. Even if the pressur is as low as 1×10^{-10} Torr, $1/\nu_{H_2}$ is only a few seconds at low energy region.

vacuum pumps and gauges

The position of vacuum pumps and gauges are indicated in figure 3.37 and details of each component are summarized in table 3.10 for upstream side and in table 3.11 for downstream side.

Magnetically levitated TMPs (Shimadzu, TMP-303M) are used to evacuate all types of residual gases, whose outlets are pumped by small TMPs (Varian, V-81) and rotary vane pump (Edwards, RV5). Two NEG pumps (Saes, CapaciTorr B1300-2 MK5) and one NEG pump (saes, CapaciTorr D400-2) are attached at downstream side and upstream side respectively for the evacuation of hydrogen. Ion gauges (Yamamoto, VX-200B and pfieffer, PRK 260) and quadrupole mass analyser (Anelva, M-066QG) are used for the measurement of the pressure.

description	manufacturer	type
Main TMP	Shimadzu	TMP-303M
backing TMP	Varian	V-81
backing rotary vane pump	Edwards	RV5
NEG pump	Saes	CapaciTorr D400-2
Nude ion gauge	Yamamoto	VX-200B
full range gauge (B-A ion/Pirani)	Pfeiffer	PBR 260

Table 3.10: List of vacuum pumps and gauges (upstream side).

description	manufacturer	type
Main TMP	Shimadzu	TMP-303
backing TMP	Varian	V-81
backing rotary vane pump	Edwards	RV5
NEG pump × 2	Saes	CapaciTorr B1300-2 MK5
quadrupole mass analyser	Anelva	M-066QG
full range gauge (B-A ion/Pirani)	Pfeiffer	PBR 260

Table 3.11: List of vacuum pumps and gauges (downstream side).

differential pumping and thermal shield

The region where the MRE is placed is cooled down to cryogenic temperature (see section 3.4.5). However both ends have to be connected to room temperature section where the vacuum is worse than cryogenic region. To reduce the inflow of the gas and thermal radiation from room temperature region to cryogenic region, an upstream thermal radiation shield made of Al pipes and a downstream radiation shield made of copper plate are installed in the UHV bore tube. Figure 3.63 shows the position of them.

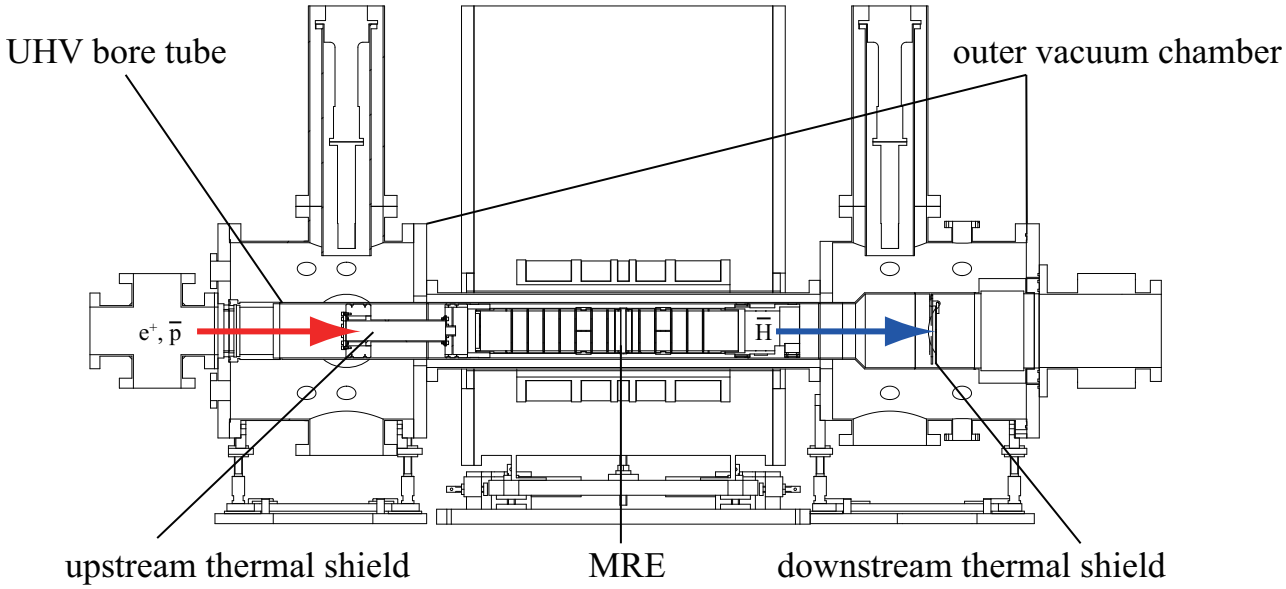

Figure 3.63: A cross sectional drawing of the cusp trap. The UHV bore tube is inserted in the outer vacuum chamber for thermal isolation. Thermal radiation shields are installed in the UHV bore tube to reduce the inflow of the gas and thermal radiation from room temperature region.

upstream thermal shield Figures 3.64 and 3.65 are an exploded and a cross sectional drawing of the upstream thermal shield. The shield consists of 5 part, (a) a 40 K support ring, (b) a connection plate, (c) 40 mm ϕ cylinder, (d) 16 mm ϕ cylinder, (e) a 5 K support ring. Since charged particles are injected through the shield as indicated by the red arrow in figure 3.63, the shape of the shield is determined so that the shield does not block the particles. Figure 3.66 shows trajectories of antiprotons whose initial position in the antiproton catching trap is 1.1 mm $< r <$ 1.5 mm, energy width is 1 eV, and extraction energy is 150 eV. By optimizing the inner diameter and the position to place, all the particles are transported into

the MRE. Table 3.12 shows conductance of each section and total conductance. In the same table, conductance without the upstream thermal shield is also shown for comparison. As can be from the table, inflow of the gas, which is proportional to conductance, decrease 6.3/380.

Thermal radiation from room temperature region is dumped to the UHV bore tube via part (a). Parts (a)-(d) are made of gold-plated aluminium alloy whose thermal conductivity is higher than that of austenitic stainless steel. On the other hand, part (e), which support the edge of part (d) and contact to 5 K region of the UHV bore tube, is made of stainless steel (SUS316L) to keep thermal conductivity low. Thermal resistance of four spokes of part (e) is *sim* 6000 K/W at 4 K and the amount of heat transferred from part (d) (40 K section) to 5 K section is as small as 6 mW. By this shield, thermal radiation from upstream side is reduced from 4.2 W to 95 mW.

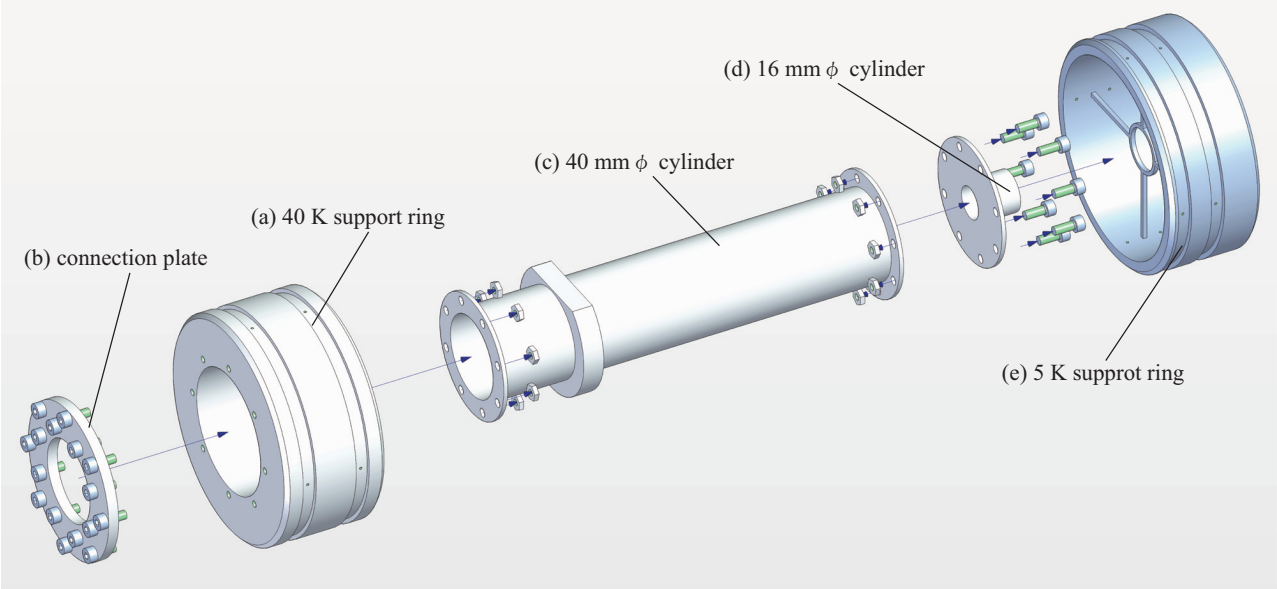

Figure 3.64: An exploded drawing of the upstream thermal shield which consists of the 40 K support ring, the connection plate, the 40 mm ϕ cylinder, 16 mm ϕ cylinder and the 5 K support ring.

downstream thermal shield Figure 3.67 shows the structure of the downstream thermal shield. It consists of a gold plated copper plate and a mechanism to move it. The shield can be opened by the actuator outside (see figure 3.37) so that the produced antihydrogen atoms can be extracted to downstream side as indicated by the blue arrow in figure 3.63. Figure 3.68 and 3.69 are isometric views of the shield in closed and opened position respectively. The

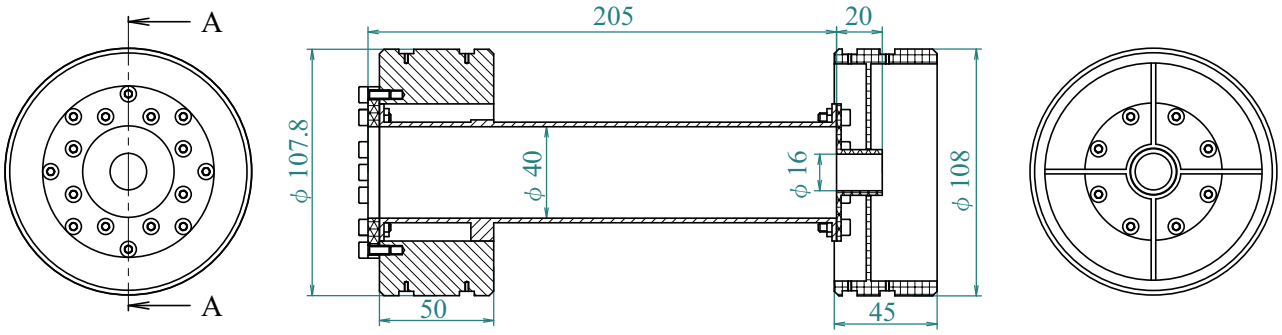

Figure 3.65: A cross sectional drawing of the upstream thermal shield.

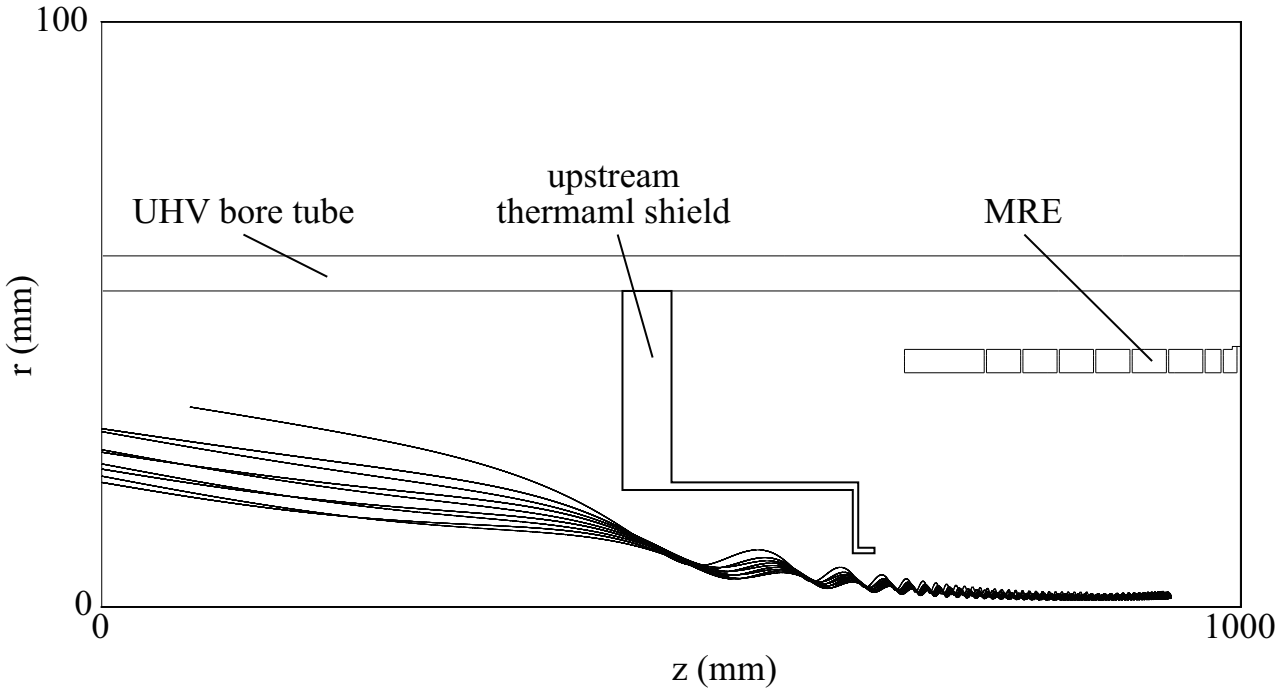

Figure 3.66: Trajectory of antiprotons. The upstream thermal shield is designed not to block the antiproton beam injected into the cusp trap. Since the magnetic field is higher near the MRE region and radius of the antiproton beam shrinks, inner diameter of the shield is smaller near the MRE.

section	conductance (l/s)
(b) connection plate and (c) 40 mm cylinder	30
(d) 16 mm cylinder	11.7
(c)-(d)	25
total	6.3
without the upstream thermal shields	380

Table 3.12: Conductance of upstream thermal shield. The conductance decrease from 380 l/s to 6.3 l/s by installing the shield.

shield almost completely covers inside of the UHV bore tube and the conductance is negligibly small. By this shield, thermal radiation from downstream side is reduced from 4.2 W to 3.2 mW.

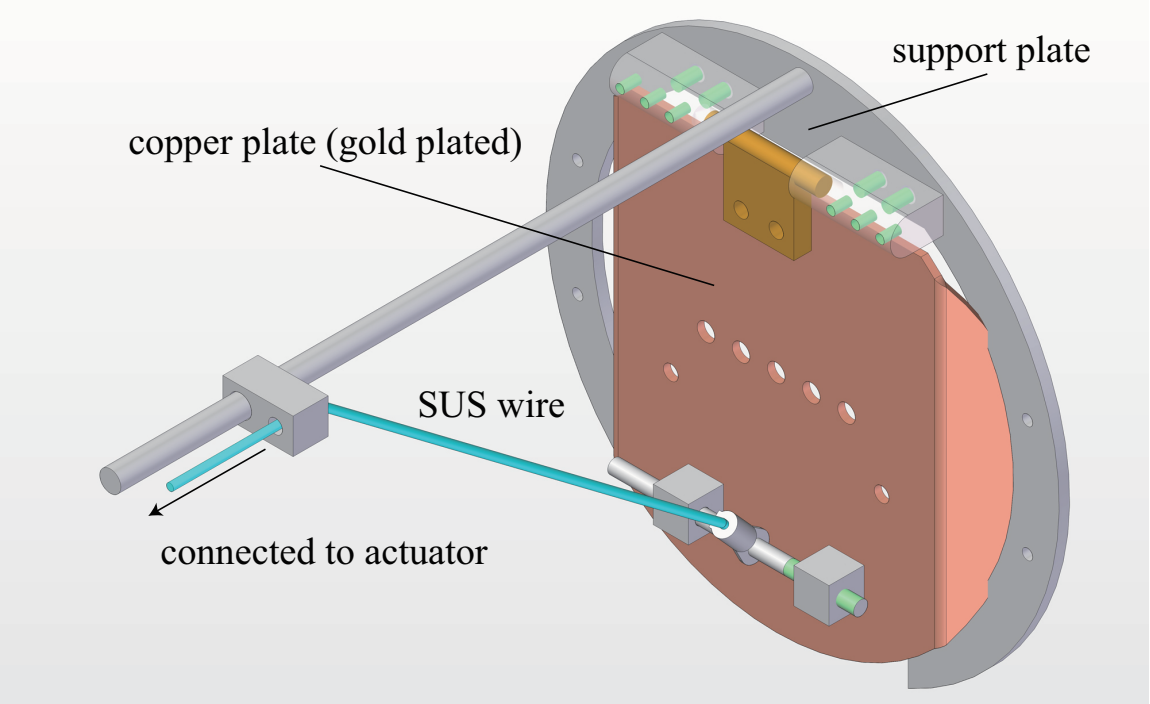

Figure 3.67: Structure of the downstream thermal shield. The copper plate can be opened by pulling the SUS wire, which is connected to the actuator at the opposite side.

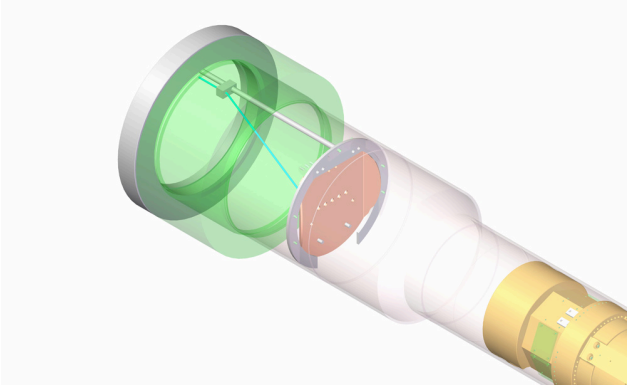

Figure 3.68: An isometric view of the downstream thermal shield in closed position.

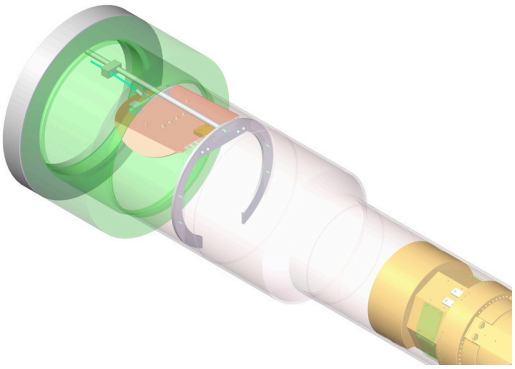

Figure 3.69: An isometric view of the downstream thermal shield in opened position.

UV light source

As is often the case with UHV equipment, the cusp trap have to be baked out to realize required vacuum before in use. In the case of the UHV bore tube of the cusp trap, it is thermally isolated from the outer vacuum chamber, usual baking procedure like heating the chamber from outside is not applicable for the tube and MRE. In addition, it is not recommended to heat up the GM refrigerators which is connected to the bore tube (see section 3.4.5). To solve this problem an ultra violet light source (RDB instruments, UVB-100, see figure 3.70) is installed to bake them. UV light can desorb the water molecules absorbed on the wall of the vacuum chamber. Figure 3.71 is a photograph of the source in operation. Figure 3.72 shows the source and its support. The source is mounted on a movable mechanism to avoid conflict with extracted antihydrogen atoms. Inserted and extracted position of the source are shown in figure 3.73.

Figure 3.70: A photograph of UV light source (RDB instruments, UVB-100).

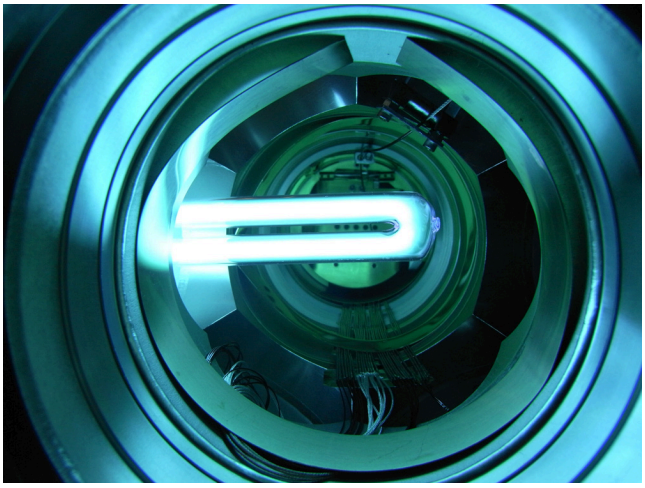

Figure 3.71: A photograph of UV light source in operation.

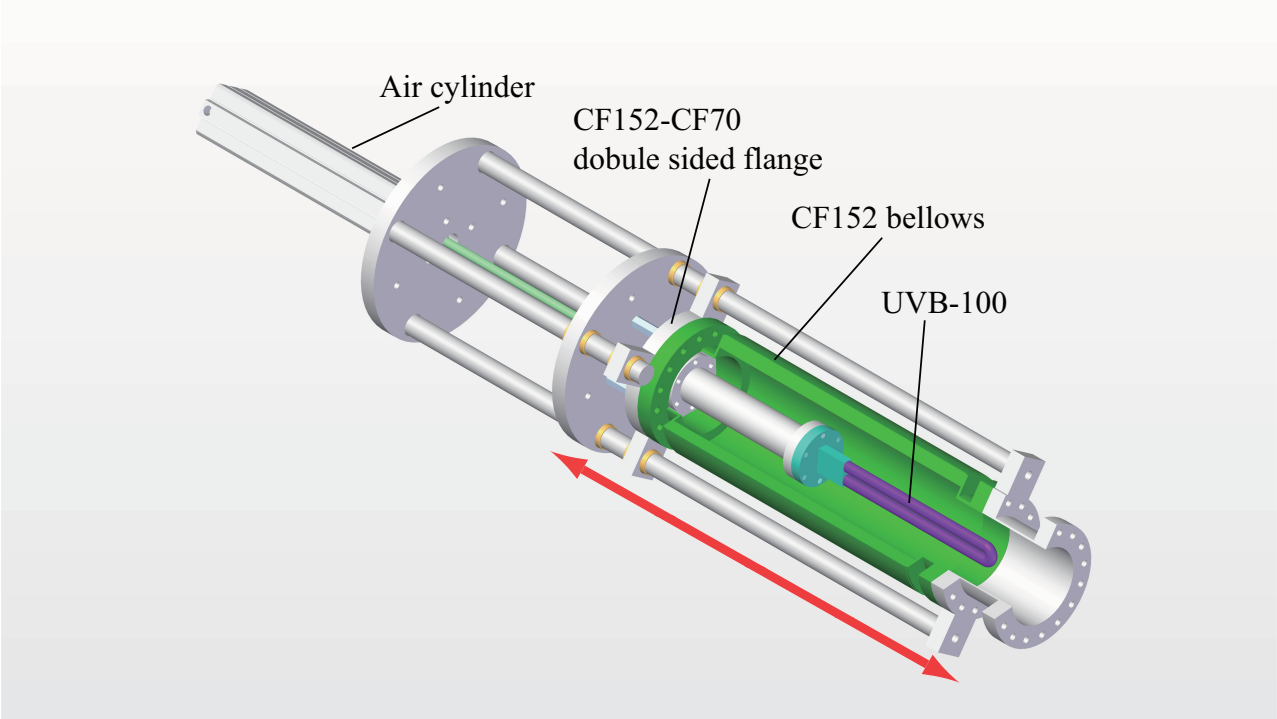

Figure 3.72: Structure of moving mechanism of the UV light source. The light source can be inserted and extracted by an air cylinder.

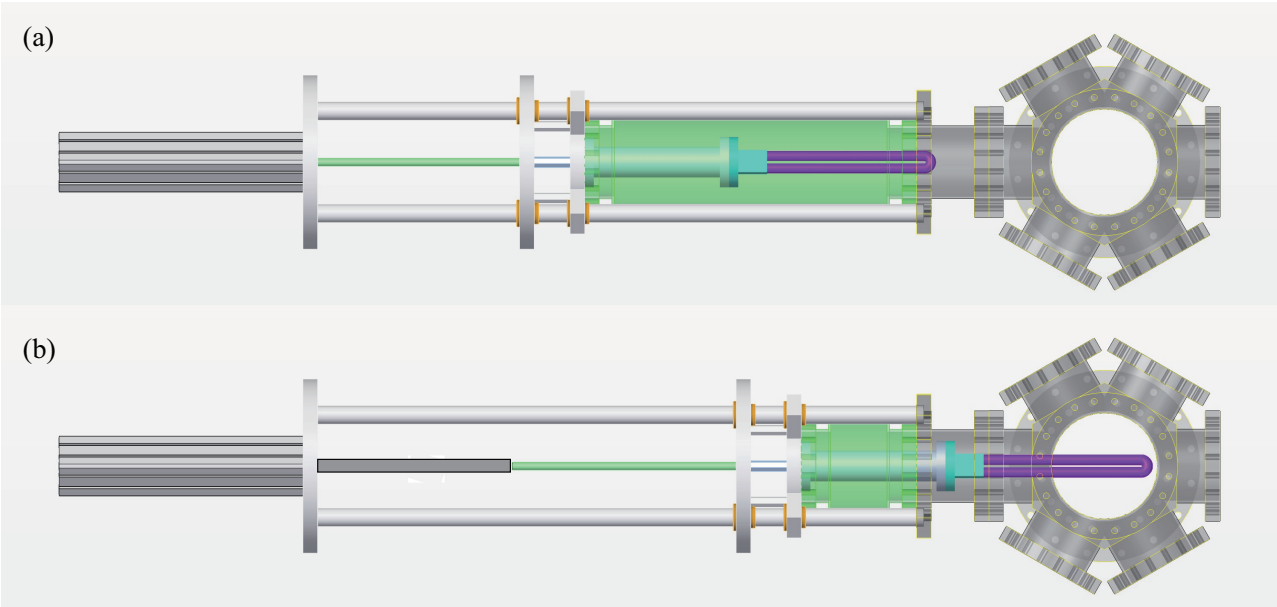

Figure 3.73: Position of the UV light source when it is extracted (a) and inserted (b).

3.4.5 Cooling system

bore cooling mechanism

The UHV bore tube of the cusp trap is cooled by 2 two-stage GM refrigerators whose specifications are summarized in table 3.13. The cooling power of the refrigerator is 1.5 W at 4.2 K (2nd stage) and 15 W at 30 K (1st stage) respectively.

manufacturer	Iwatani
type	HE15
cooling power at 4.2 K	1.5 W
cooling power at 30 K	15 W
reachable temperature without heat load	3.2 K

Table 3.13: Specifications of the refrigerators used to cool the UHV bore tube of the cusp trap.

Figure 3.74 shows the structure of the cooling mechanism and figure 3.75 is a cross sectional view of a plane indicated by A-A' in figure 3.74. All the components of the cooling system are installed in the outer vacuum chamber (OVC). The UHV bore tube is connected to the room temperature flange at each end through bellows to increase thermal resistance. The tube is thermally anchored to the 1st stage of the refrigerators. The 2nd stage of the refrigerators and the UHV bore tube are connected by copper rods, strips and collar made of 6N (99.9999 %) high purity copper. Thermal conductivity of the 6N copper is 11300 W/mK at 4 K which is about 50 times higher than oxygen free copper (OFC) (see table 3.14). The strips and the collar are surrounded by copper cylinders (radiation shields) made of OFC (see also figure 3.76). These radiation shields are connected to the 1st stage of the refrigerators. In addition, layers of super insulator are inserted between the OVC and the copper cylinder to reduce heat load to the copper cylinder. Figure 3.77 is a photograph of the UHV bore tube and the copper collar. Two 300 mm long collar, which are divided into four azimuthally (i.e. 8 pieces in total), are bound tightly to the UHV bore tube by stainless steel (SUS) sheets whose ends are spot welded each other. To obtain good thermal contact between the collar and the tube, silver foils embossed with a check pattern of 2 mm pitch are put between them and the remaining space is further filled with Apiezon N grease (see figure 3.78).

In these configuration, heat loads to the system are calculated. Table 3.15 is the list of them. As can be seen from the table, heat load via radiation is dominant for the second

stage. Considering the total heat roads to the 1st stage and 2nd stage are 6.7 W and 0.8 W respectively, the cooling power of the two refrigerators has enough margin. More details of the cooling system are described in ref. [68].

	thermal conductivity (W/Km) at 4 K
6N copper	11300
OFC	200
SUS 316L	0.34

Table 3.14: List of thermal conductivity of metals used in the UHV bore cooling system.

position	type	source	heat load
First stage	Radiation	Tube around refrigerator	400 mW
		tube around UHV bore	1100 mW
		upstream	1200 mW
		downstream	1100 mW
	conduction	upstream	1100 mW
		downstream	1000 mW
	total		6700 mW
Second stage	radiation	upstream	250 mW
		downstream	420 mW
	conduction	upstream	60 mW
		downstream	70 mW
	total		800 mW

Table 3.15: List of heat load to the UHV bore tube.

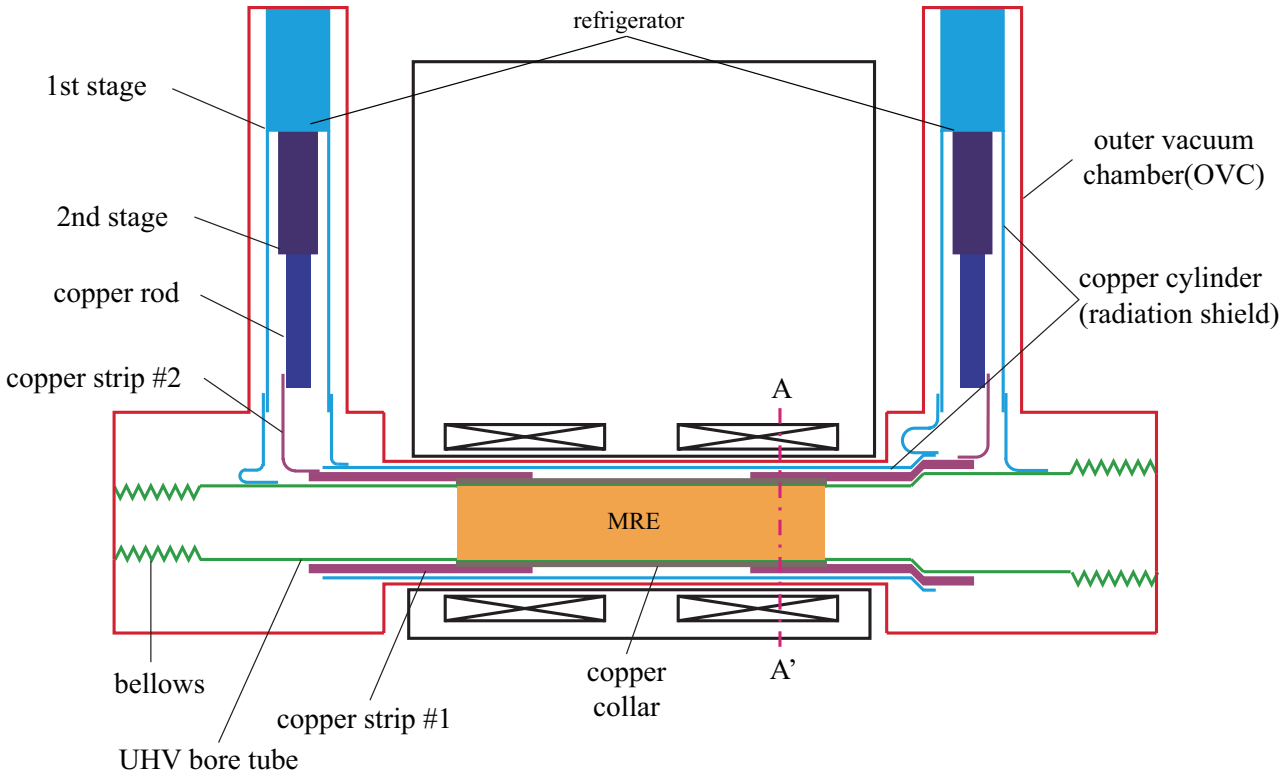

Figure 3.74: A schematic drawing of the UHV bore cooling system. The UHV bore tube is surrounded by the copper collar which is connected to the 2nd stages of the refrigerators by the copper rods and copper strips. The copper cylinders cover the copper collar, the strips, the rods and the 2nd stages of the refrigerators to shield thermal radiation. The cylinders are connected to the 1st stages of the refrigerators. The MRE is cooled via thermal contact with the UHV bore tube.

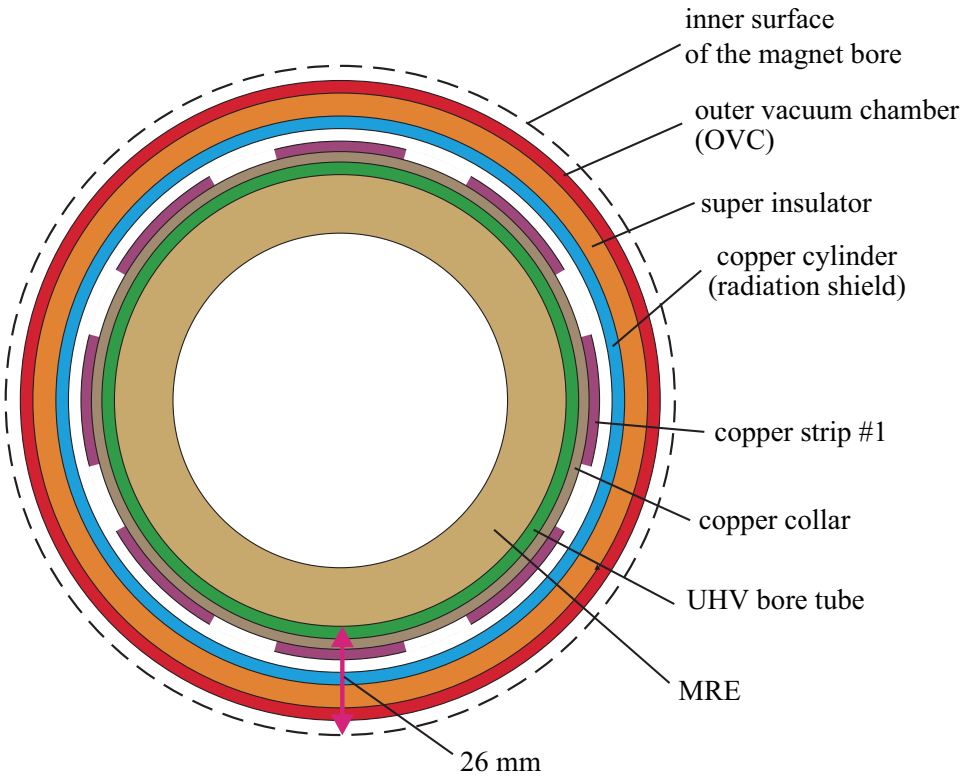

Figure 3.75: A cross sectional view of the UHV bore tube cooling system at central region. All the components of the cooling system are installed within narrow (26 mm) space.

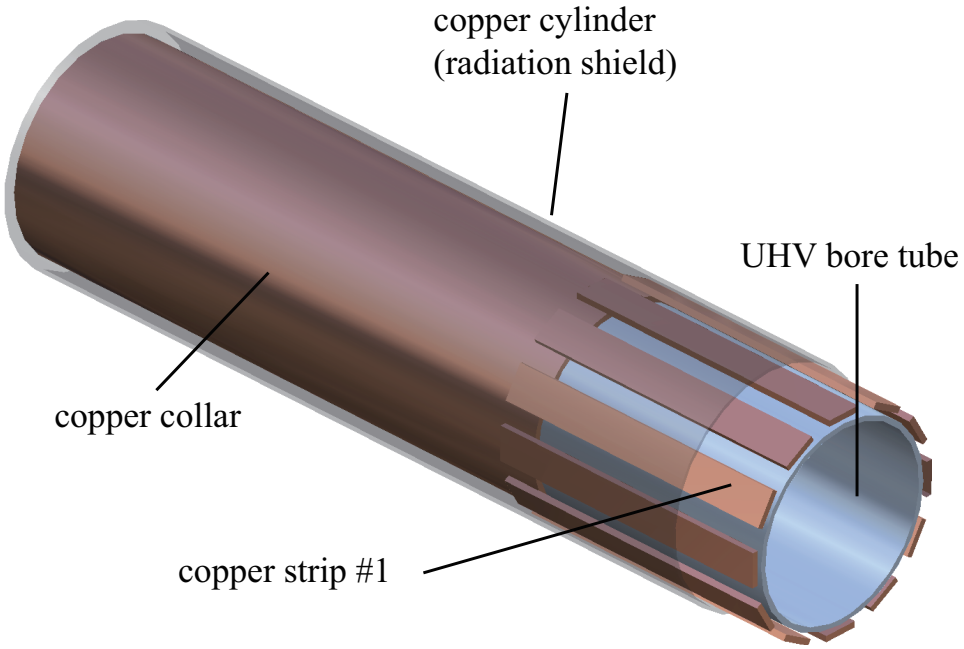

Figure 3.76: An isometric view of the UHV bore tube, the copper collar, the copper strips, and the copper cylinder.

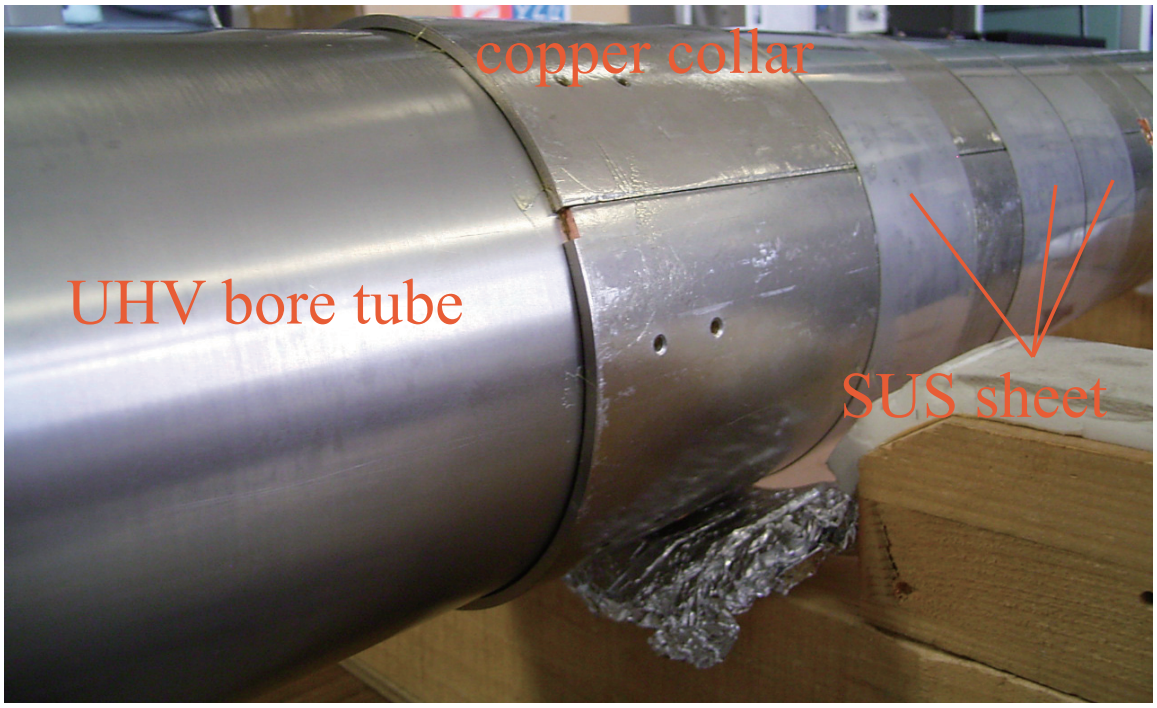

Figure 3.77: A photograph of the UHV bore tube surrounded by 6N copper collars fixed by stainless steel sheets. The copper collars are segmented by four azimuthally. Each piece is 300 mm in length, 2.5 mm in thickness. Eight pieces are used in total to cover central 600 mm region.

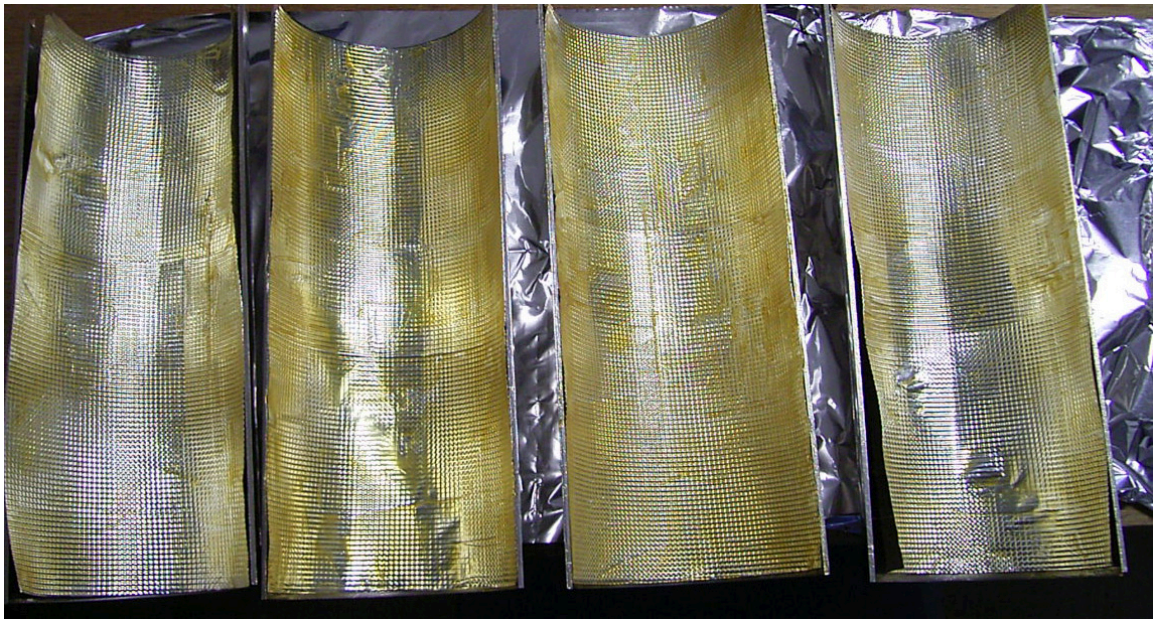

Figure 3.78: A photograph of the checked Ag foils with Apiezon N. They are inserted between the UHV bore tube and the copper collars to increase thermal contact.

MRE cooling mechanism

The MRE is cooled by thermal contact with the UHV bore tube. Two types of thermal contact is used (see figure 3.79). The contact A (Multi-Contact, LAIAS/480/0,15/15 AG) is used between the DSR/USR and the UHV bore tube. The contact B (Taiyo kanaami, shield fingers A-340-00) made of beryllium copper (BeCu) covered by 0.1 mm thickness Ag foil is used between the support rods and the UHV bore tube (see figure 3.80).

There are two sources of heat load to the MRE, one is radiation form both side and the other is conduction through wiring. The amount of each heat load is summarized in table 3.16. Total amount of the heat load is estimated 148.8 mW. Considering there are 17 electrodes, heat load to the each ring electrode seems to be 5 to 10 mW.

radiation from upstream side	95 mW
radiation from downstream side	3.2 mW[13]
cable (core wire)	0.2 mW/wire × 23[14]= 4.6 mW
cable (shield pipe)	2 mW[15]/pipe × 23 = 46 mW
total	148.8 mW

Table 3.16: List of heat load to the MRE.

Contrary to the DSR, USR, and support rods, the ring electrodes themselves could not contact directly to the UHV bore because they must be electrically isolated from the ground potential. Although the ring electrodes are supported by high thermal conductivity insulator columns (see figure 3.44), for further increasing thermal conductivity, extra copper wire (heat conduction wire) is attached between each ring electrode and support rod (see figure 3.81). Figure 3.82 shows the structure around the heat conduction wire. A Kapton insulated single core copper wire of 1.7 mm in diameter is connected to the support rod directly and to ring electrode through rectangular insulator of 2 mm thickness made of AlN. The heat resistance of the wire is about 50 K/W and considering the heat load to each electrode (10 mW see table 3.16), the temperature difference between support rod and ring electrode is less than 5 K.

[13]When the downstream thermal shield is in closed position

[14]There are 23 cable to the MRE (15 (ring electrode) + 2 (segmented electrode) × 4)

[15]The shield pipes are contacted to the UHV bore at 40 K region for thermal anchor

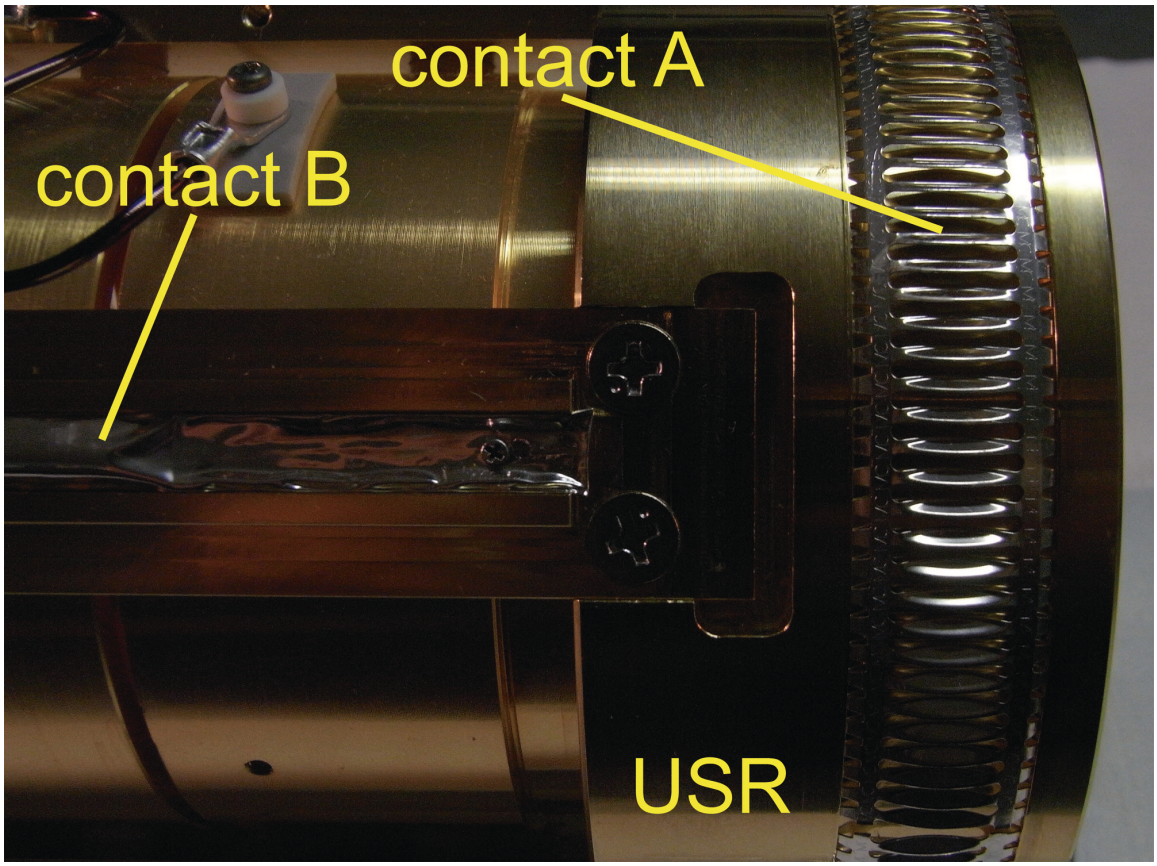

Figure 3.79: A photograph of thermal contact between the USR/DSR and the UHV bore tube (contact A) and between the support rod and the UHV bore tube (contact B).

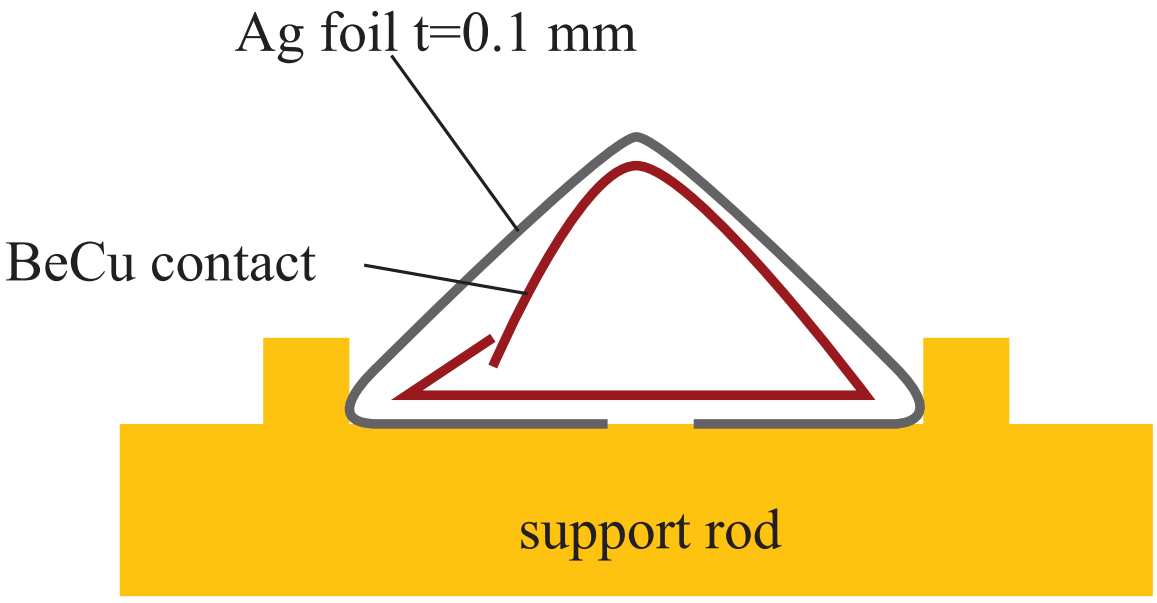

Figure 3.80: A cross sectional view of the contact B. BeCu contact (Taiyo kanaami, shield fingers A-340-00) is covered by Ag foil of 0.1 mm thickness.

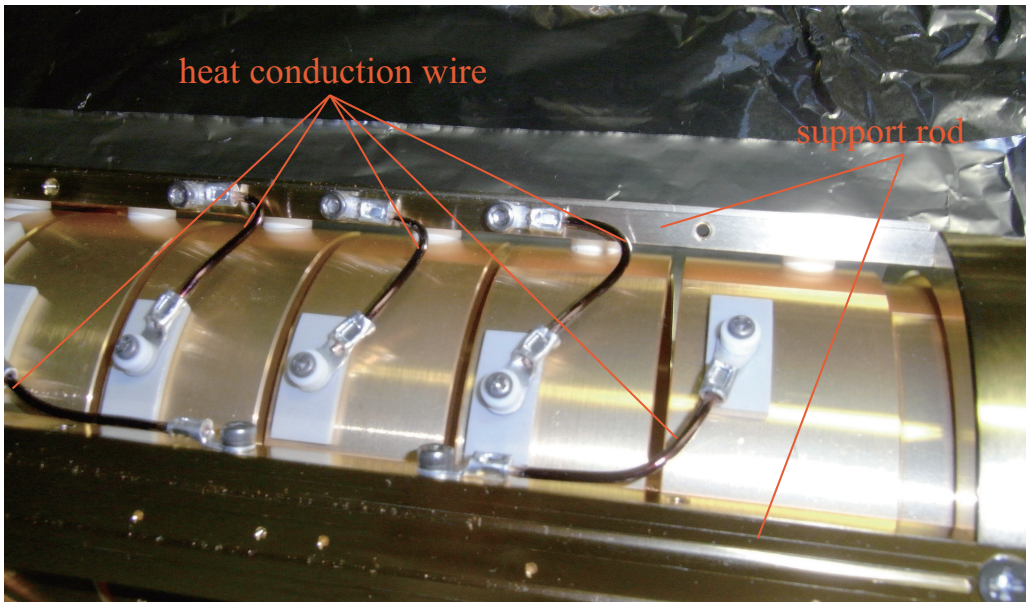

Figure 3.81: A photograph of the heat conduction wires. The wires connect ring electrode and support rods thermally.

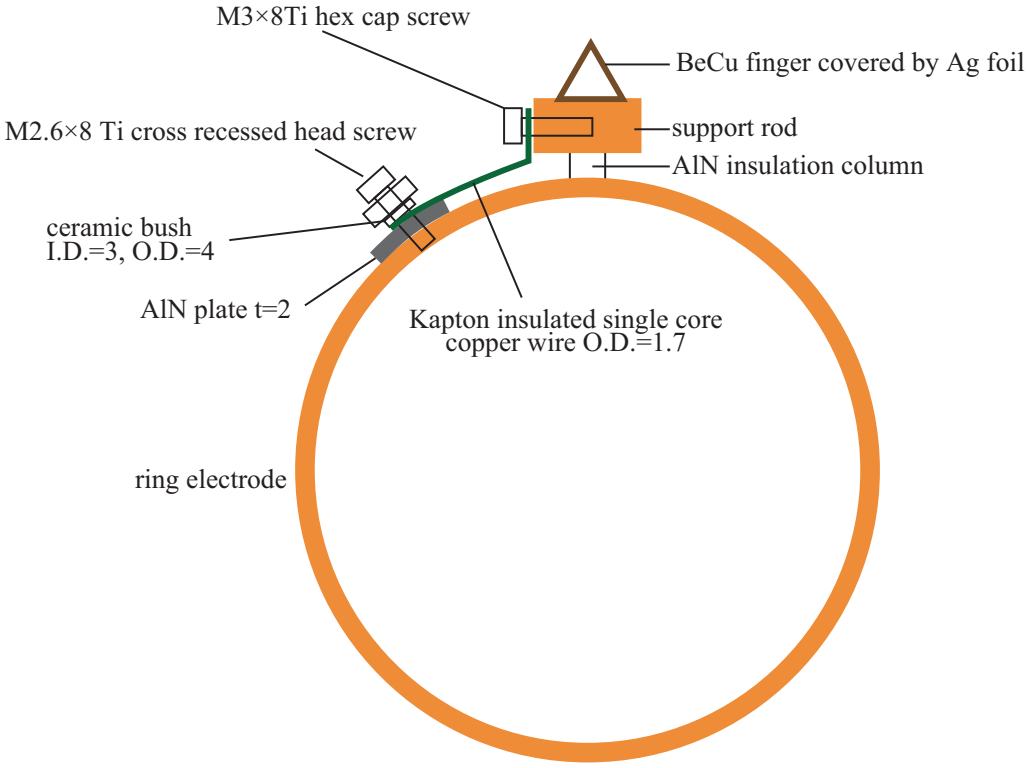

Figure 3.82: Structure around the heat conduction wire. The Kapton insulated copper wire of 1.7 mm in diameter (green) connect the support rod and the ring electrode through the AlN plate (grey).

cooling test

Figure 3.83 and 3.84 shows the position of temperature sensors for the UHV bore tube and for the MRE respectively. The temperature are monitored by cernox temperature sensor (Lakeshore, CX-1030-SD). The sensor can be used from 0.3 K to 420 K and the error induced by the magnetic field is small[16]. The resistance of the sensors are measured and converted to temperature by a controller (Lakeshore, 331S) which is connected to a PC via GPIB interface.

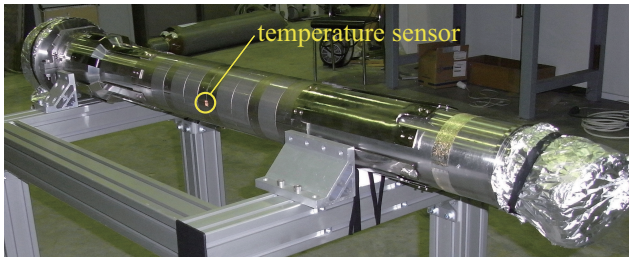

Figure 3.83: Position of the temperature sensor (UHV bore). The sensor is attached in the middle of the UHV bore tube in axial direction.

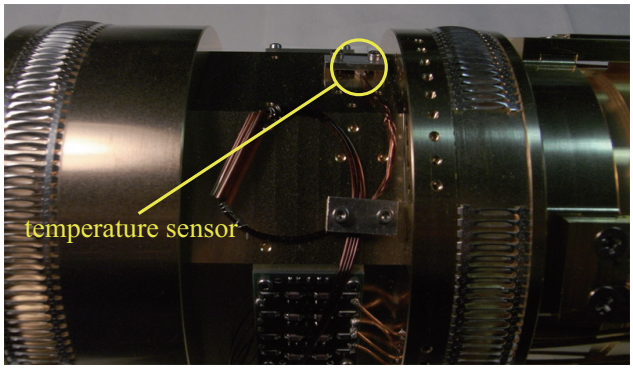

Figure 3.84: Position of the temperature sensor (MRE). The sensor is attached on the DSR.

Figure 3.85 shows typical cooling curve of the UHV bore tube and the MRE of the cusp trap. It takes about 10 hours to cool the UHV bore tube from room temperature to 10 K.

Figure 3.86 shows time dependence of the temperature when the downstream thermal shield gets opened or closed. Time constant of heating or cooling is about hundreds seconds. The temperature changes 0.3 K (UHV bore tube) and 5 K (MRE) respectively.

[16]relative error is below 0.1 % at 4.2 K and 2.5 T

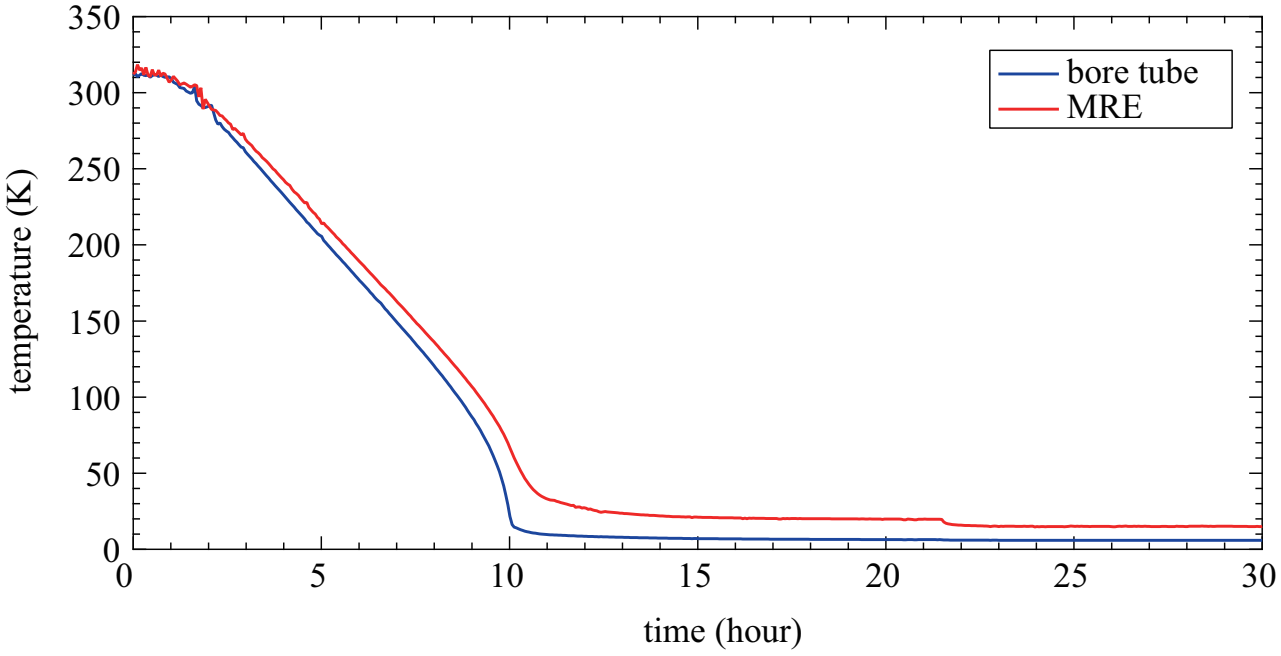

Figure 3.85: Typical cooling curve of the UHV bore tube and the MRE. It takes about 10 hours to cool the UHV bore tube from room temperature to 10 K.

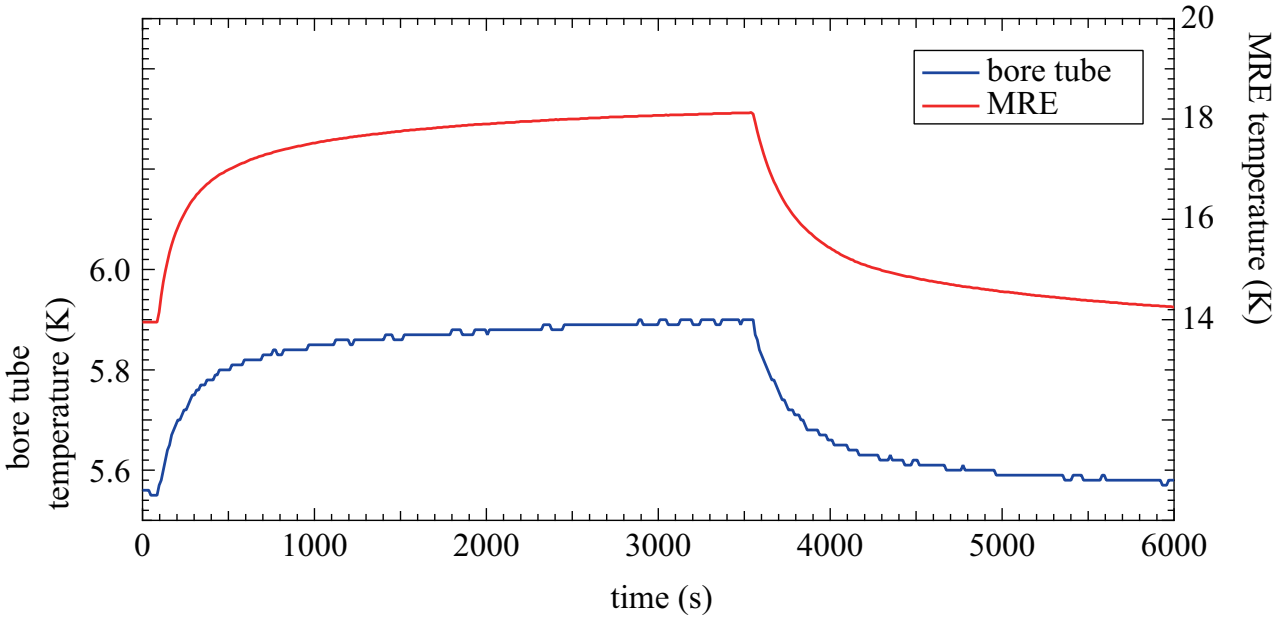

Figure 3.86: Time dependence of the temperature of the UHV bore tube and the MRE when the downstream thermal shield gets opened or closed. Time constant of heating or cooling is about hundreds seconds. The temperature changes 0.3 K (UHV bore tube) and 5 K (MRE) respectively.

3.4.6 Control system

electrode control

Figure 3.87 is a connection diagram of the components used to control voltages applied to the MRE. The voltages of all electrodes but the U9 electrode[17] can be controlled independently. The system consists of

1. two 8 ch digital to analogue converter (DAC) modules (National Instruments, PXI-6733) whose output range is -10 V to 10 V and resolution is 16 bit,

2. instrumentation amplifiers (cusp inst. amp, see figure D.8 for circuit drawing) of unity gain to cut common mode noise from the DAC,

3. inverting power amplifiers (cusp power amp, see figure D.3) of gain 40 using power operational amplifier (Apex, PA-94),

4. passive single order RC low pass filters (RC LPF1, see figure D.17) whose time constant is variable by rotary switches[18],

5. a function generator (NF, WF1974) and LC splitters[19] (mini circuit, ZSCJ-2-2), which are used to apply rotating electric field (see section 5.2).

6. RC mixers (RC mix 1 and RC mix 2, see figure D.18 and figure D.7 respectively) to superimpose pulse or AC signal on DC voltage applied to the MRE.

Table 3.17 shows specifications of the power amplifier. The input range and gain of it are -10 V to 10 V and -40 respectively resulting in output range from 400 V to −400 V. Figure 3.88 shows the response of the amplifier. Blue and red curves represent input and output signals respectively. Slew rate of the amplifier is 560 V/μs. Figure 3.89 shows offset voltages and gain errors of the system. Red bars indicate the output voltages when the set values (V_{set}) are 0 V. Blue and green bars indicate the difference of the output voltages from the set values when they are 100 V and -100 V respectively. Considering the ideal resolution of the system is 12 mV, which is determined by the resolution of the DAC, measured values are almost reaches to the limit.

[17]The cable of the U9 electrode is connected that of the U8 electrode at the feedthrough.

[18]Most of the experiment are carried out with $\tau = 100\mu s$.

[19]The splitter outputs two signals for one input signal. The phase of one signal is the same as that of the input signal and the phase of the other signal is shifted by 180 degree from the input signal.

Figure 3.90 shows frequency responses of the LC splitter for several input voltages. The vertical axis represents the gain (i.e. the output voltage of the splitter divided by the input voltage). As can be seen from the figure, the gain is almost flat in the range from 10 kHz to 10 MHz, which covers the frequency range required for the compression of positron cloud in our experimental condition (see section 5.2).

input range	-10 V to 10 V
gain	-40 (finely tunable by program and variable resister)
maximum power supply voltage	$\pm$420 V
slew rate	560 V/μs
DC offset	adjustable by program see figure 3.89 for result
gain error	see figure 3.89 for result

Table 3.17: Specifications of the power amplifier.

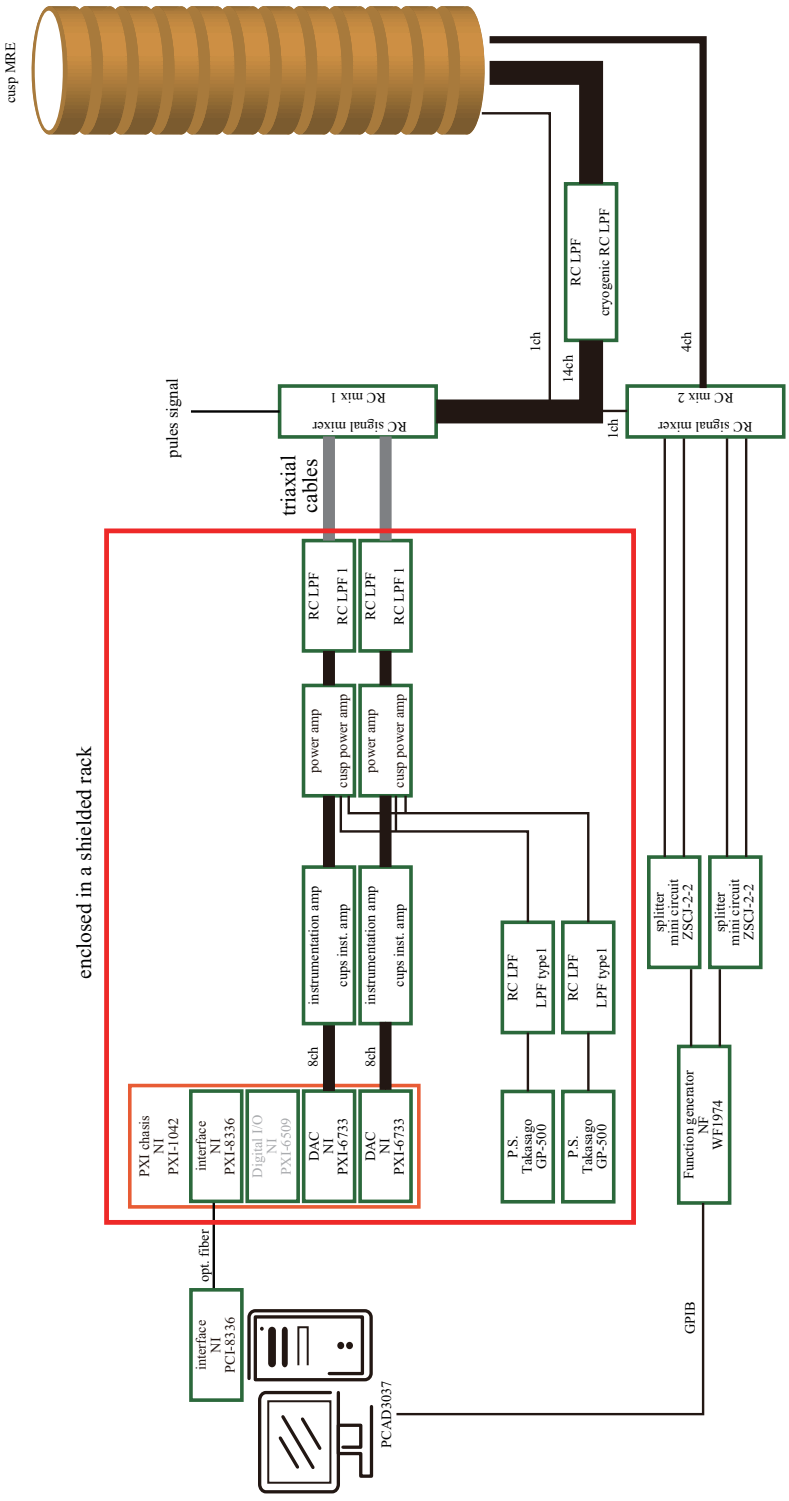

Figure 3.87: A connection diagram of the components used to control the voltages applied to the MRE. Signals from the DCAs are amplified by power amps and applied to the MRE via RC signal mixer. The instrumentation amps and RC low pass filters are inserted in the lines to reduce noise. The function generator is connected to the segmented electrode via splitters and RC signal mixer to apply rotating electric field.

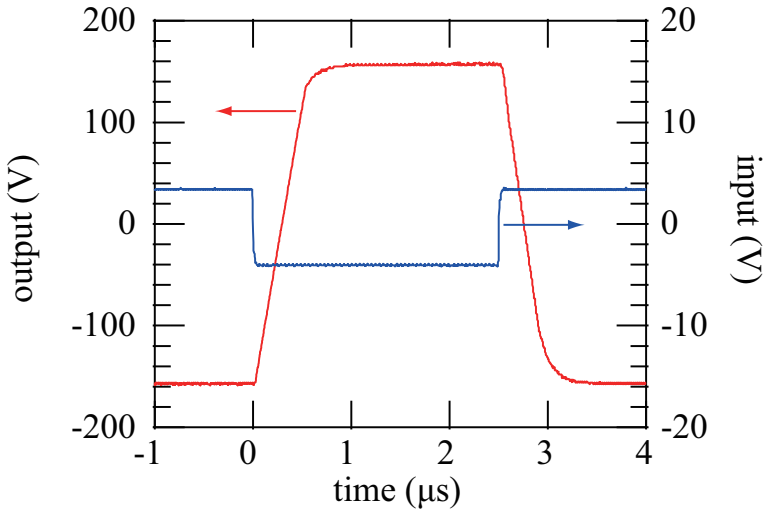

Figure 3.88: Response of the power amplifier. Blue curve represents input signal and red curve represents output signal.

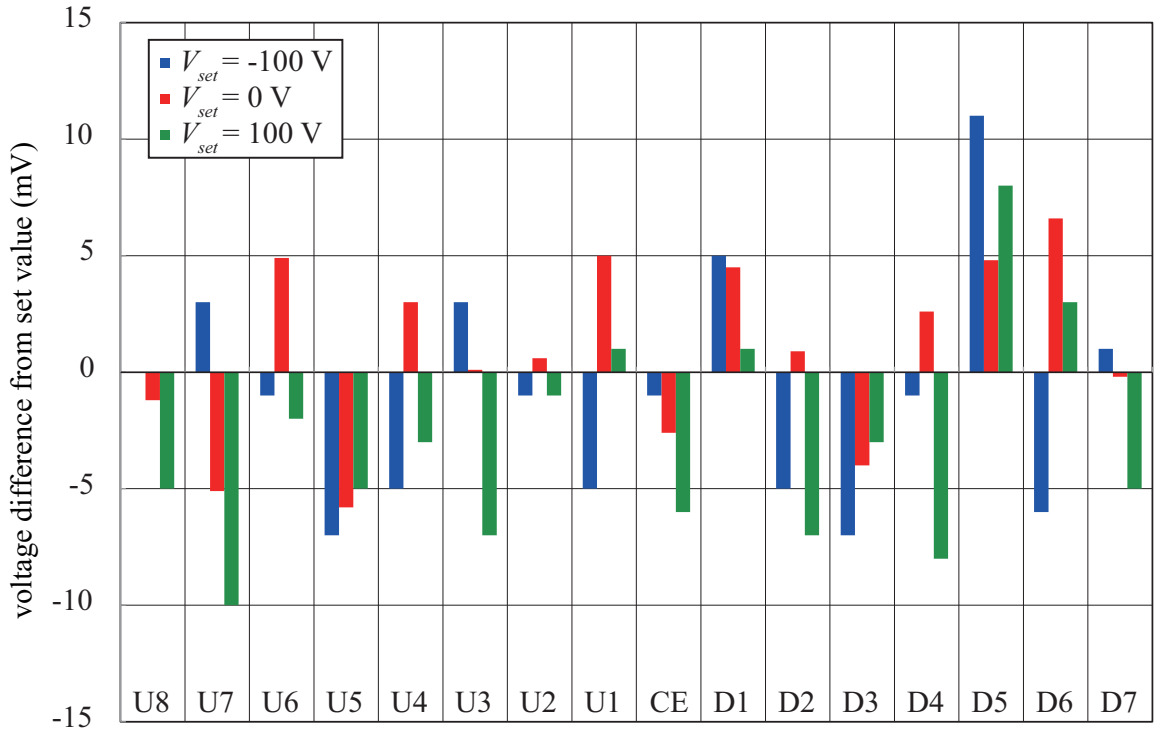

Figure 3.89: Offset and gain error of power amplifier. Red bars indicate the output voltages when the set values (V_{set}) are 0 V. Blue and green bars indicate the difference of the output voltages from the set values when they are 100 V and -100 V respectively.

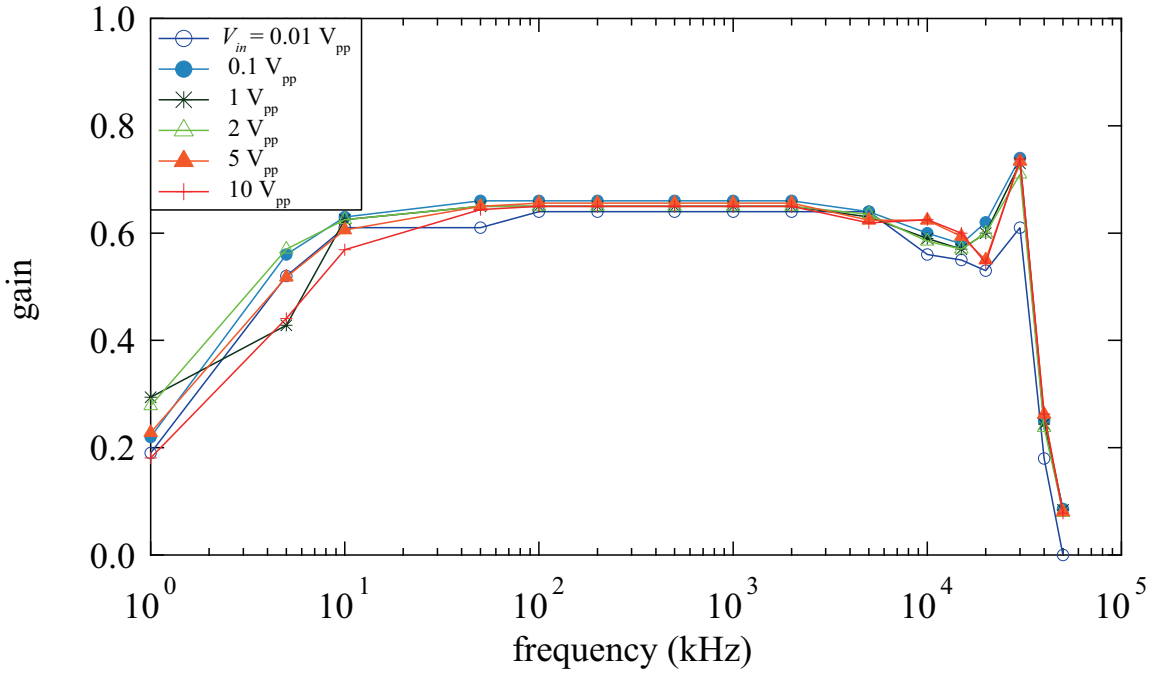

Figure 3.90: Frequency responses of the splitter (mini circuit, ZSCJ-2-2) for several different input voltage ranging from 0.01 V to 10 V. The gain is flat between 10 kHz and 10 MHz independent from the input voltage.

pulse control

To capture pulsed beam of positrons or antiprotons in the cusp trap, we have to change the voltage applied to the MRE rapidly[20]. Here, we estimate the time scale required to capture positrons. The velocity of positron whose kinetic energy is E eV is given by $v = 590\sqrt{E}$ mm/μs. The kinetic energy of positrons in the cusp trap is about 20 eV[21]. The length of the potential to capture positrons is about 150 mm. Thus it takes about 100 ns for the positrons to go and return the potential. Consequently, it is required to change the voltages by a few hundred V within a few tens nano seconds. Considering the slew rate of the power amplifier is 560 V/μs (see table 3.17), it does not satisfy the condition. Then we introduced high speed high voltage switches, whose rise time is about 50 ns for 100 V pulse height, to apply pulse voltages to the electrodes.

Figure 3.91 shows the connection diagram of a DC and a pulse voltages to a ring electrode schematically. The pulse voltage from the switch is superimposed on the DC voltage from the power amplifier via a capacitor.

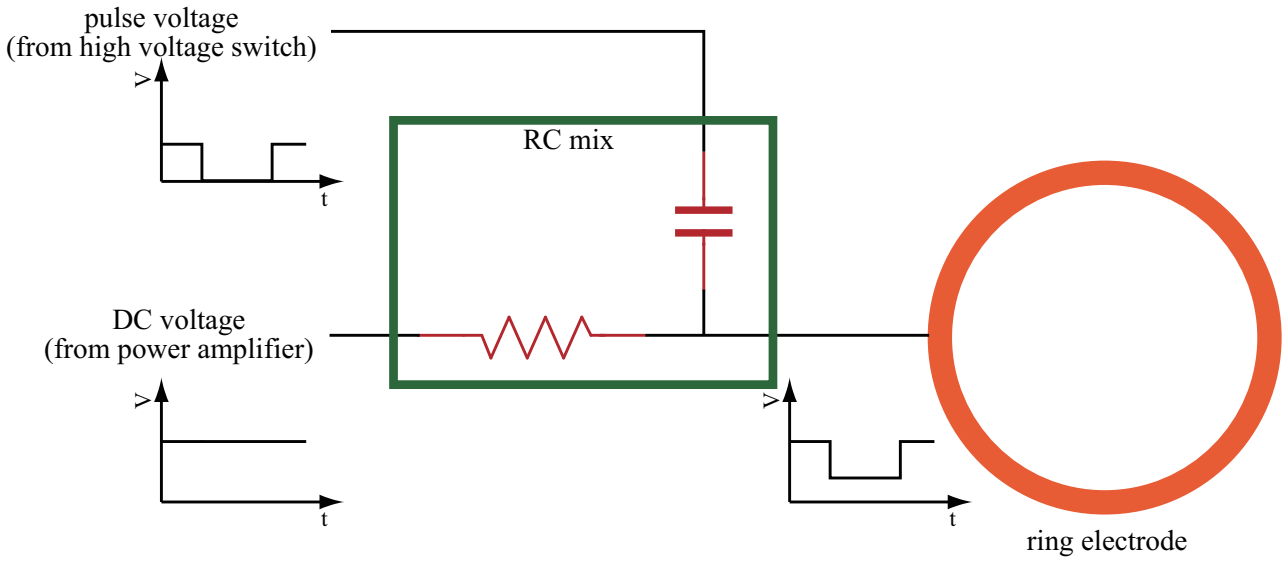

Figure 3.91: Connection diagram of a DC and a pulse voltages to a ring electrode. The pulse voltage is superimposed on the DC voltage via capacitor.

Figure 3.92 shows a connection diagram of the pulse control system and figure 3.93 shows a connection diagram of the trigger controller with a truth table. The trigger controller (Trig

[20] Details of the procedures are described in section 4.2 and 5.1.

[21] Although the extraction energy of positrons from the positron accumulator is typically about 100 eV, they are decelerated by the potential created by the MRE of the cusp trap (see figure 5.3).

controller 1, see figure D.20) is used to switch the flow of trigger pulses to the high voltage switches for flexible operation. There are five switches (sw 1 - sw 5) in the controller, which can be toggled by external voltages. Blue lines in the figure indicate the control voltage of the switches while black allows indicate the logic pulses. When the control voltage is low, the terminal a in each switch is connected to the terminal c and when the control voltage is high, the terminal b is connected to the terminal c. For example, when we inject positrons to the cusp trap, we set the extraction coil select and the HV switch 1 / 2 select as low. The positron extraction trigger is sent to the Delay via sw 2 and sw 4.

positron catching The procedure to extract positrons from the positron accumulator and catch them in the cusp trap is as follows

1. Extraction coil select and HV switch 1 / 2 select of the trigger controller are set as low.
2. The master control PC of the positron accumulator (PCAD3038) send order to a PXI digital I/O module (National Instruments, PXI-6509).
3. The I/O module send TTL pulse to the trigger controller and the pulse is sent to the digital delay generator (stanford, DG645) via sw 2 and sw 4.
4. The delay generator send TTL pulses to high voltage switches used for the extraction of positrons from the accumulator (HV switch 3, see figure D.1) and for the catching of positrons in the cusp trap (HV switch 1, see figure D.1).
5. Two high voltage switches are triggered then extraction pulse and catching pulse are applied to the MRE of the positron accumulator and that of the cusp trap via RC signal mixers (RC mix 2, see figure D.19 and RC mix 1, see figure D.18) respectively. The amplitude of the extraction and catching pulse is determined by DC power supplies (matsusada, PL-120-0.6), which are controlled by a PC controlled DAC module (National Instruments, PXI-6723).

antiproton catching The procedure to extract antiproton from the antiproton catching trap and catch them in the cusp trap is similar to the procedure above.

1. Extraction coil select of the trigger controller is set as low and HV switch 1 / 2 select is set as high.

2. One of the PC (PCAD3019) send order to the CAMAC output register.

3. The register send a pulse to the digital delay generators (Thorlabs, DG100 (a) and (b)).

4. The delay generator (a) send a TTL pulse to the trigger controller via TTL OR module. The pulse is sent to the high voltage switch used for the catching of antiprotons in the cusp trap (HV switch 2, see figure D.2) via sw 3, sw 5 and a TTL buffer module.

5. The delay generator (b) send a TTL pulse to high voltage switch used for the extraction of antiprotons from the catching trap (HV switch 4).

6. Two high voltage switches are triggered, then extraction pulse and catching pulse are applied to the MRE of the antiproton catching trap and that of the cusp trap via RC signal mixers (RC mix 3 and RC mix 1) respectively. The amplitude of the catching pulse is determined by DC power supplies (Kikusui, PMC-350-0.2A), which are controlled by a PC controlled DAC module (National Instruments, PXI-6723).

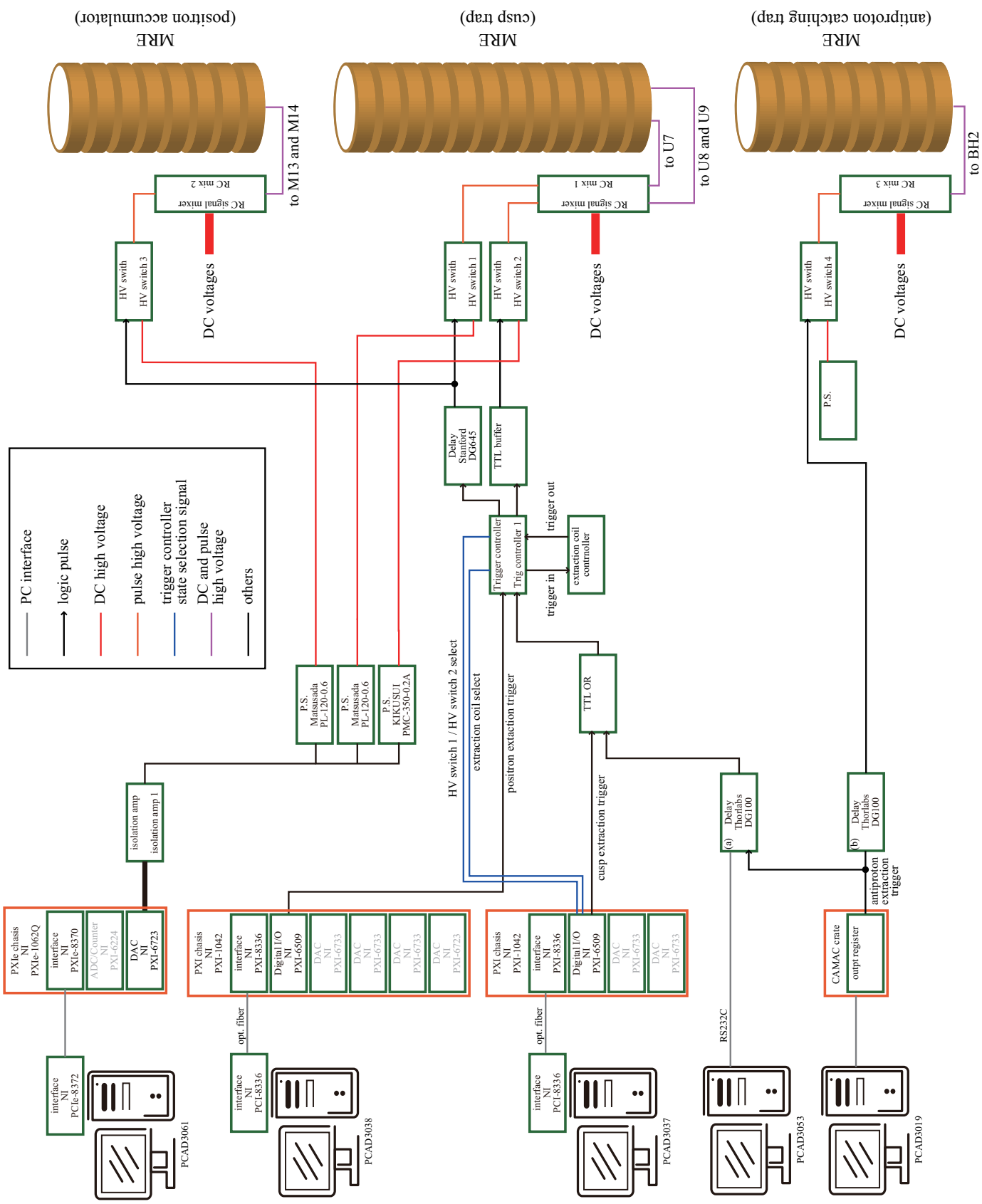

Figure 3.92: A connection diagram of the electric pulse control system.

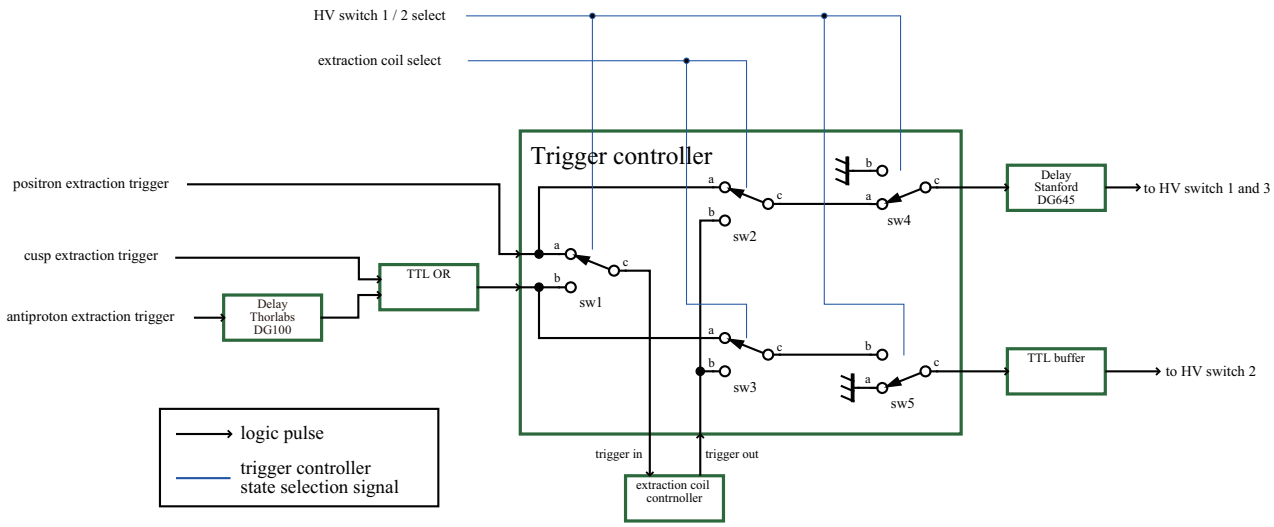

operation	extraction coil select	HV switch 1 / 2 select	signal flow
positron injection to the cusp trap	L	L	positron extraction trigger - sw 2 - sw 4 -Delay
positron extraction from the cusp trap	H	H	cusp extraoction trigger - TTL OR - sw 1 - extraction coil controller - sw 3 - sw 5 - TTL buffer
antiproton injection to the cusp trap	L	H	antiproton extraction trigger - TTL OR - sw 3 - sw 5 -TTL buffer
antiproton extraction from the cusp trap	H	H	cusp extraoction trigger - TTL OR - sw 1 - extraction coil controller - sw 3 - sw 5 - TTL buffer

Figure 3.93: A connection diagram of the trigger controller and a truth table. Two signals drawn by blue lines switch the relays in the Trigger controller and control the flow of the trigger signals.

noise reduction

As is described in section 2.4, the production rate of the antihydrogen atoms decrease as the temperature of positrons increase. Since electronic noise can be a candidate of the heating source of the positrons and this experiment was carried out inside the AD ring where high power RF signals are used to control the decelerator, we took some measures to reduce the noise of the control system of the MRE.

Figure 3.94 is an outline view of the control system. The components of the electrode control system, which are shown inside the red rectangle in figure 3.87, are enclosed in a shielded rack. In addition, to reduce ground impedance, chassis ground of each equipment is connected to copper bar inside the rack (see figure 3.94 right).

Figure 3.94: A photograph of modules to control the voltages applied to the MRE of the cusp trap. To reduce noise, the system is enclosed in a shielded rack (left and middle) and chassis ground of each equipment is connected to a copper bar (right).

We used triaxial cables (SUHNER, G_02332) of 15 m length between the control system and the MRE (see figure 3.87) to reduce unexpected pick up of external noise. Figure 3.95 shows a structure of the cable. The inner conductor is covered by double shields (outer shield and inner shield). To maximize the noise reduction effect, we tested several possible connections since the effect varies depending on the position to connect the shields to the ground. Figure 3.96 is a schematic drawing of tested connections. We measured the output of the 'RC LPF 1' (see figure 3.87) by a spectrum analyser (Agilent, E4411B). Connections in the left side

column show the configuration to connect the cables to the output of 'RC LPF 1', while those in right side column show the configuration to connect the cables to the spectrum analyser. For example, in connection C, the outer shield of the cable is connected to the case ground and the inner shield is floated at the control system side. Figure 3.97 shows measured noise power when we used the connection F-3, in which noise reduction effect was most efficient among all the other connections. Results when we used the connection A-1 (ordinary BNC cable and receptacle) and B-1 (ordinary BNC cable and insulated receptacle) are shown in the same figure for comparison. As can be seen from the figure, noise power was reduced in almost all of the frequency range from ∼0 to 100 MHz.

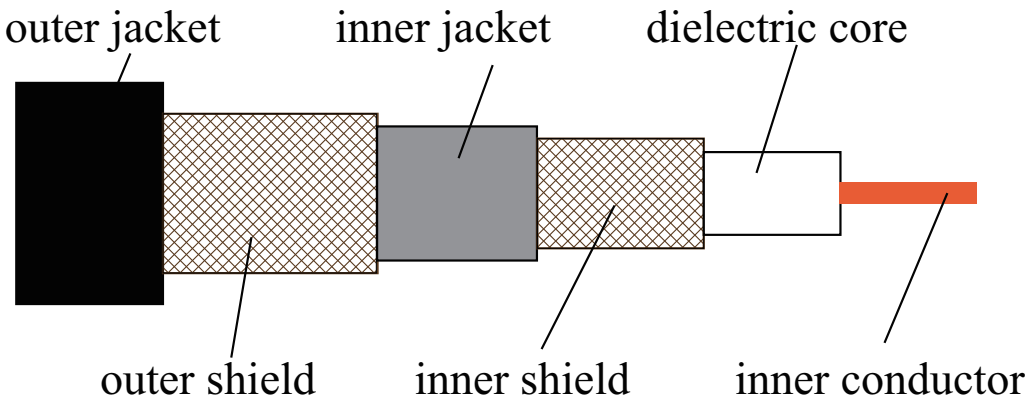

Figure 3.95: Structure of a triaxial cable. The inner conductor is doubly shielded by braided wires.

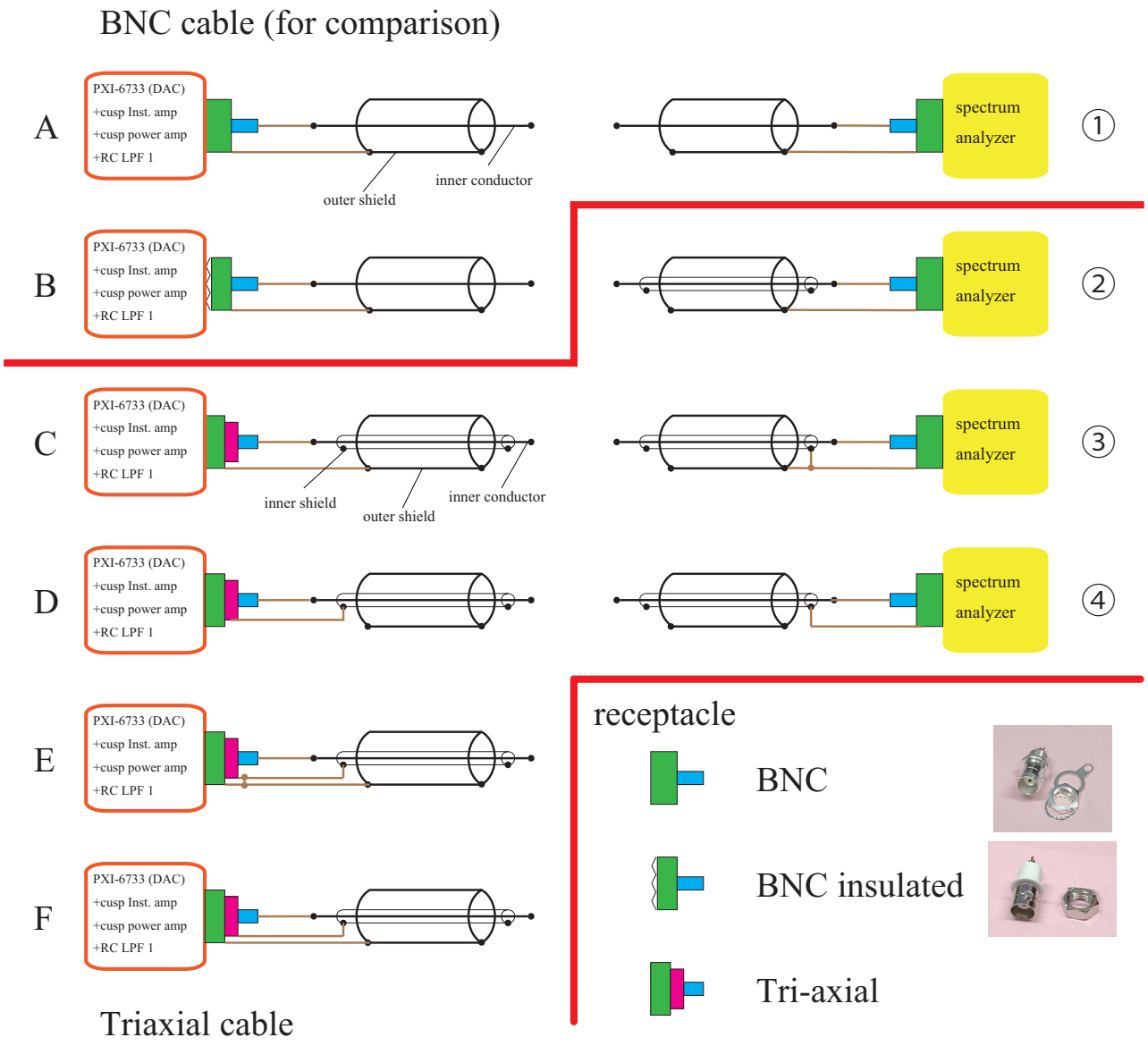

Figure 3.96: A schematic drawing of tested connections. To maximize the noise reduction effect, we tested several possible connections since the effect varies depending on the position to connect the shields to the ground.

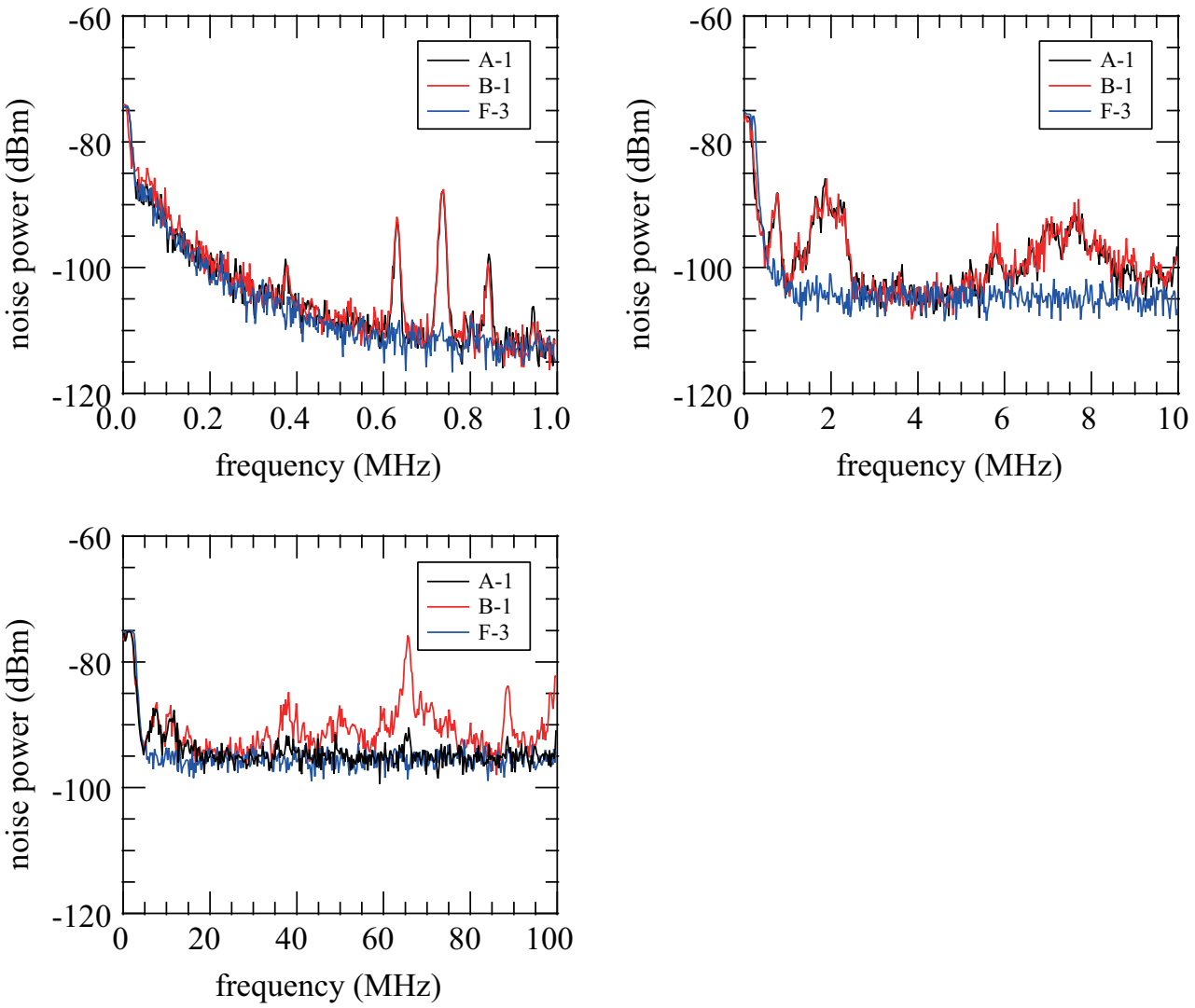

Figure 3.97: Measured noise power for the connection F-3, A-1, and B-1 as a function of frequency. In all frequency ranges, the noise power is reduced in the case of F-3 connection compared with A-1 or B-1 connection.

performance measurement We measured the noise of the control system using the spectrum analyser (Agilent, E4411B) under the real experimental condition (i.e. All cables are connected and the AD is in operation.). The spectrum analyser was connected to the cable via a tee at the feedthrough. Figure 3.98 shows the results in a variety of frequency range. Red curves in the figure represent measured noise power while blue curves represent baseline of the spectrum analyser. As can be seen from the figure, noise level is almost same as the baseline level in all frequency range. We note that small unknown component around 2 MHz can be removed by the cryogenic filter attached to the MRE (see figure 3.52).

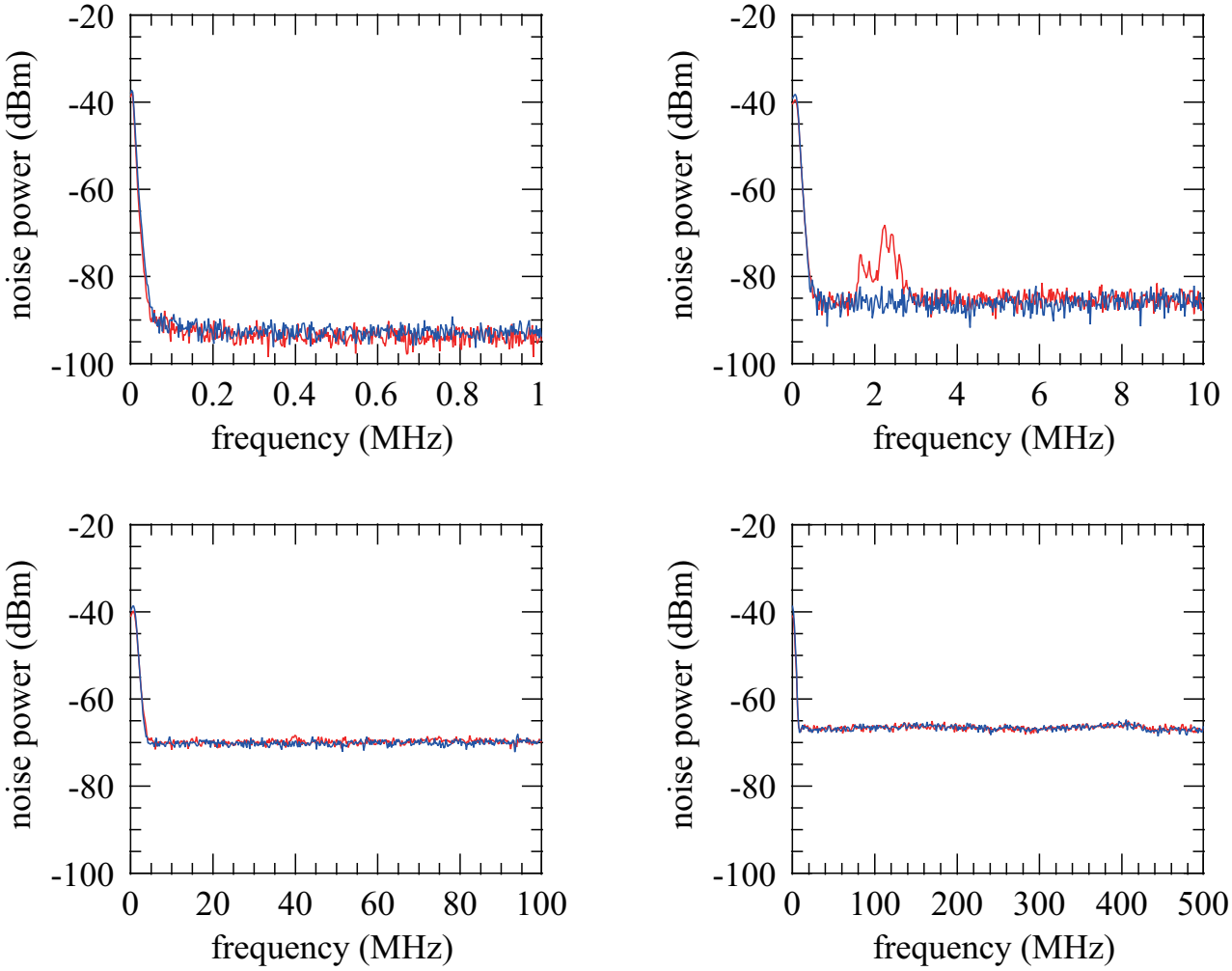

Figure 3.98: Noise spectrum of the control system of the cusp MRE in a variety of frequency ranges. Red curves represent measured noise power while blue curves represent baseline of the spectrum analyser. Except for the small peak around 2 MHz, the noise power is almost below the detection limit.

3.4.7 miscellaneous

adjustable support mechanism

Figure 3.99 shows adjustment mechanism of the cusp magnet. The magnet is fixed on an Al alloy plate (plate A) which can be moved by pushing with fine threaded screws fixed on the plate B, which is fixed on the upper support. Relative positions between the plate A and the plate B (shown by red arrows in the figure) can be measured by dial depth gauge using the hole A and notch A. By this way, they can be adjusted less than 1 mm precision.

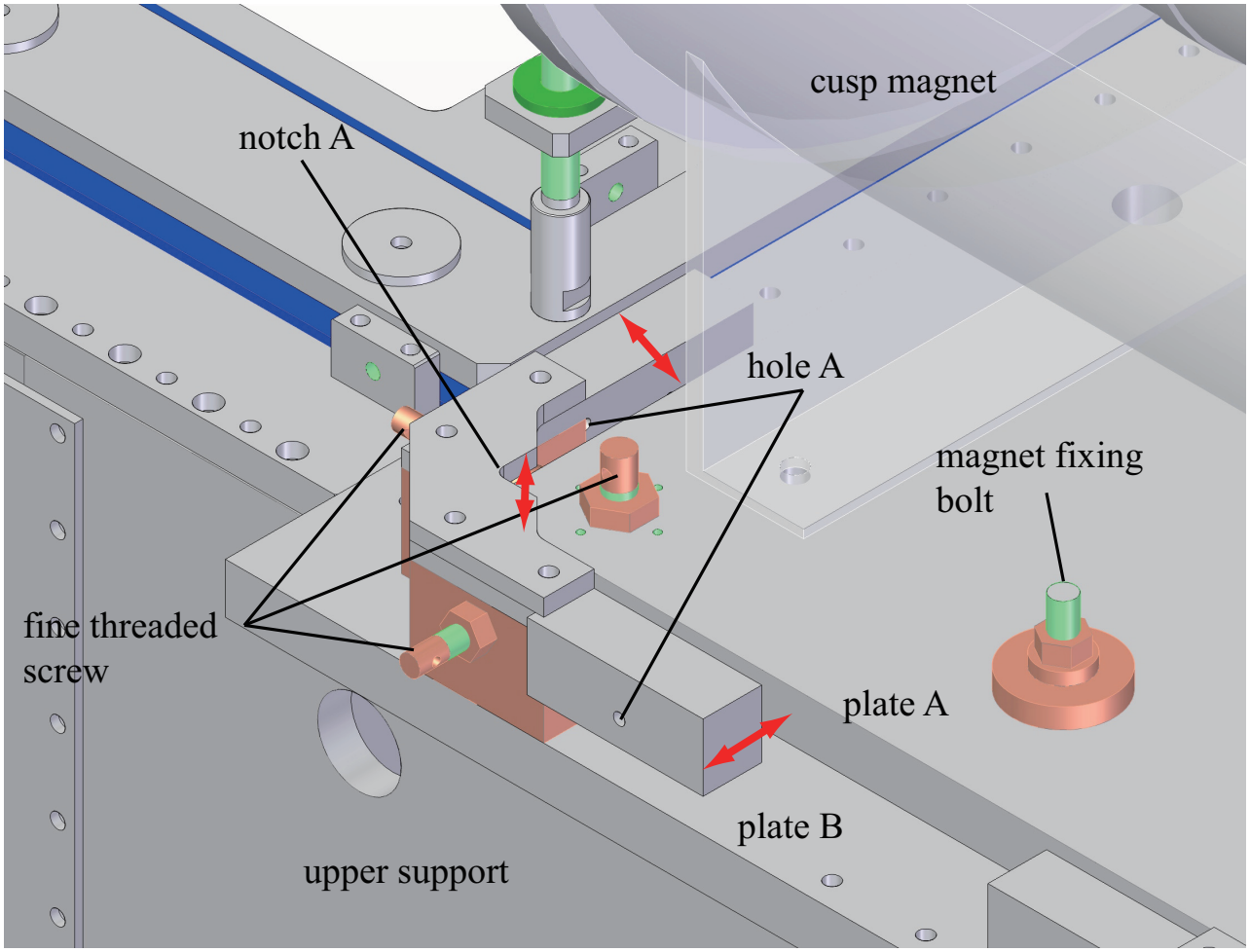

Figure 3.99: Magnet position adjustment mechanism. The magnet is fixed on the plate A which can be moved by pushing with fine threaded screws. Relative positions between the plate A and the plate B (shown by red arrows) can be measured by dial depth gauge using the hole A and notch A.

Figure 3.100 shows adjustment mechanism of the cusp trap. The upper support is put on Teflon plates fixed on the lower support. X and Y direction of the upper support can be

adjusted by fine threaded screws A and B. Z direction can be adjusted by four legs.

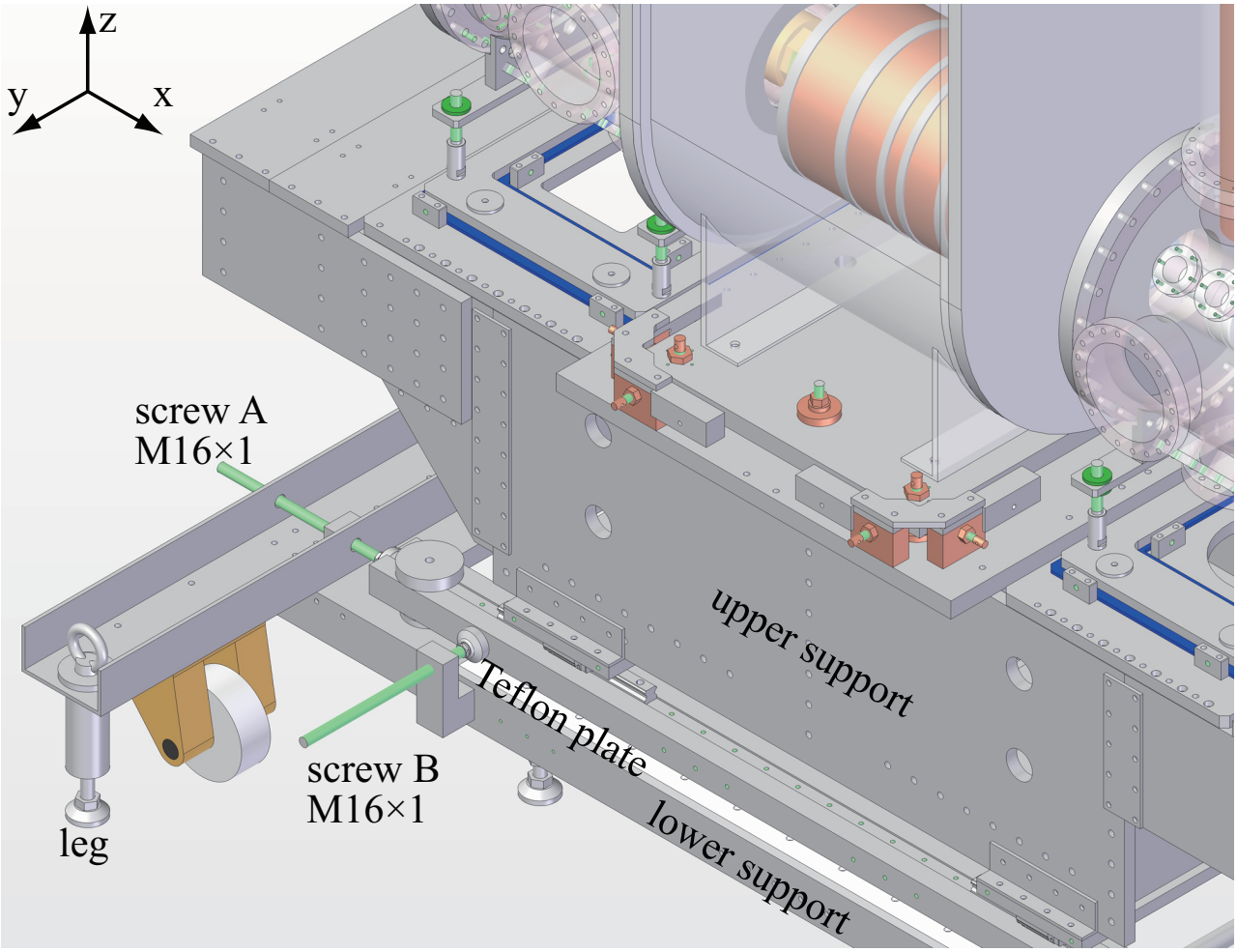

Figure 3.100: Cusp trap position adjustment mechanism. The position of the upper support, relative to lower support can be adjusted by screws. The height can be adjusted by the legs.

electron gun

A movable electron gun is attached on a port of the vacuum chamber in upstream side (see figure 3.37). It is used to test the confinement of charged particles and to cool the antiprotons in the cusp trap by electrons, if necessary.

Figure 3.101 is an isometric view of the electron gun. The electron emitter is mounted on a movable mechanism actuated by an air cylinder. It is inserted only when the electron is injected to avoid conflict with charged particles. Figure 3.102 is a cross sectional and back view of the electron emitter. Electrons emitted from a barium sintered cathode (JRC, NJK1120A) are controlled by extraction electrode.

Figure 3.103 shows connection diagram to control the electron gun. A PC controlled PXI digital I/O module (National Instruments, PXI-6509) send TTL pulse (extraction trigger) to the electron gun controller (see figureD.15 for circuit drawing), then a FET switch in the controller is triggered and the voltage applied to the extraction electrode is changed to 0 V[22]. Electron beam is extracted as long as extraction trigger continue, whose duration can be changed on the control program.

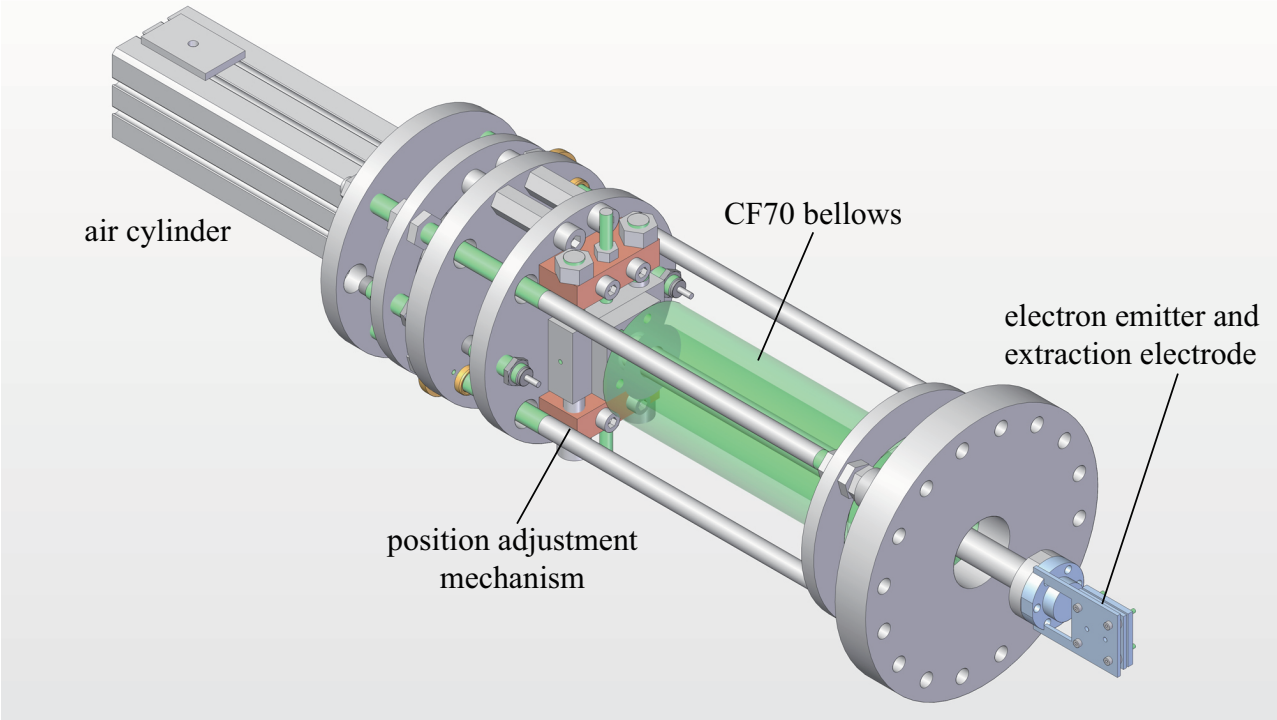

Figure 3.101: An isometric view of movable electron gun. The gun is inserted and extracted by the air cylinder. The position of the gun can be adjusted by the screws.

[22]The extraction electrode is biased to -9 V relative to the cathode voltage to suppress the emission of electrons when extraction trigger is not applied.

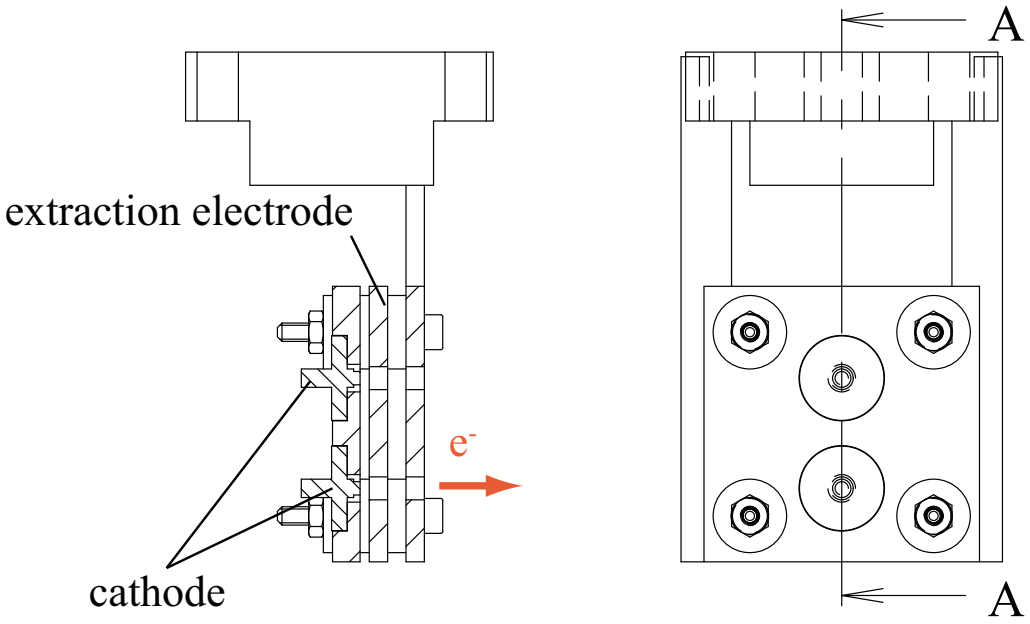

Figure 3.102: A cross sectional and back view of the electron emitter. Two cathodes are mounted on the plate and the extraction electrode is placed in front of the cathodes.

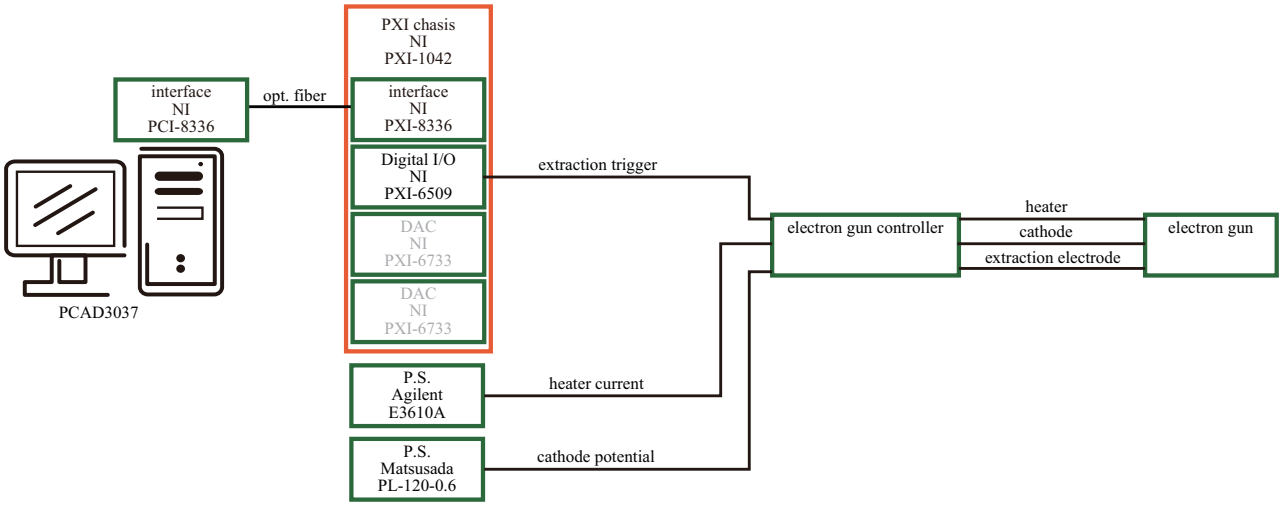

Figure 3.103: Connection diagram to control the electron gun. Extraction trigger from the digital I/O module switches the voltage applied to the extraction electrode and electrons are extracted.

3.5 Detectors

3.5.1 3D detector

The 3D detector was developed in collaboration with Brescia group for the detection of the antihydrogen atoms. Figure 3.104 is a schematic drawing of the 3D detector and the cusp trap seen from top. It consists of two pairs of two modules(#1-#4) of scintillator bars. Figure 3.105 shows the structure of one module. Each module consisted of 64 horizontal and 64 vertical scintillator bars (960 mm length and 19 mm $\times$ 15 mm in cross section) with wavelength shifting fiber of 1 mm ϕ inserted at the center. The fibers were bundled to one every 32 channels on both sides. On one side, 64[23] ch (8$\times$8) multianode PMTs (Hamamatsu, H7546B) were attached to all the bundles and the light from each fiber was read out individually. On the other side, single anode PMTs (Sens Tech, P30CW5) were attached to the horizontal or vertical bundles of four of two modules. The output signals from the single anode PMTs were used to trigger the DAQ system and to count the number of annihilations. We call the single anode PMTs as trigger PMTs.

When a pion passed through one module of the detector, at least one of the vertical and one of the horizontal bar gave signals and the hitting position was determined (see figure 3.105). Using two modules in one side, a line of pion trajectory can be reconstructed. Since the multiplicity of charged pion originating from one antiproton annihilation is roughly three, there was considerable chance that more than one pions were detected at the same time. In this case, the annihilation point was reconstructed three dimensionally as a cross point of the lines (see figure3.104). We call this operation mode of the detector as the imaging mode.

Each module can be also used as a large scintillator plates. Combination of the modules # 2 and # 3 covers 1/3 of the total solid angle. We call this operation mode of the detector as the counting mode. Figure 3.106 shows a connection diagram of the 3D detector in the counting mode. The signals from the trigger PMTs were first discriminated and summed up by each module. Then sum signals of the two modules were created by NIM circuit. These signals were recorded by the PXI Express DAQ module (National Instruments, PXIe-6224). At the same time voltages applied on the MRE were recorded by the same module via buffer amplifiers (buffer amp module 1, see figure D.12 for the circuit drawing). A set of data was recorded by a PC via PXI Express interface. Typical sampling rate we used was 5 kHz.

[23] Although each PMT has 64 anodes, we used every second anode to avoid cross talk.

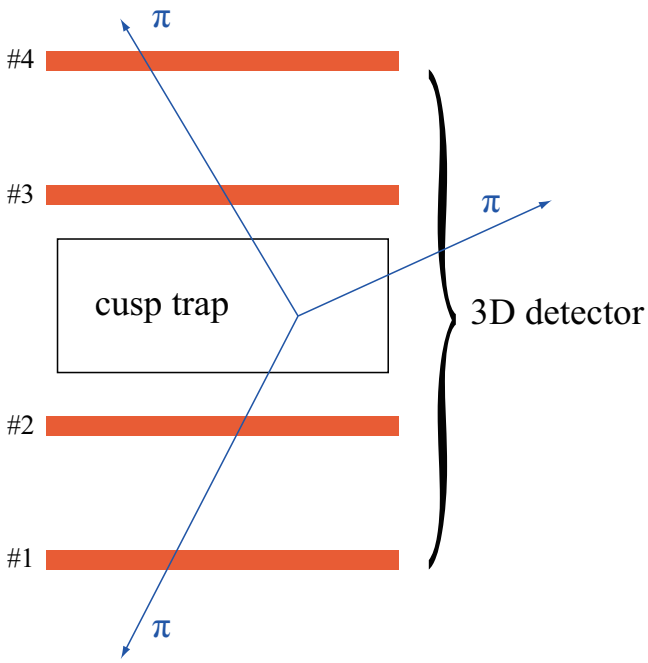

Figure 3.104: A schematic drawing of the 3D detector and the cusp trap (top view). The detector consists of four modules and detect pions originated from the annihilation of antiprotons.

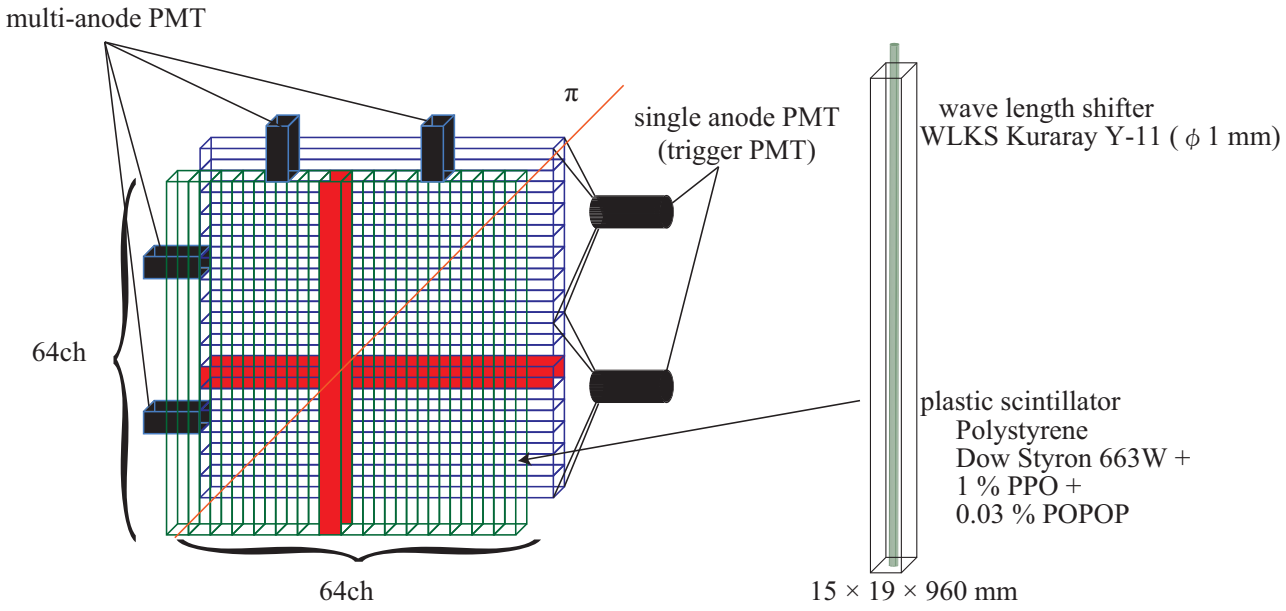

Figure 3.105: Structure of one module of the 3D detector. Each module made from 64 vertical and 64 horizontal scintillator bars. The wave length shifters are inserted in all bars and they are read by multianode PMTs. The position where a pion pass through in the module can be determined by the position of the bars which emitted light.

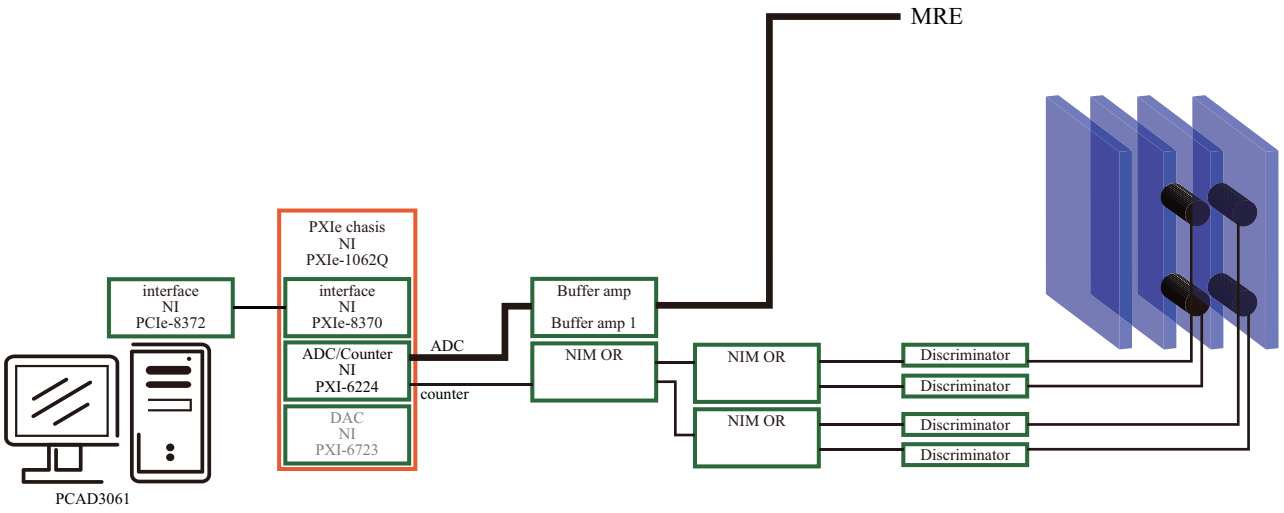

Figure 3.106: A connection diagram of the 3D detector in the counting mode. The signals from the trigger PMTs are discriminated and summed up. The number of the count is recorded by the PXI Express DAQ module (PXI-6224) along with the voltages applied to the MRE.

3.5.2 Track detector

Two set of track detectors (one for the antiproton catching trap and the other for the cusp trap) were prepared. Although these detectors are able to monitor the annihilation position, we used them to count the number of annihilation of antiprotons in the present work. Figure 3.107 shows the configuration of the track detectors. One set of the track detector consisted of two long plastic scintillator bars (2 m length, 4 cm $\times$ 6 cm cross section) with PMT at each end. When a pion passed through both of the bars, PMT attached to them gave signal.

Figure 3.108 shows a connection diagram of the track detector. The signal from each PMT was first divided into two. One of them was discriminated and connected to the coincidence modules. The coincidence signal of four PMTs was recorded by the Scalar. This signal was also used to trigger the DAQ system (ADC gate, PC trig, TDC start). All the data were recorded in a PC via CAMAC network crate controller (Toyo, CC/NET).

In 2010, the efficiency of the detectors was determined by simulation using GEANT and found to be 0.5 % for the antiproton catching trap and 0.8 % for the cusp trap. In the present work, these detectors were used to determine the number and the confinement time of antiprotons (see section 4.2 and 4.3).

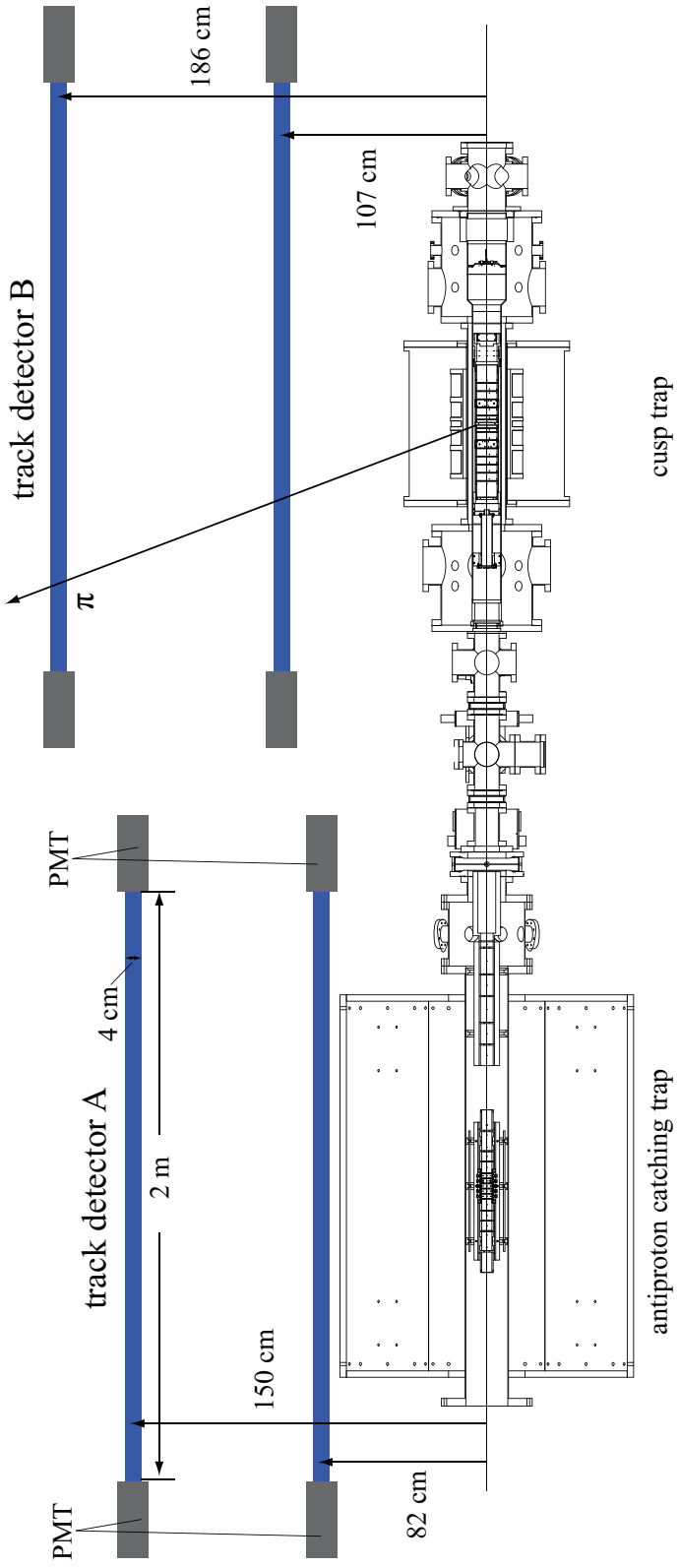

Figure 3.107: Configuration of the track detectors. One set of the track detector consisted of two long plastic scintillator bars with PMT at each end. The track detector A covers the antiproton catching trap while the track detector B covers the cusp trap.

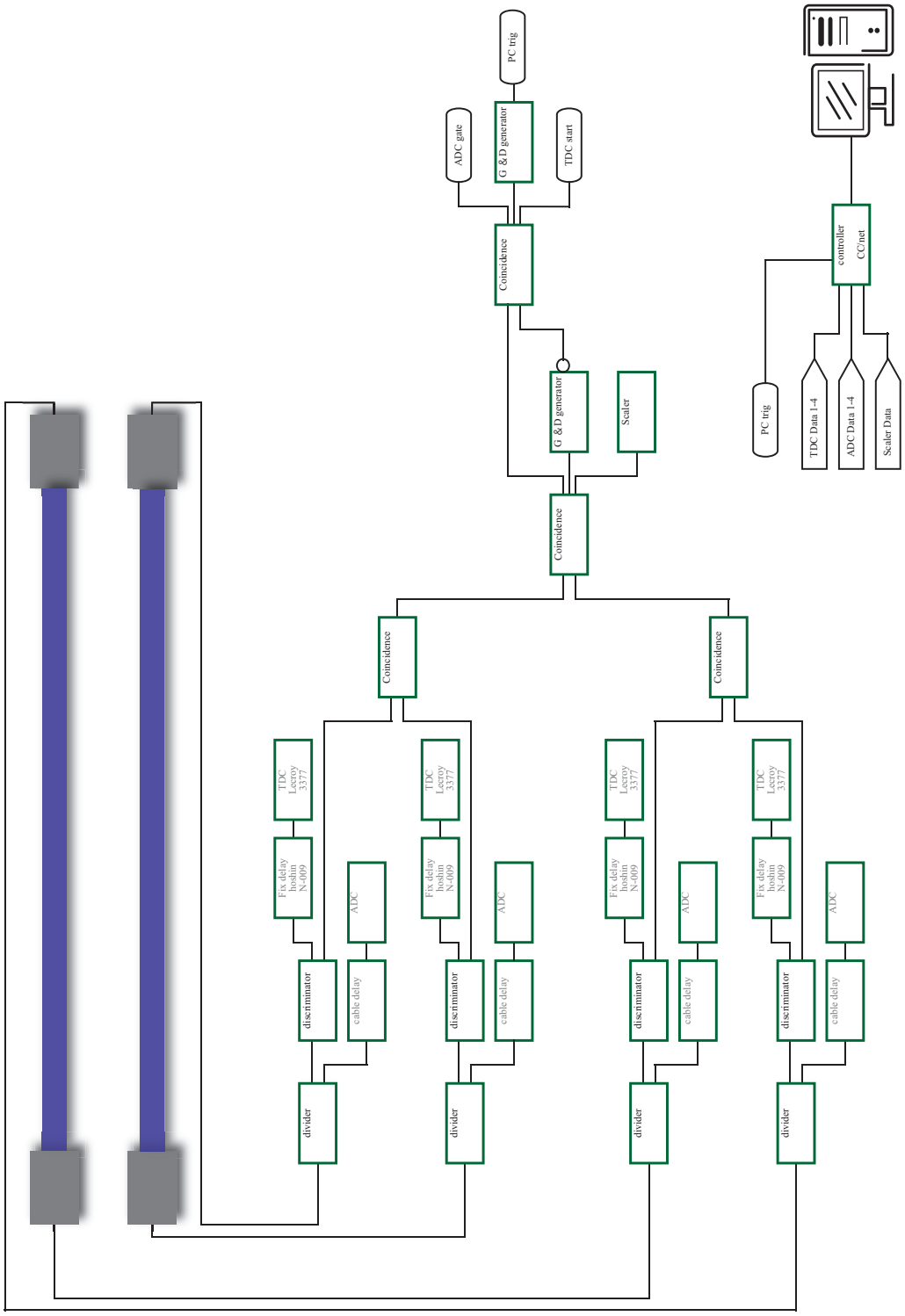

Figure 3.108: A connection diagram of the track detector. The signal from each PMT is divided, discriminated, and send to the coincidence modules. The number of the count is recorded by the scalar. This signal is also used to trigger the DAQ system (ADC gate, PC trig, TDC start).

3.5.3 MCPPS detector

The MCPPS detectors which consists of a MCP (Roentdek, MCP40) and a phospher screen (Arios, SG63-2) were installed in the cusp trap and in the positron accumulator to measure the profile and the number of charged particles. The position of each detector is shown in figure 3.37 for the cusp trap and in figure 3.17 for the positron accumulator. Figure 3.109 shows an isometric and cross sectional view of the detector used in the cusp trap. Charged particles extracted to the detector hit the surface of the MCP, then secondary electrons were emitted. The electrons were intensified by the MCP and exited from the other side of the MCP and hit the phospher screen. The image on the screen was reflected by the mirror and taken by the CCD camera. We call this operation as the imaging mode. The detector for the cusp trap was mounted on a linear and rotation motion feedthrough, and the detector for the positron accumulator was mounted on linear motion feedthrough. They were inserted only when they were in use. Specifications of the detector are summarized in table 3.18.

Figure 3.110 shows a connection diagram of the detector in the imaging mode. Bias voltages for the MCPs and the phospher screens were applied by high voltage power supplies (Iseg, NHQ214M) which were remotely controlled by the output voltages of the DAC module (National Instruments, PXI-6723) through low pass filters. The images of the charged particles taken by the CCD cameras were captured by the image capture card (National Instrument, PCI-1410) and stored in a PC.

One of the detector used in the cusp trap was also used to count the number of the positrons in the trap. We used this mode to measured the energy distribution of positrons (see section 5.3) and call this operation mode as the counting mode. Figure 3.111 shows a connection diagram of the detector in the counting mode. The intensified electrons by the MCP were collected on the phospher screen and amplified by the pre-amplifier (pre amp 1, see figure D.16 for circuit drawing). The signals were discriminated and converted to TTL pulses. The number of the pulses were recorded by the PXI DAQ module (National Instruments, PXIe-6224[24]) whose maximum count rate is 80 MHz. At the same time voltages applied on the MRE were recorded by the same module via buffer amplifiers (buffer amp module 1, see figure D.12 for the circuit drawing). A set of data was recorded by a PC via PXI Express interface. Typical sampling rate we used was 5 kHz.

[24]This module has 2 ch counters and 32 ch ADCs

	cusp trap	positron accumulator
motion feedthrough	Huntington, VF169-18 with air cylinder	Huntington, L-2271-4
MCP	Roentdek, MCP40 × 2	Roentdek, MCP40 × 1
phospher screen	ARIOS, SG63-2	same as left
active diameter of MCP	47 mm	same as left
diameter of phospher screen	63 mm	same as left
image capture board	National Instruments, PCI-1410	same as left

Table 3.18: Specifications of the MCPPS detectors.

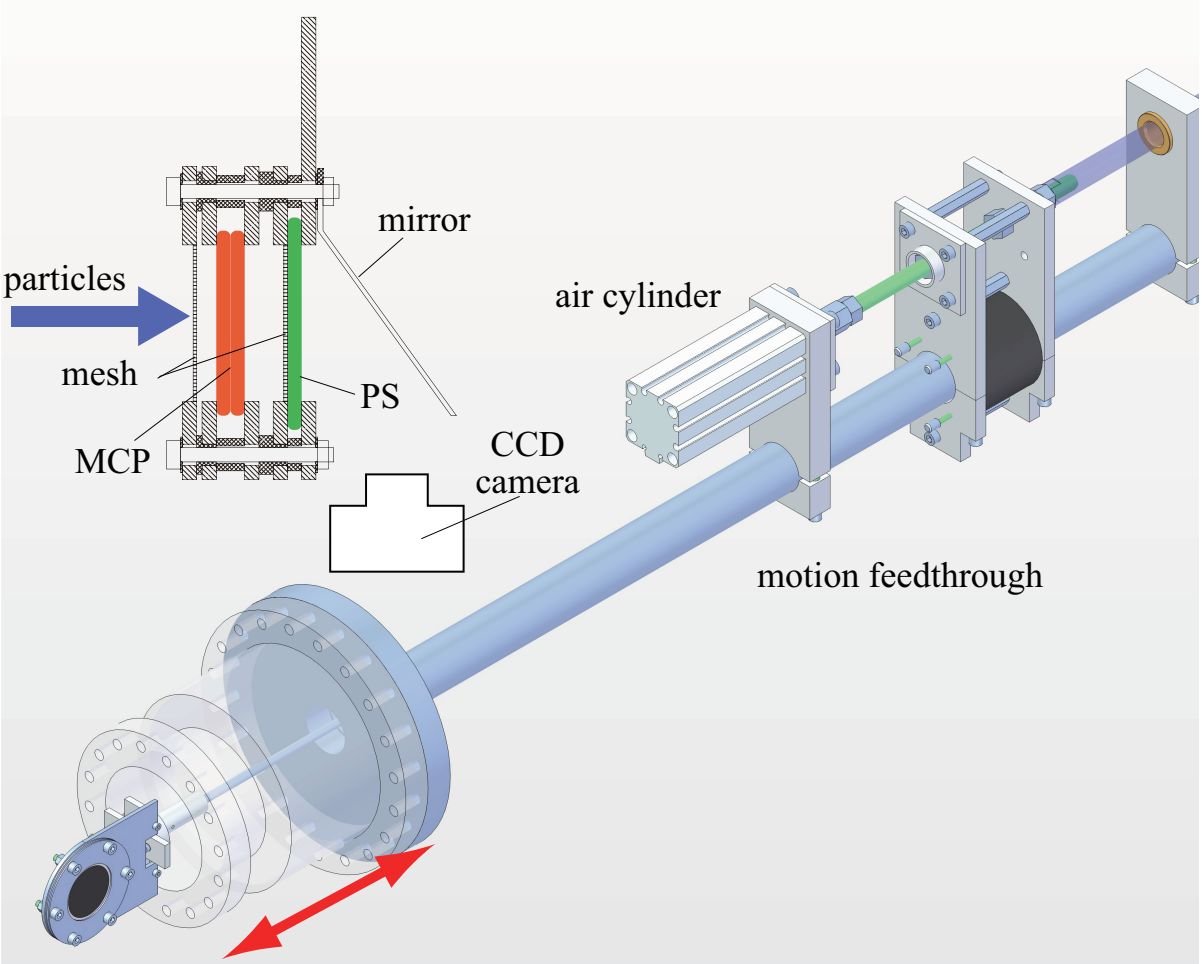

Figure 3.109: An isometric and a cross sectional view of the MCPPS detector used in the cusp trap. The detector consists of the MCP, the phospher screen and the mirror. They are mounted on the movable mechanism. Images of the charged particles extracted to the detector is taken by the CCD camera.

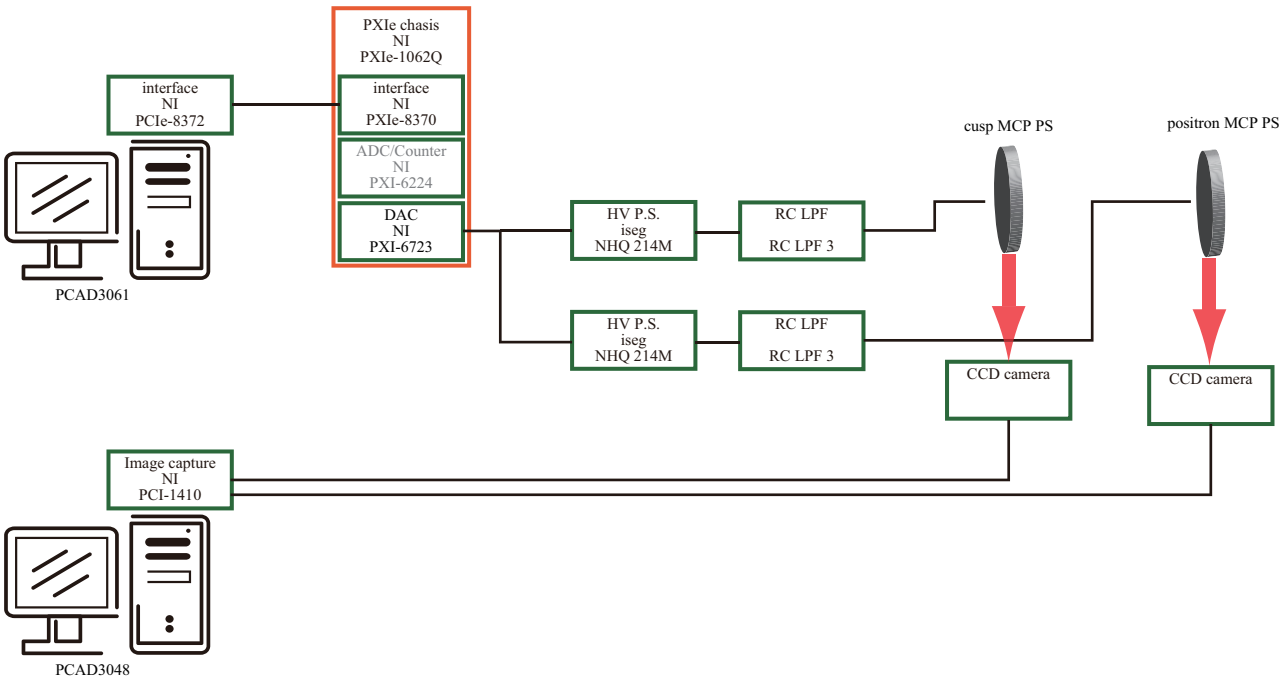

Figure 3.110: A connection diagram of the MCPPS detectors to capture the image of the charged particles. Images taken by the CCD cameras are read out and recorded by the image capture board (PCI-1410). High voltages applied to the detector is controlled by the DAC.

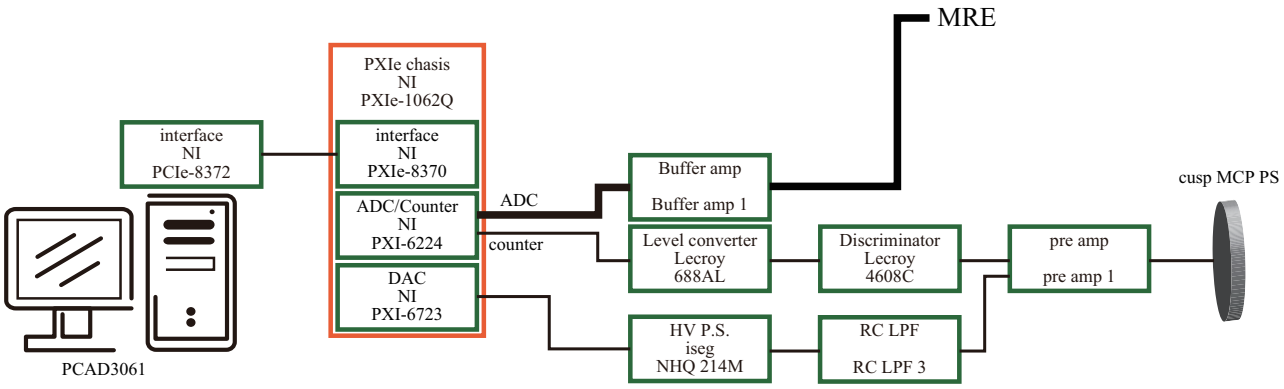

Figure 3.111: A connection diagram of the MCPPS detectors to count the number of charged particles. Electric pules from the detector is amplified, discriminated, level converted and send to the DAQ module (PXI-6224). The number of the pulses is recorded by the module along with the voltage applied to the MRE.

3.5.4 Scintillators for antiproton and positron monitor

Two plastic scintillator plates were used to observe the annihilation timing of positrons and antiprotons during transport test. Figure 3.112 shows a connection diagram of the detectors. Output signals from the PMTs were connected directory to the digital oscilloscope (Agilent, DSO6034A) and data were sent to the PC via GPIB interface.

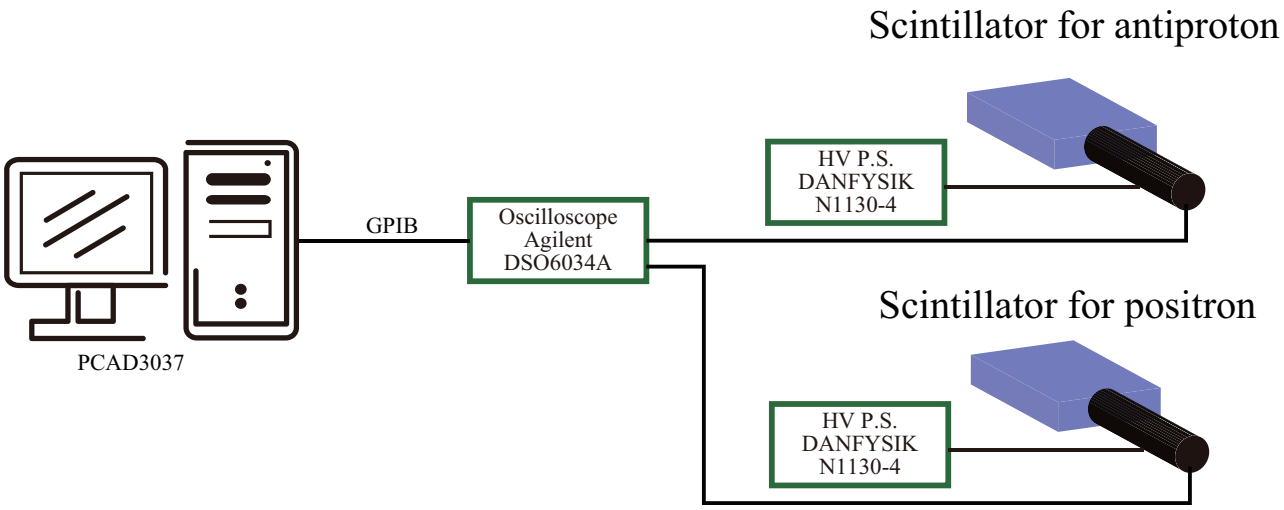

Figure 3.112: A connection diagram of the scintillators. Signals from the PMTs are connected directly to the Oscilloscope.

3.6 Control program

Control programs of the apparatus are mainly written by Labview version 8 series and the programs are running on several Linux PCs connected to local area network by Ethernet. Figure 3.113 shows typical flow of the control programs to produce antihydrogen atoms. Red arrows in the figure represent the trigger pulse while black arrows represent the relation between the main program and subprograms.

1. The positron trap control runs independently and accumulate positrons in the cusp trap.
2. The positron trap control stops when enough positrons are accumulated in the cusp trap.
3. The master control runs and calls the antiproton catching trap control and the CAMAC DAQ control.
4. The antiproton catching trap control starts preparation to catch and cool antiprotons, at the same time calls the cusp trap control.
5. The antiproton catching trap control waits for the trigger from AD and the cusp trap control waits for the software permission from the antiproton catching trap control.
6. When the trigger pulse from the AD arrives, the antiproton catching trap control proceeds to next step.
7. Certain seconds before the extraction of the ultra-low energy antiproton beam, the antiproton catching trap control sends the software permission to the cusp trap control.
8. By receiving the software permission, the cusp trap control starts to run and stops again at a point to catch antiprotons.
9. At the time of extraction of ultra-low energy antiproton beam, a TTL signal is sent to the input terminal of the PXI digital I/O module in the cusp trap control system.
10. Receiving the TTL signal, the cusp trap control restarts and calls PXI Express DAQ program.

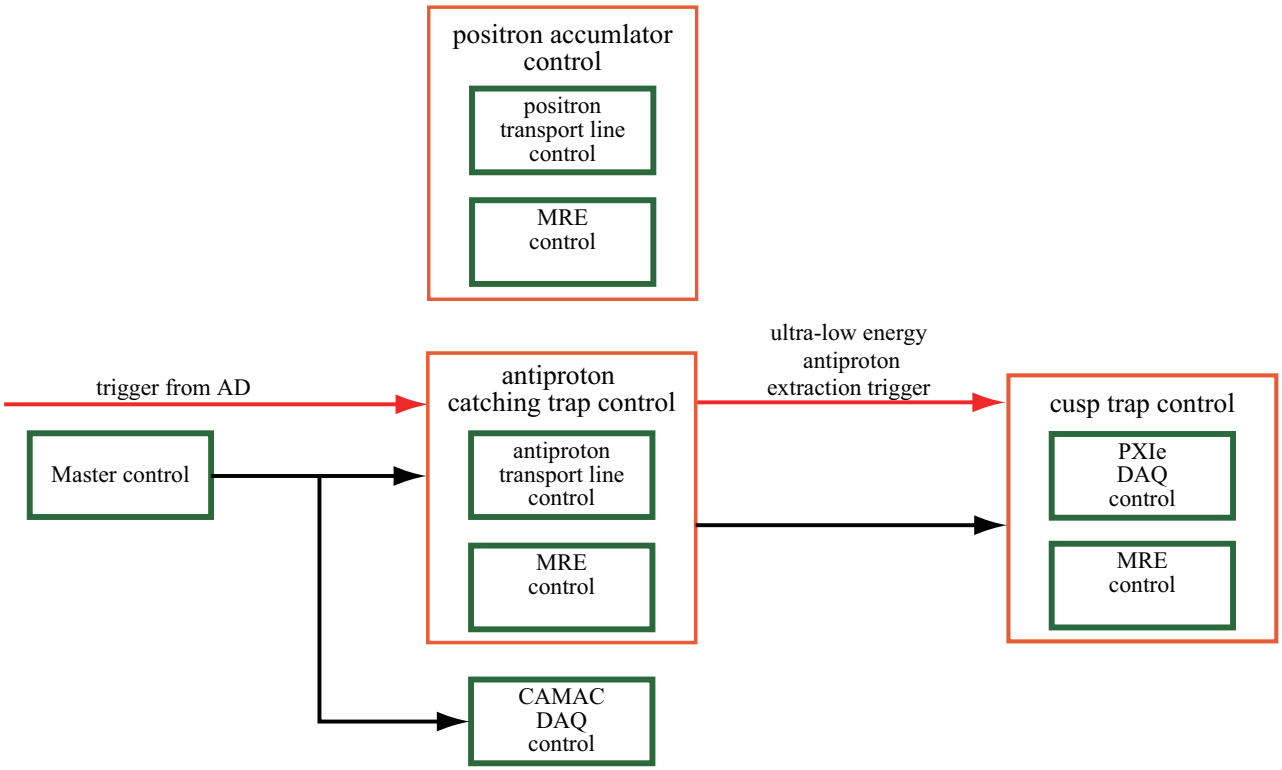

Figure 3.113: A flow of control program. Red arrows in the figure represent the trigger pulse while black arrows represent the calling relation between the main program and subprograms. The aster control program calls the CAMAC DAQ control program and the antiproton catching trap control programs. The antiproton catching trap control programs call the cusp trap control programs. On the other hand, positron accumulator control programs run independently.

Chapter 4

Confinement of antiprotons in the cusp trap

Since the confinement of the ions in non-uniform magnetic field has been rarely carried out, stable confinement of antiprotons in the cusp trap itself is a challenge. In section 4.1, transport of antiprotons is described. In section 4.2, catching process of antiprotons in the cusp trap is described. In section 4.3, confinement time of antiprotons in the cusp trap is presented under various and realistic conditions. In section 4.4, position calibration of the 3D detector using confined antiprotons in the cusp trap is described.

4.1 Transport ultra-low energy antiprotons

Antiprotons were extracted as a pulsed beam from the antiproton catching trap and injected into the cusp trap. For the efficient catching of antiprotons in the cusp trap, length of the beam should be as short as possible. Figure 4.1 shows potential curves on axis for the extraction of antiprotons in the catching trap. To reduce the pulse width of extracted beam, antiprotons were confined in a narrow potential whose bottom is at the BH2 electrode (red curve). Then the voltage applied to the BH2 electrode was changed from -50 V to -155 V by a pulse voltage switch, accordingly the potential changed from red curve to blue curve and pulsed antiproton beam was extracted.

Figure 4.2 (a) shows a cross sectional drawing of the apparatus used for the transport of the antiproton beam. The beam was focused by electro-static lens (extractor electrodes) and guiding coils (coil A, coil B) and transported into the cusp trap. For the efficient transport of

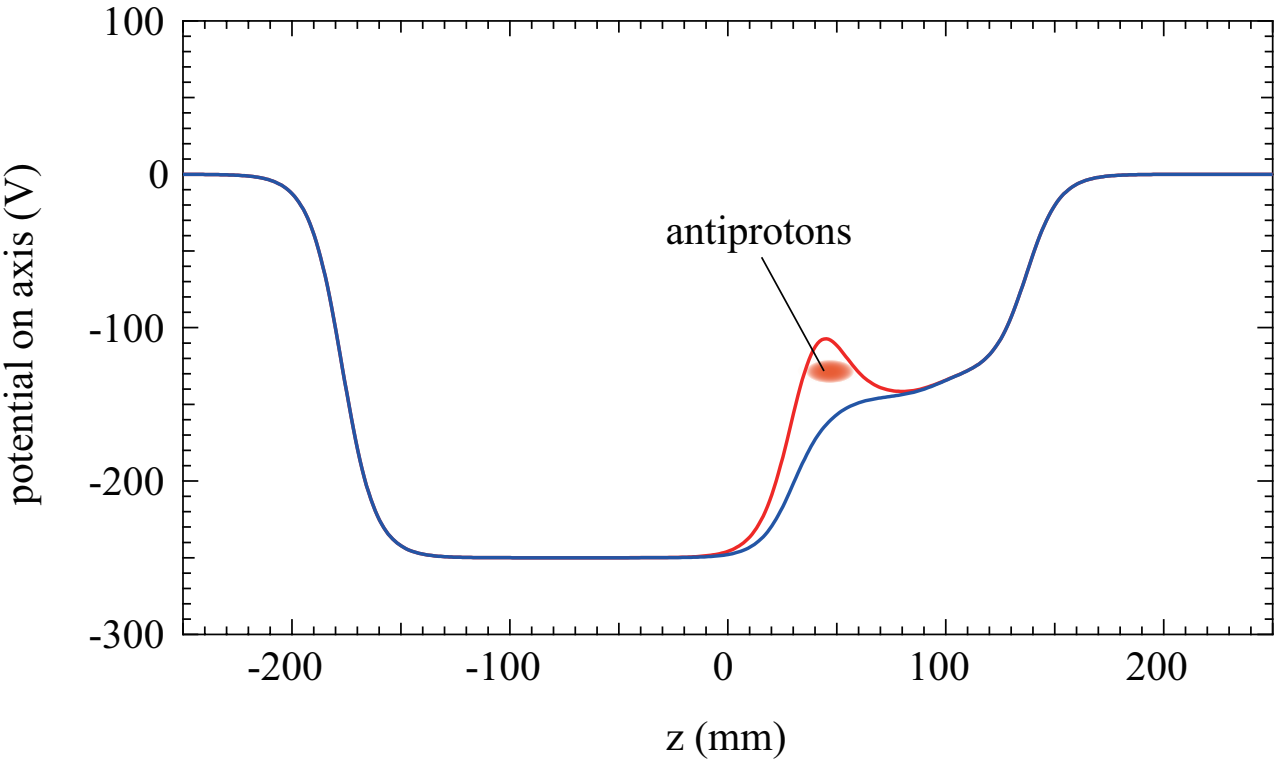

Figure 4.1: Potential curves on axis in the antiproton catching trap used for the pulse extraction of the antiprotons. Red curve represents narrow potential before the extraction, and blue curve represents the potential after the pulse voltage is applied on the BH2 electrode.

the beam, we carried out trajectory simulation of antiprotons. Figures 4.2 (b), (c), (d), and (e) shows time of flight of antiprotons, magnetic field on axis, electric potential on axis, and trajectories of antiprotons respectively. Calculation was conducted using TriComp [1] under various extractor voltage and guiding coil current. The optimized setting is summarized in table 4.1 and initial conditions used in the trajectory calculation is shown in table 4.2.

voltage of the extractor (L0)	400 V
voltage of the extractor (E)	0 V
magnetic field of coil A	10 mT
magnetic field of coil B	10 mT

Table 4.1: Optimised parameters for the transport of antiprotons.

number of antiprotons	100
radial position	$r \leq 0.25$ mm randomly distributed
axial position	42 mm $\leq z \leq$ 48 mm randomly distributed
energy distribution	Maxwell distribution at 1 eV
direction	isotropic

Table 4.2: Initial conditions of antiprotons used in the trajectory calculation. We define z=0 as the center of the MRE of the antiproton catching trap.

Extracted antiprotons were monitored by a scintillator which was located near the cusp trap and 2 m away from the beamline axis to cover wide area[2]. Typical results when antiprotons were successfully caught in the cusp trap is shown in 4.3 (black) along with the data when the gate valve GV1 (red) or the GV3 (blue) was closed and almost all of the antiprotons annihilated on each valve. Pulse width of the beam was roughly 0.5 μs both at the position of the GV1 and GV3, which was obtained by fitting the data with Gauss function. Mean energy of the beam was about 220 eV, which was determined by the interval of the peak positions of the red and blue curves and the distance between the GV1 and the GV3. On the other hand, considering the effective length of the potential well to catch antiprotons in the cusp

[1] TriComp is a name of software for a 2D trajectory calculation (see [69] for more details).

[2] If the detector was located near the beam axis, the solid angle varied rapidly as the distance in the axial direction increased.

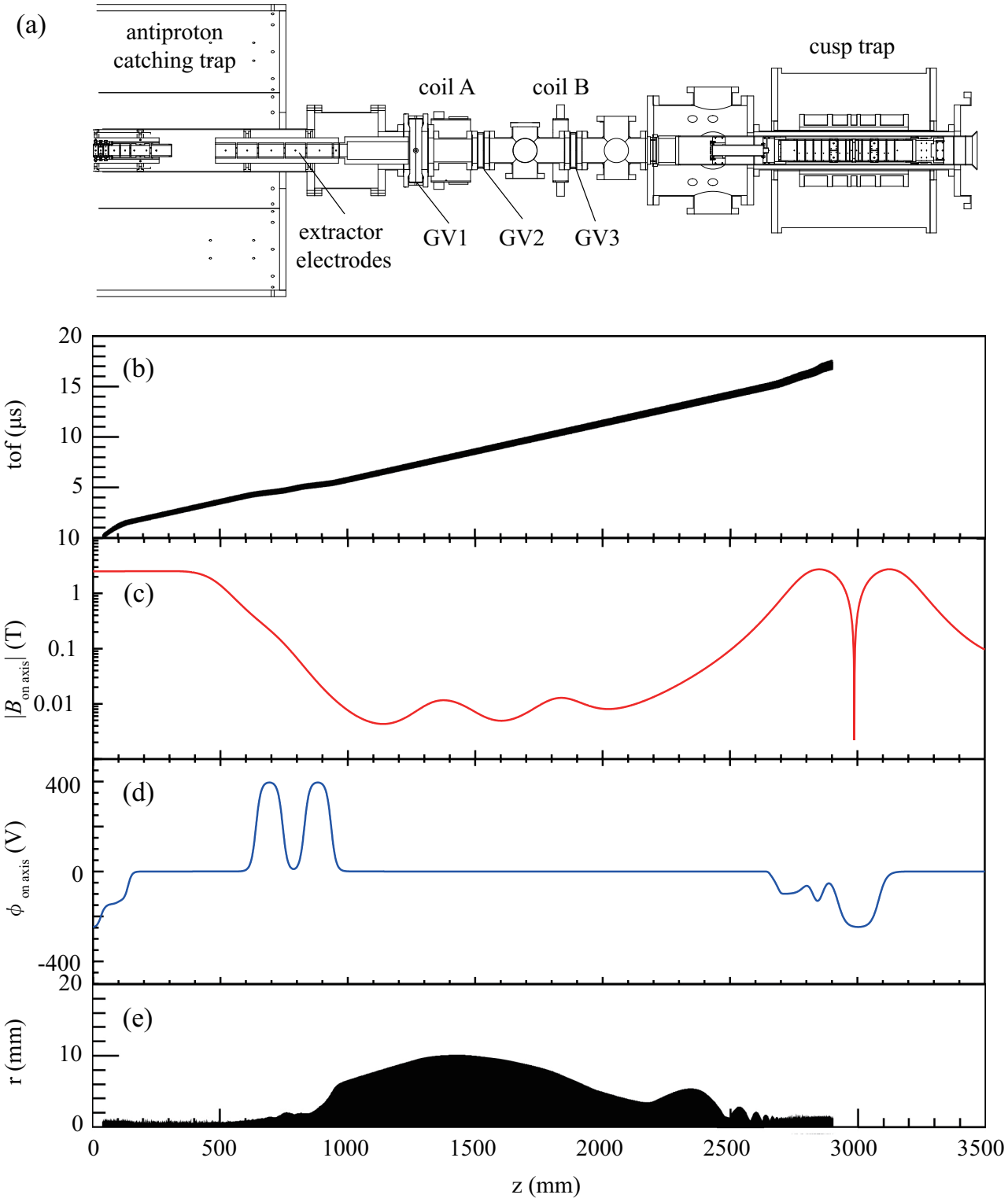

Figure 4.2: A cross sectional drawing of the antiproton catching trap, the antiproton transport beamline, and the cusp trap (a). Time of flight of antiprotons (b), magnetic field on axis (c), electric potential on axis (d), and trajectories of antiprotons (e) are drawn as a function of the distance in the axial direction (z).

trap was about 150 mm and the speed of the antiproton whose kinetic energy is E_{kp} eV is given by $14\sqrt{E_{kp}}$ mm/μs, the length of the pulse should be less than 1.5μs to catch the whole antiprotons in the pulse. Thus, whole antiprotons in the extracted pules were expected to be caught since the observed pules width was well shorter than the required value and significant expansion of the pulse width did not observed between the GV1 and the GV3. Annihilation position of antiprotons along the axis was able to be obtained from the TOF, and the position information was sometimes used to solve problems like sudden decrease of transport efficiency.

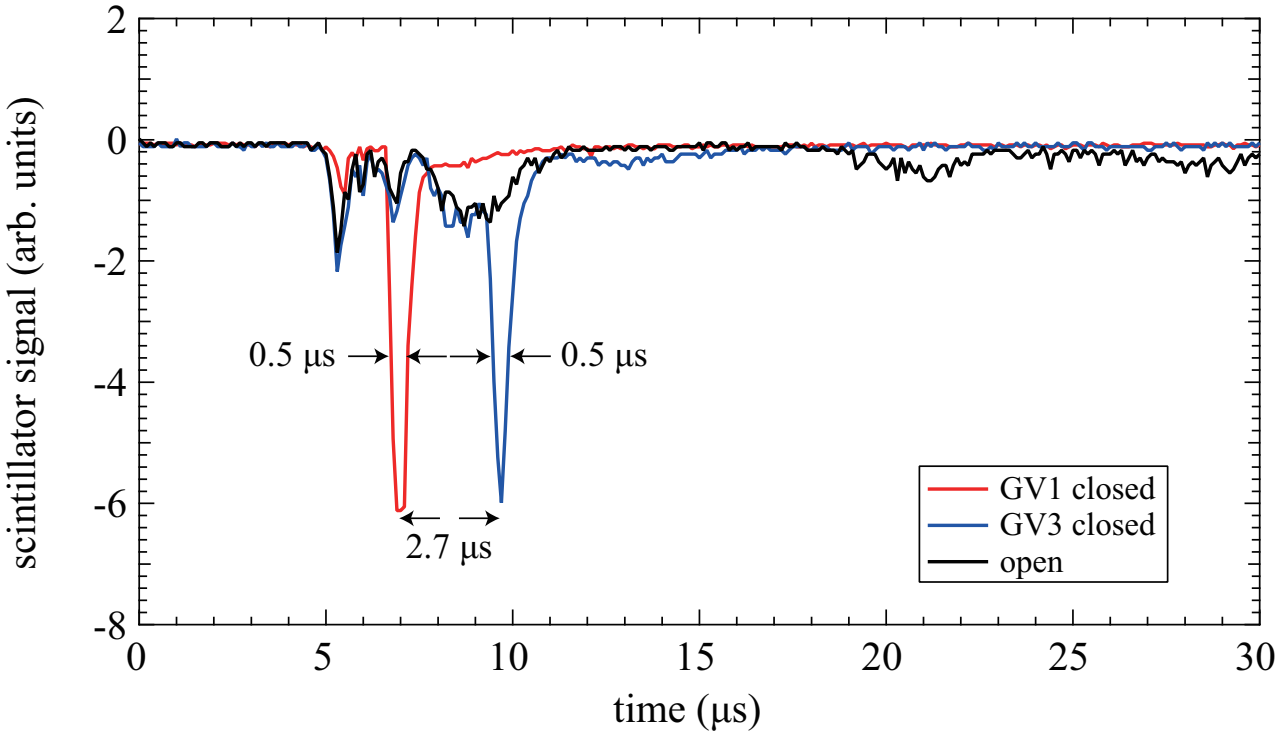

Figure 4.3: Typical signal from the scintillator to monitor the antiproton transport. When antiprotons were caught in the cusp trap successfully, no annihilation peak appeared (blue curve). On the other hand, when the gate valve GV1 or GV3 (see figure 4.2 (a) for the position of each gate valve) was closed and almost all of the antiprotons annihilated at that point, a large peak appeared at the corresponding timing. Pulse width of the beam is about 0.5 μs at GV1 and GV3.

4.2 Catching antiprotons in the cusp trap

potential operation of the cusp MRE

Figure 4.4 shows the potential curves on axis used to catch antiprotons in a harmonic potential (b) and in a nested (c) potential in the cusp trap. To catch the antiproton beam, the potential was switched from the red curve to the blue curve at the timing of the antiproton beam extraction, then it was switched back to the red curve before antiprotons were reflected and escaped from the cusp MRE. To maximize the number of antiprotons caught in the cusp trap, the timing to switched back the potential (t_w) was scanned by monitoring the annihilation signal from the scintillator.

counting trapped antiprotons

Figure 4.5 shows potential curves to count the number of antiprotons caught in the cusp trap. First, if antiprotons were confined in a nested potential (black), the potential was changed to a harmonic potential (red) before the extraction to avoid unexpected capture of antiprotons in a local minimum of the nested potential. Then, by slowly lowering the potential wall of the entrance side (indicated by red arrow), emerging antiprotons, which immediately hit the wall of the vacuum chamber and emitted annihilation products, were counted by the track detector.

Typical data taken by this method is shown in figure 4.6. In this example, the voltage applied on the electrode U8 and U9 were gradually decreased for 10 s (a) and the integrated count of the annihilation signal increased (b). The difference of the integrated count before and after the extraction, which is shown in the figure as $n_p(0)$, is proportional to the number of antiprotons caught in the cusp trap. As was described in section 3.5.2, the detection efficiency of the track detector is 0.8 %, the number of antiprotons caught in the cusp trap ($N_p(0)$) can be obtained by $N_p(0) = n_p(0)/0.008$. In this case, as can be seen from the figure, $n_p(0) = 3200$ and $N_p(0) = 4 \times 10^5$. In addition, the annihilation count rate can be obtained by differentiating the integrated count as shown in figure 4.6 (c).

control the number of antiprotons

As described in section 3.1.6, by stacking several antiproton pulses from the AD in the antiproton catching trap, the number of antiprotons in the catching trap can be increased. Figure 4.7 shows a relation between the number of antiprotons caught in a nested potential prepared

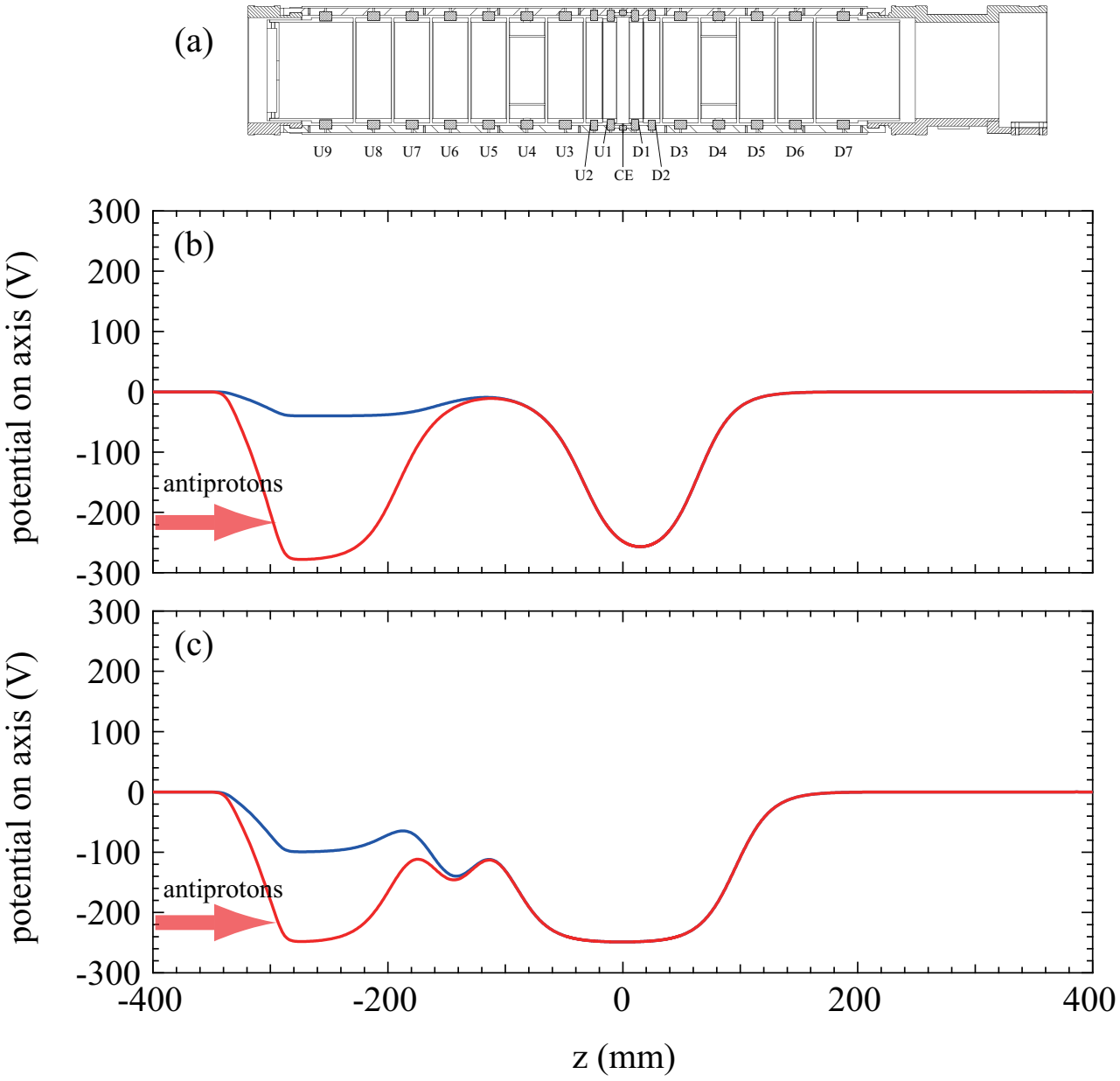

Figure 4.4: A cross sectional drawing of the MRE of the cusp trap (a). Potential curves in the cusp trap to catch antiprotons in a harmonic potential (b) and in a nested potential (c). To catch the antiproton beam, the potential was switched from the red curve to the blue curve at the timing of the antiproton beam extraction, then it was switched back to the red curve before antiprotons were reflected and escaped from the cusp MRE.

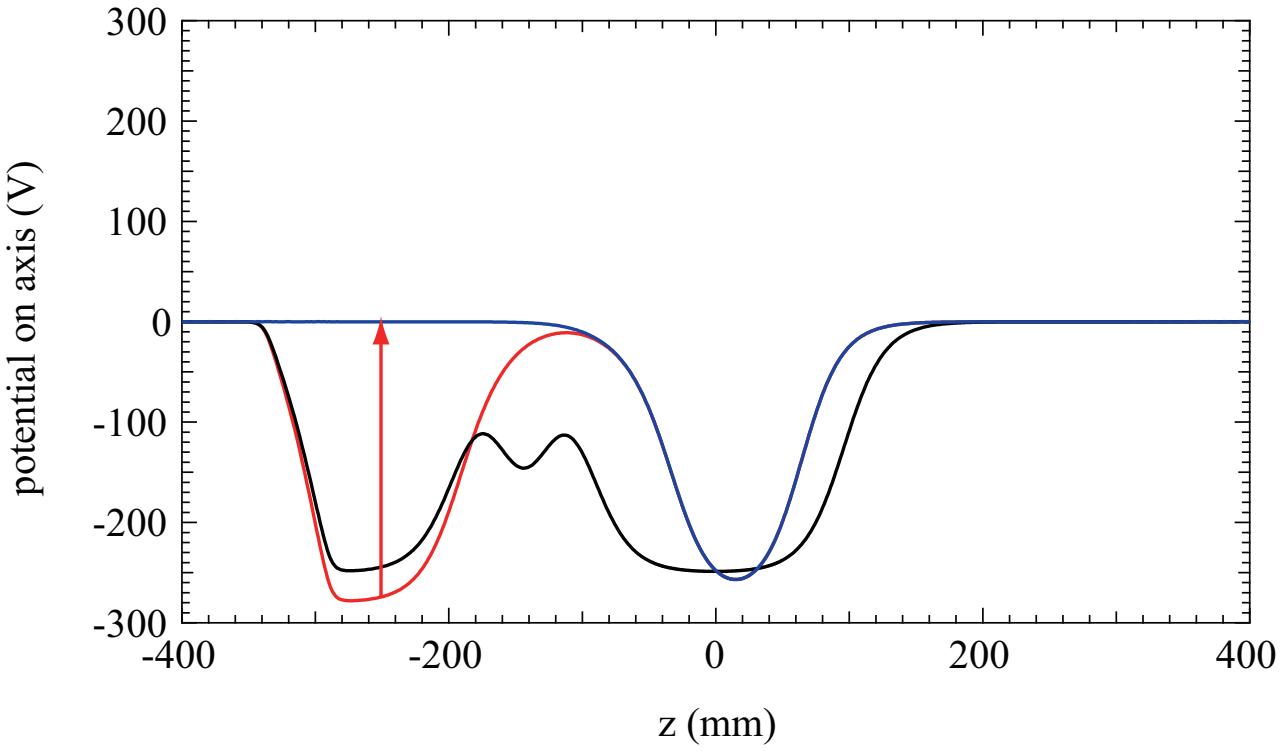

Figure 4.5: Potential curves on axis used to count the number of antiprotons caught in the cusp trap. If antiprotons were confined in a nested potential (black), the potential was changed to a harmonic potential (red). Then the potential wall of the entrance side was decreased slowly as shows by the red arrow and antiprotons were extracted to the left side.

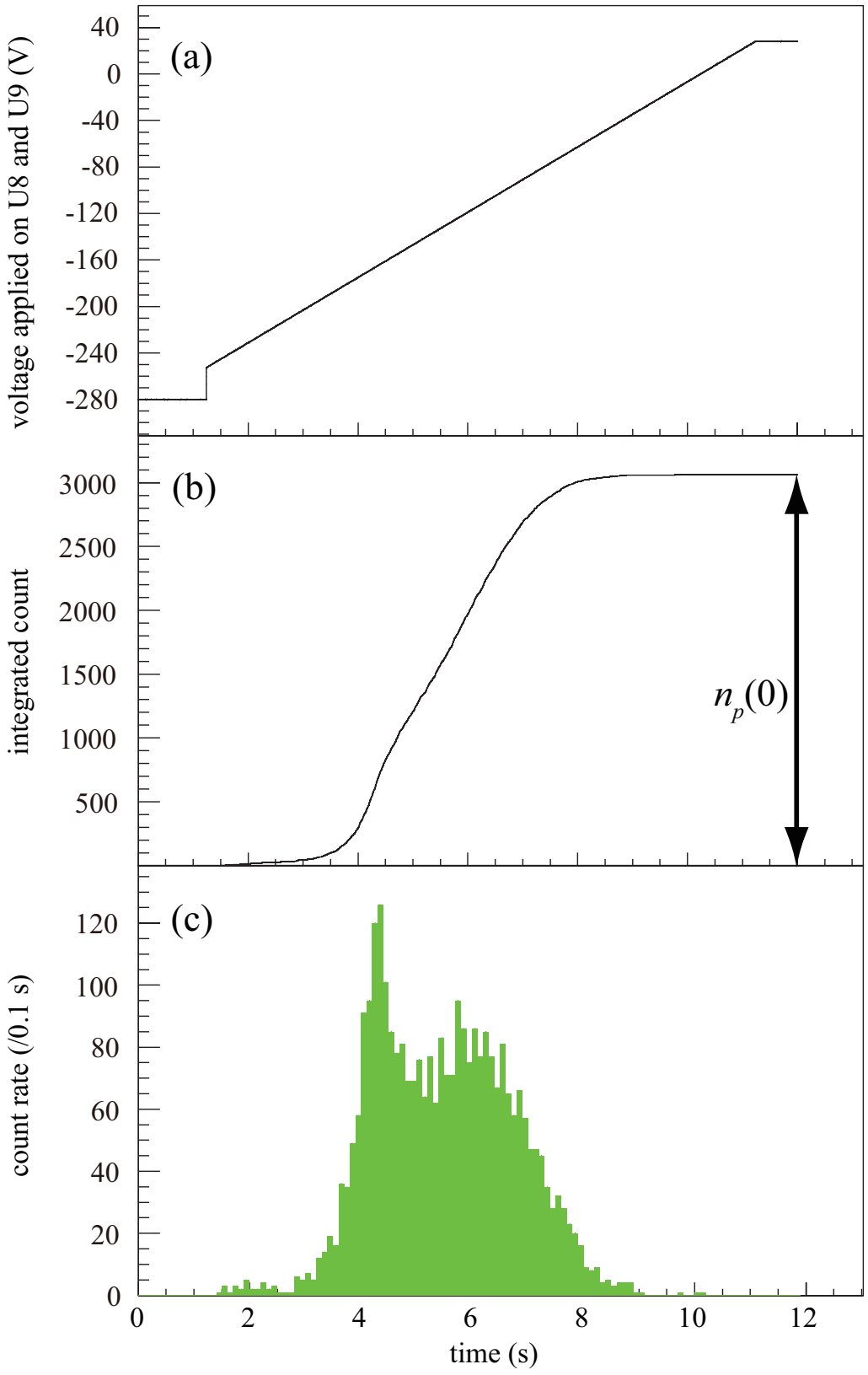

Figure 4.6: Voltage applied on the U8 and U9 electrodes (a). Integrated annihilation count taken by the track detector (b). The $n_p(0)$ in the figure is total number of annihilation signal during the extraction which is proportional to the number of antiprotons confined in the cusp trap. Annihilation count rate obtained by differentiating the integrated count (c).

in the cusp trap and the stacking number in the antiproton catching trap. When the stacking number was five, about 1.3 million antiprotons were confined in the cusp trap.

On the other hand, by changing the timing to switch back the potential (t_w), we succeeded to adjust the number of antiprotons caught in the cusp trap. Figure 4.8 shows $N_p(0)$ as a function of t_w. The number of antiprotons was reduced to 1/7 when $t_w = 15$ μs instead of $t_w = 16.5$ μs, which was commonly used value.

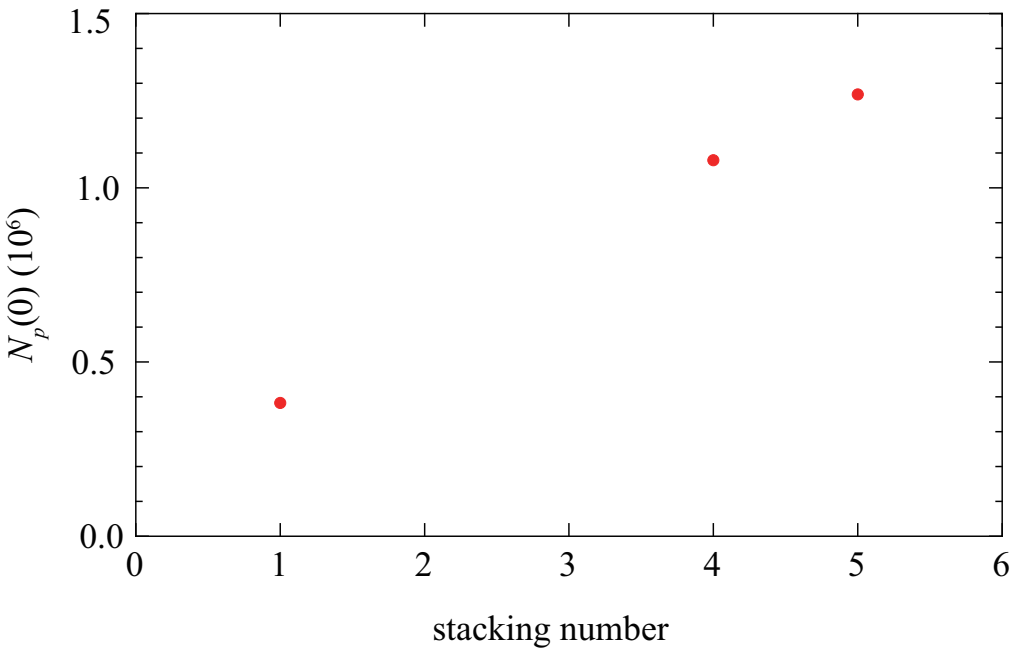

Figure 4.7: Number of antiprotons caught in a nested potential in the cusp trap as a function of the number of stacking operation in the antiproton catching trap. About 0.4 million antiprotons were caught in the cusp trap for one injection pulse from the AD. When the stacking number was five, as much as 1.3 million antiprotons were confined in the cusp trap.

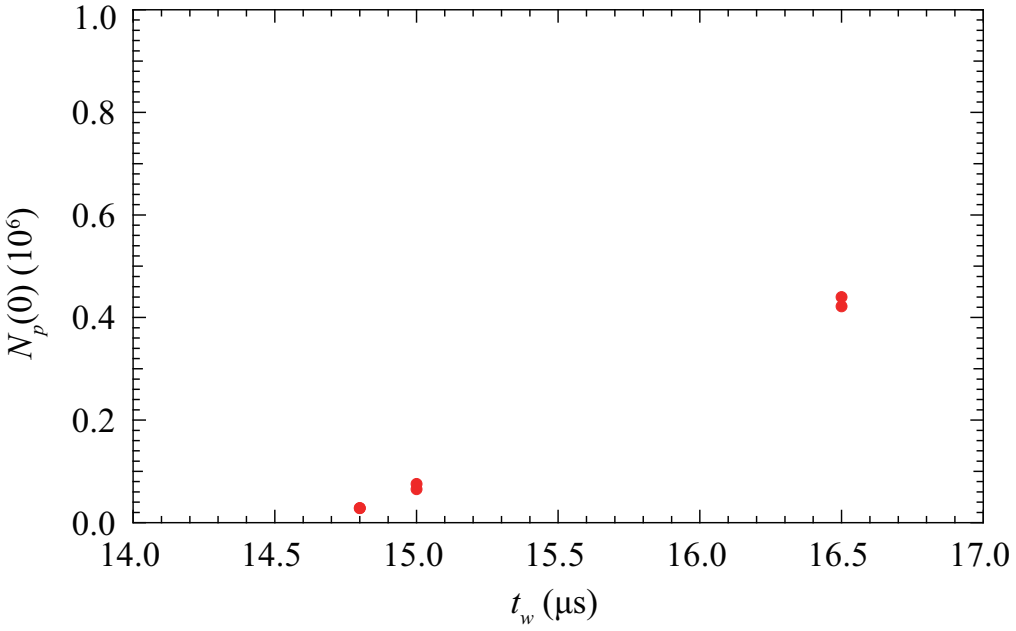

Figure 4.8: Number of antiprotons caught in a nested potential in the cusp trap as a function of t_w. By changing t_w, the number of antiprotons in the cusp trap can be controlled.

4.3 Confinement time of antiprotons in the cusp trap

As described in section 3.4.4, although the antiproton itself is a stable particle and do not annihilate in complete vacuum, in real experiments, it annihilates with residual gases. Since it takes at least several seconds for the production of antihydrogen in our condition and annihilation signals of antiprotons make background to the signal from the antihydrogen, how long antiprotons can be confined in the cusp trap is an important issue. Consequently, we define an effective confinement time (T_{conf}) and measured it under various and practical conditions as below.

1. Catch antiprotons in the cusp trap with pre-loaded electrons for the cooling[3].
2. Keep them for t_{keep} s with monitoring the annihilations by the track detector.
3. Extract remaining antiprotons slowly and count their number.
4. Obtain the confinement time (T_{conf}) by the equation[4]

$$T_{conf} = \frac{-t_{keep}}{\log(1 - \frac{n_p(t_{keep})}{n_p(0)})}, \tag{4.1}$$

   where $n_p(t)$ is the integrated annihilation count at time=t[5]

Normally, we set t_{keep}=300 s.

[3]As shown in figure 3.62, the mean free time of antiprotons varies depending on the energy of antiprotons We are interested in the confinement time of antiprotons whose energy is low since the production rate of antihydrogen atoms increases as described in section 2.4. Thus antiprotons were cooled by pre-loaded electrons down to sub-electron volt where the expected mean free time get insensitive to the energy of antiprotons.

[4]This equation assumes exponential decrease of the number of antiprotons remaining in the trap

[5]We define the origin of the time as the injection timing of antiprotons from the catching trap.

achieved confinement time of antiprotons

Figure 4.9 shows integrated annihilation count (top) and annihilation rate per 1 s (bottom) as a function of the time. Confinement time in this case was as long as T_{conf}=4800 s. Considering the discussion in section 3.4.4, the vacuum in the cusp trap was expected to be around 1×10^{-13} Torr. In addition, from measured count rate and detection efficiency, annihilation rate of the antiprotons in the cusp trap was about 100 to 200 per second, which was expected to be well below the signal level in our production and detection method of the antihydrogen atoms (see chapter 6).

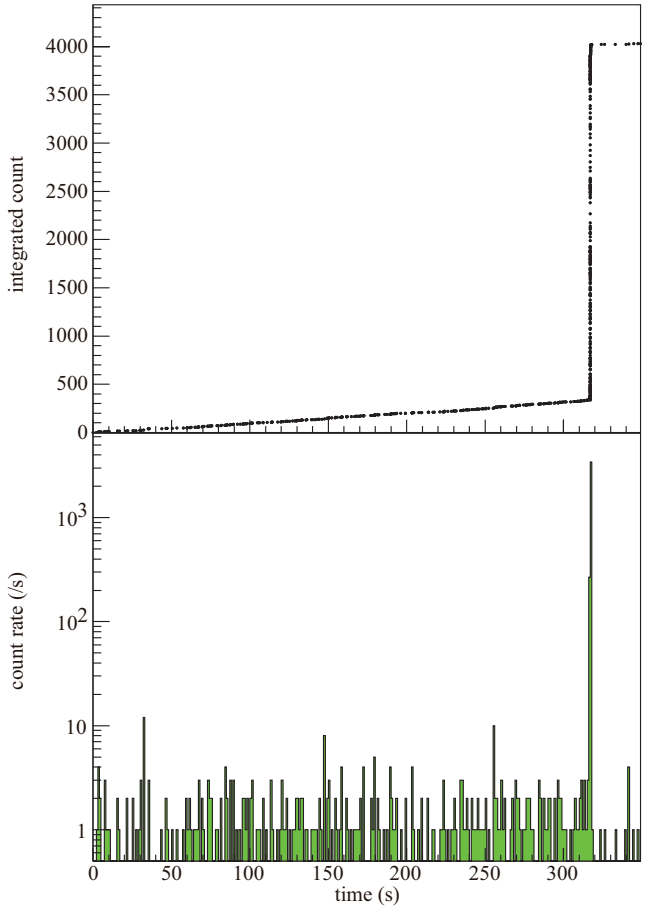

Figure 4.9: Integrated annihilation count (top) and count rate per 1 s (bottom) as a function of time. In this case, T_{conf}= 4800 s. Most of the antiprotons did not annihilate with residual gases and extracted after 300 s of confinement in the cusp trap.

stability in nested potential

Figures 4.10 and 4.11 show the confinement time of antiprotons in a harmonic potential and in a nested potential[6] respectively. In the harmonic potential case, T_{conf}=4300 s and in the nested potential case T_{conf}=2700 s. Although the T_{conf} in the nested potential is shorter than that of the harmonic potential case, still the value is well acceptable and no significant loss of the antiprotons was observed stem from the nested potential configuration. These proofs of stable and long-time confinement of antiprotons in the nested potential, which was used in the production of the antihydrogen atoms, was an important step.

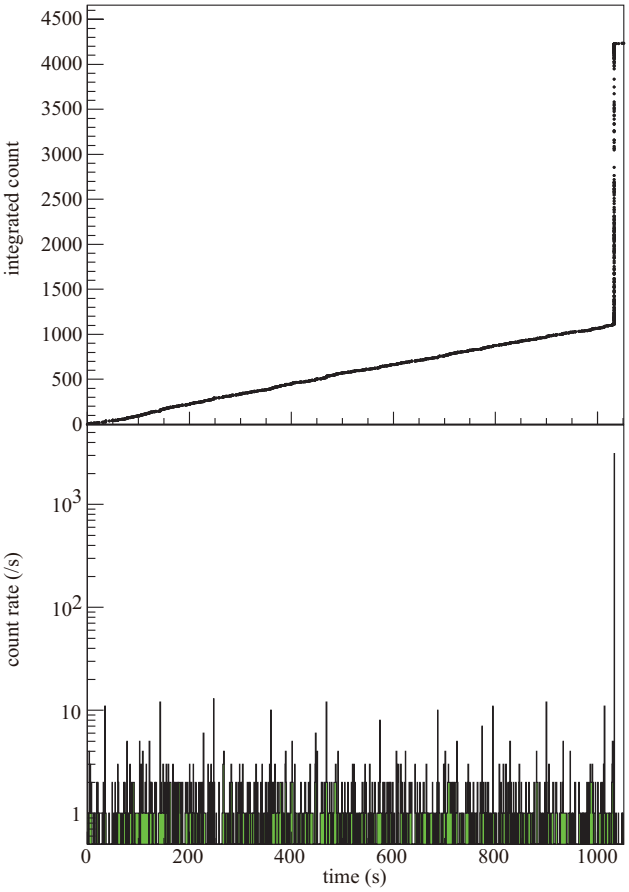

Figure 4.10: Integrated annihilation count (top) and count rate per 1 s (bottom) as a function of time. Antiprotons were confined in a harmonic potential, t_{keep}=1000 s and T_{conf}=4300 s.

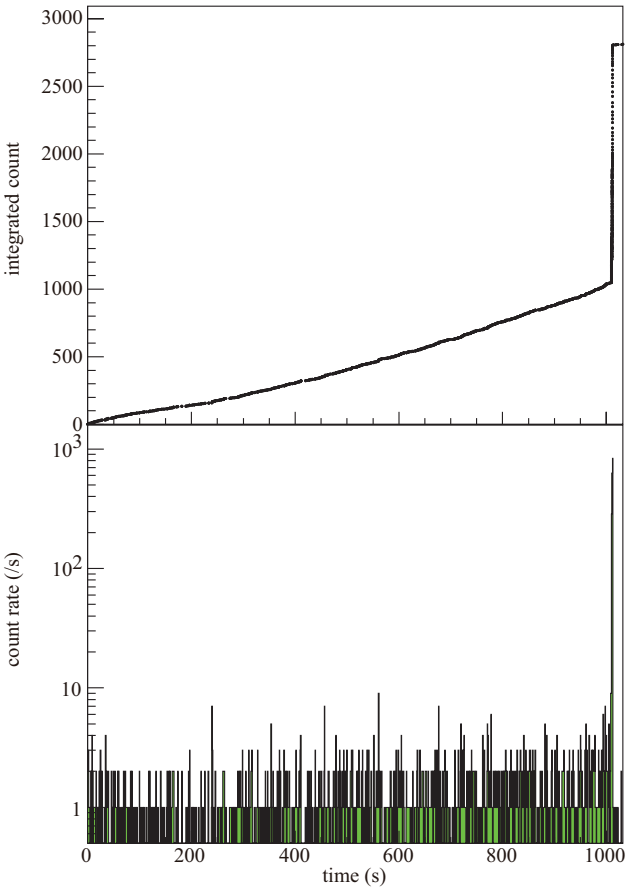

Figure 4.11: Integrated annihilation count (top) and count rate per 1 s (bottom) are shown as a function of time. Antiprotons were confined in a nested potential, t_{keep}=1000 s and T_{conf}=2700 s.

[6]In this case, t_{keep}=1000 s.

effect of positron stacking operation

Change of the T_{conf} before and after positron stacking operation in the cusp trap was examined. As is described in section 3.2, the positron accumulator used the buffer gas for the accumulation of positrons and the vacuum in the accumulator was nearly $1 \times 10^{-6} Torr$ Consequently, inflow of the gases from the positron accumulator to the cusp trap at the time of positron transport was inevitable. To evaluate the effect of the inflow of the gases on T_{conf}, we measured the confinement time before and after positron stacking operation in the cusp trap. Figure 4.12 shows the data before the stacking operation. In this case T_{conf}=2600 s. On the other hand, figure 4.13 shows the data after 40 times of the positron stacking operation. In this case T_{conf}=2000 s. Care must be taken that also in this run, positrons were not confined in the trap.

As anticipated, the confinement time got worse from 2600 s to 2000 s, after the stacking operation, however, the difference was small and the confinement time was still acceptable value.

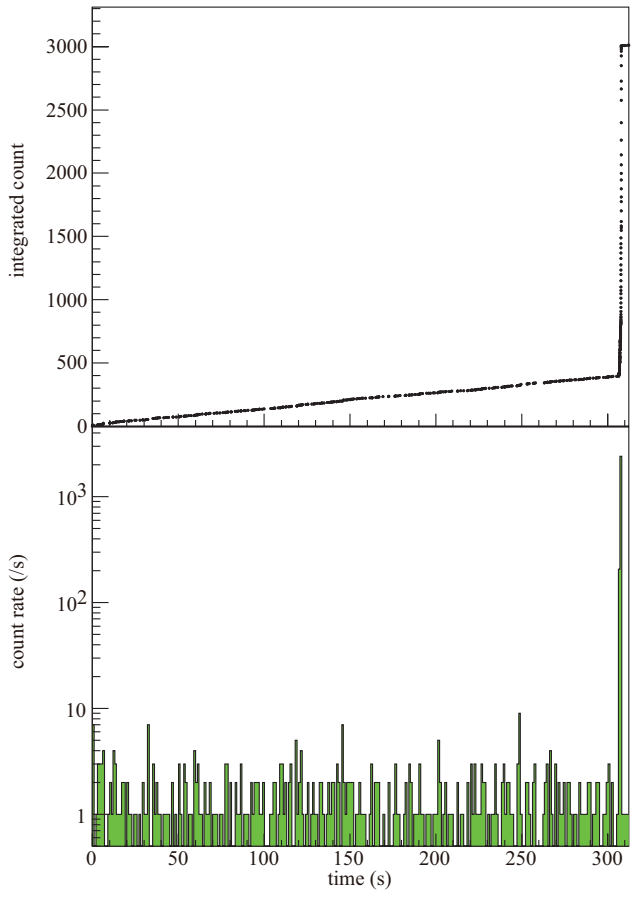

Figure 4.12: Integrated annihilation count (top) and count rate per 1 s (bottom) as a function of time. Antiprotons were confined in a nested potential, t_{keep}=300 s and T_{conf}=2600 s. This data was taken before the positron stacking operation in the cusp trap.

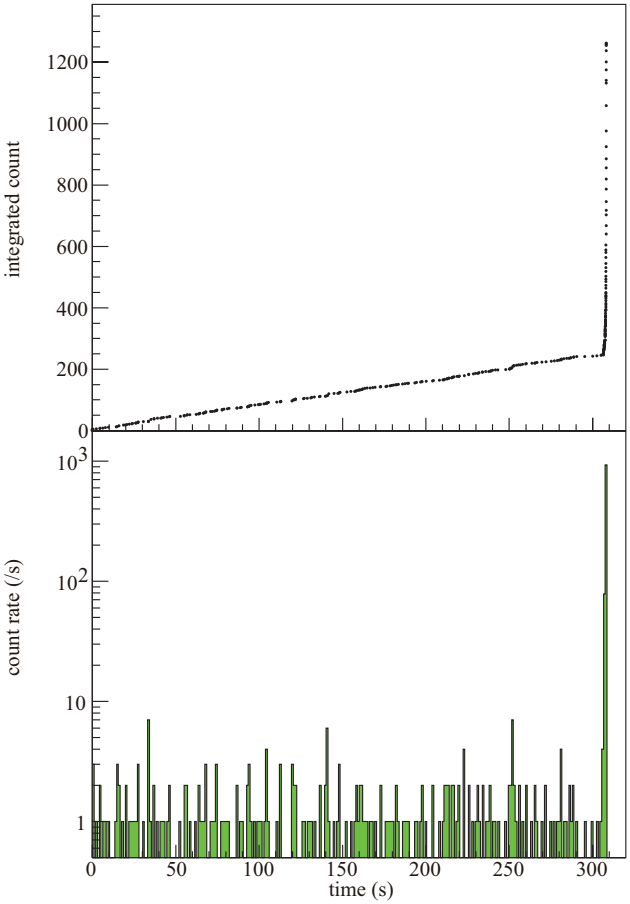

Figure 4.13: Integrated annihilation count (top) and count rate per 1 s (bottom) as a function of time. Antiprotons were confined in a nested potential, t_{keep}=300 s and T_{conf}=2000 s. This data was taken after 40 times of the positron stacking operation in the cusp trap.

MRE and bore tube temperature dependence

As described in section 3.4.4, the environmental temperature and the vacuum is correlated closely. Thus the confinement time of antiprotons at different MRE and bore temperature was measured. Figure 4.14 shows the data when the MRE temperature was 20.6 K, and the bore tube temperature was 6.8 K. The confinement time was as short as T_{conf}=370 s. On the other hand, figure 4.15 shows the data when the MRE temperature was 16.5 K and the bore tube temperature was 6.2 K, which is ordinary value. Although the differences of the temperature were only 4 K for the MRE and 0.6 K for the bore tube, the confinement time was as long as T_{conf}=2200 s.

We note that, from the figure 3.62, the confinement time of the antiproton is a few hundred second even when the vacuum is 1×10^{-12} Torr. Thus the difference of the vacuum can not be measured by ordinary vacuum gauges.

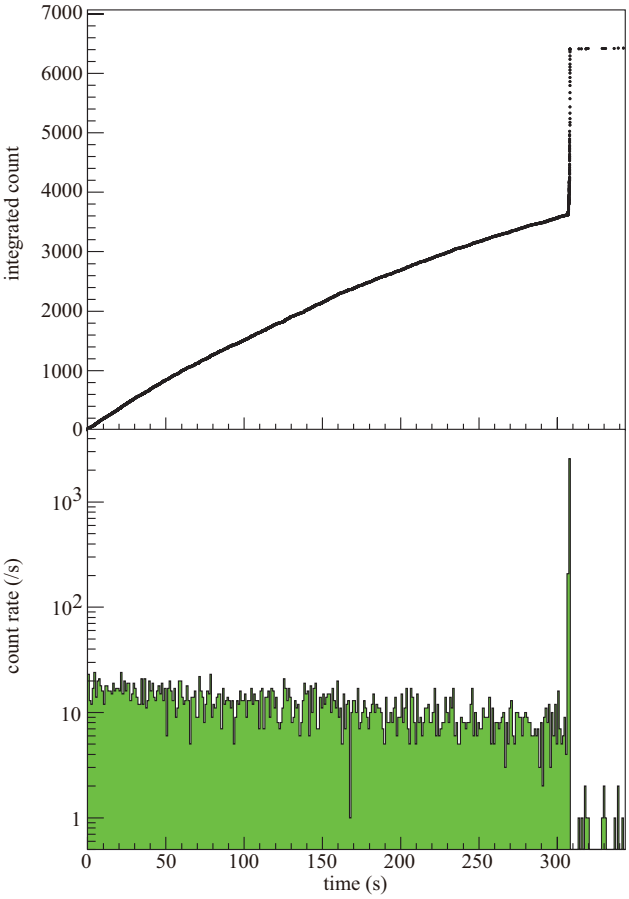

Figure 4.14: Integrated annihilation count (top) and count rate per 1 s (bottom) as a function of time. Antiprotons were confined in a nested potential, t_{keep}=300 s and T_{conf}=370 s. The temperature of the MRE was 20.6 K and that of the bore tube was 6.8 K.

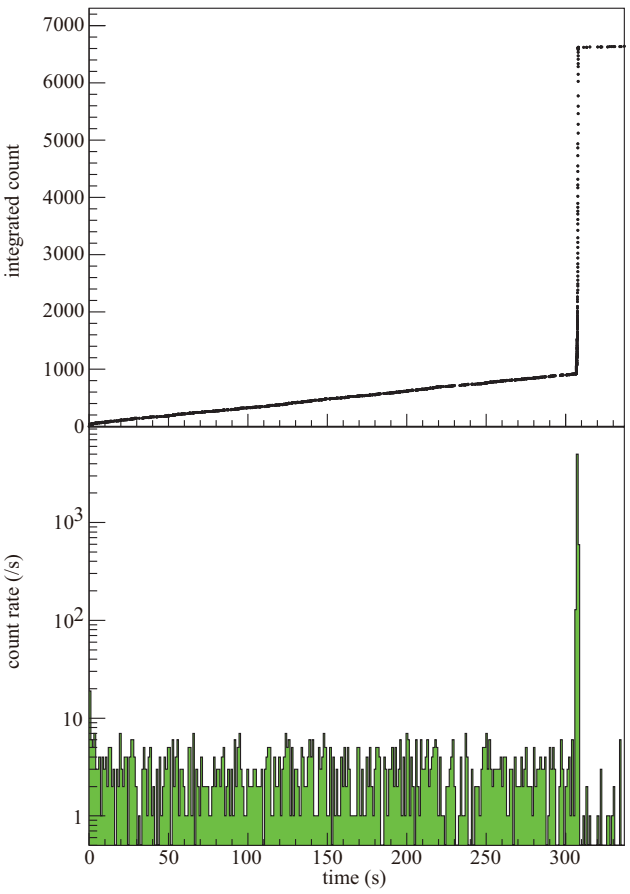

Figure 4.15: Integrated annihilation count (top) and count rate per 1 s (bottom) as a function of time. Antiprotons were confined in a nested potential, t_{keep}=300 s and T_{conf}=2200 s. The temperature of the MRE was 16.5 K and that of the bore tube was 6.2 K.

outgassing treatment by opening the downstream thermal shield

Even though the temperature of the system was kept required value, the confinement time of antiprotons gradually got worse as the number of positron stacking operation in the cusp trap increased. Thus, the temperature is not a satisfactory condition for the long-time confinement of antiprotons. From trials, it is considered to be a necessary condition. However, practically the deterioration of the confinement time was able to be recovered by outgassing treatment of about 20 minutes; just opening the downstream thermal radiation shield. Figures 4.16 and 4.17 show the data before and after the outgassing treatment respectively. In the former case, $T_{conf} = 570$ s and in the latter case, $T_{conf} = 1700$ s.

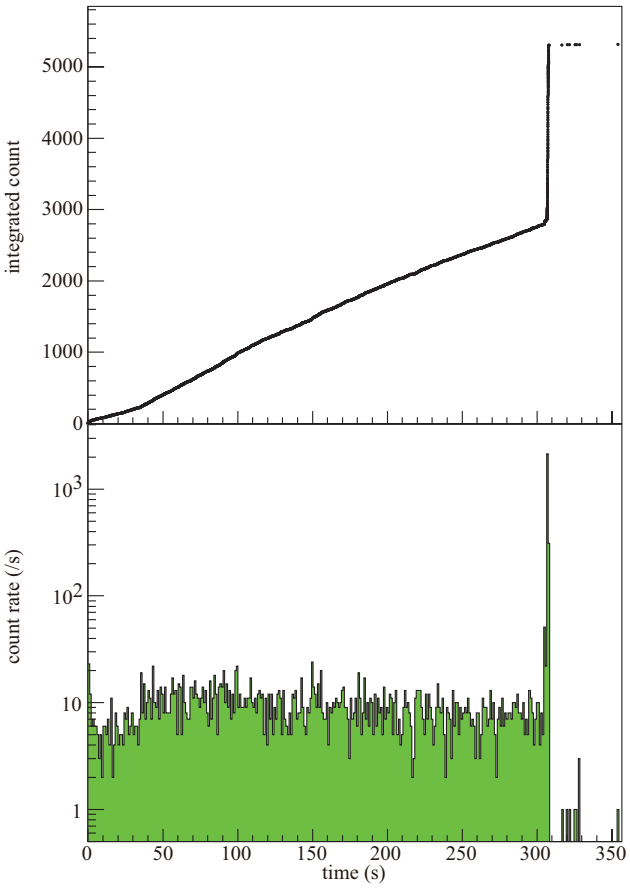

Figure 4.16: Integrated annihilation count (top) and count rate per 1 s (bottom) as a function of time. Antiprotons were confined in a nested potential, t_{keep}=300 s and T_{conf}=570 s. The data was taken before the outgassing treatment.

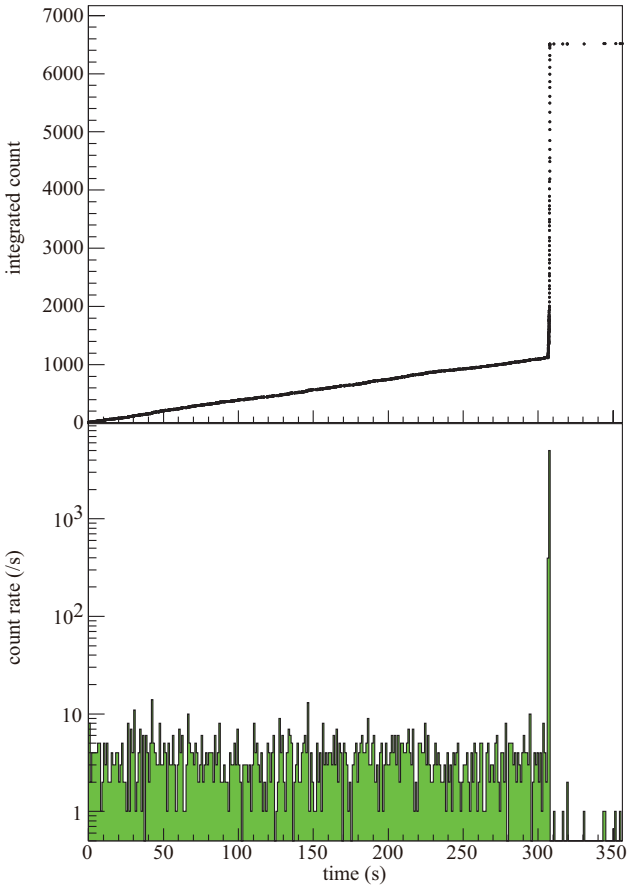

Figure 4.17: Integrated annihilation count (top) and count rate per 1 s (bottom) as a function of time. Antiprotons were confined in a nested potential, t_{keep}=300 s and T_{conf}=1700 s. The data was taken after the outgassing treatment of about 20 minutes.

summary of confinement time

1. Stable confinement of antiprotons in the cusp trap was successfully achieved.
2. The confinement time T_{conf} was typically more than 2000 s. This considered to be enough for the production and detection of the antihydrogen atoms.
3. No abrupt loss of the antiproton was observed both in the harmonic and nested potential.
4. The effect of the inflow of the gases from the positron accumulator during the transport of positrons was limited and acceptable.
5. Slight change of the environmental temperature affect the T_{conf} strongly, however, care must be taken that the temperature was not a satisfactory condition but a required condition.
6. By outgassing treatment of the bore tube and the MRE, the deteriorated T_{conf} was able to be recovered.

4.4 Position calibration of the 3D detector

As described in section 3.5.1, the 3D detector used to detect the antihydrogen atoms can identify the position of the antiproton annihilation. We carried out the calibration of the detector using antiprotons, to obtain position informations correctly. Figures 4.18 (a), (b), and (c) show the cross sectional drawing of the MRE of the cusp trap, potential curves to confine antiprotons, and annihilation position distribution of antiprotons in axial (z) direction. First, antiprotons from the catching trap were captured, immediately moved to a narrow potential drawn by purple curve whose bottom was the U7 electrode. They were cooled by the pre-loaded electrons to settle them down to the bottom of the potential well and kept for 300 s. The annihilation signals were recorded, positions of them were reconstructed and the histogram was fitted by the Gaussian function to obtain the central position of the annihilation distribution. Then antiprotons were captured, moved to another potential, and the same measurement was carried out. Repeating the measurement, we obtained the central positions of the annihilation distribution for several confinement potential wells. Figure 4.19 shows the central positions of the annihilation distribution (i.e. where the antiprotons actually were) as a function of the bottom position of the confinement potential well (i.e. where the antiprotons were expected to be). The line in the figure is a linear fit of the data. The inclination of the line was 1.00 and the offset was 5.6 mm. By this way, the 3D detector was calibrated in z direction.

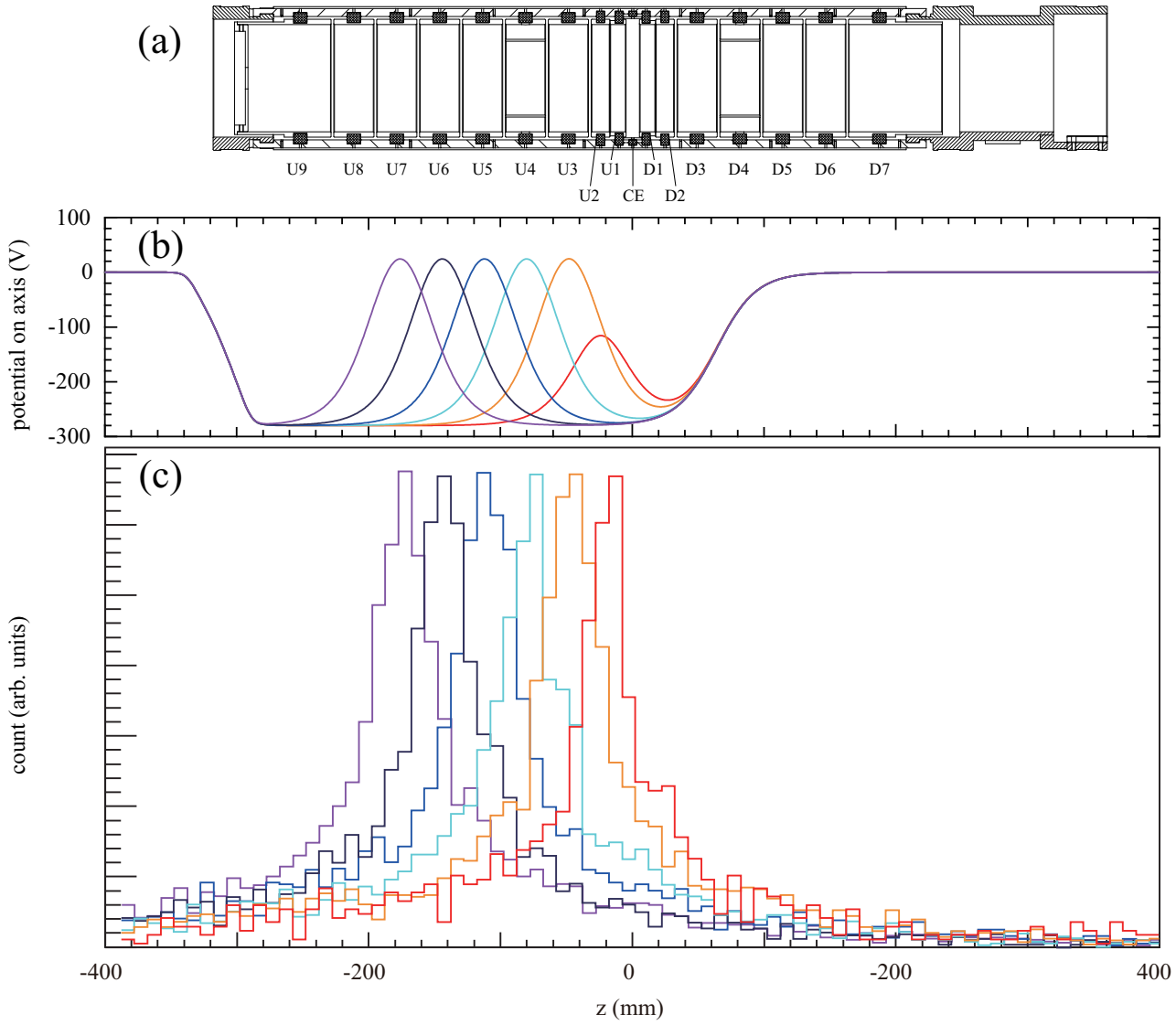

Figure 4.18: A cross sectional drawing of the MRE of the cusp trap (a), potential curves to confine antiprotons (b), and the annihilation distributions of antiprotons (c). To calibrate the 3D detector, we confined antiprotons in a variety of potentials whose bottom positions differ each other and observed position distribution of annihilations signals. Antiprotons were cooled by pre-loaded electrons to settle them down to the bottom of the potentials and confined for 300 s in each potential.

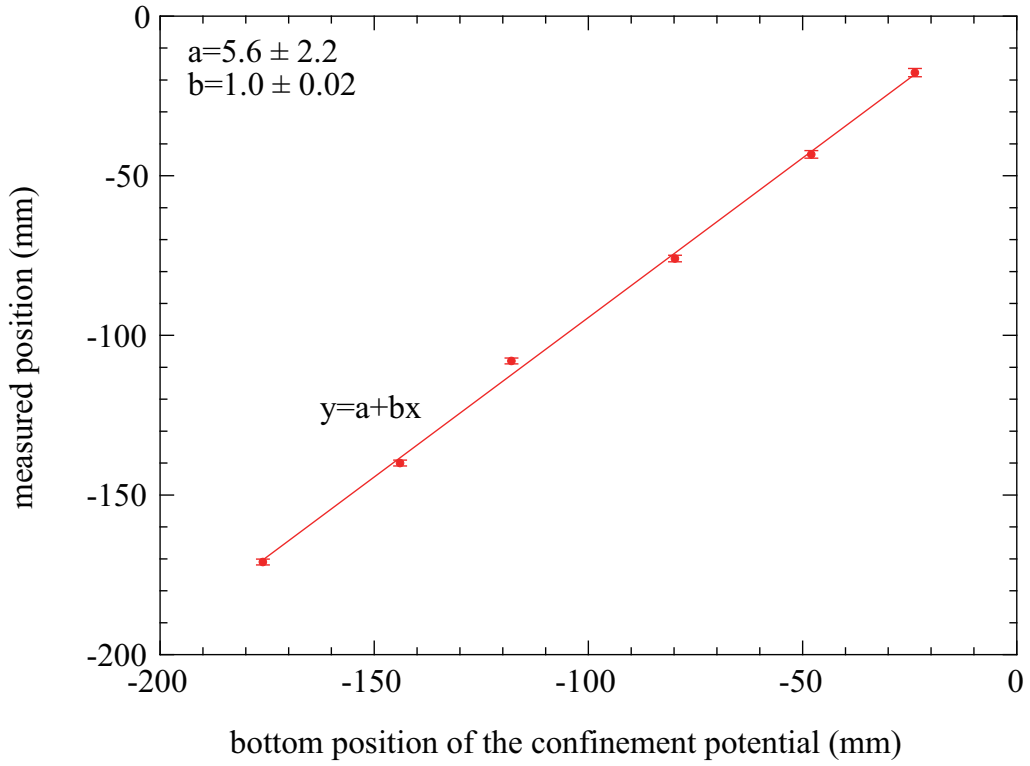

Figure 4.19: Measured central positions of the annihilation distribution of antiprotons as a function of the bottom position of the confinement potential well. The line in the figure is a linear fit of the data.

Chapter 5

Confinement of positrons in the cusp trap

In this chapter, we describe transport of the positrons from the positron accumulator to the cusp trap and properties of them in the cusp trap. In section 5.1, transport simulation, operation, and results of positrons from the accumulator to the cusp trap are described. In section 5.2, two techniques, i.e. stacking operation of positrons and compression of positron cloud in the cusp trap, are described to prepare high density positrons for the efficient production of antihydrogen atoms. In section 5.3, results of the positron temperature measurement are shown. The temperature of the positrons is a key parameter as discussed in section 2.4.

5.1 Transport low energy positrons to the cusp trap

trajectory calculation

For the efficient transport of positron, we carried out trajectory simulations. Since the transport line of positrons was not straight but have two corners (see section 3.3.2), three dimensional calculation was required for the trajectory simulation. In the present work, Particle studio [70] was used for the simulation. Figure 5.1 shows a result of a trajectory simulation. Initial energy of positrons was 100 eV and the initial position distribution was -3 mm $\leq x \leq 3$ mm and -3 mm $\leq y \leq 3$ mm, which was roughly the same as the expected size of positrons in the accumulator. In this simulation, in addition to the magnetic field of the positron accumulator, the cusp trap, and the transport coils, magnetic field of the antiproton trap was taken into account since the stray field of the antiproton catching trap was considered to affect

the trajectory of positrons. From the simulation, optimised current settings of the positron transport coils were determined as shown in table 5.1.

	coil current (A)	magnetic field (mT)
pos coil 1	50	50
pos coil 2	72	80
pos coil 3	72	80
pos coil 4	72	80
pos coil 5	90	80
coil B	50	35

Table 5.1: Optimised current settings and corresponding magnetic fields of transport coils used for positron transport.

potential manipulation

Figure 5.2 shows the potential curves in the positron accumulator. Positrons were accumulated in the bottom of the potential well drawn by blue curves. After the accumulation, the potential curve was changed to the black one for the preparation for extraction. Then the potential curve was changed to the red one by applying pules voltage to the M13 and M14 electrodes and positrons were extracted as a pulse beam.

Figure 5.3 shows the potential curves in the cusp trap. To catch the positron beam, the potential was switched from the blue curve to the red curve at the timing of the positron beam extraction, then it was switched back to the blue curve before positrons were reflected and escaped from the cusp MRE. The operation was similar to that to catch antiprotons in the cusp trap. However, single pulse of the positron beam was not able to provide enough number of positrons, stacking operation[1] in the cusp trap was required. Thus certain hight of the potential wall of the upstream side remained not positrons already confined in the cusp trap to escape.

[1]We defined the meaning of the stacking operation in section 3.1.6

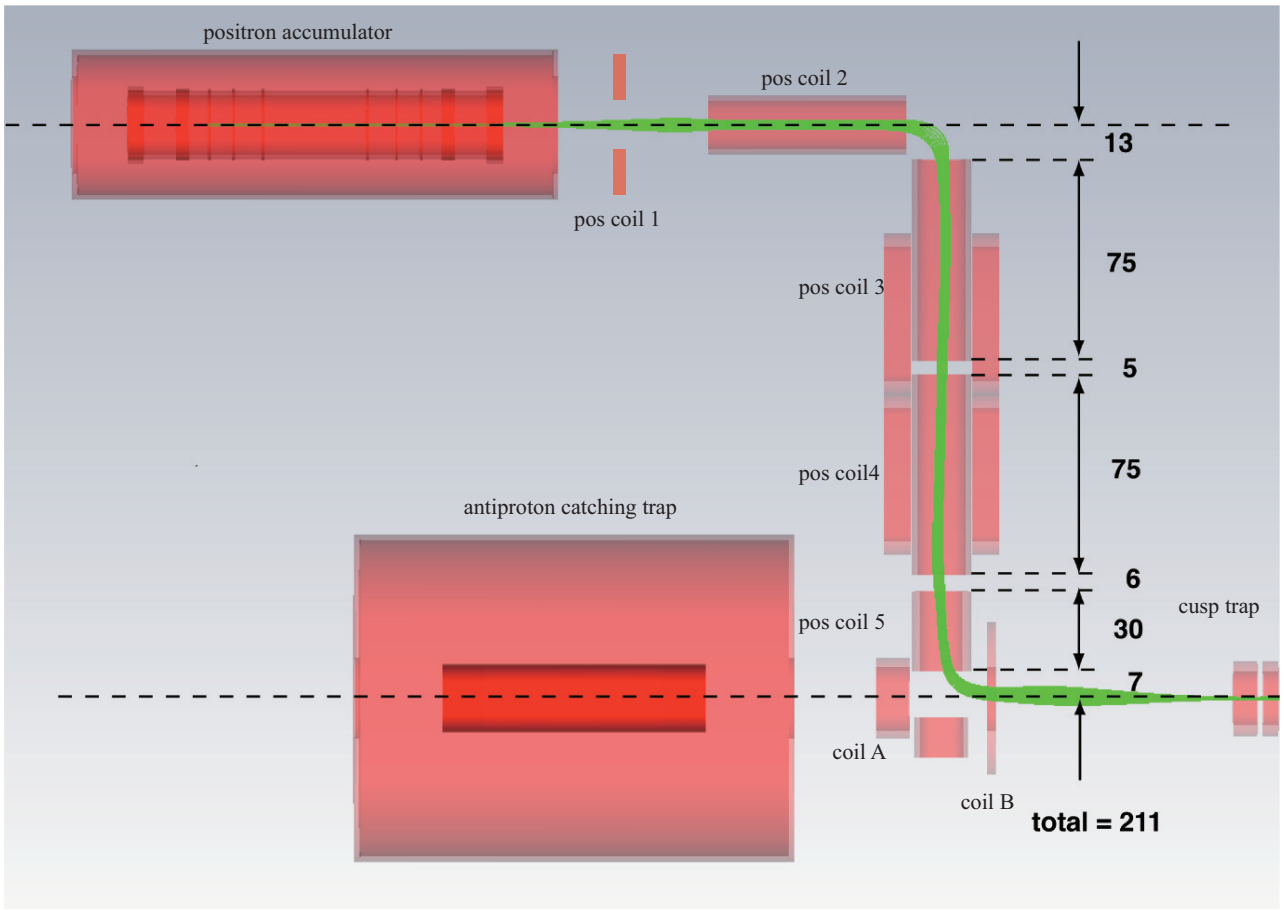

Figure 5.1: A result of a trajectory simulation. Initial energy of positrons was 100 eV and the initial position distribution was -3 mm $\leq x \leq 3$ mm and -3 mm $\leq y \leq 3$ mm. As can be seen from trajectories (green), positrons were successfully transported to the cusp trap guided by coils.

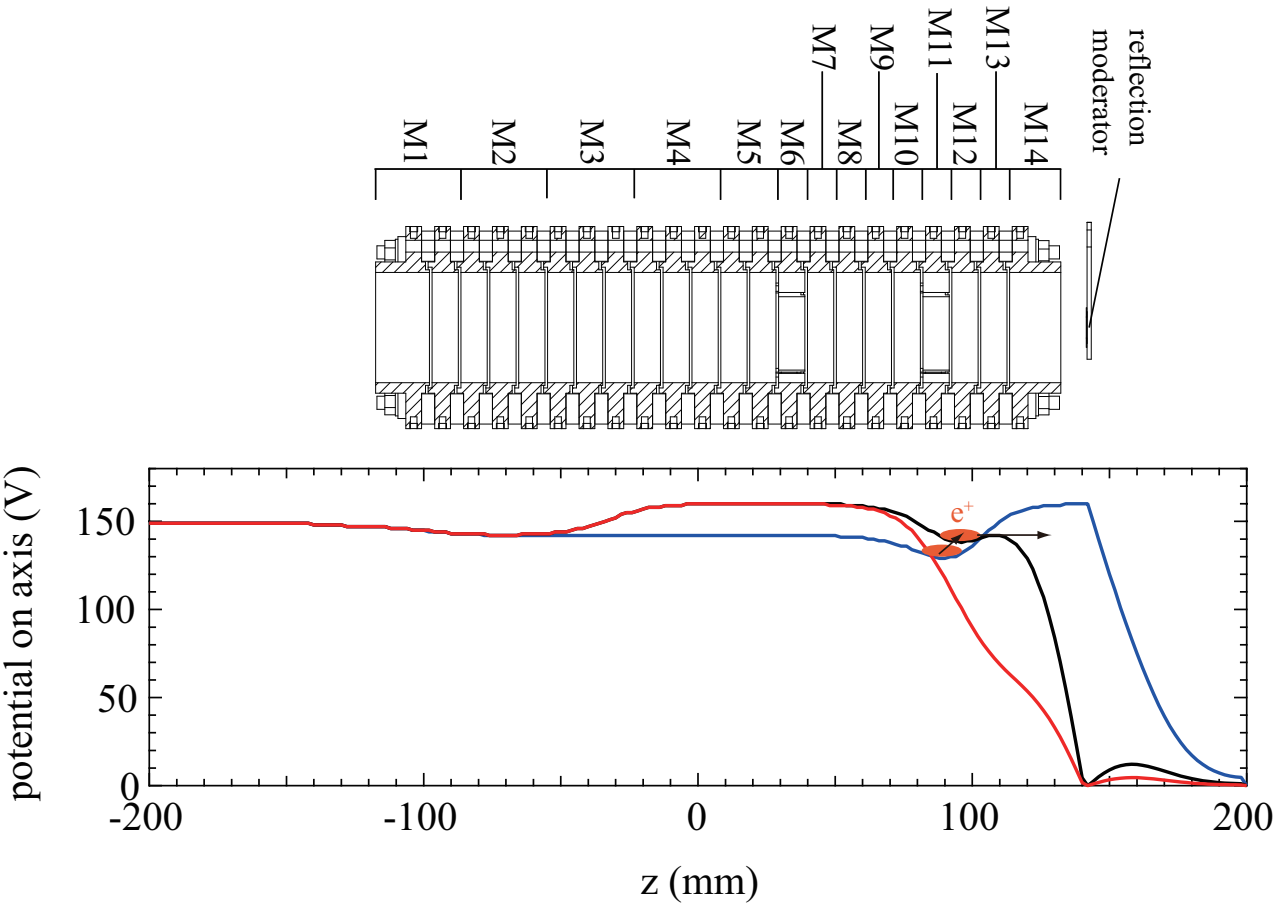

Figure 5.2: Potential curves in the positron accumulator; during accumulation (blue), preparation for extraction (black), and extraction (red).

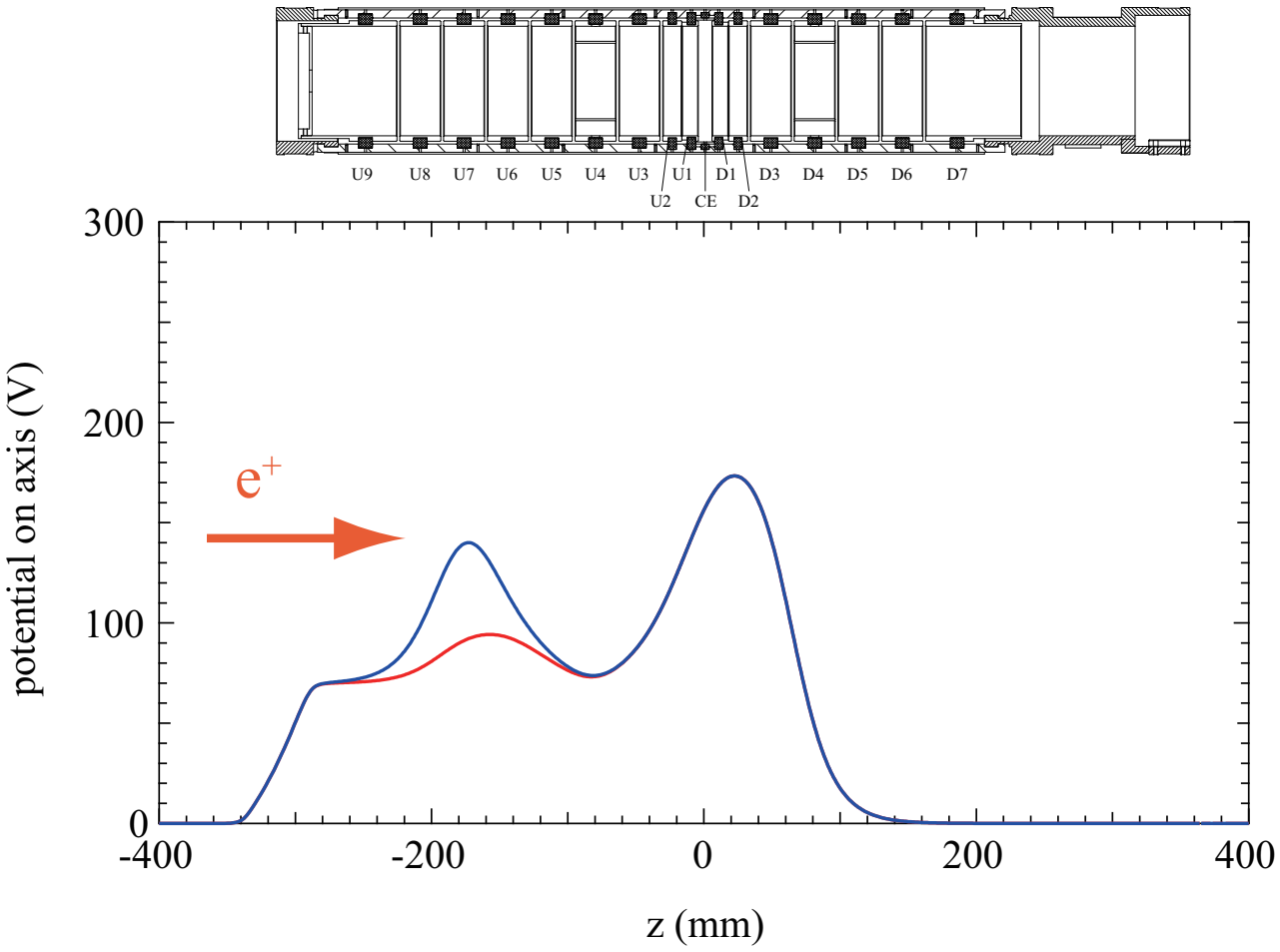

Figure 5.3: Potential curves in the cusp trap to catch positrons. The potential was switched from the blue curve to the red curve at the timing of the positron beam extraction, then it was switched back to the blue curve before positrons were reflected and escaped from the cusp MRE.

catch timing

To maximize the number of the positrons caught in the cusp trap, timing to change the potential was scanned. Figure 5.4 shows the number of positrons caught in the cusp trap per one injection as a function of the setting of the delay generator, which determines the timing. Since delays originated from the cable length were a few hundred nano second, which was comparable to the TOF of the positrons from the accumulator to the cusp trap, the values of the horizontal axis in the figure 5.4 did not coincide with the value of the TOF. As can be seen from the figure, there is a peak around 1030 ns. When we used this value, total transport efficiency, which was a ratio of the number of positrons caught in the cusp trap versus the number of positrons extracted from the positron accumulator, was about 40 % to 50 %. The number of the positrons caught in the cusp trap per one injection was 1×10^6.

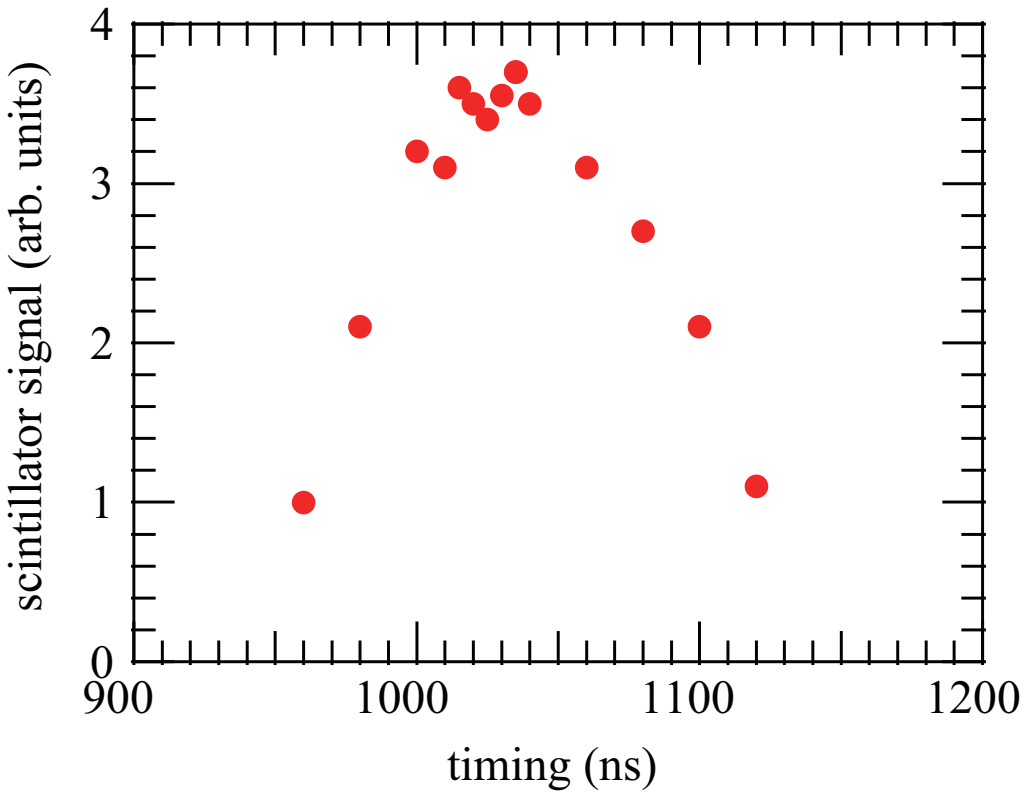

Figure 5.4: The number of positrons in the cusp trap as a function of the setting of the delay generator. There is a peak around 1030 ns and we used this value.

5.2 Manipulations to prepare high density positrons in the cusp trap

As was discussed in section 2.4, the recombination rate of the antihydrogen atoms is proportional to the density of positrons in the radiative recombination process or to the square of the density of positrons in the three body recombination process. Thus, if we can prepare higher density cloud of positrons in the cusp trap, the production rate of the antihydrogen atoms increases. On the other hand, the number of the positrons extracted from the accumulator and the transport efficiency of them have already been optimized as described before. Thus to increase the density of positrons in the cusp trap, some operations in the cusp trap are required.

There are two possibilities. One is the stacking operation which can increase the number of positrons in the cusp trap and the other is the compression of the positron cloud by applying RF voltage on the segmented electrodes, which is called rotating wall technique.

stacking operation

Figure 5.5 shows the number of positrons caught in the cusp trap as a function of the number of the stacking operation. The number of positrons was measured as follows. Positrons in the cusp trap were extracted to the MCPPS detector and annihilated on the detector. Then the annihilation products were detected by a scintillator located near the MCPPS detector. Care must be taken that in the present configuration, the measured number of positrons decrease if a part of the positrons annihilate with the bore tube before reaching to the MCPPS detector since the solid angle to the scintillator decrease. This can happen when the cloud of the positrons in the cusp trap expanded before the extraction. Because the trajectories of positrons whose radial position were far from the axis of the magnetic field diverged largely when they were extracted to the region where the magnetic field was weak (see figure 3.53). Thus we measured the number of positron both when we compressed[2] the positron cloud and when we did not compress the positron cloud to discern whether the positrons were lost during the stacking operation or not.

As is seen in the figure, the number of positrons increased linearly until around 20 times stacking operation. However, if we did not compress the positron cloud, the number of

[2]Compression of the cloud of the positrons are described in next paragraph.

positrons was saturated. On the other hand, if we compress the cloud, the number of positrons increased at least 60 times stacking operation. Though the production rate of antihydrogen atoms increases with the density of positrons, considering required time to the stacking operation (50 s for one cycle), most of the antihydrogen production experiments were carried out with 40 or 60 times stacking operation in the present work.

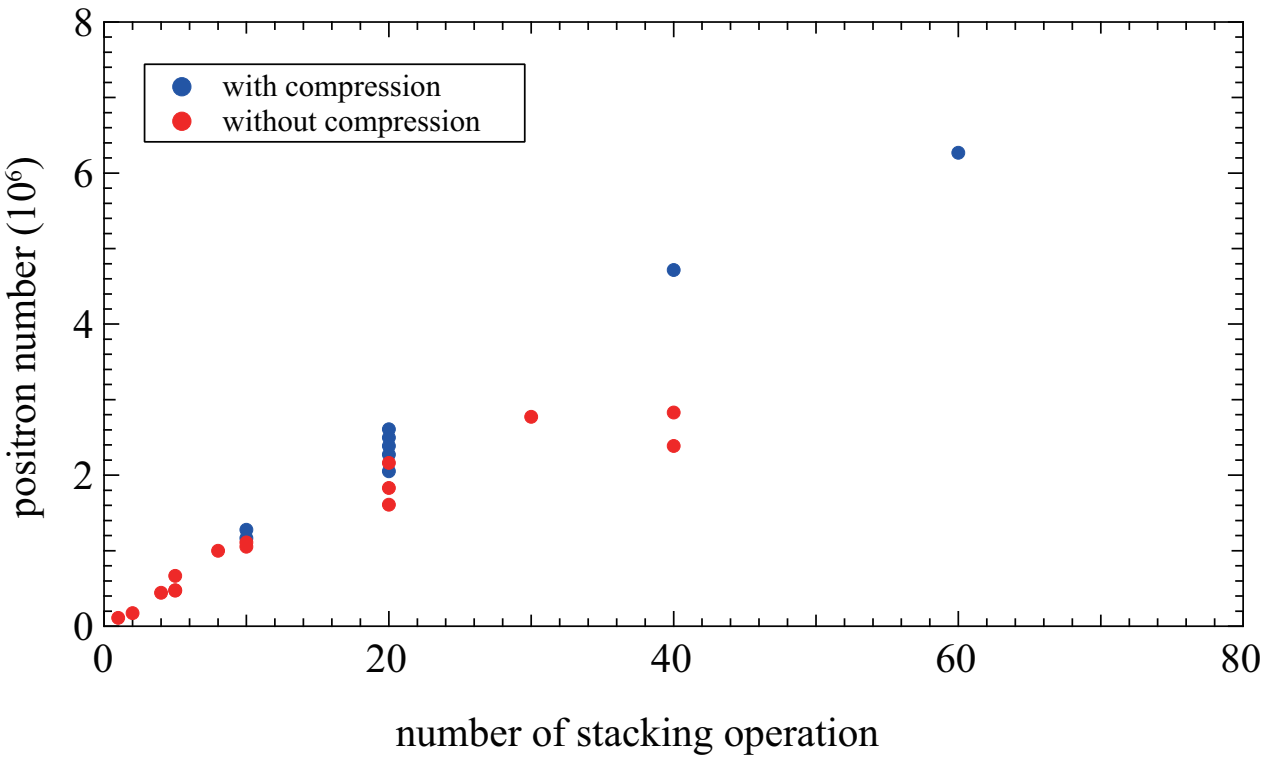

Figure 5.5: The number of positrons extracted from the cusp trap as a function of the number of the stacking operation; without compression (red circles), with compression (blue circles). If the cloud of positrons was not compressed, observed number of positrons looks saturated. This is mainly because positron cloud expanded during the stacking operation and a part of positrons hit the inner wall of the bore tube before reaching to the detector when positrons were extracted to measure their number.

Compression of positron cloud in the cusp trap

Since the production rate of the antihydrogen atoms depends on the density of positrons, if we can compress the positron cloud, the rate increases even the number of positrons in the cusp trap is the same.

Compression of the charged particle cloud by applying rotating electric field on the segmented electrode (rotating wall technique) has been proved to be a useful method [71, 72] A simple explanation of this technique is as follows.

1. A cloud of charged particles whose density is n_0 in the magnetic field B rotates at a frequency where Coulomb force and centrifugal force balance with confining force by magnetic field as shown in figure 5.6.

2. The equation of motion of a particle whose radial position is r can be written as

$$mr\omega_r^2(r) = -qE_r(r) + qr\omega_r(r)B \tag{5.1}$$

   where m and q are the mass and charge of the particle, $E_r(r)$ the electric field in radial direction created by other particles, and $\omega_r(r)$ angular frequency of the rotation of the particle.

3. This equation has two root.

$$\omega_r(r) = \omega_r^{\pm} = \frac{\omega_c}{2}\left\{1 \pm \sqrt{1 - \frac{2\omega_p^2}{\omega_c^2}}\right\} \tag{5.2}$$

   where ω_c is the cyclotron frequency given by $\omega_c = qB/m$ and ω_p the plasma frequency given by $\omega_p = \sqrt{\rho q^2/m\epsilon_0}$. As can be seen from the equation, the particle in the cloud rotates at a frequency independent of their radial position, which means that the cloud is considered to be "rigid". Thus $\omega_r^{\pm}$ are called rigid rotor frequency[3].

4. This fact leads to that the radius of the cloud can be controlled by applying the torque externally to the cloud and changing the $\omega_r^{\pm}$.

5. The torque can be generated by applying sinusoidal voltages whose phases are different by $\pi/2$ each other to the segmented electrodes as shown in figure 5.7.

[3] In the present work, $\omega_r^+ = 440$GHz and $\omega_r^- = 360$ kHz when $n = 1 \times 10^8/\mathrm{cm}^3$

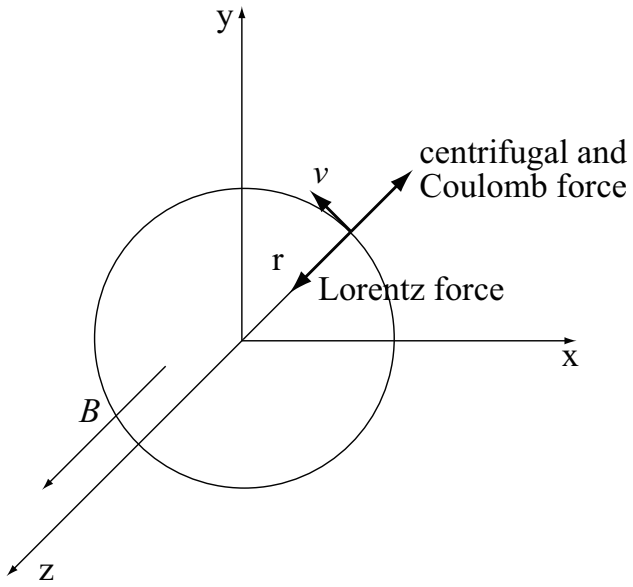

Figure 5.6: Forces exerted on the charged particles in the magnetic field. Particles rotate around the magnetic field axis and centrifugal force and Coulomb force balance with Lorenz force.

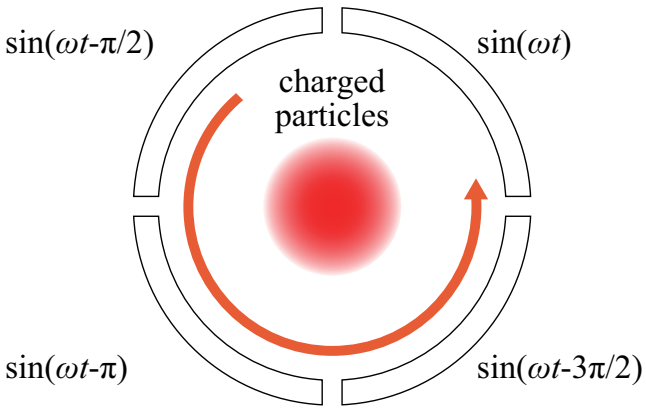

Figure 5.7: Concept of the rotating wall technique. Sinusoidal voltages whose phases are different by $\pi/2$ each other are applied on the azimuthally four-segmented electrodes and a rotating electric field is generated.

Although most of the foregoing works were carried out in the uniform magnetic field, we proved that this technique was also efficient for the electron cloud in the cusp trap whose magnetic field is not uniform [73, 74]. However, applicability of the technique to the positron cloud whose initial number, density and radius is different from those of the electron cloud, have been an open question. Thus we applied this technique to the positron cloud and surveyed the parameters (frequency and amplitude).

Figure 5.8 shows images of the positron cloud extracted from the cusp trap for several different amplitude of the rotating electric field V_{rot}. In these measurements, the number of staking operation was 40, rotating electric field (frequency was swept from 12 MHz to 13 MHz) was applied after the first injection of positrons and continued just before the extraction. Then positrons were extracted to the MCPPS detector and the image was recorded by the CCD camera.

When the rotating electric field was not applied, the image of the extracted positron cloud covers full of the screen. Considering the ratio of the magnetic field strength at the detector and at the confinement region in the cusp trap (see section 3.53), the diameter of the cloud in the trap was more than 6 mm. On the other hand, with increasing the V_{rot}, the image shrinks and the diameter on the screen reaches as small as 5 mm in $V_{rot} = 10$ V case. This means that the diameter in the trap was 0.6 mm and more than 8 times compression of the diameter were achieved. By this way, we succeeded to prepare a high density (10^8 /cm^3) positron cloud in the cusp trap.

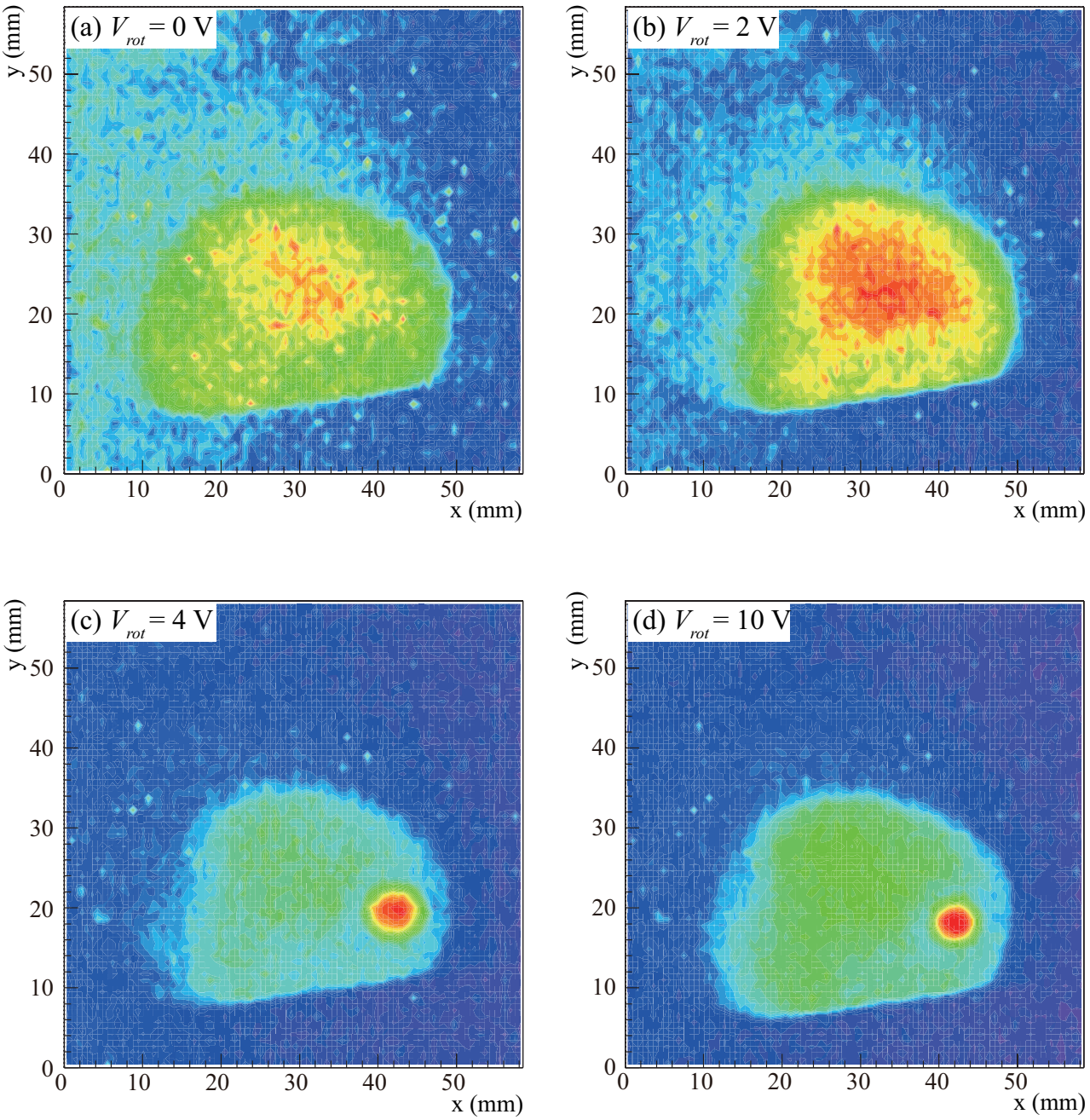

Figure 5.8: Images of the extracted positron cloud; V_{rot} = 0 V (a), V_{rot} = 2 V (b), V_{rot} = 4 V (c), V_{rot} = 10 V (d). As increasing V_{rot}, the cloud of positrons shrinks. When V_{rot}=10 V, the diameter of the cloud at the detector was 5 mm and in the trap 0.6 mm.

expansion of positron cloud

Although we succeeded to compress the positron cloud in the cusp trap, how long the compressed configuration was able to be kept was not clear. In addition, it was also not clear whether the cloud expanded or not by the injection of antiprotons.

Figure 5.9 is an image taken 60 s after the end of the rotating electric field application. Antiprotons were not injected in this case. The diameter of the positron cloud expanded in a certain degree and it was about 13 mm on the screen. On the other hand, figure 5.10 is an image taken after the same time but antiprotons were injected after the end of the rotating electric field application. The image covers full of the screen.

From these images, the injection of antiprotons accelerates the expansion of the positron cloud although the cloud expands in a certain degree without injection of antiprotons. On the other hand, according to the results of ALPHA [75], the expansion was not observed. One possible explanation is the difference of the ratio of the number of positrons and antiprotons. In our experiment, the ratio (number of positrons/number of antiprotons) is about 10 (see chapter 6). In ALPHA experiment, it is about 100. Thus the perturbation to the positrons by antiprotons is larger in our experiment than in ALPHA's experiment. We note that the density of the positrons during the mixing process was not as high as 10^8 /cm^3.

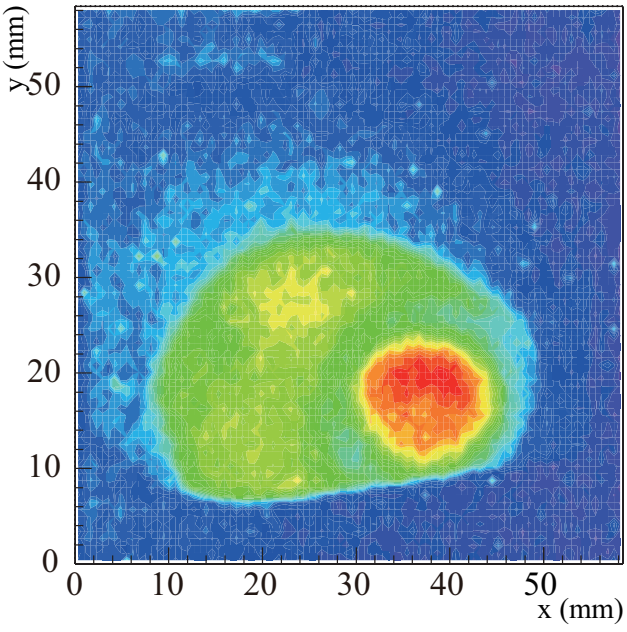

Figure 5.9: An image of the positron cloud without injection of antiprotons.

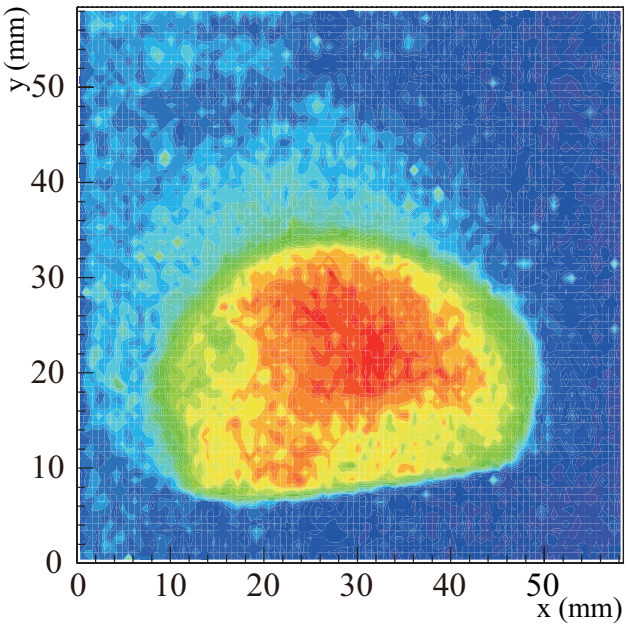

Figure 5.10: An image of the positron cloud with injection of antiprotons.

5.3 positron temperature measurement

As discussed in section 2.4, the production rate of the antihydrogen atoms increases when the relative velocity of antiprotons and positrons decreases. Since the mass of the positron is much lighter than that of the antiproton, relative velocity is determined by the velocity of the positrons when their energies are the same. We assume the energy distribution of positrons as Maxwell distribution and use the word temperature for simplicity. It is known that charged particles confined in the magnetic field automatically lose their energy in the direction perpendicular to the magnetic field by the synchrotron radiation. The time constant τ_{rad} of the cooling is given by [76]

$$\tau_{rad} = \frac{3\pi\epsilon_0 m^3 c^3}{q^4 B^2} \text{ s} \tag{5.3}$$

where ϵ_0 is the permittivity of free space, m the mass of the charged particle, c the speed of light, q charge of the charged particle, and B the strength of the magnetic field. Substituting the constants, we obtain

$$\tau_{rad} = \frac{2.6}{B^2} \text{ s} \tag{5.4}$$

for positrons. On the other hand, the temperature of positrons can be heated up by black body radiation from the environment and the electric noise from the electrode control system. Thus we measured the temperature of positrons in the cusp trap.

procedure to measure positron temperature

The principle to measure the temperature of positrons is simple, i.e. count the number of positrons escaping from the potential well by slowly decreasing the height of the potential wall and reconstruct the energy distribution of them. However the space charge of trapped positrons modifies the effective height of the potential wall and the amount of this effect changes as the number of trapped positrons changes during extraction. A detail procedure to measure and analyse the temperature of positrons is as follows.

1. Accumulate positrons in the cusp trap.

2. Move positron to upstream side of the maximum point of the magnetic field to avoid unintentional capture by mirror effect. Figures 5.11 (a), (b), and (c) show a cross sectional view of the MRE, magnetic field on axis, electric potential on axis respectively.

During the accumulation, positrons were confined in the potential shown by blue curve. However, as can be seen from the figure 5.11 (b) and (c), the bottom of the potential is downstream side of the maximum point of the magnetic field which is indicated by dashed line. It is known that the charged particles are reflected when they are extracted to the direction where the stronger magnetic field is applied if the angle (θ) between the direction of the velocity vector and the direction of the magnetic field at a position $\boldsymbol{r}$ satisfies the condition

$$\sin\theta \geq \frac{B(\boldsymbol{r})}{B_{max}} \tag{5.5}$$

where the $B(\boldsymbol{r})$ is the magnetic field at the position $\boldsymbol{r}$ and the B_{max} the maximum magnetic field on the path of the charged particle. This is called mirror effect. If a part of positrons is reflected by this effect and do not reach the detector, one can not evaluate the energy distribution of positrons correctly. In our present configuration, we have to extract positrons upstream side, since the detector is located upstream side as shown in figure 5.11 (a). To avoid the effect, positrons were moved, before the extraction, to the potential whose bottom is upstream side of the maximum point of the magnetic field which is shown by red curve in figure 5.11 (c).

3. Wait for 50 s in the potential shown by red curve. When we change the potential and move positrons, they can be heated up by the operation. But the temperature eventually get equilibrium again via the synchrotron radiation. The time constant of the cooling is expressed by the equation 5.4. In the present condition $B = 2$ T, which gives $\tau \sim 0.7$ s. However, this is valid for the temperature perpendicular to the magnetic field T_{perp}. On the other hand, there is no cooling mechanism for the temperature parallel to the magnetic field T_{para}. The T_{parp} and T_{para} relax via the collisions between positrons. Since we can measure only T_{para} by the method described here, we have to wait for enough time to relax the temperature. The waiting time was determined experimentally. Figure 5.12 shows the normalize number of extracted positrons as a function of the externally applied potential on axis for several different waiting time. As can be seen from the figure, it takes about 50 s for the temperature of positron to relax. Thus we waited for 50 s, before the extraction of positron, in the potential drawn by red curve in figure 5.11 (c).

4. Extract positrons by slowly decreasing the height of the potential wall of upstream side

as shown in figure 5.11 (d) and count the number of emerging positrons by the MCPPS detector. At the same time, voltages applied on the MRE were recorded by the ADC. Figures 5.13 (a) and (b) show the voltage applied on the U8 and U9 electrodes and the number of positrons counted by the MCPPS detector as a function of time. Typical extraction time was about 1 s as can be seen from figure 5.13 (b), which was 50 times shorter than the waiting time before the extraction (50 s). Thus we do not have to care about the change of the temperature during the extraction.

5. Calculate the externally applied potential depth on axis (ϕ_c) at each moment from the voltage applied on the electrodes as shown in figure 5.13 (c).

6. Plot the integrated number of the positrons (Q_{esc}) as a function of the effective potential depth on axis as shown in figure 5.13 (d) and fit the plot by the function [77]

$$\frac{d \ln Q_{esc}}{d(e\phi_c)} = \frac{-1}{kT} \tag{5.6}$$

where e is the unit charge, k the Boltzmann constant[4]. Then we obtain the value of the temperature T in the equation. We note that from the equation 5.6, the Q_{esc} is normalized or not does not affect the temperature. The temperature depends on the inclination of the plot. On the other hand, care must be taken that the temperature changes depending on the region to fit since the space charge created by the trapped particles changes during the extraction. To minimize the effect, we fitted the region where only small part of positrons was escaped and most of the particles were still remained in the trap. To be more precise, we used the data where the inclination of the plot was constant as indicate by red region in figure 5.13 (d) since practically the temperature obtained by this method did not change as long as the inclination of the plot did not change.

[4]see appendix B for the derivation of the function

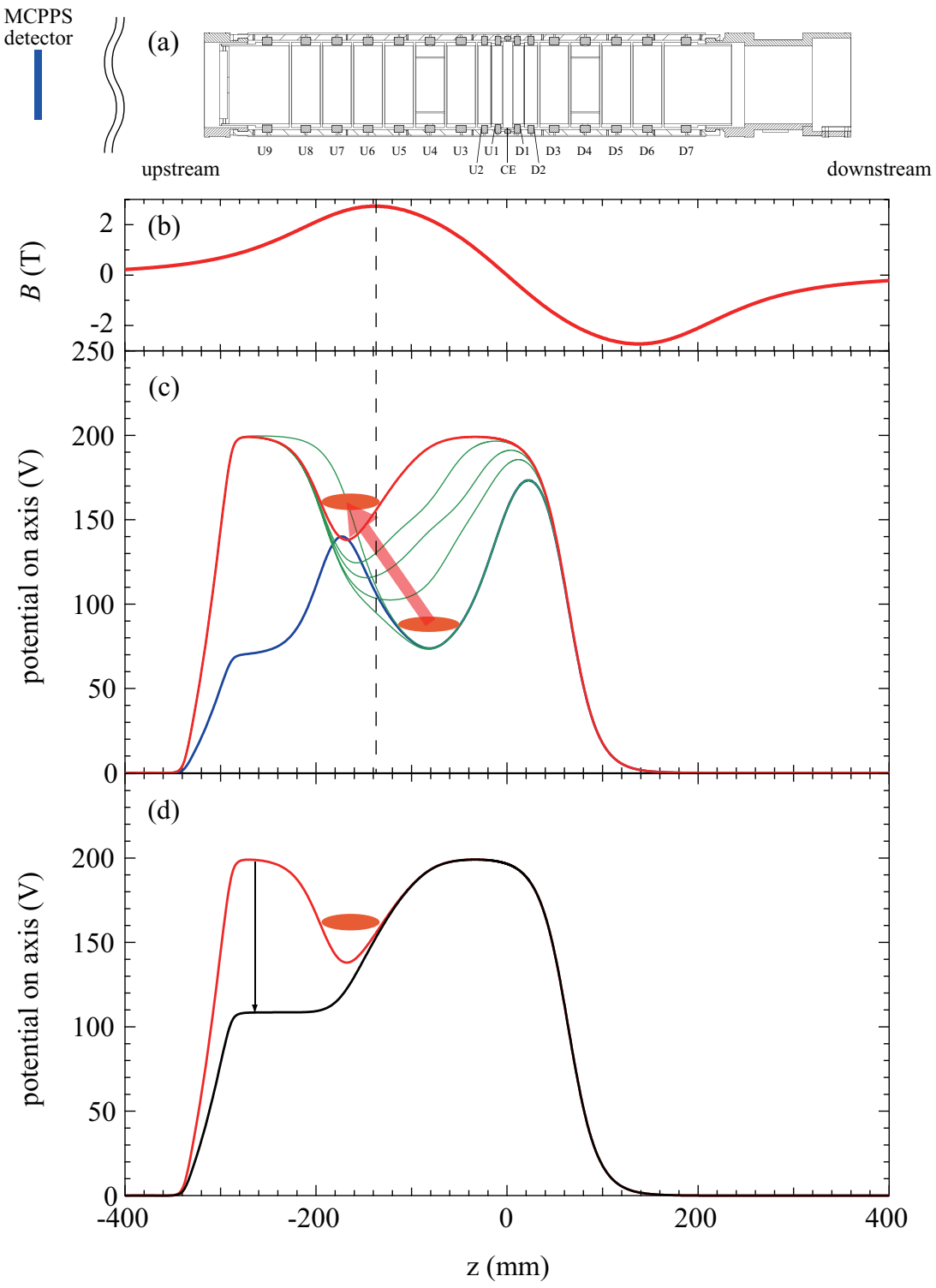

Figure 5.11: A cross sectional drawing of the MRE. The direction of the MCPPS detector are indicated by blue rectangle (a). Magnetic field on axis (b). Electric potential curves on axis (c) and (d). Potential curve was changed from blue one to red one via several steps drawn by green curves before the extraction. Then the potential wall of left side was decreased slowly as shown by black arrow and positrons were extracted.

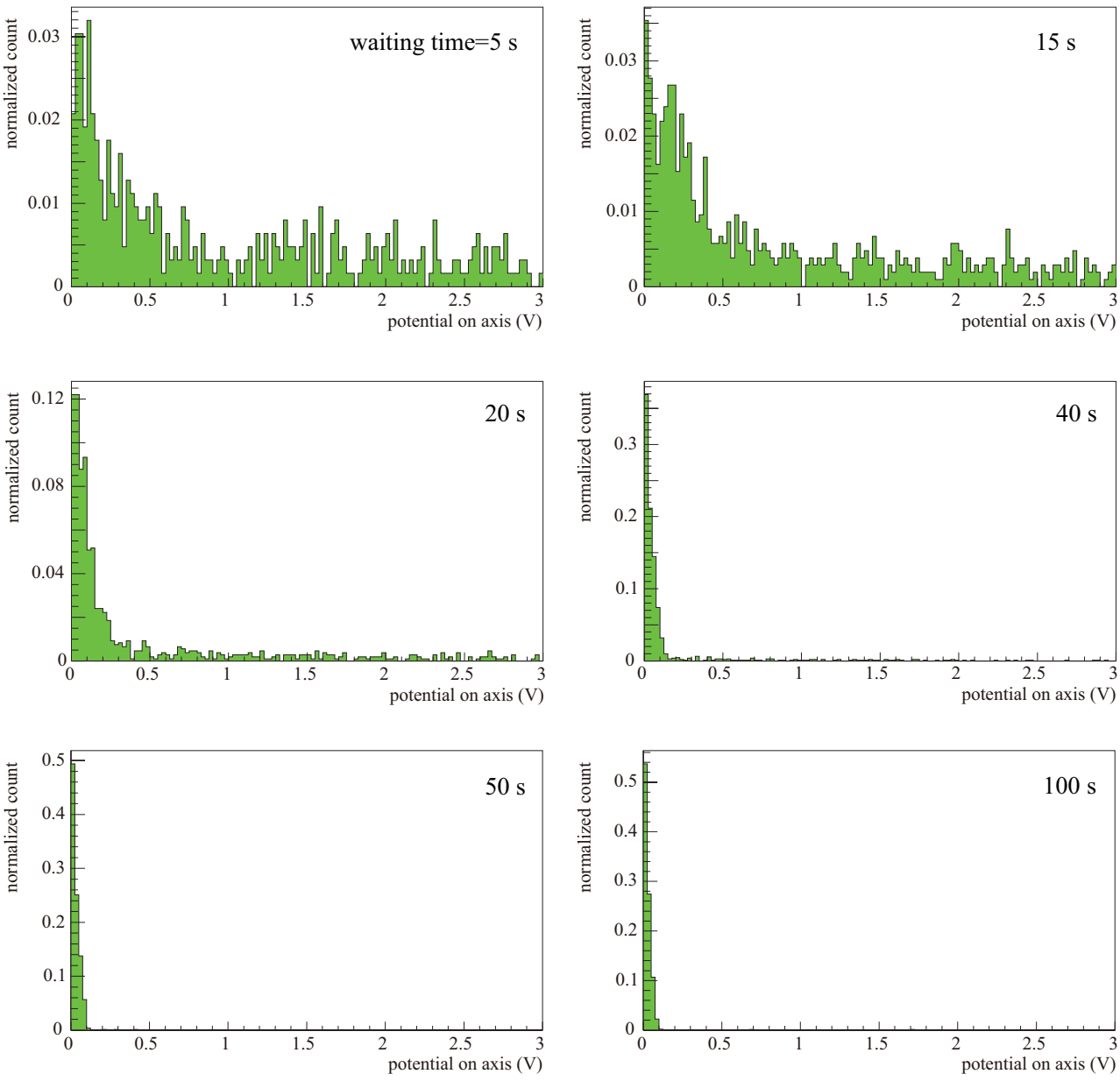

Figure 5.12: Extracted number of positrons as a function of the effective potential depth on axis for different waiting times. Data are normalized by the total number. As increasing the waiting time before the extraction, distribution gets narrower and the potential energy where positrons start escaping gets lower.

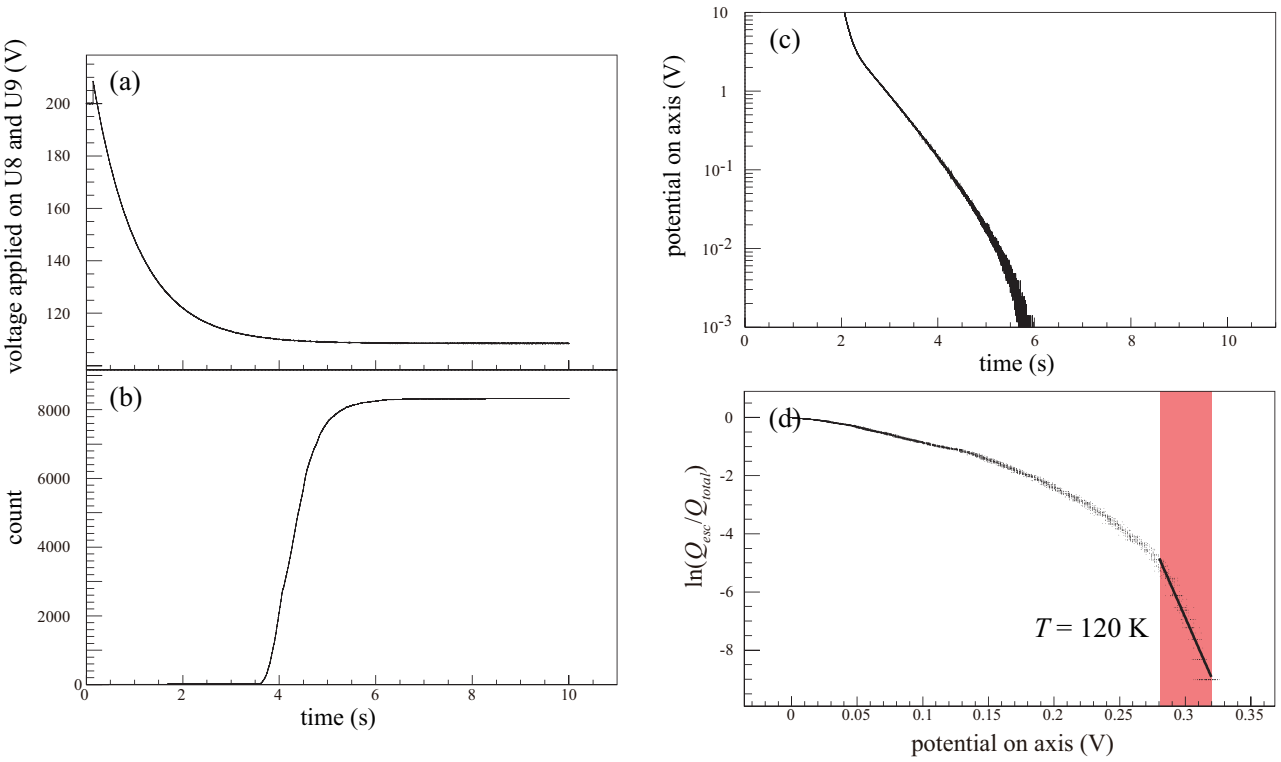

Figure 5.13: Voltage applied on the U9 and U8 electrodes (a) and integrated number of extracted positrons (b) as a function of time. Calculated externally applied potential depth on axis as a function of time (c). Integrated number of extracted positrons as a function of the potential depth on axis (d). Data are normalized by the total number Q_{total} and fitting region is shown by red. In this case $T = 120$ K.

achieved positron temperature

Figures 5.14 (a1), (b1), (c1), and (d1) ((a2), (b2), (c2), and (d2)) show integrated number (number) of extracted positrons as a function of the potential depth on axis when the number of stacking operation is 1, 2, 4, and 8 respectively. Results of the fitting are shown by Red lines in the figure (a1-d1) and the obtained temperatures are also shown near the lines. The number of the stacking operation are shown in the top of each graph. As was described, the potential depth where positrons start to escape, changes when the number of positrons in the cusp trap changes due to the space charge of trapped positrons. Figure 5.14 shows the temperature of positrons as a function of the number of the staking operation (i.e. number of trapped positrons in the cusp trap). As can be seen from figure, there was no dependence on the number of the staking operation and the measured temperatures were around 150 K. According to the result of other group [53][5], this value is promising for the efficient production of the antihydrogen atoms. Considering the environmental temperature is about 15 K, the temperature of the positron is rather high. Black body radiation from the hole of the upstream thermal shield or electric noise from the power amplifiers can be candidates for the heating source, however the exact reason for the obtained value is still an open question.

[5]The temperature of positrons was reported as 180 ± 50 K

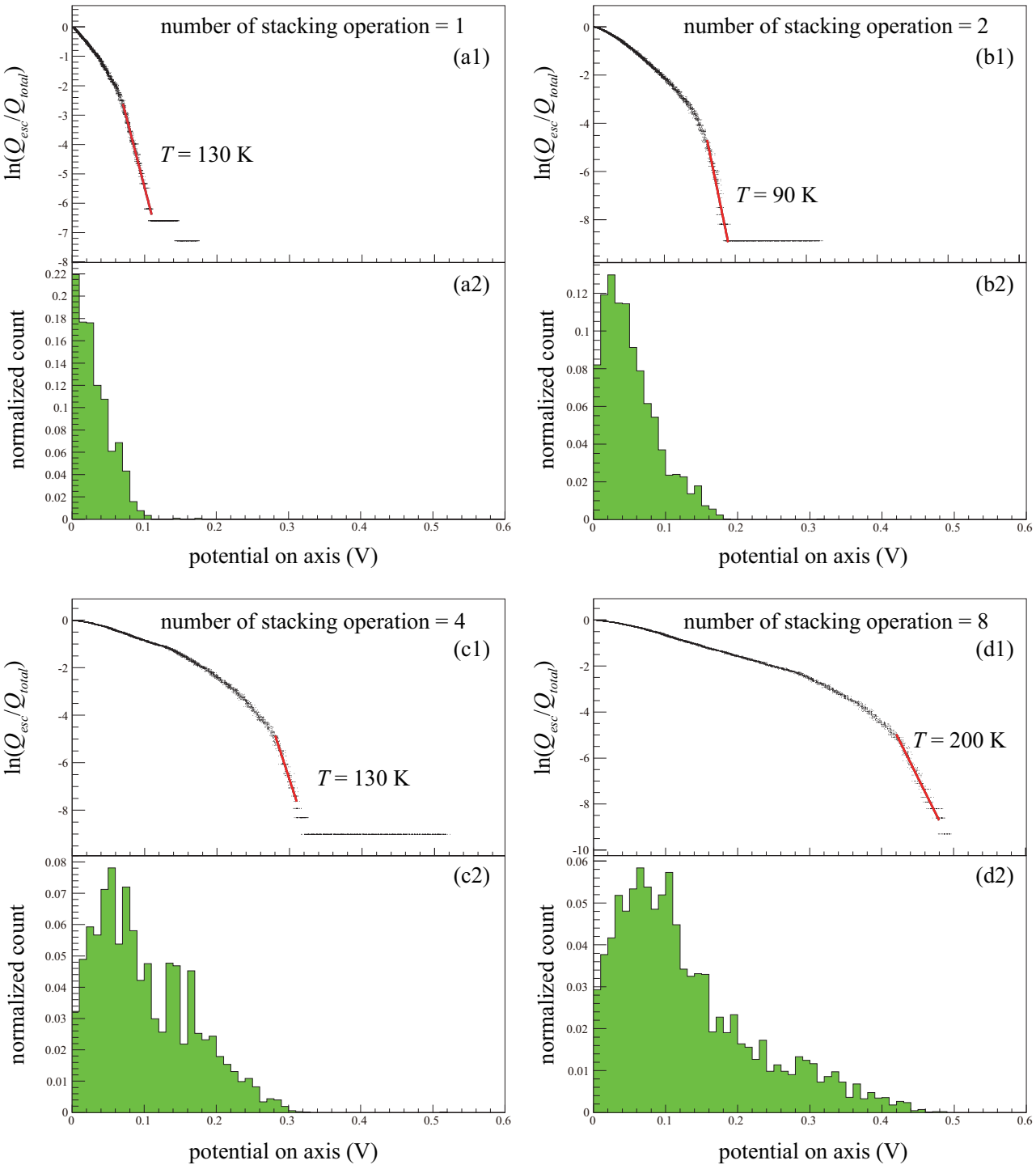

Figure 5.14: Integrated number (a1-d1) and number (a2-d2) of extracted positrons as a function of the potential depth on axis, when the number of stacking operation is 1 (a), 2 (b), 4 (c), and 8 (d). Red lines in the figures are fit results. As increasing the number of stacking operation, potential energy where positrons start escaping increases due to the space charge. However, temperature, which depends on the inclination, does not depend on the number of stacking operation.

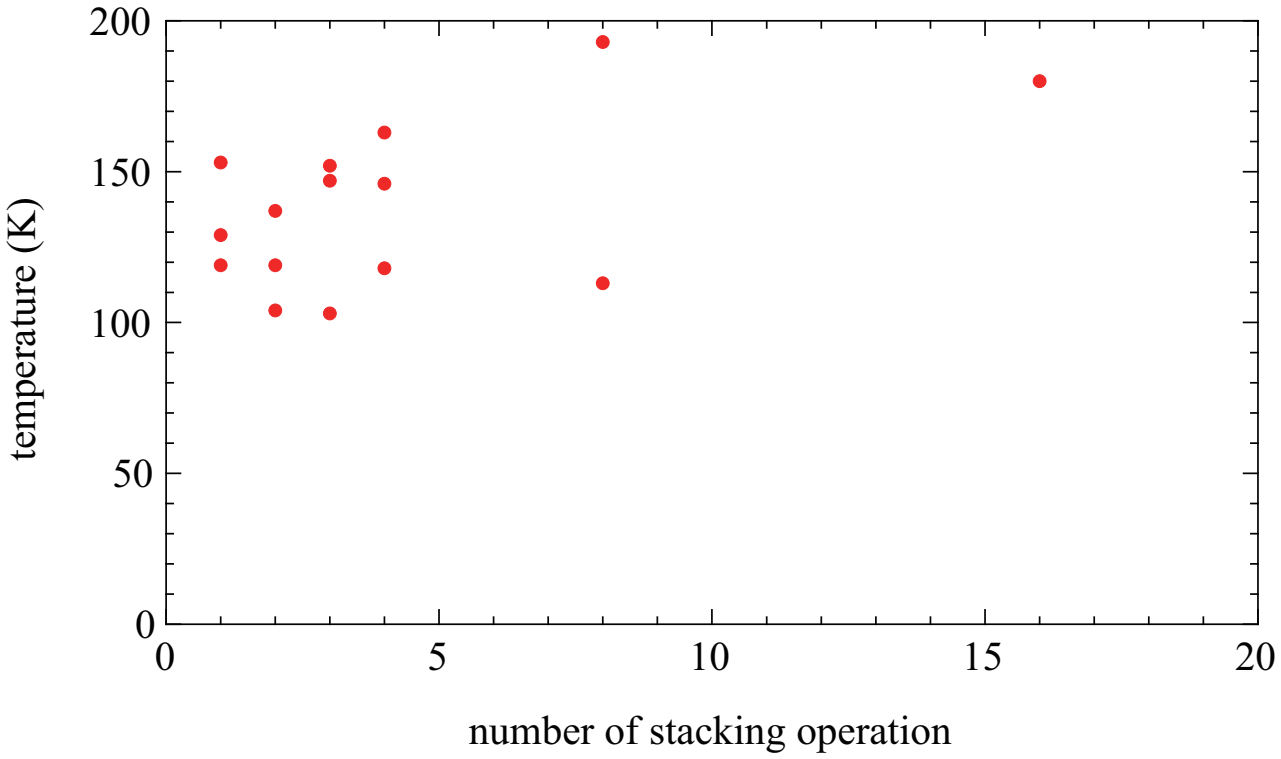

Figure 5.15: Temperature of positrons for different number of the stacking operation. Temperature does not depend on the number of stacking operation. The measured temperature of positrons in the cusp trap was around 150 K.

Chapter 6

Antihydrogen production and detection

In this chapter, the production process of antihydrogen atoms is described. In section 6.1, the detection method of antihydrogen atoms is considered. In section 6.2, the method to produce antihydrogen atoms is explained. In section 6.3, results are presented. First we present the evidence of the production of antihydrogen atoms, then we discuss the time evolution of the production rate, and dependence of the production rate on the number of positrons and antiprotons. Finally we evaluate the principal quantum number of produced antihydrogen atoms.

6.1 Detection method of antihydrogen atoms

Antihydrogen atoms can be detected by monitoring its annihilation products. However, if we produce antihydrogen atoms by mixing antiprotons and positrons in the trap, there are many antiprotons some of which annihilate with residual gas and also emit annihilation products. Thus we have to distinguish antihydrogen from antiproton in some way. We have already seen two method to distinguish them in chapter 1 and we adopt field-ionization method developed by ATRAP [11]. In this method shown in figure 1.3, a part of antihydrogen atoms produced in the nested trap are ionized by the strong electric field prepared near the recombination area and antiprotons are captured in the potential well indicated as ionization well. One can estimate the number of antihydrogen atoms produced and ionized by counting the number of antiprotons in the ionization well. In addition if one eject the antiprotons in the nested

trap before counting the number of antiprotons in the ionization well, annihilation signal of antiprotons which did not recombined with positrons are completely removed. The number of antihydrogen atoms detected by this method depend on how deeply an antiproton and a positron are bounded. This means that one can estimate the binding energy of the produced antihydrogen atoms by changing the strength of the electric field in the ionization well.

6.2 Production method of antihydrogen atoms

A method to produce antihydrogen atoms is in principle simple. We have only to mix positrons and antiprotons in the trap. Figure 6.1 (a), (b), and (c) shows a cross sectional view of the MRE, magnetic field on axis, and typical potential curves on axis for the production of antihydrogen atoms. Typical operations were as follows.

1. Positrons were accumulated in the potential configuration ϕ_1 (see section 5.1). The number of stacking operation was 40 or 60 (see section 5.2). The cloud of positrons was compressed by rotating wall technique during the accumulation process (see section 5.2).

2. The potential was varied from ϕ_1 to ϕ_2 via several intermediate potentials (see figure 6.2) with the positron cloud kept compressed at the center of the nested potential.

3. Antiprotons were injected from the antiproton catching trap into the cusp trap and captured in the potential ϕ_3 (see section 4.2), and mixed with the preloaded positrons.

Positrons were heated by injected antiprotons, then cooled via synchrotron radiation, and eventually captured by antiprotons to form antihydrogen atoms. Although antiprotons in the nested trap had no chance to move beyond the nested potential, antihydrogen atoms moved freely because they are neutral, and a part of them reached the field-ionization trap (FIT). Antihydrogen atoms in high Rydberg states were field-ionized and their antiprotons were accumulated in the FIT. Electrodes D4 and D5 (indicated by red in the figure 6.1 (a)) were used as a bottom of the FIT. We define V_{FI} as voltage applied on them when the potential configuration was ϕ_2. In addition we define t as the time measured from the injection of antiproton.

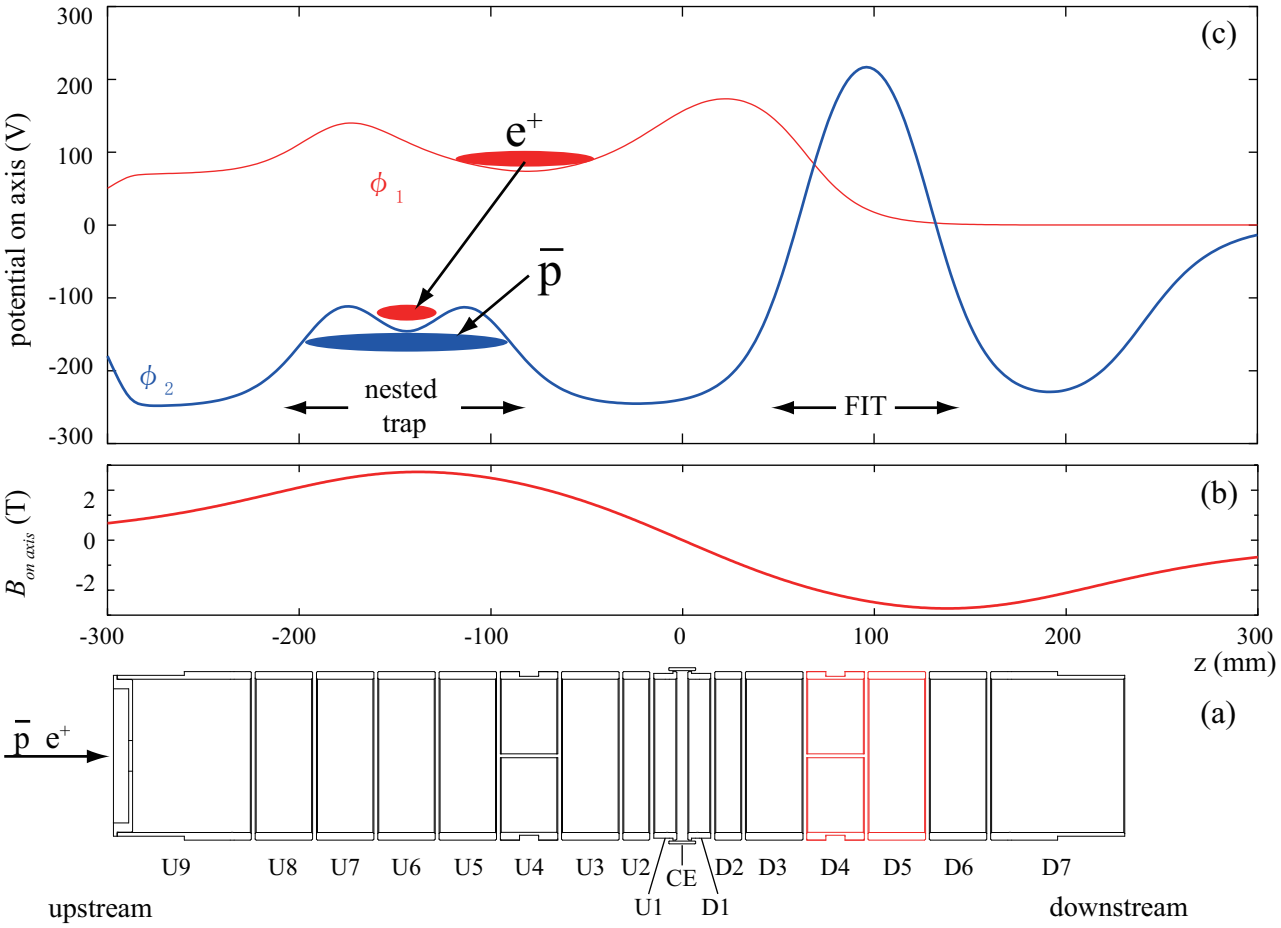

Figure 6.1: A cross sectional drawing of the MRE of the cusp trap (a), the magnetic field on axis (b), and the electric potential curves on axis (c). First, positrons were accumulated in the potential ϕ_1, then they were moved to the center of the nested trap and antiprotons were injected. At the same time, field ionization trap (FIT) is prepared beside the nested trap to ionize and capture produced antihydrogen atoms.

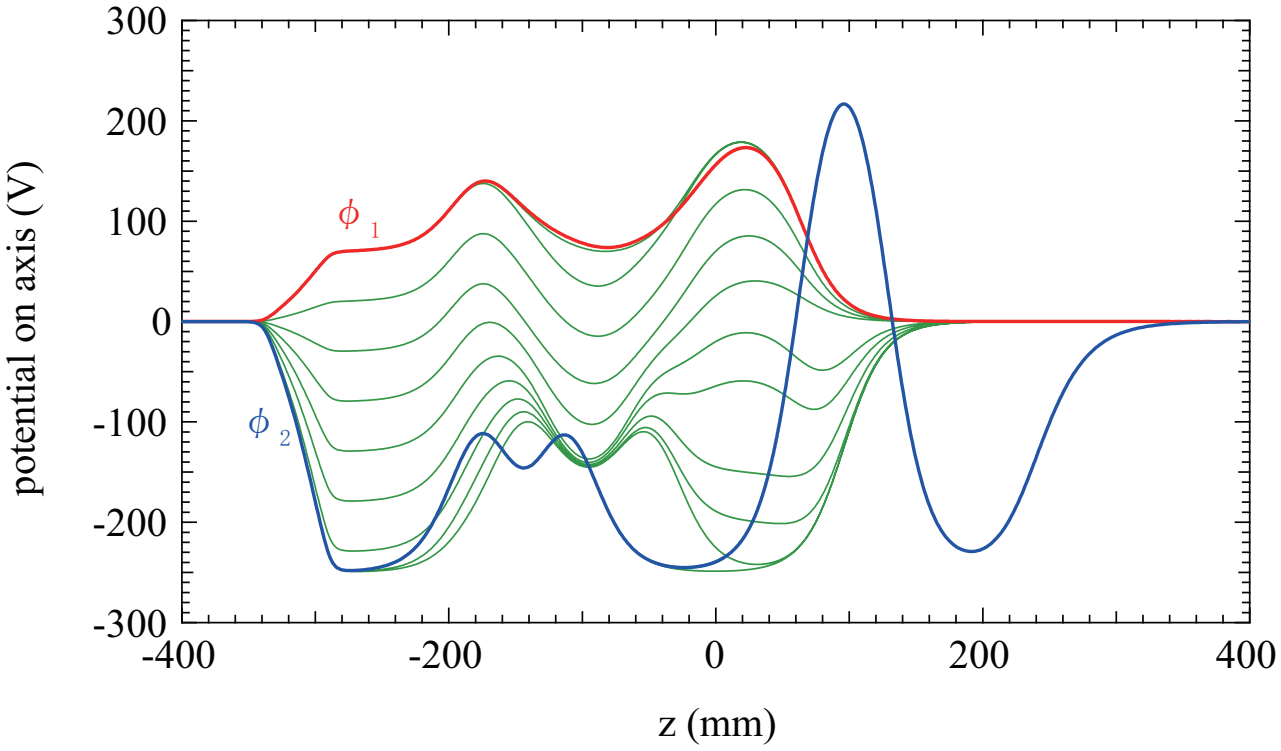

Figure 6.2: Potential configuration was varied from ϕ_1 to ϕ_2 via several intermediate configurations drawn by green curves.

6.3 Results

6.3.1 Confirmation of antihydrogen production

First of all, the production of the antihydrogen atoms was confirmed as below. Figure 6.3 shows potential configurations to count the number of antiprotons confined in the FIT.

1. Antiprotons in the nested trap were ejected to upstream side by changing the potential from ϕ_2 to ϕ_3.

2. Antiprotons in the FIT were ejected to downstream side by changing the potential from ϕ_3 to ϕ_4.

Figure 6.4 shows the count of the 3D detector as a function of time τ when antiproton were confined and mixed with positrons(a) and antiprotons were confined without positrons(b) along with the voltage applied on D4 electrode (V_{D4})[1]. Here, we define $\tau = 0$ as the time when we changed the potential to count the number of antiprotons in the FIT. In this measurement V_{FI} was 0 V and the timing when the potential was changed from ϕ_2 to ϕ_3 was $t = 50$ s i.e. antiprotons and positrons were mixed for 50 s.

There is a peak of annihilation signals around $\tau_1 = 0$ s only when positrons were present in the nested trap even through the operations and the conditions were same but the existence of positrons. From these results, we confirmed the production of antihydrogen atoms.

[1]It took about 1 ms to change the voltages applied on the electrodes of the MRE. This time is determined by the time constant of the low pass filters between the electrodes and the power amplifiers.

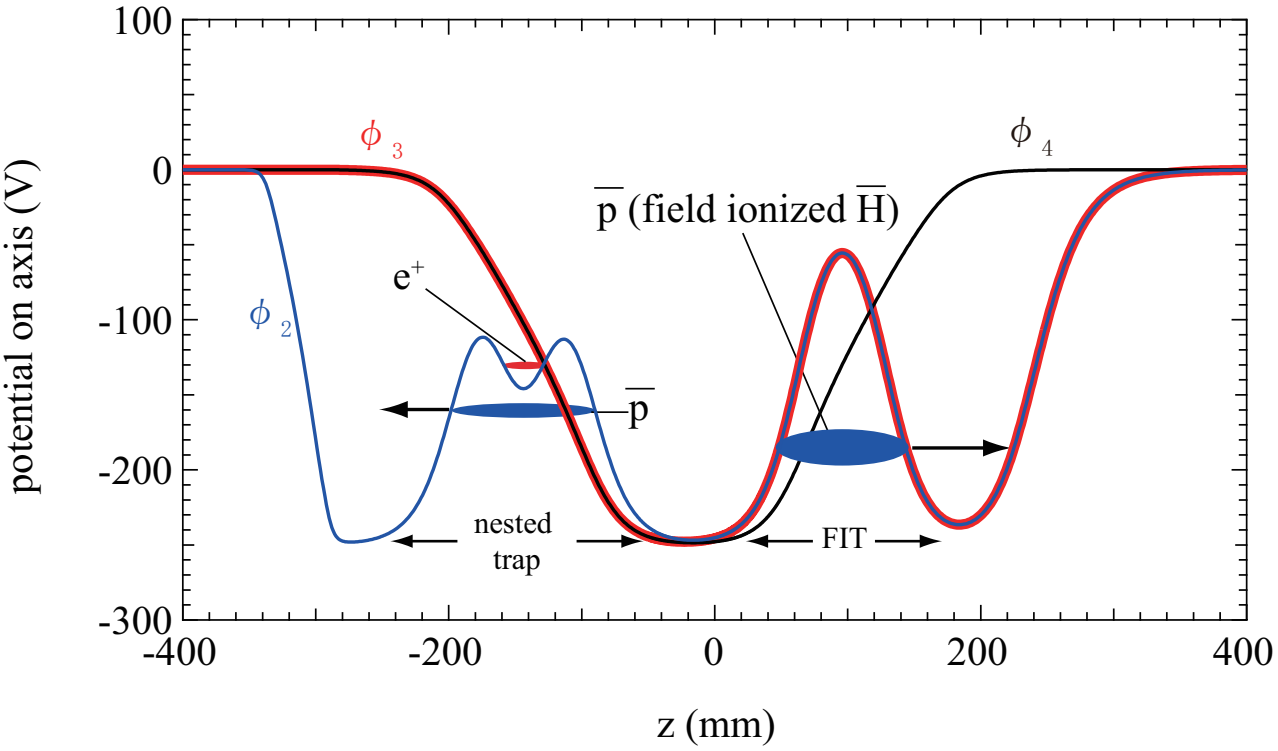

Figure 6.3: The potential curves to count the number of antiprotons confined in the FIT. The potential was changed from ϕ_2 to ϕ_3 to eject antiprotons in the nested trap. Then the potential was changed from ϕ_3 to ϕ_4 to count the number of antiprotons in the FIT.

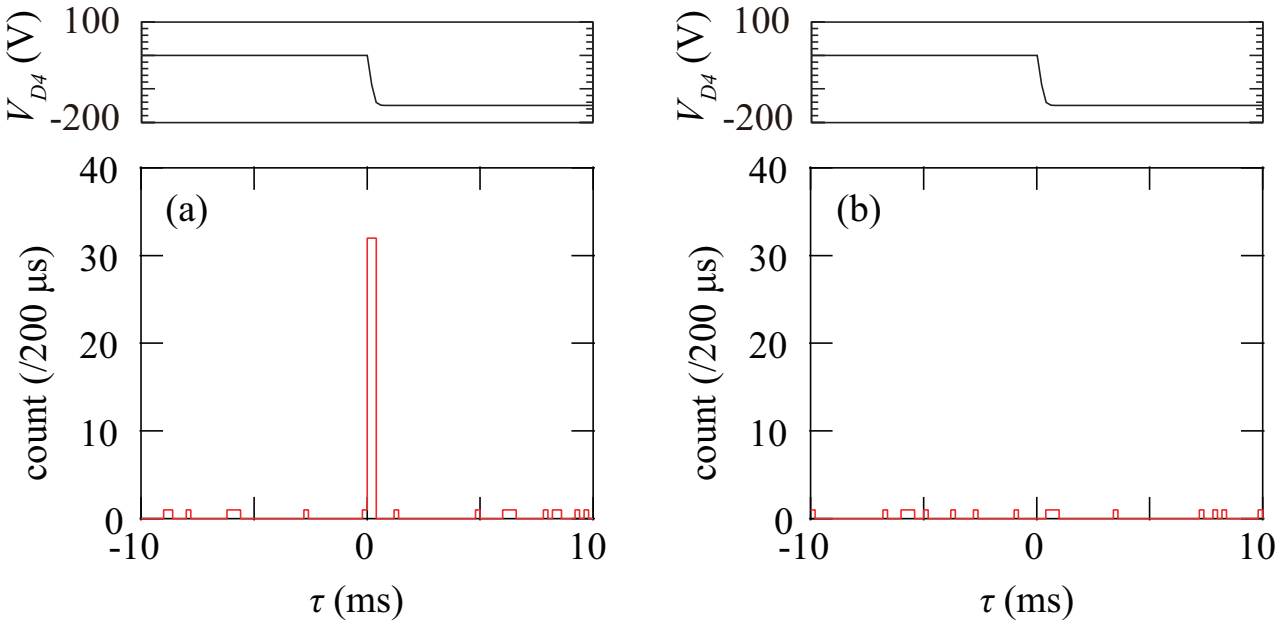

Figure 6.4: Histograms of the count of the 3D detector as a function of time τ. The voltage applied on the D4 electrode is shown to indicate the timing when we open the FIT to count antiprotons in the FIT. Antiprotons were confined and mixed with positrons in the cusp trap (a) while they were confined without positrons (b). Only when they were mixed with positron, the peak of the annihilation signal was observed.

As discussed in section 2.4, the production rate of the antihydrogen atoms decrease as the temperature of the positron increase. We tried to control the production rate of the antihydrogen atoms by heating up the positrons via applying RF electric voltages on the U4 (segmented) electrodes where the cryogenic filters were not attached.

Figure 6.5 shows the count of annihilation signals as a function of τ when we did not apply an RF voltages (a) and when we applied sinusoidal RF voltages of 10 V whose phases were shifted by 90 degrees (i.e. we applied rotating electric field like the field used to compress the positron cloud.). It is known that charged particles in the trap can be heated efficiently when the frequency of the externally applied field and the bounce frequency of the charged particles are matched. In our experimental condition the bounce frequency of positrons in the nested trap was about 26 MHz. We swept the frequency of the RF voltage from 12 MHz to 13 MHz, which is about half of the bounce frequency to heat up the positron efficiently. The RF voltages were applied during the whole period of the mixture. In both cases, the number of positrons was 4×10^6 and the number of the antiprotons was 4×10^5.

We note that in these measurement, the FIT was opened 10 times every five seconds with keeping antiprotons and positrons in the nested trap. Thus the background count in figure 6.5 is higher than that in figure 6.4. The data shown in figure 6.5 are the sum of the data obtained each opening of the FIT.

In figure 6.5 (a) (i.e. without heating), an annihilation peak is clearly seen while in figure 6.5 (b) (i.e. with heating), the peak is completely disappeared even though the positrons and antiprotons were confined in the nested trap[2]. This fact supports the production of antihydrogen atoms.

[2]We confirmed that the number of positrons in the cusp trap after the mixture was the same in both cases.

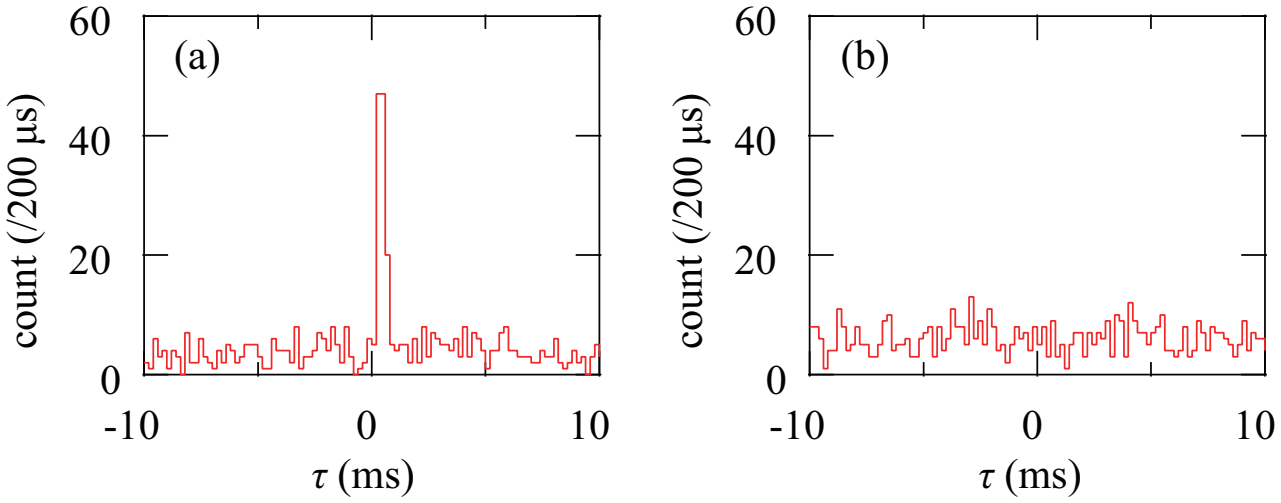

Figure 6.5: Histograms of the count of the 3D detector as a function of time τ without RF heating (a) and with RF heating (b). Suppression of antihydrogen production by the RF heating is clearly seen.

6.3.2 Time evolution of the production rate of the antihydrogen atoms

As we confirmed the production of antihydrogen atoms, the next to understand the dynamics of the antihydrogen production. Consequently, we measured the time evolution of the production rate.

Figure 6.6 shows the potential configurations used to measure the time evolution of the production rate. The potential was changed from ϕ_2 to ϕ_5 every 5 s for 0.1 s. To explain the operation more clearly, we show a figure 6.7 which shows the voltage applied on the D4 electrode as a function of time. As described above, the D4 electrode corresponds to the bottom of the FIT and the voltages were changed when the FIT was opened. At $t = 0$ s antiprotons were injected in positrons in the cusp trap. At $t = 5$ the potential was changed to ϕ_5 for 0.1 s and returned to ϕ_2. The same operation was repeated 20 times and we obtained the annihilation signal at each opening of the FIT as a function of τ_i.

Figure 6.8 (a) shows the number of antiprotons accumulated in the FIT every 5 s as a function of t. In this measurement, 3×10^5 antiprotons were mixed with 3×10^6 positrons and V_{FI} was 350 V. The number increased in the first 30 s and then slowly decreased in the next 80 s yielding 70 antiprotons per mixture. Assuming the result of the simulation of the detection efficiency (see section 6.3.4), the total number of antihydrogen atoms in high Rydberg states was estimated to be at least 7×10^3 per mixture. In other word, the antihydrogen formation efficiency was about 2 %.

Next we check the annihilation position distribution of the antiprotons to find the reason why the production rate decrease after $t = 30$ s even though the antiprotons and positrons were still presented in the nested trap. Figure 6.8 (b) and (c) show the annihilation position distribution of the antiprotons along the beam axis measured with the 3D detector for 0 s $< t <$ 60 s and 60 s $< t <$ 120 s respectively. Blue curve in the figure is the potential curve in which antiprotons and positrons were confined. A sharp single peak is seen in figure 6.8(b) near the positron trapping position (z=-144 mm). On the other hand, in the case of figure 6.8 (c), the peak gets broader than that of figure 6.8 (b) with an indication of two bumps near the potential maxima of the nested trap (z=-175 mm and z=-113 mm). The latter observation showed that antiprotons were axially separated from the positrons after several tens of seconds. This axial separation can explain why the antihydrogen production rate decreased and almost disappeared after 100 s.

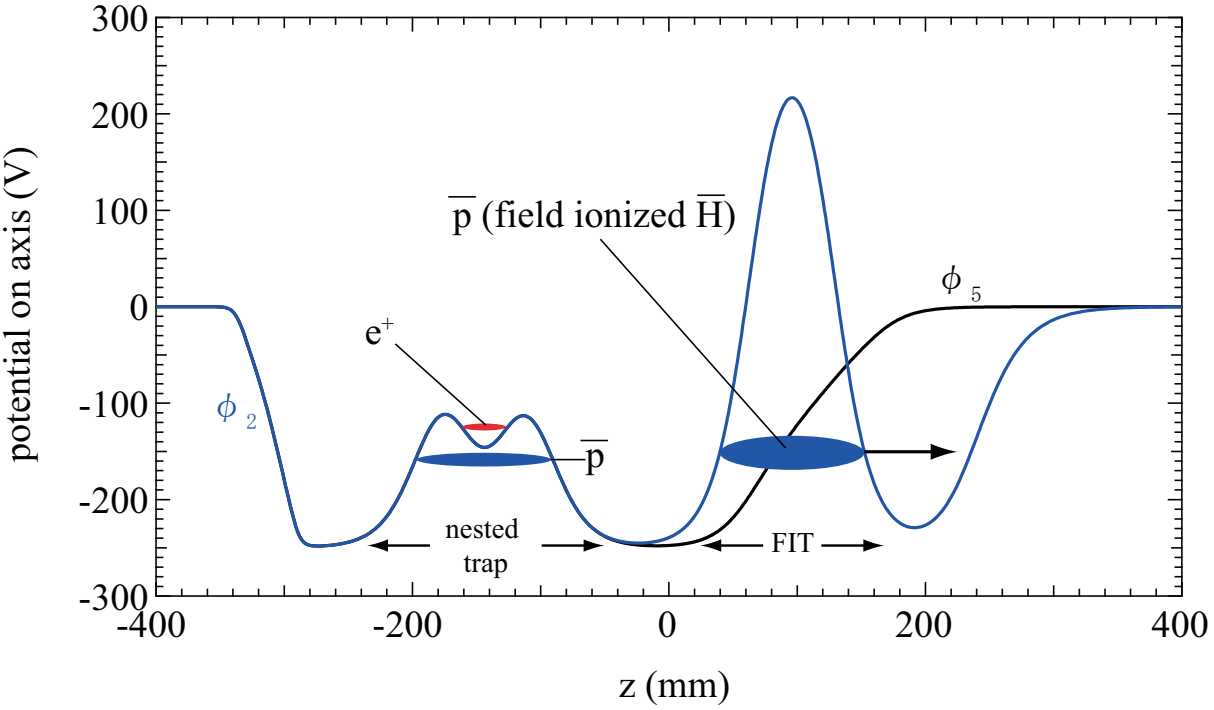

Figure 6.6: Potential configurations to measure the time evolution of the production rate of antihydrogen atoms. Potential curve was changed from ϕ_2 to ϕ_5 repeatedly and the number of antiprotons in the FIT was measured every 5 s.

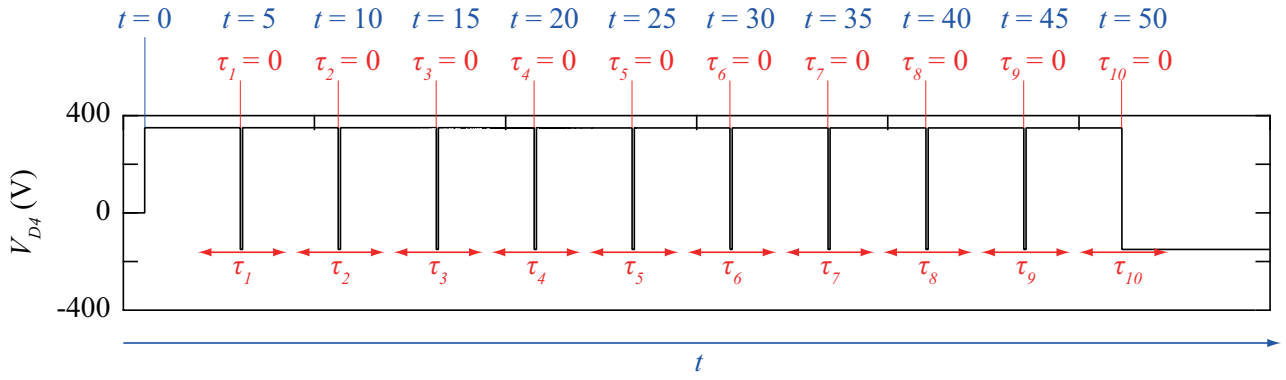

Figure 6.7: Relation among t and τ_i's. Voltage applied on the D4 electrode (V_{D4}) is shown as a function of t to indicate the timing when the FIT was opened.

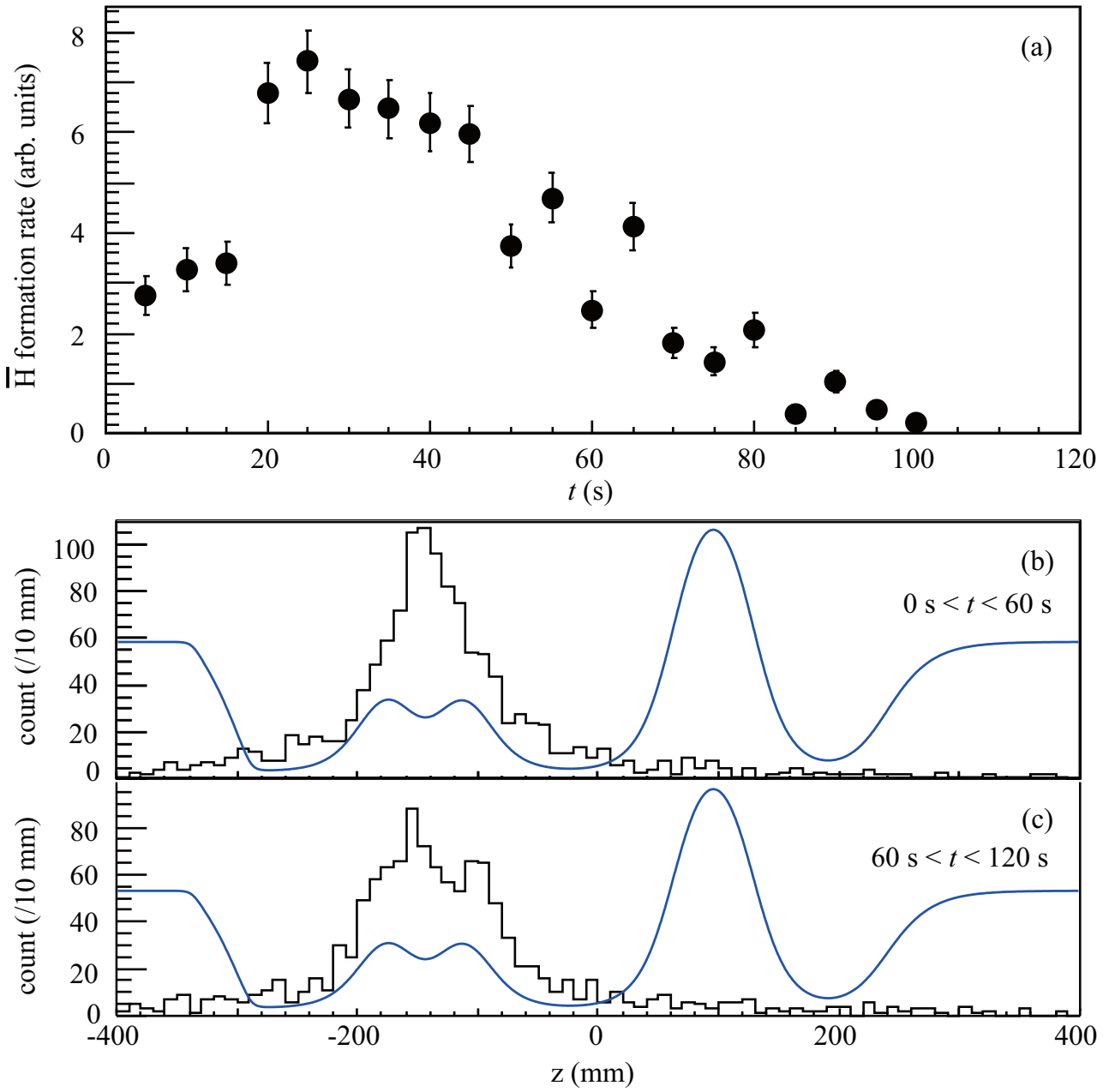

Figure 6.8: The number of field-ionized antihydrogen atoms accumulated in the FIT monitored by opening the FIT every 5 s. Each data point was obtained as a sum of 19 trials (a). The annihilation position distribution observed by the 3D detector for 0 s $< T <$ 60 s (b) and 60 s $< T <$ 120 s (c). Blue curve represents the potential in which antiprotons and positrons were confined (ϕ_2).

6.3.3 Positron and antiproton number dependence of antihydrogen production rate

The dependence of the antihydrogen production rate on the number of antiprotons and positrons were measured.

First we changed the number of positrons by changing the number of the stacking operation (see figure 5.5). Figure 6.9 shows the dependence of the number of antihydrogen atoms on the number of positrons. In these measurements the number of antiprotons was 4×10^5. As the number of the positrons increased, the number of antihydrogen atoms increased, however it saturated after the number of positrons reached around 4×10^6. Since the production rate is proportional to the square of the density of the positrons (see section 2.4), this saturation was surprising. ATRAP had reported [11] similar saturation[3] , the reason of this dependence is still an open question.

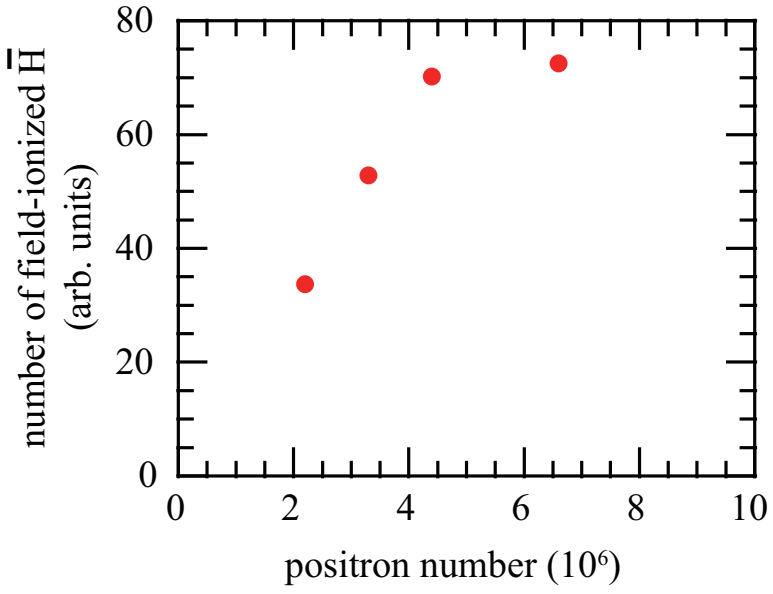

Figure 6.9: The number of field-ionized antihydrogen atoms as a function of the number of positrons.

[3]The number of positrons at saturation point were one order of magnitude lower (see ref.[11]).

Next we changed the number of antiprotons in the cusp trap by the procedure described in section 4.2. Figure 6.10 (a) and (b) shows the number of antihydrogen atoms produced in first 100 s and conversion efficiency from antiproton to antihydrogen atom as a function of the number of antiprotons respectively. In these measurement, the number of positrons was 6×10^6. In addition, we used the value of the detection efficiency calculated in section 6.3.4 to obtain the conversion efficiency.

The time evolution of the production rate in these measurement are shown in figure 6.11. The number of antihydrogen atoms increased as the number of antiprotons increased as expected. In the case of injection of 1.1×10^6 antiprotons, decrease of the number of antihydrogen atoms partially due to the lack of data taking time. Because the production rate is not decreased so much compared with the other cases (see figure 6.11). On the other hand, the conversion efficiency increased monotonically as the number of the antiprotons decreased. The efficiency was as high as 7 % when the number of antiprotons was 7×10^4. One possible explanation to the dependence of conversion efficiency on the number of antiproton is expansion of the positron cloud. As discussed in section 5.2, the positron cloud expand by the injection of antiprotons. This effect considered to be more serious as the number of antiprotons increase.

For the time evolution of the production rate, as the number of antiprotons increased, the rate peaked (indicated by arrow in figure 6.11) later and the production period became longer. This observation is consistent with an expectation that it will take longer time for positron to cool antiprotons for larger number of antiprotons.

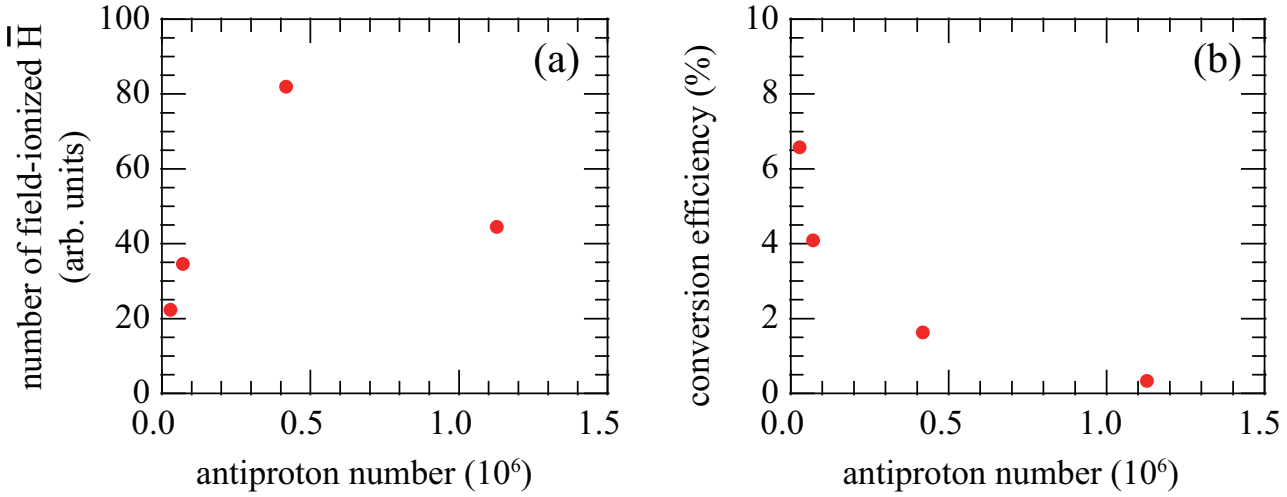

Figure 6.10: The number field-ionized antihydrogen atoms (a) and the conversion efficiency (b) as a function of the number of antiprotons. To derive the conversion efficiency, we used the detection efficiency calculated in section 6.3.4.

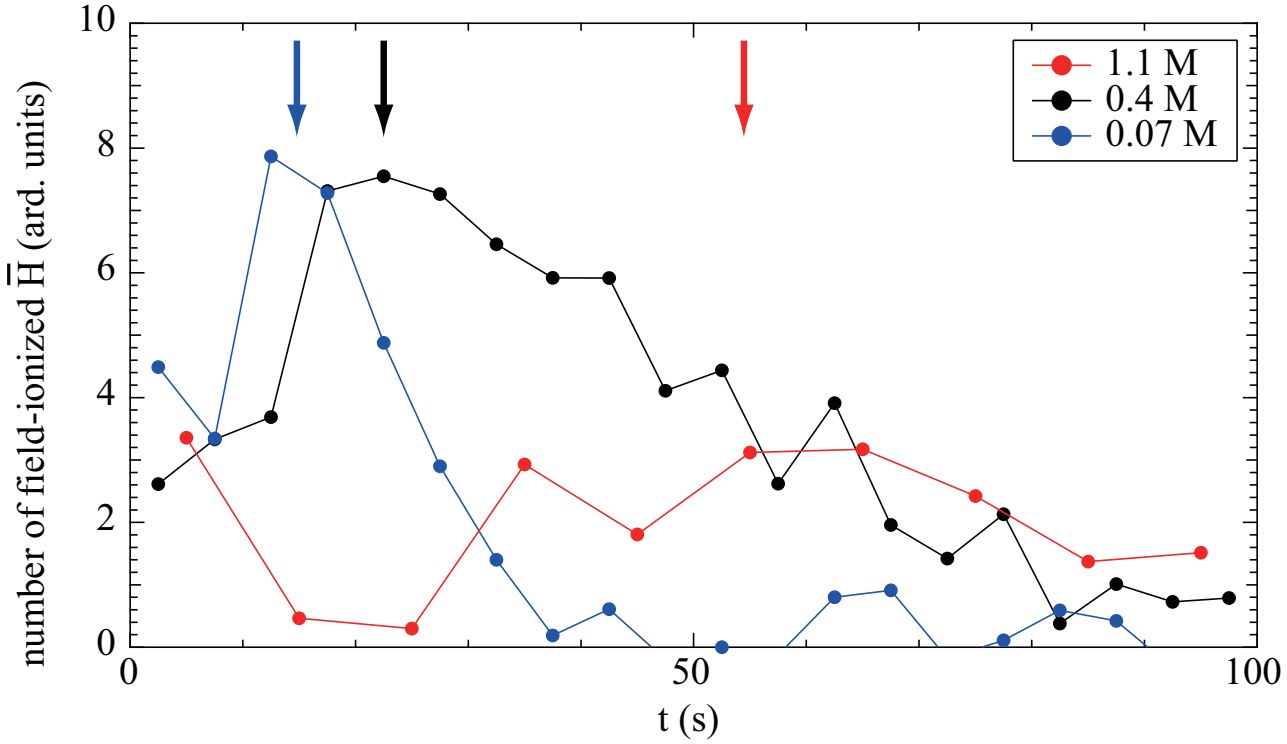

Figure 6.11: Time evolution of the production rate of antihydrogen atoms for three different antiproton numbers. As increasing the number of antiprotons, production rate peaked later as indicated by arrows and the production period became longer.

6.3.4 principal quantum number of field-ionized antihydrogen atoms

The detection efficiency of the antihydrogen atoms by the field-ionization method depends on the strength of the electric field around the FIT and the binding energy of the atom. Since the strength of the electric field which an atom feels varies depending on its trajectory[4], we calculated the detection efficiency of the antihydrogen atoms for several principal quantum number (n) and V_{FI}'s taking into account the two-dimensional distribution of the electric field in the cusp trap.

Simulation

The detection efficiency of the antihydrogen atoms by the field-ionization method depend on both the efficiency of the 3D detector and the efficiency of the field-ionization of the antihydrogen atoms. Considering the multiplicity of the charged pions (3) from annihilation of an antiproton and solid angle of the detector (1/3), the former efficiency considered to be almost 100 %. The latter depends on the strength of the electric field of the FIT and the binding energy of the antihydrogen atoms. Although the principal quantum number (n) is not a good quantum number in the strong magnetic field, we assume ,for the simplicity, the the binding energy of the antihydrogen atoms can be expressed as $E = 13.6/n^2$ eV, which is the result when no external field is applied. The minimum electric field (F) which can ionize the antihydrogen atom in n state are derived classically as follows.

1. The potential energy ($V(\boldsymbol{r})$) of positron in antihydrogen atom in the electric field F in the direction of z is given by

$$V(\boldsymbol{r}) = -\frac{e^2}{4\pi\varepsilon_0 r} - eFz \tag{6.1}$$

   where ε_0 is permittivity of vacuum and e unit charge.

2. The equation 6.1 has a saddle point at

$$\boldsymbol{r_0} = (0, 0, z_0) = \left(0, 0, \sqrt{\frac{e}{4\pi\varepsilon_0 F}}\right). \tag{6.2}$$

3. The value of $V(\boldsymbol{r})$ at $(0, 0, z_0)$ is given by

$$V(\boldsymbol{r_0}) = -2\sqrt{\frac{e^3 F}{4\pi\varepsilon_0}}. \tag{6.3}$$

[4]Electric field is stronger near the electrodes than on the axis (see figure 6.12)

4. The binding energy (E_n) of the antihydrogen atom whose principal quantum number is n is given by

$$E_n = \frac{E_{Ry}}{n^2} \tag{6.4}$$

where E_{Ry} is the Rydberg energy.

5. Assuming the atom is ionized when $E_n = -V(r_0)$, F is given by

$$\frac{E_{Ry}}{n^2} = 2\sqrt{\frac{e^3 F}{4\pi\varepsilon_0}} \tag{6.5}$$

$$F = \frac{\pi\varepsilon_0 E_{Ry}^2}{e^3 n^4} \tag{6.6}$$

$$= 3.2 \times 10^8 n^{-4} \text{ V/cm}. \tag{6.7}$$

Figure 6.12 shows the 2D map of the electric field and potential on the axis when $V_{FI} = 360$ V and a cross sectional view of the MRE of the cusp trap. In order the atom to be ionized and captured in the FIT, the n have to satisfy two conditions.

1. The n is small enough not to be ionized by the electric field of the nested trap. We define this value as $n_{max}(\theta, V_{FI})$[5].

2. The n is large enough to be ionized by the electric field of the FIT. We define this value as $n_{min}(\theta, V_{FI})$.

Both $n_{max}(\theta, V_{FI})$ and $n_{min}(\theta, V_{FI})$ are functions of the V_{FI} and the emission angle (θ) with respect to the axis.

The procedure of the simulation is as follows.

1. Assuming that antihydrogen atoms are produced at the center of the nested trap (z=-144 mm, r=0 mm), calculate the electric field along θ. Figure 6.13 shows a result as a function of z for several different θ. As the θ increase, the electric field which atom feels around the FIT increase because the atom come close to the electrode. But if the θ is too large, the atom hit the electrode before reaching the FIT.

2. Calculate $n_{max}(\theta, V_{FI})$ and $n_{min}(\theta, V_{FI})$ from the result above and the equation 6.7. Figure 6.14 shows result. The atom whose n and θ is in the region shown by red can be ionized and detected.

[5]In the present configuration, $n_{max} \sim 55$.

3. Integrate the data by θ with the weight of solid angel[6]by the formula 6.8, obtain the detection efficiency $\varepsilon(V_{FI}, n)$ as a function of n.

$$\varepsilon(V_{FI}, n) = \int_{\theta} \delta(n, \theta, V_{FI}) \frac{2\pi \sin\theta d\theta}{4\pi} \tag{6.8}$$

where $\delta(n, \theta, V_{FI})$ is a function, $\delta(n, \theta, V_{FI}) = 1$ when n and θ are in the region shown by red in figure 6.14 otherwise $\delta(n, \theta, V_{FI}) = 0$.

4. Calculate $\varepsilon(V_{FI}, n)$ for different V_{FI}'s and obtain the map of $\varepsilon(V_{FI}, n)$.

Figure 6.15 shows the results of the simulation. The $\varepsilon(V_{FI}, n)$ are drawn as a function of n for different V_{FI}'s. The detection efficiency of the antihydrogen atom by the field-ionization method in our configuration is expected to be about 1.1% when $V_{FI} \geq 200$ and $n \sim 50$ for example.

[6]We assumed that the produced antihydrogen atoms were emitted isotropically.

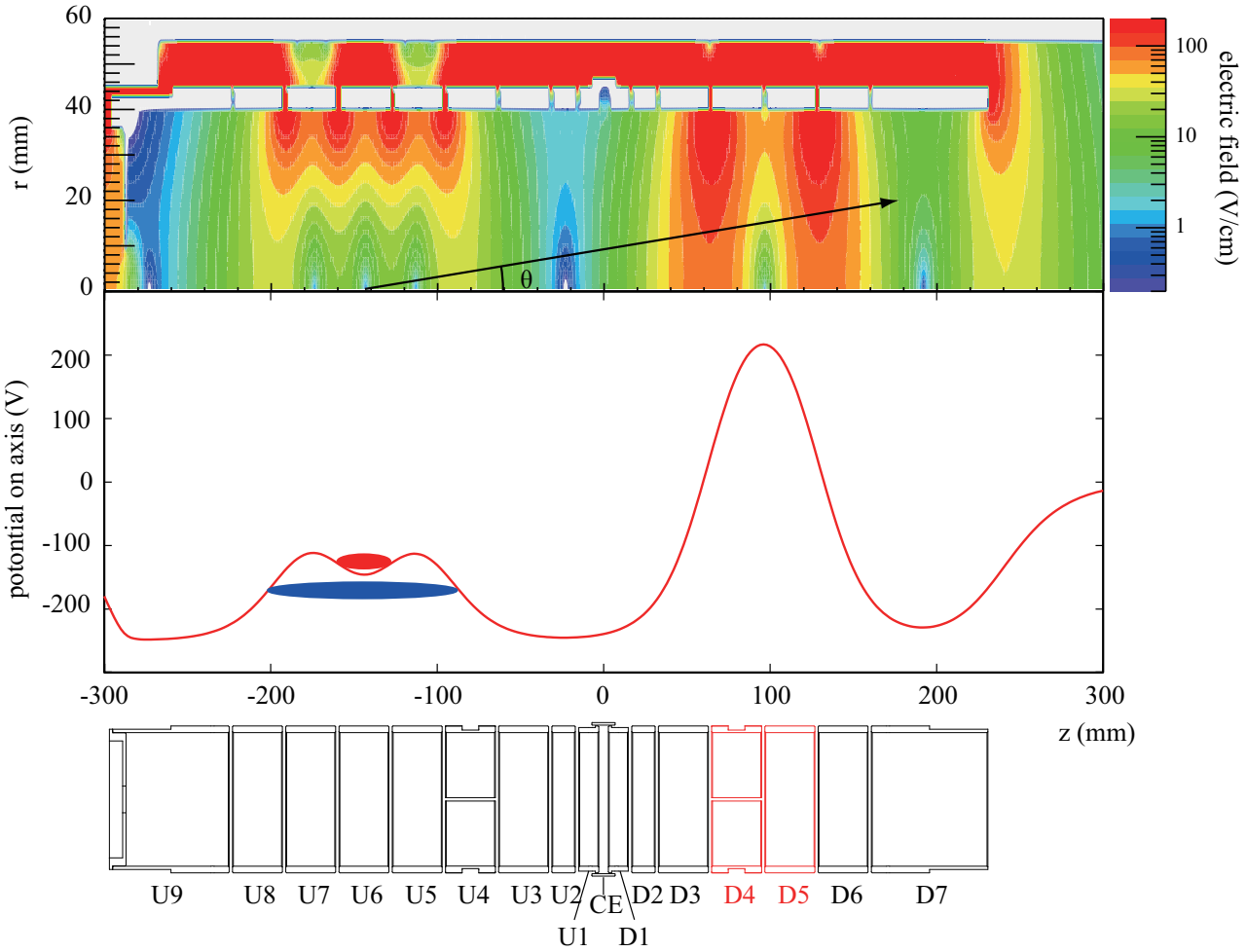

Figure 6.12: A 2D map of the electric field (top), electric potential on axis with the indication of the position of positrons and antiprotons (middle), a cross sectional drawing of the MRE of the cusp trap (bottom). A black arrow in the top indicates a trajectory of antihydrogen atom produced at z=-144 and r=0 flighting to a certain direction whose angle to the beam axis is θ.

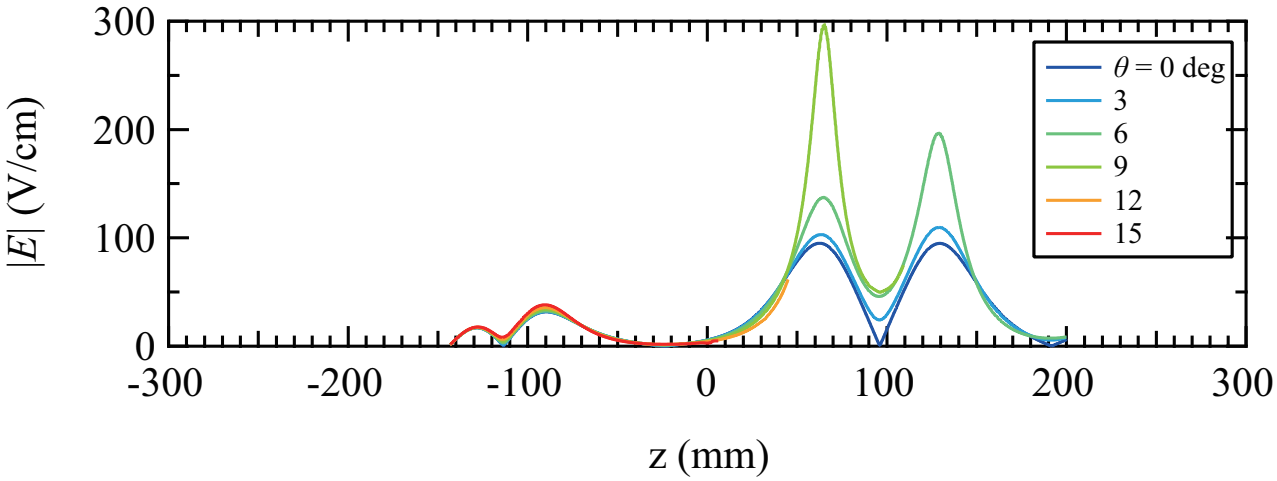

Figure 6.13: The electric field strength which antihydrogen atoms feels during the flight for several different θ as a function of z. In this case, $V_{FI} = 360V$. As θ increase, the maximum field increase since the atom pass closer to the electrode. When θ is too large, the atom hit the electrode before reaching to the FIT. This is why the red and the orange line stop $z < 200$ mm.

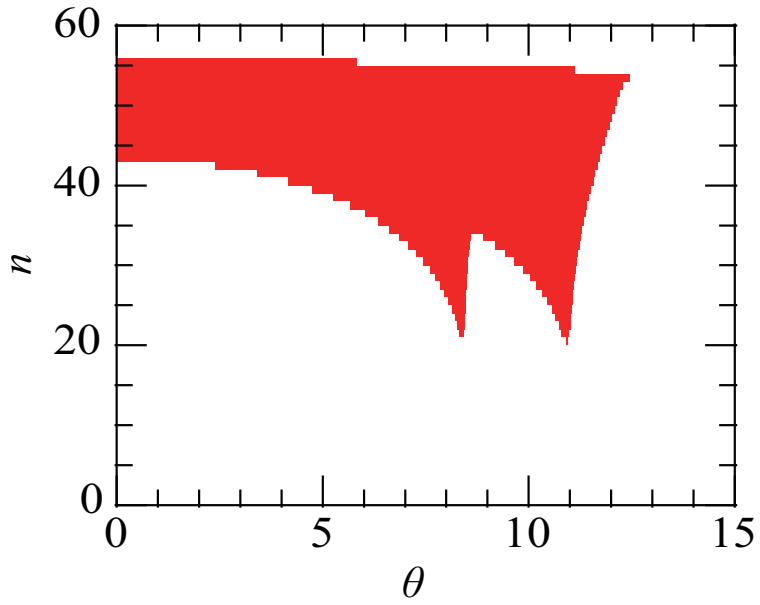

Figure 6.14: The region where antihydrogen atoms can be field-ionized in the case of $V_{FI} = 360V$. If the principle quantum number (n) and emission angle (θ) of the atom is in the region, it is detected.

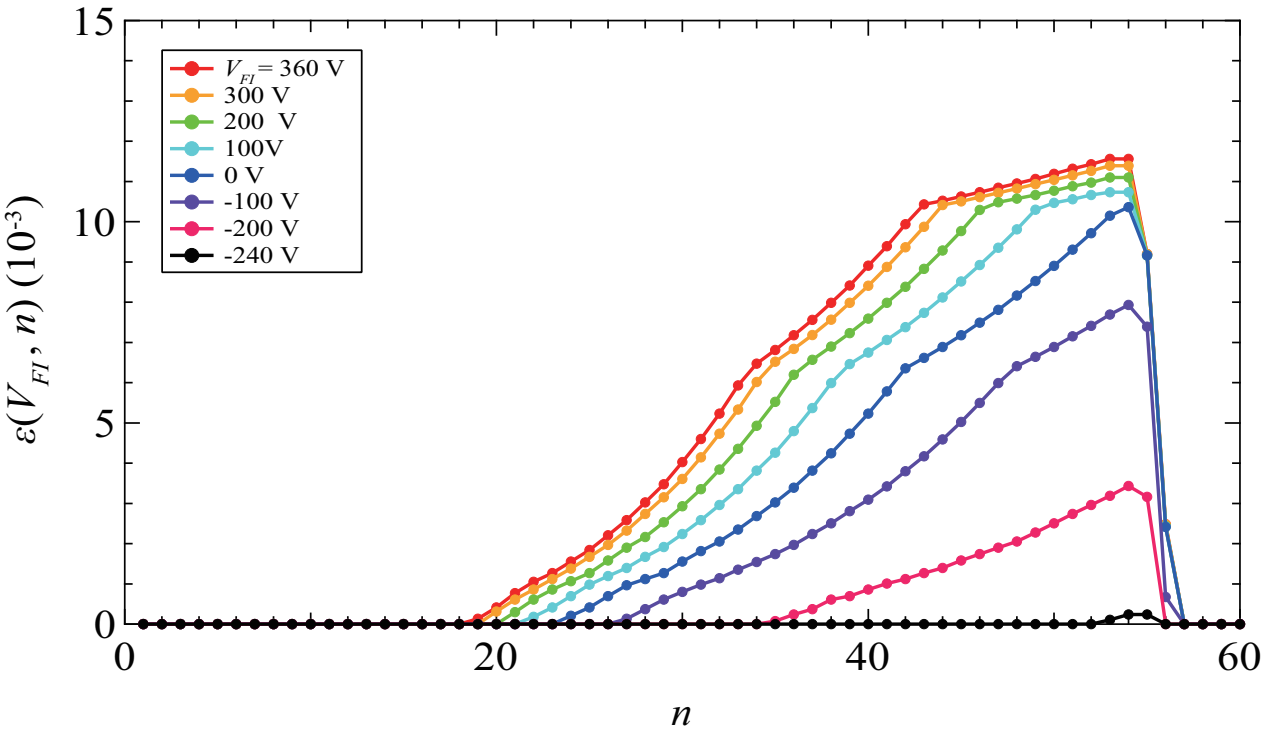

Figure 6.15: Detection efficiency ($\varepsilon(V_{FI}, n)$) as a function of n for several differentV_{FI}'s. If n is too small, the atom can not be ionized. If n is too large, the atom is ionized before escaping from the nested trap. Maximum detection efficiency, when V_{FI} =360 V, is about 1.1 %, which is roughly the same as solid angle to the FIT i.e. almost all of the atoms arrived at the FIT are ionized and detected.

experiment

In order to estimate n of the produced antihydrogen atoms, we measured the number of the antihydrogen atoms with changing the V_{FI} (i.e. changing the strength of the electric field in the FIT). Potential configurations used in this measurement are shown in figure 6.16 (a). The solid circles in figure 6.16 (b) show the number of field-ionized antihydrogen atoms as a function of V_{FI}. It is seen that the number of the field-ionized atoms increased as V_{FI} increased, and saturated. The seven curves in figure 6.16 are the result of the simulation described above and correspond to field-ionization probabilities of antihydrogen atoms, which are scaled to the experimental value at $V_{FI} = 350$V. The present observation is consistent with the curves for $n \sim 45$ and/or 50. Considering the result of the simulation shown in figure 6.15, the detection efficiency of the antihydrogen atom by field-ionization method in our configuration is about 1.1 % when $V_{FI} = 350$ V. Using this value, we can obtain the total number of field-ionized antihydrogen atoms and the conversion efficiency of the antiprotons to antihydrogen atoms, which is presented in the previous sections.

In the meantime, we remind the equation 2.14, which relate n and temperature of positrons T. Substituting the values of constants, we obtain

$$T = \frac{1.57 \times 10^5}{an^2}. \tag{6.9}$$

This equation gives $T = 63$ K for $n = 50$ and $T = 78$ K for $n = 45$ respectively when a=1. These values are consistent within a factor of 2 or 3 with the temperature of positrons measured independently (see section 5.3), even though the analysis is classical and simple.

On the other hand, there was possibility that the antihydrogen atoms in low n states were created. Figure 6.17 shows the annihilation position of antiprotons when they were confined with positrons (black) and without positrons (red). As can be seen from the figure, there is a peak at the center of the nested trap only when antiprotons were confined with positrons. This means that a part of the antihydrogen atoms was not ionized by the strong electric field near the electrodes (see figure 6.12). Figure 6.18 shows the annihilation position of antiprotons when they were confined with positron (black). Red curves shows calculated detection efficiency of antihydrogen atoms for several n's. In this calculation, antihydrogen atoms of specific n (i.e. specific biding energy) were emitted from the position (r=0 mm z=-144 mm) to the direction $0° < \theta < 180°$. Then the electric field on the path was calculated. When the binding energy of the atom was greater than the electric field, the atom reached the electrodes and we can detect

its annihilation. Thus, if the binding energy of the atoms was enough large compared with the electric field, like figure 6.18 (a), the detection efficiency is determined by solid angle. On the other hand, if the binding energy is small enough, most of the atoms were ionized before reaching the electrodes and were not able to detect as shown in figure 6.18 (h). This figure suggest that antihydrogen atoms, whose n was small, were produced.

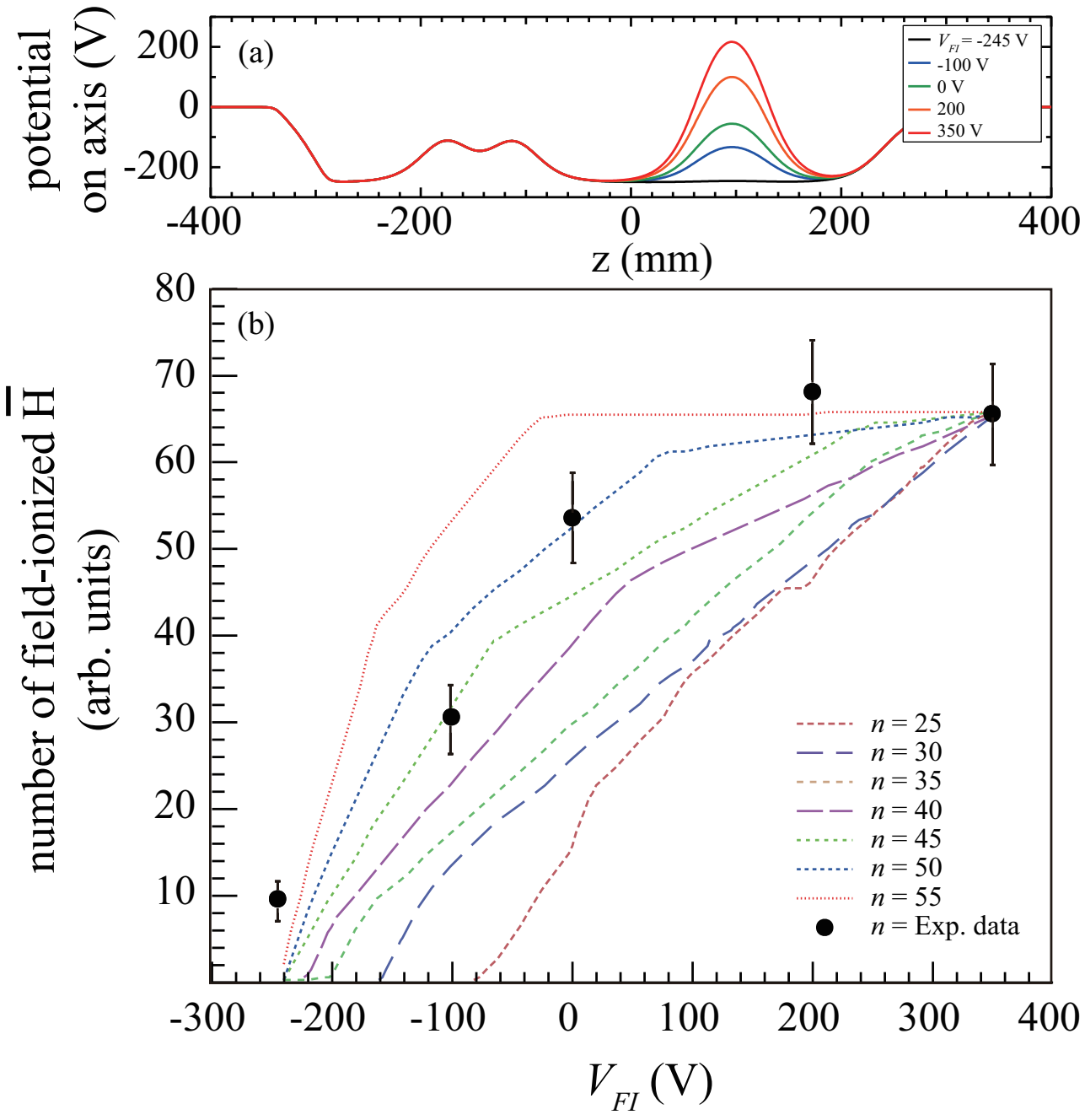

Figure 6.16: Potential curves used to evaluate the n of field-ionized antihydrogen atoms (a). The number of field-ionized antihydrogen atoms as a function of the V_{FI} (b). The solid circles show the experimental results. Seven curves correspond to calculated field-ionization probabilities of antihydrogen atoms. The probabilities are scaled to the experimental value at 350 V.

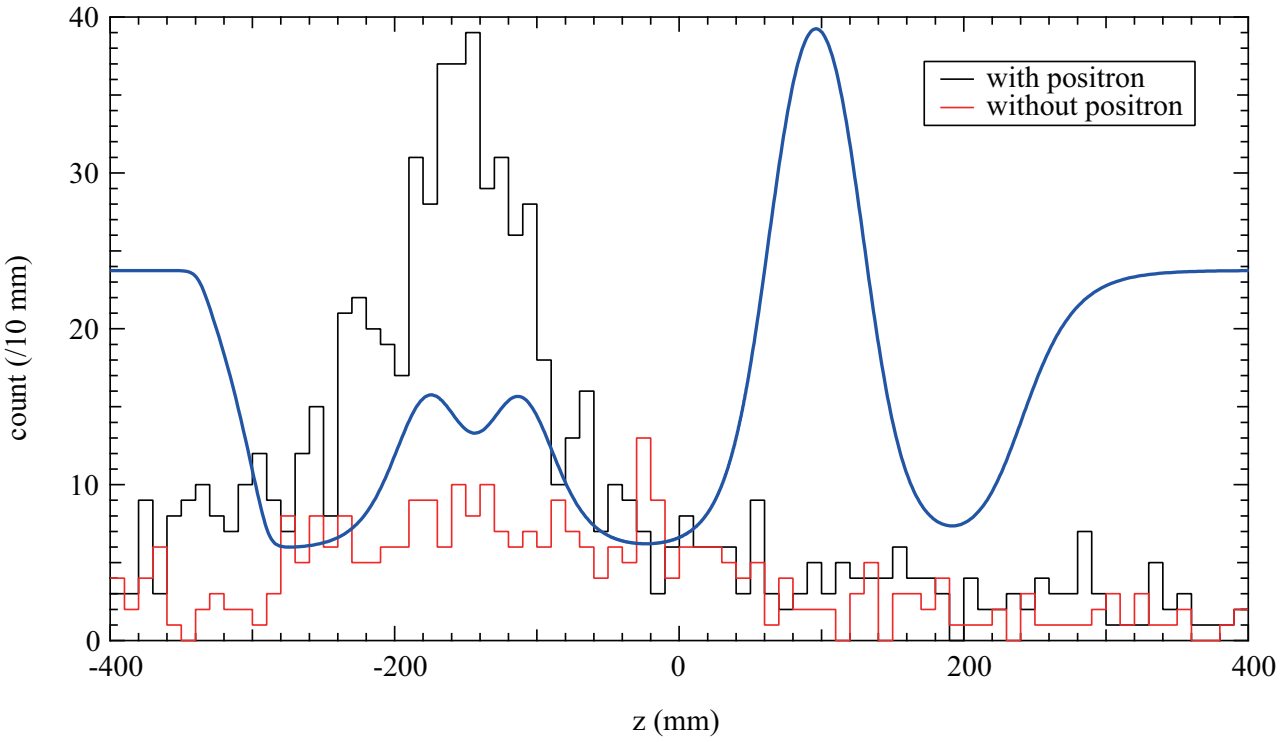

Figure 6.17: Annihilation position distribution of antiprotons when they were confined with positrons (black) and without positrons (red). Blue curve represent the potential on axis. Annihilation signal around the nested trap increased when the production of antihydrogen atoms were expected.

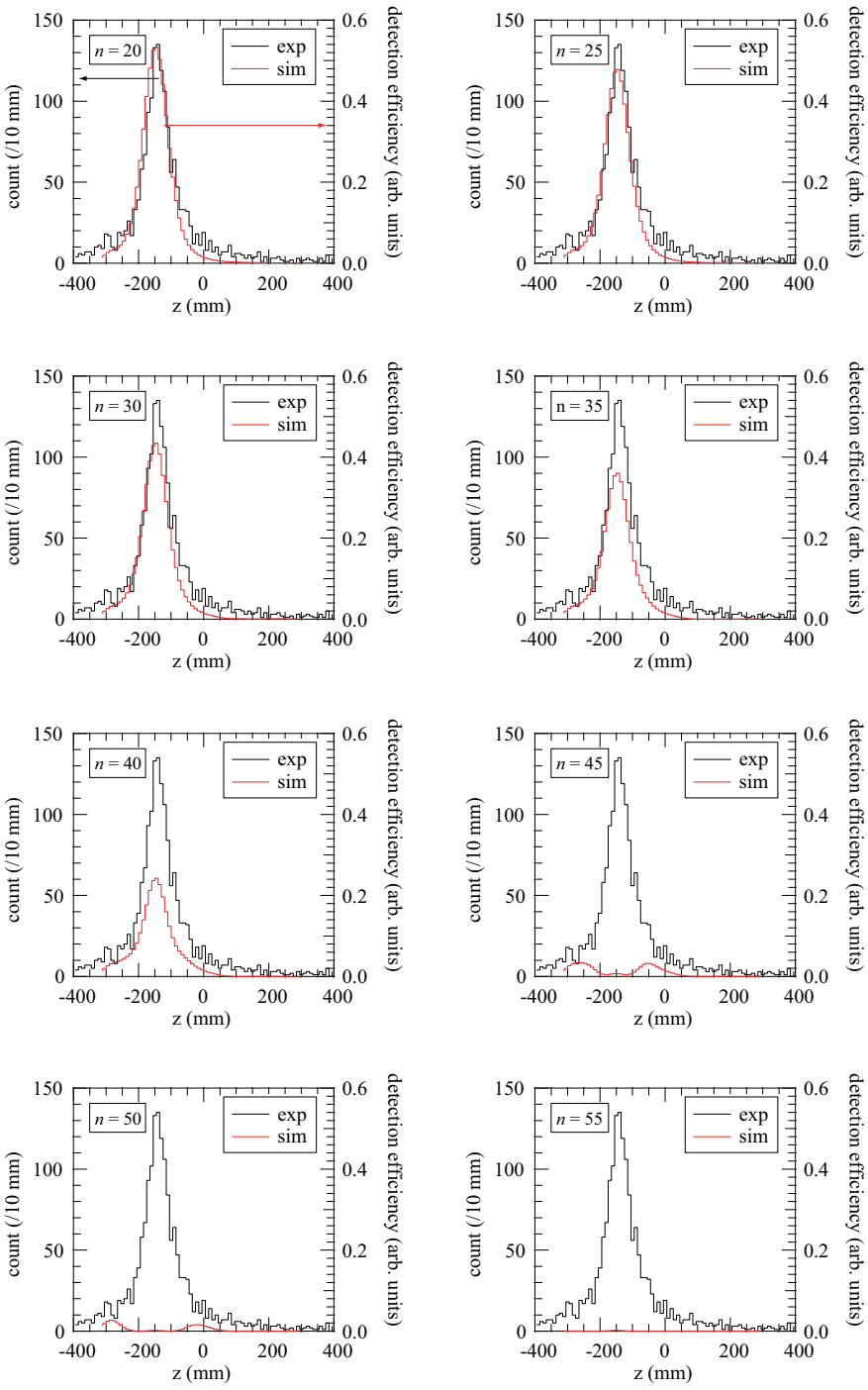

Figure 6.18: Experimentally measured annihilation position distribution of antiprotons (black). Calculated annihilation distribution of antiprotons when antihydrogen atoms, in a specific n state, are emitted isotropically from the center of the nested trap (red). In this calculation, we assume that the atom which is ionized before reaching the electrode can not be detected. Resolution of the detector is taken into account in the calculation. These data suggest that the atoms in small n state, which can not be detected by the field-ionization method, are produced.

Chapter 7

Conclusion

We have developed the cusp trap for the production of the antihydrogen atoms. In the way to the production of the antihydrogen atoms, we confirmed stable (more than thousand seconds) confinement of antiprotons, stacking of positrons, and compression of the positron cloud by the rotating wall technique in the cusp trap. Also we developed the antiproton catching trap, the compact all-in-one positron accumulator, the transport beamline for the ultra-low energy antiproton and positron beam, 3D detector to detect the antihydrogen atoms, and MCPPS detector to diagnose the charged particles.

As a result of these long and various development of the apparatus and techniques, we have succeeded to produce a large number of cold antihydrogen atoms in the cusp trap. We also confirmed the production of the antihydrogen atoms by controlling the temperature of the positrons. We measured the dependence of the production efficiency and time evolution of the production rate of the antihydrogen atoms on the number of positrons and antiprotons. The conversion efficiency of antiprotons to the antihydrogen atoms was as high as 7 %, and now we are in the way of optimization. The principle quantum number of the produced antihydrogen atoms was evaluated by measuring the number of field-ionized antihydrogen atoms as a function of the depth of the field ionization trap or the annihilation position distribution of antiprotons.

These success opens for the first time a realistic path to make the stringent test of the CPT symmetry with an extracted antihydrogen beam and will play an important role in the expanding antimatter physics.

Appendix A

Accelerators, RFQD and beamlines

A.1 AD and accelerator complex

Low energy antiproton beam suitable for the antihydrogen production experiment is available only at antiproton decelerator (AD) in CERN today.

Figure A.1 is a schematic drawing of accelerators related to the production of low energy antiproton beam in CERN. Protons are accelerated by a linac (LINAC2), a booster synchrotron (PSB) and a main synchrotron (PS) to 26 GeV/c, then they are extracted to an iridium target at the entrance of the AD to produce antiprotons by pair creation.

The produced antiprotons are collected by a magnetic horn and injected into the AD[78, 79, 80, 81]. Figure A.2 [26] shows a typical operation cycle of the AD and layout of the AD including experimental area. The antiprotons are decelerated and cooled from 3.5 GeV/c (2.7 GeV) to 100 MeV/c (5.3 MeV) in stages by stochastic[82] and electron cooling, then they are extracted to the beamline in our experimental area. Typical operation cycle of the AD is about 100 s. The bunch length of the beam is about 100 ns and the number of antiprotons per bunch is $3 - 4 \times 10^7$. The circumference of the AD is about 200 m and our experimental area is inside the ring.

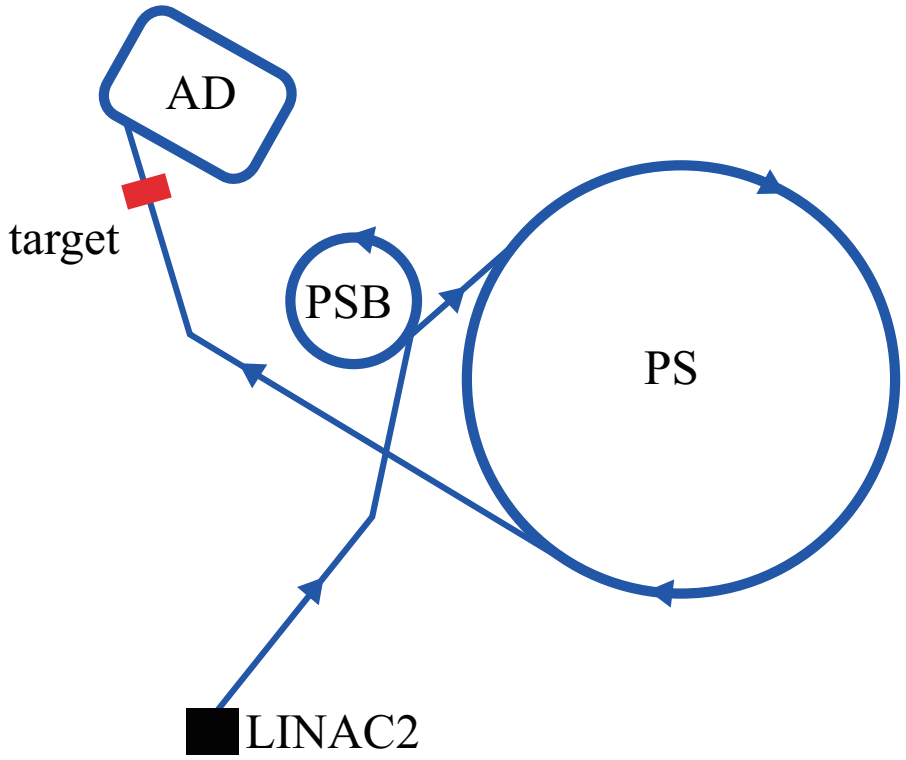

Figure A.1: Accelerators and decelerator used for the production of low energy antiproton beam. Antiprotons are created at the target by protons accelerated with the LINAC2, the PSB, and the PS.

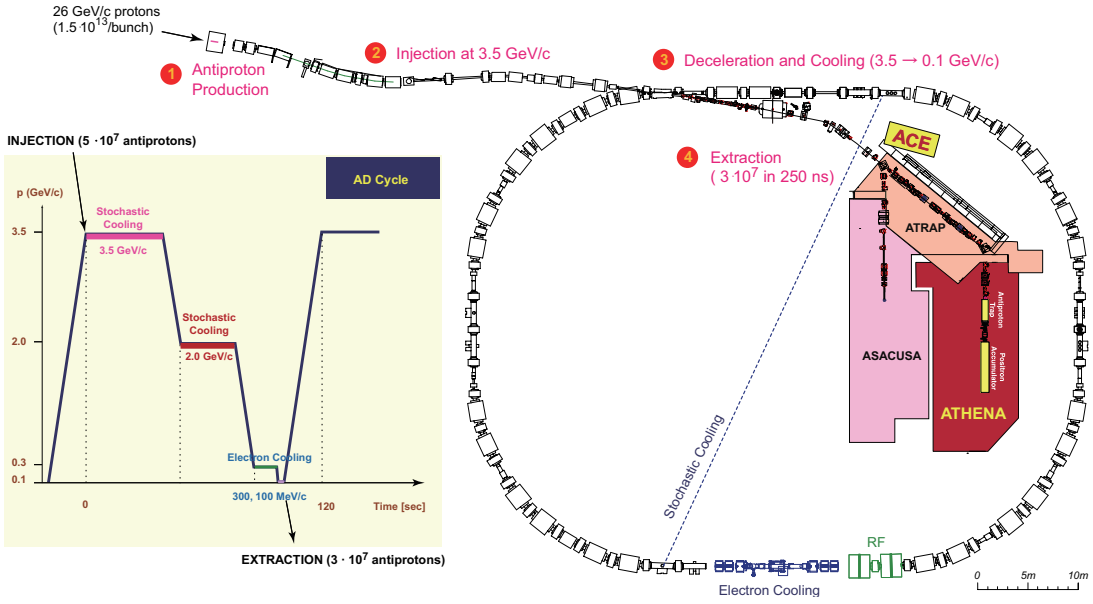

Figure A.2: Typical operation cycle of the AD (left) and layout of the AD. Produce antiprotons are cooled successively to 100 MeV/c and extracted to the experimental area in the ring.

A.2 Beamline for 5.3 MeV antiprotons

Figure A.3 shows the configuration of extraction beamline for the 5.3 MeV antiprotons. In this section, antiprotons are guided and focused by several dipole and quadrupole magnet to the radio frequency quadrupole decelerator (RFQD) for further deceleration to 10-120 KeV. Several wire chamber (MWPCxx) and two scintillators (scintillator/watchdog # 1 and # 2) are located to monitor the profile of the antiproton beam. The beam can be tuned by ourself changing the current of the coils, if necessary

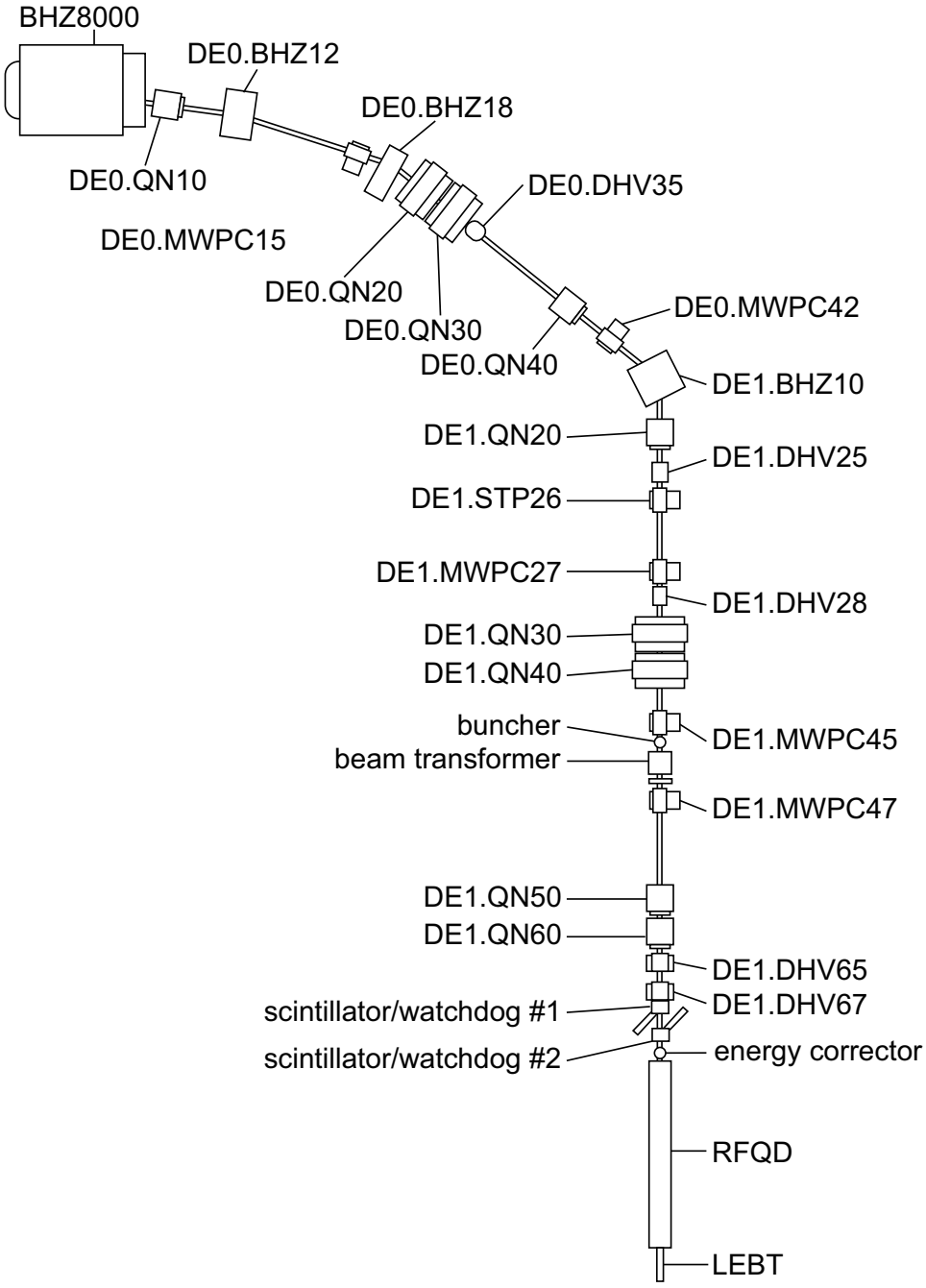

Figure A.3: Configuration of extraction beamline for the 5.3 MeV antiprotons. Antiprotons are guided by several magnets (BHZxx, DHVxx, QNxx). Multi-wire proportional chambers (MWPCxx) and scintillators are installed to monitor the beam profile.

A.3 RFQD

The RFQD was designed and constructed for further deceleration of antiprotons. RFQ is a type of linear accelerator usually used as pre-accelerator for larger accelerator rings. In contrast, the RFQD uses its modulation to decelerate antiprotons from 5.3 MeV to 63 KeV.

The RFQD consists of 4 rods and 34 RF cells (see figure A.4), which are electrically floated from the ground potential. By changing the floating voltage, we can tune the output energy of antiprotons from 10 keV to 120 keV. Details on the RFQD can be found in [83, 84, 85].

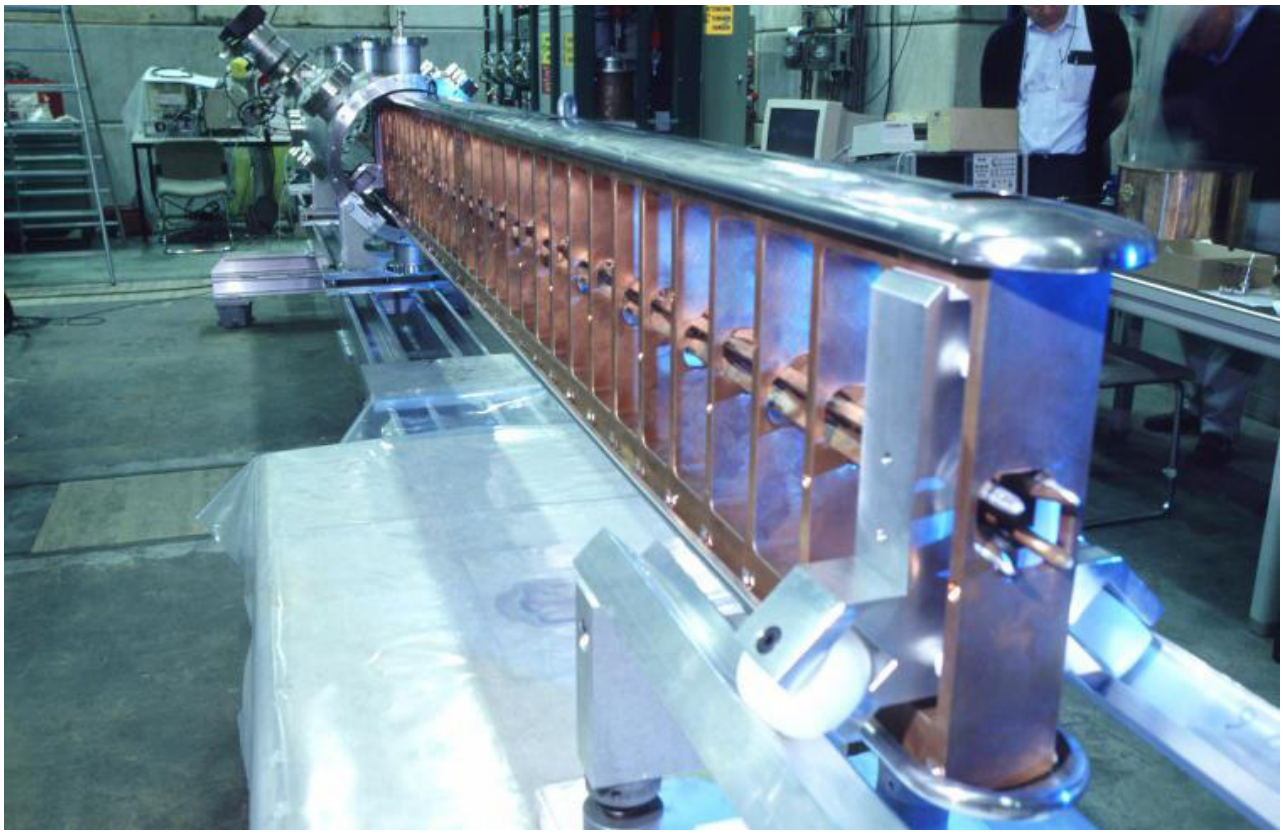

Figure A.4: A photograph of rods and RF cells of the RFQD.

Appendix B

positron temperature analysis method

We summarize the method to analyse the temperature of positrons confined in the cusp trap[1]. A basic idea is that we measure the amount of charge escaping from the trap by slowly decreasing the height of potential wall (see figure 5.11). For example, when one positron is confined in the cusp trap, we can measure its kinetic energy, parallel to the magnetic field, by decreasing the heigh of potential wall and record its value when the positron escapes from the trap. However, when space charge of the confined particles is greater than the kinetic energy of them, we have to take into account that effect[2].

As a preparation for the analysis we define some notations as below.

- T: Temperature of the charged particles parallel to the magnetic field line.
- e: Unit charge.
- k: Boltzmann constant.
- N: Number of particles in the trap before the extraction.
- ϕ_c: Potential on axis created by external voltages.
- ϕ_p: Potential created by space charge of the particles in the trap.
- $E(\phi_c)$: Minimum kinetic energy of the particles required to escape over the confining potential ϕ_c (i.e. $E(\phi_c) = q(\phi_c - \phi_p)$).

[1]The method is described in detail in ref. [77].

[2]For example, when 1×10^8 charges are confined in a sphere whose radius is 1 mm, the electric potential on the surface of the sphere is about 0.6 V.

- $F(E)$: Energy distribution function of positrons.
- $Q_{esc}(\phi_c)$: Amount of the leaked charges, when the confinement potential is ϕ_c.

When we decrease the height of the potential wall to extract positrons, $Q_{esc}(\phi_c)$ is given by

$$Q_{esc}(\phi_c) = eN \int_E^\infty \frac{dE'}{\sqrt{E'}} F(E'), \tag{B.1}$$

as long as the number of positrons in the trap does not change so much. If we assume that the energy distribution of positrons in the trap is Maxwell distribution; i.e.,

$$F(E) = \frac{1}{\sqrt{\pi kT}} \exp\left(\frac{-E}{kT}\right) \tag{B.2}$$

then the integral in equation B.1 can be evaluated and we obtain

$$Q_{esc}(\phi_c) = eN\mathrm{erfc}\left(\sqrt{\frac{E}{kT}}\right) \tag{B.3}$$

where erfc is the complementary error function. Here, we remind the asymptotic equation below[3]

$$\mathrm{erfc}(x) = \frac{e^{-x^2}}{x\sqrt{\pi}} \left\{ 1 + \sum_{n=1}^{\infty} (-1)^n \frac{(2n)!}{n!\,(2x^2)^n} \right\}. \tag{B.4}$$

Substituting equation B.4 into equation B.3, we obtain

$$Q_{esc}(\phi_c) = eN \left\{ \frac{e^{-x^2}}{x\sqrt{\pi}} \left(1 - \frac{1}{2x^2} + \cdots \right) \right\} \tag{B.5}$$

where $x = \sqrt{\frac{E}{kT}}$. Then we take logarithm and differentiate by $e\phi_c$, we obtain

$$\frac{d\ln Q_{esc}}{d(e\phi_c)} = \frac{-1}{kT}\left(1 + \frac{1}{2x^2} - \frac{1}{2x^4 - x^2}\right) \tag{B.6}$$

$$\sim \frac{-1}{kT} \tag{B.7}$$

[3]This equation is valid when $x > 1$.

Appendix C

Extraction of antihydrogen atoms

For the measurement of the hyperfine splitting of the antihydrogen atoms, the extraction of the synthesized antihydrogen to the downstream side where the microwave cavity and analysing magnet are placed is necessary. Although the cavity and the magnet is still under construction, we developed a detector used for the spectroscopy and carried out first trial to extract antihydrogen atoms to the detector.

C.1 Antihydrogen detector using an MCP and plastic scintillators

Figure C.1 shows the detector which consists of a MCP with delay line anode and plastic scintillators, with the cusp trap. The detector is connected to downstream side of the cusp trap via a bellows. Four plastic scintillator plates (shown by red in the figure) surround the vacuum chamber in which the MCP is located and two plastic scintillator plate (veto counter, shown by blue in the figure) are attached to a vacuum pipe of the cusp trap. Figure C.2 is an isometric view of the vacuum chamber and the MCP of the detector. The MCP is mounted on a linear motion feedthrough to measure the emittance if necessary.

Since the solid angle to the detector is small (1.5×10^{-4}), the expected number of antihydrogen atoms reaching the detector is less than 150 per one cycle of extraction (a few tens seconds) even if 10^6 antiprotons were injected in the cusp trap and all of them are converted into antihydrogen atoms. Thus the strict background reduction is required. There are two major background source, one is pions from the annihilation of the antiproton inside the cusp trap and the other is the cosmic ray.

Here we consider the situation that an antihydrogen atom annihilate on the MCP. Then the MCP gave a signal and annihilation products pass through the scintillators surrounding the MCP (shown by red in figure C.1). On the other hand, it is rare that the annihilation products originated from antiproton annihilation in the cusp trap hit both the MCP and the scintillators. In addition, when the pions from the cusp trap hit the scintillators, they have to pass through the veto counters (see figure C.1). Thus imposing the conditions that the MCP and the scintillators were hit and veto counters were not hit, we can eliminate the pions from the cusp trap.

For further reduction of the background, we focus on the amount of the charge outputted from the MCP. Figure C.3 shows the ADC signal of the MCP, which is proportional to the amount of the charge outputted from the MCP, as a function of time t. During $200 < t < 230$, antiprotons are slowly extracted to the detector. Figure C.4 is a projection of the data during the period when antiprotons are not extracted ($0 < t < 200$) and when they are extracted ($200 < t < 230$). As can be seen from the figures, large ADC signals (more than 120) are observed when antiprotons are extracted to the detector. Thus cutting the data using the ADC signal, we can select the data originated from the antiproton annihilated on the MCP. Since the antiproton is confined in the trap by electric potential, antiproton annihilation on the MCP considered to be originated from antihydrogen atoms.

With these strategy and configuration, simulation was carried out using GEANT4 and the expected detection efficiency of the antihydrogen annihilated on the MCP was 70 %.

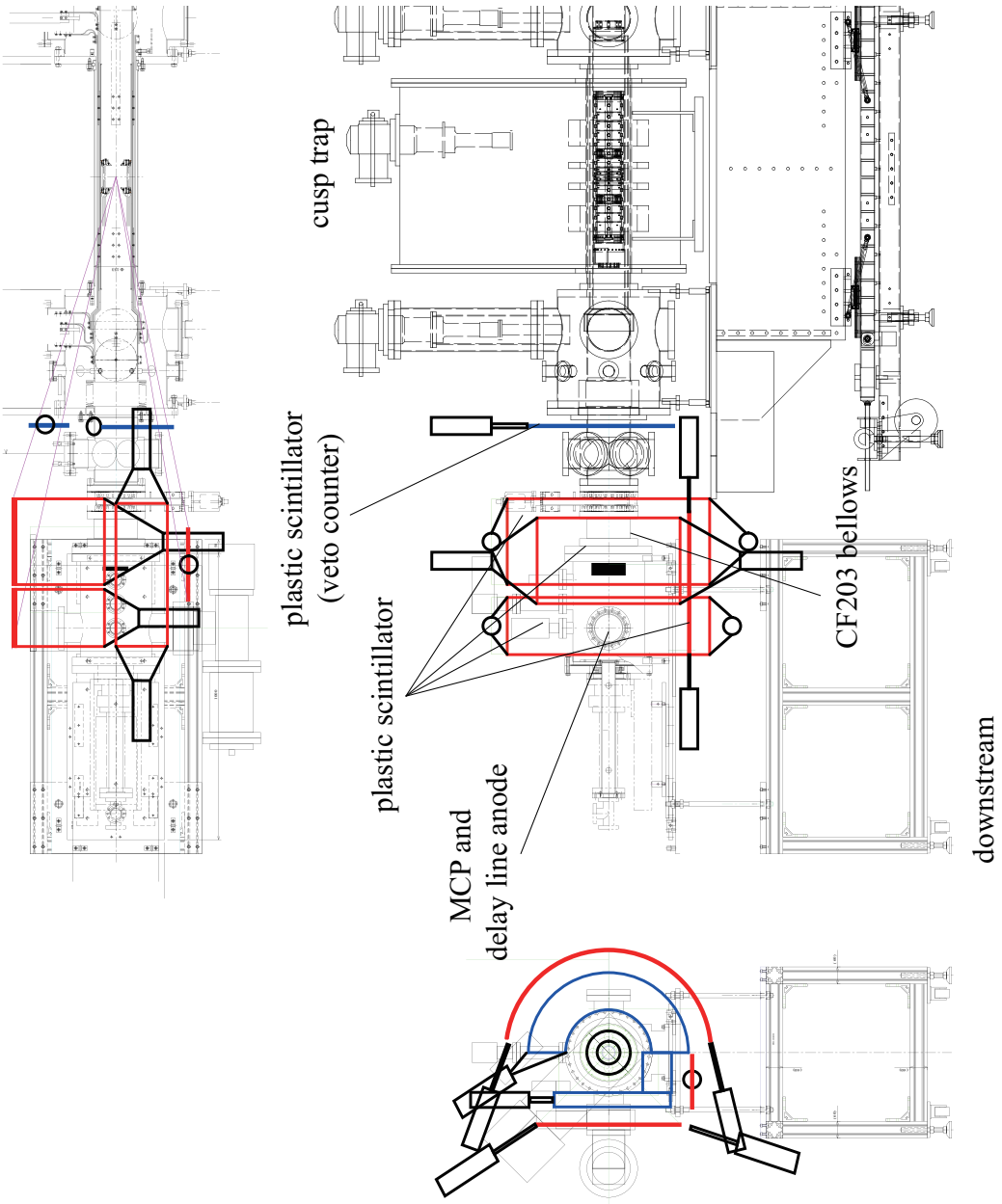

Figure C.1: A schematic drawing of the antihydrogen detector with the cusp trap. Plastic scintillators (shown by red) surround the vacuum chamber in which the MCP and delay line anode are placed. Veto counters (shown by blue) are installed between the cusp trap and the chamber.

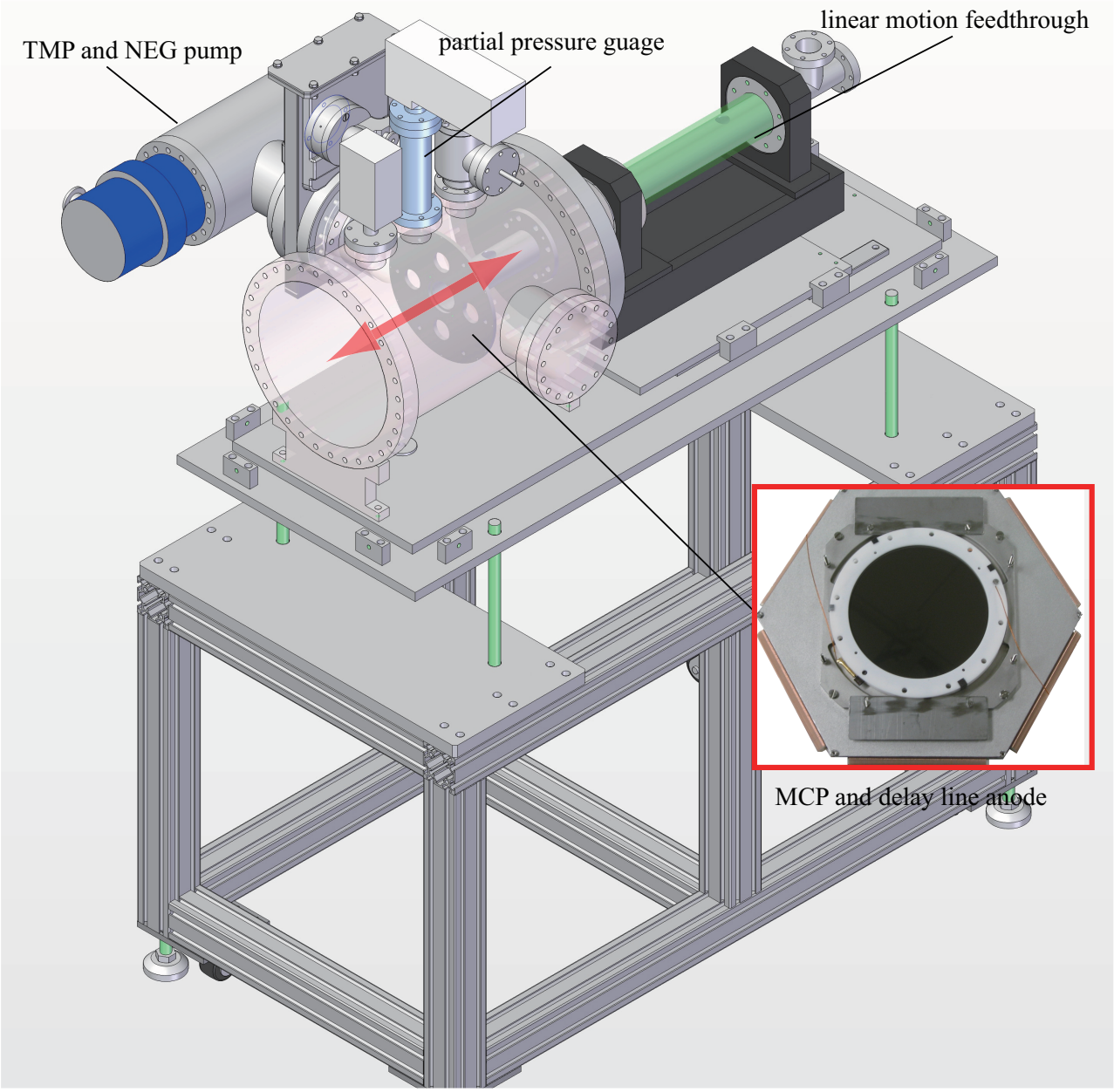

Figure C.2: An isometric view of the antihydrogen detector and a photograph of the MCP. The MCP with delay line anode (Roentdek, HEX-80) is mounted on a linear motion feedthrough to measured the emittance of the extracted antihydrogen beam. The chamber is evacuated by a TMP and a NEG pump.

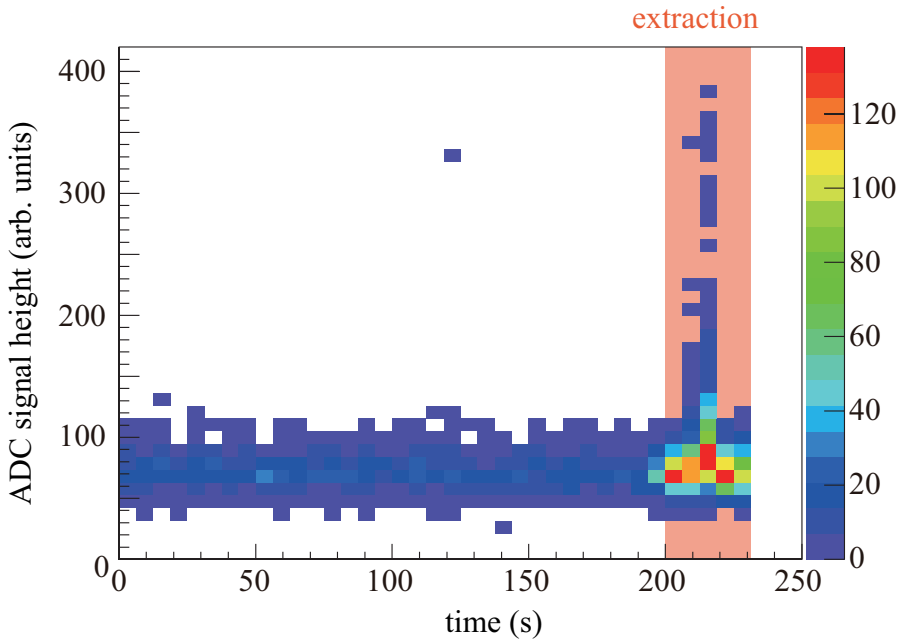

Figure C.3: ADC signal height, which is proportional to the amount of charge outputted from the MCP, is shown as a function of time. Antiprotons were extracted to the MCP during 200 s $< t <$ 230 s.

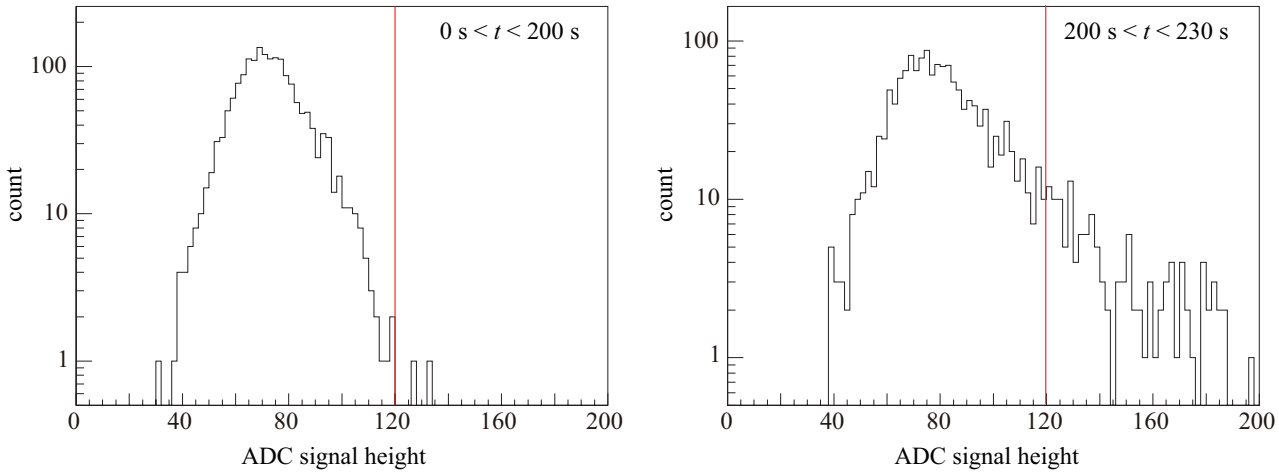

Figure C.4: Projection of the histogram shown in figure C.3 for 0 s $< t <$ 200 s (left) and for 200 s $< t <$ 230 s (right).

C.2 Trial of antihydrogen beam extraction

We carried out, for the first time, the trials of the extraction of the antihydrogen atoms to the antihydrogen detector. Table C.1 is the summary of the number of events for different cut conditions along with the background. The DAQ was triggered by the signal from the MCP. In the analysis, we put the conditions that the ADC signal height was larger than 120 (red line in figure C.4), and for the coincidence timing between the signal from the MCP and that from the scintillators was less than 50ns. The event which survive the ADC cut was 37 and 2 of them hit one of the scintillators (see extraction run row in the table). On the other hand, when antiprotons were not confined in the cusp trap (background run 1) and when antiprotons and positron were mixed but the gate valve between the cusp trap and the detector was closed (background run 2), there were no event which survive the ADC cut and hit more than one scintillators.

Though the result of the extraction of the antihydrogen is very preliminary, by the tuning of the mixing conditions of the antiprotons and positrons and more efficient production of the antihydrogen atoms, extraction and detection of the antihydrogen beam is expected in the near future.

	MCP hit	1 coin[1]	2 coin	ADC cut	ADC cut + 1 coin
extraction run	15640	11	4	37	2
background run 1[2]	1786	0	0	4	0
background run 2[3]	624	2	0	2	0

Table C.1: Summary of the number of the events for several cut conditions.

[1]The n coin means that the number of signals from the scintillators which coincide with the signal from the MCP is n.

[2]Without antiprotons and positrons.

[3]Antiprotons and positrons mixed but the gate valve between the detector and the cusp trap was closed.

Appendix D

Circuit diagrams

In this chapter, some circuit drawings used in the present work are shown.

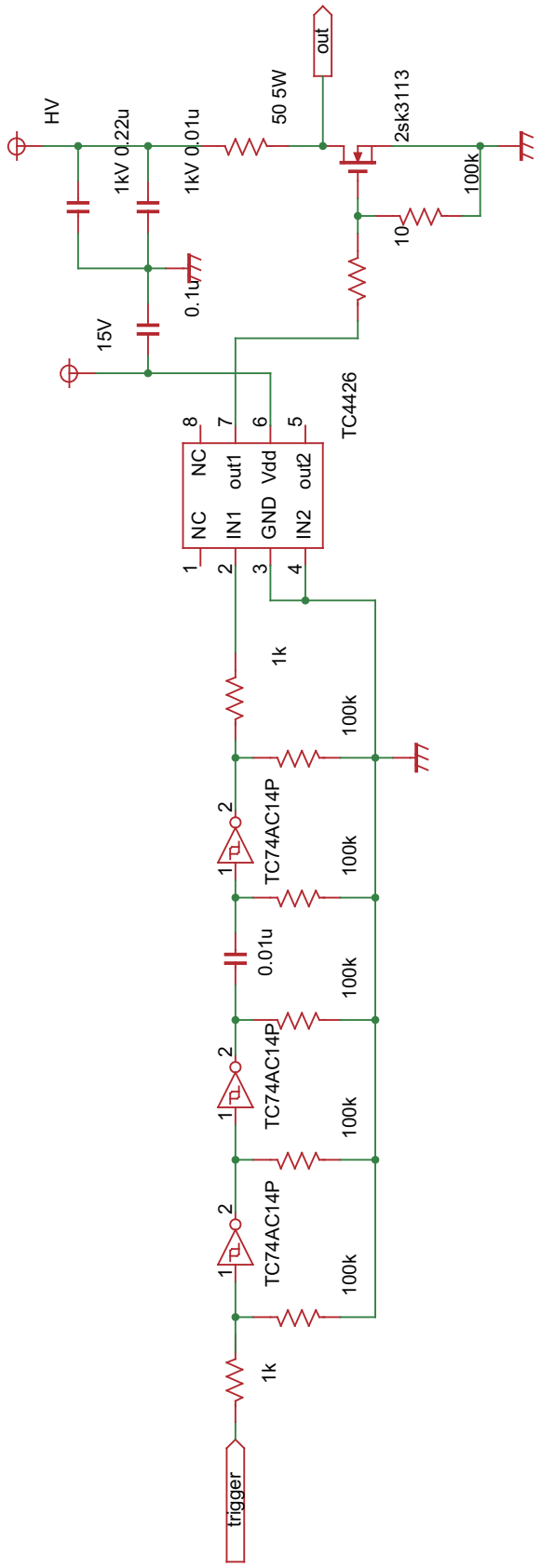

Figure D.1: A circuit drawing of the high voltage switch used to extract and capture positrons (HV switch 1 and HV switch 3).

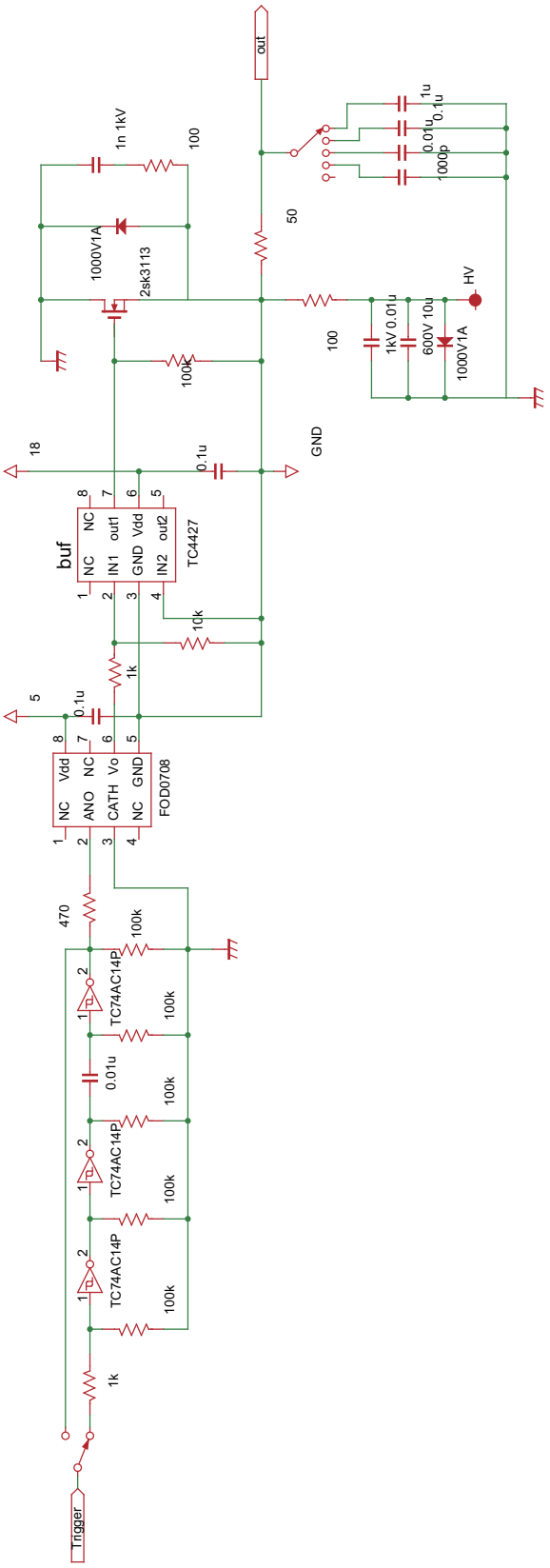

Figure D.2: A circuit drawing of the high voltage switch used to capture antiprotons (HV switch 2).

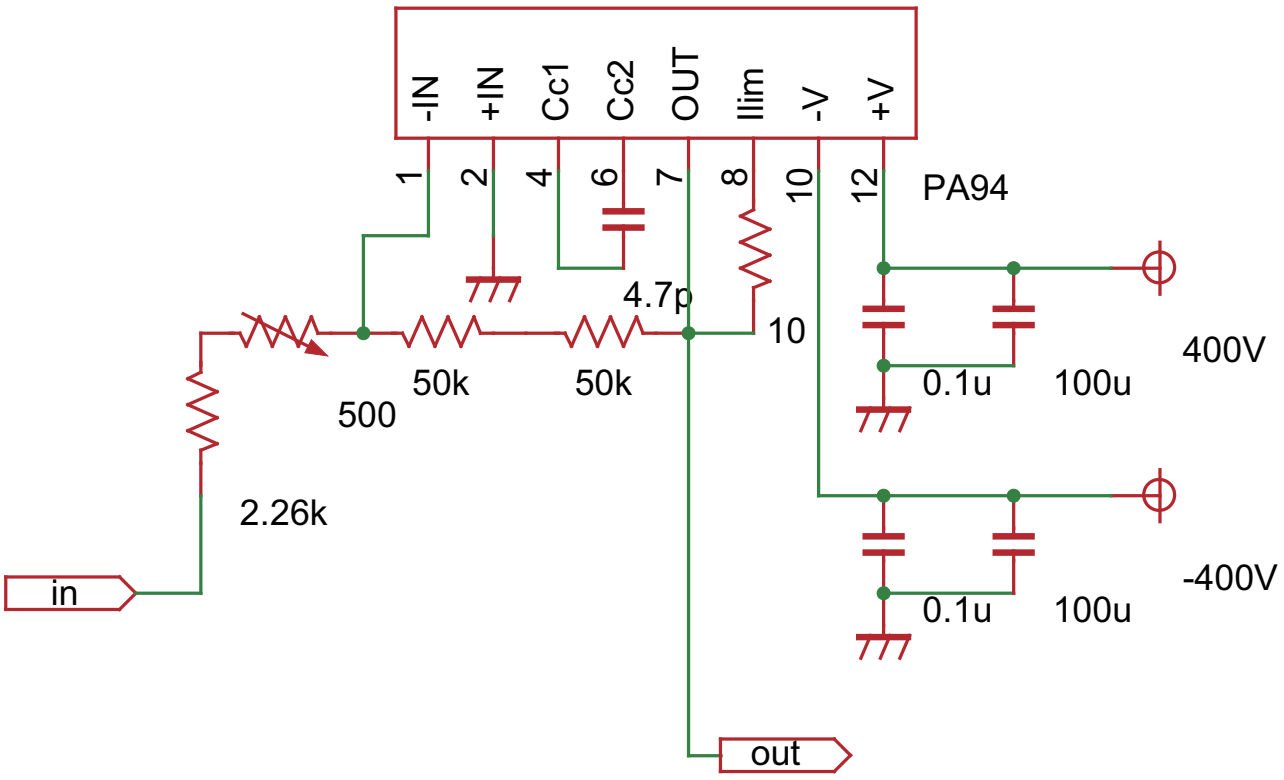

Figure D.3: A circuit drawing of the power amplifier used to control the voltage applied to the MRE of the cusp trap (cusp power amp).

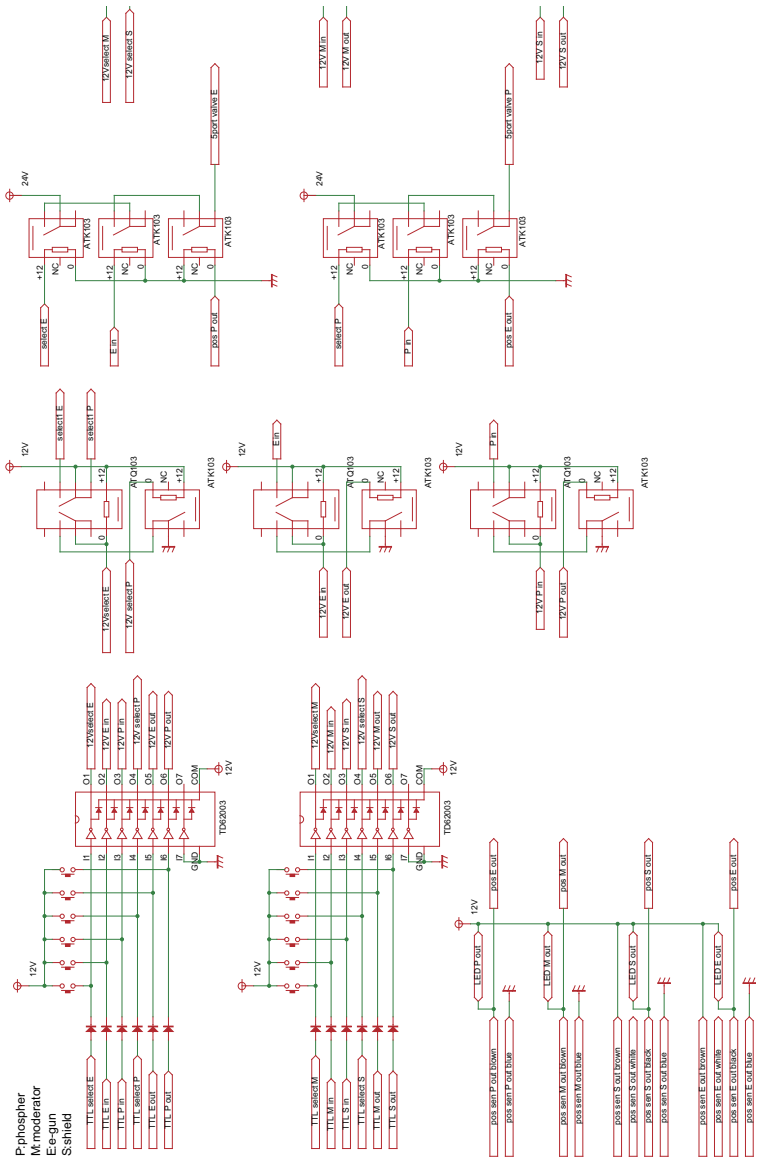

Figure D.4: A circuit drawing of the controller of the compressed air used in the positron accumulator.

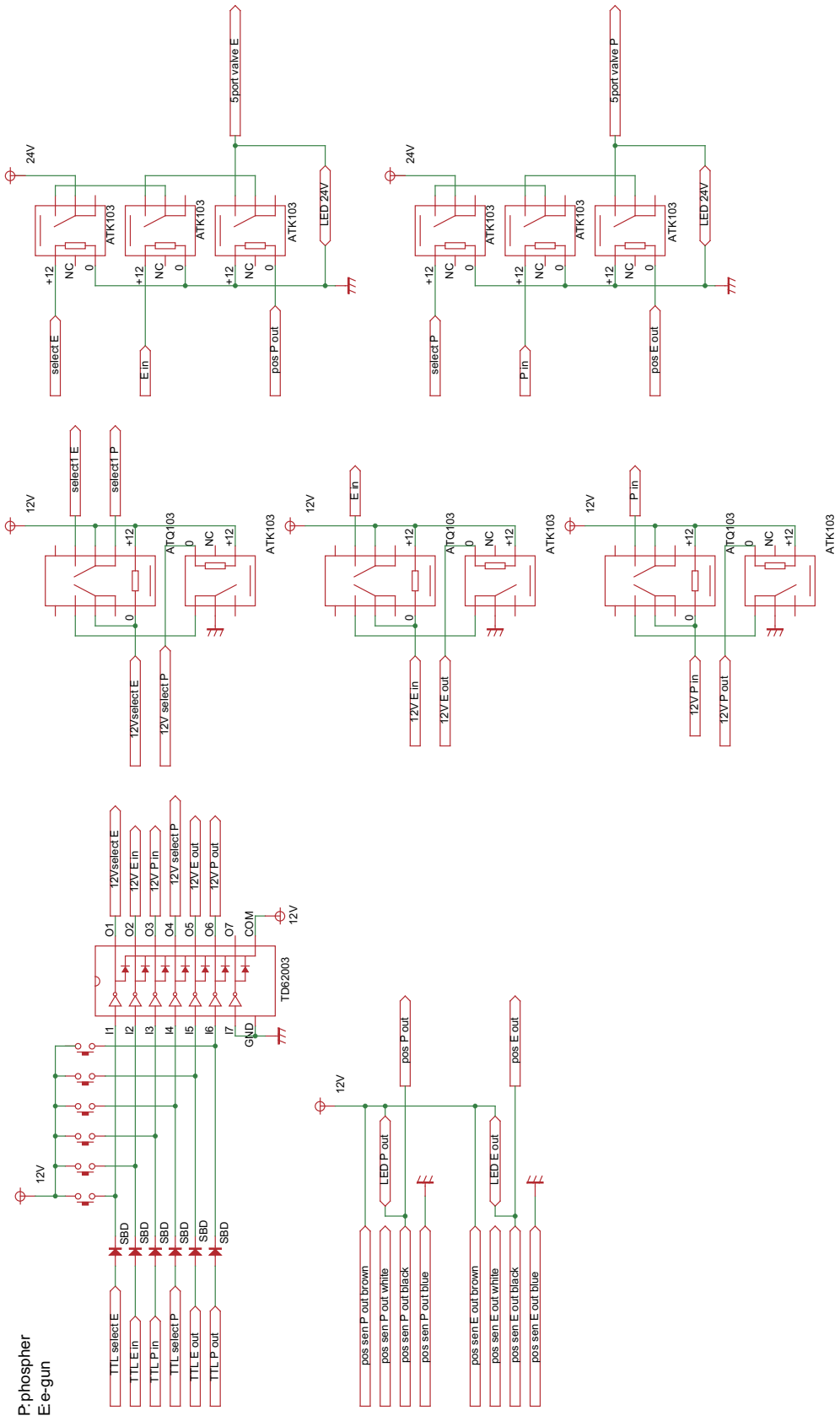

Figure D.5: A circuit drawing of the controller of the compressed air used in the cusp trap (for the electron gun and the MCPPPS detector).

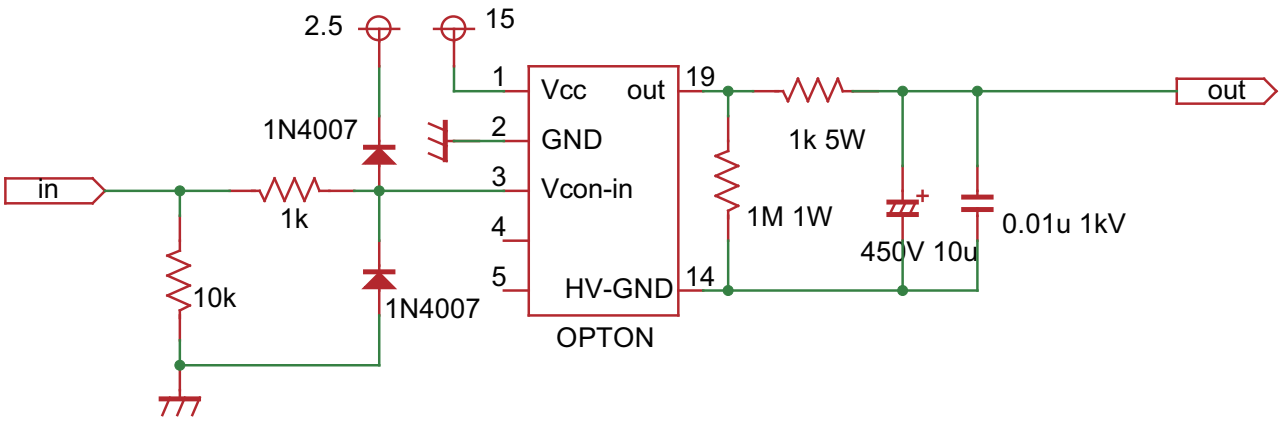

Figure D.6: A circuit drawing of the power amplifier used to control the voltage applied to the MRE of the positron accumulator (OPTON-1PC).

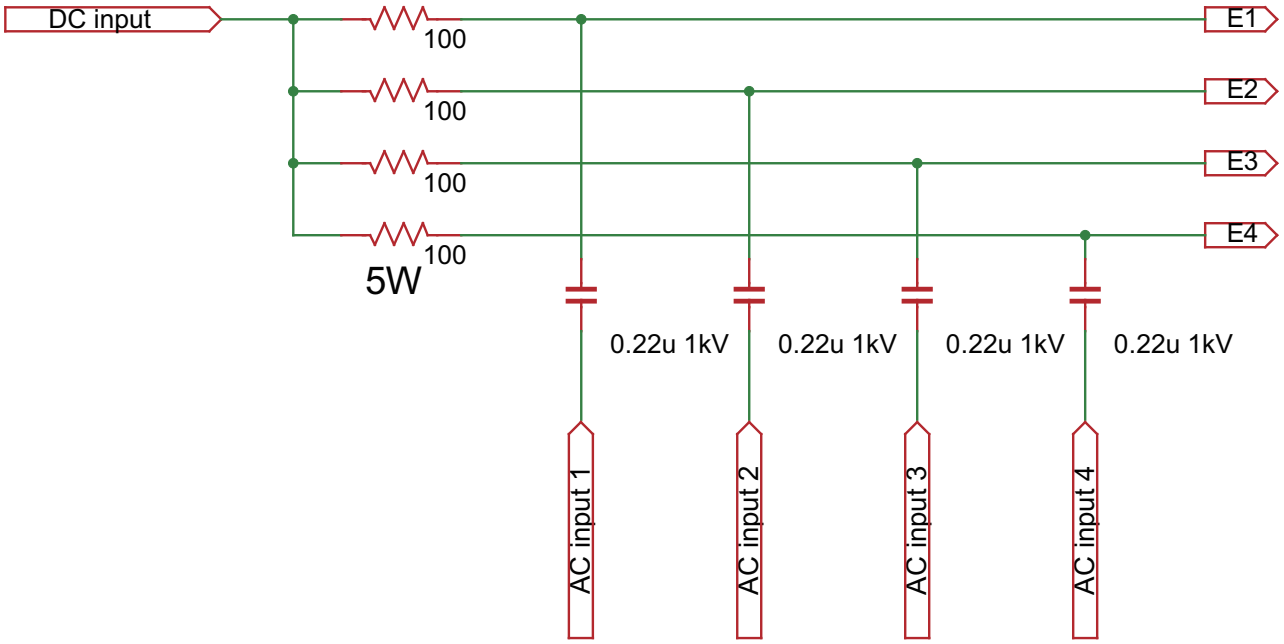

Figure D.7: A circuit drawing of the RC mixer used to mix the signals from function generator (NF, WF1974) with the DC voltage (RC mix 2).

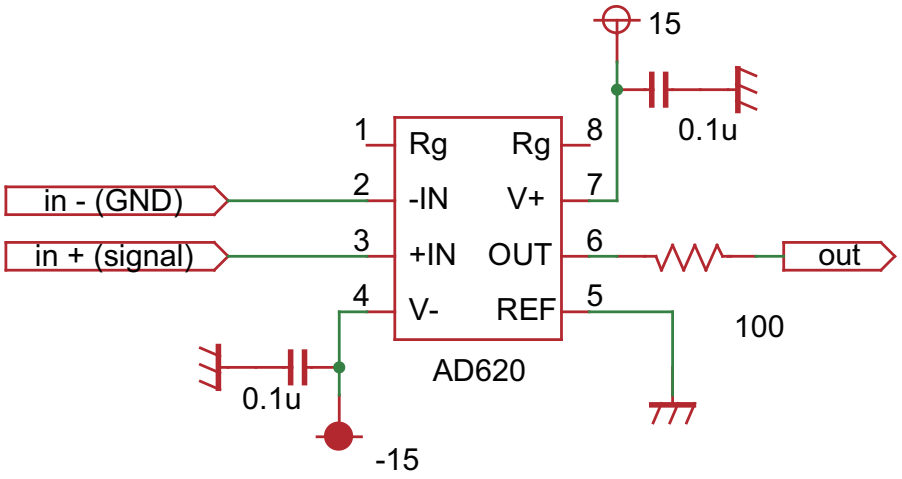

Figure D.8: A circuit drawing of the instrumentation amplifier used in the cusp trap

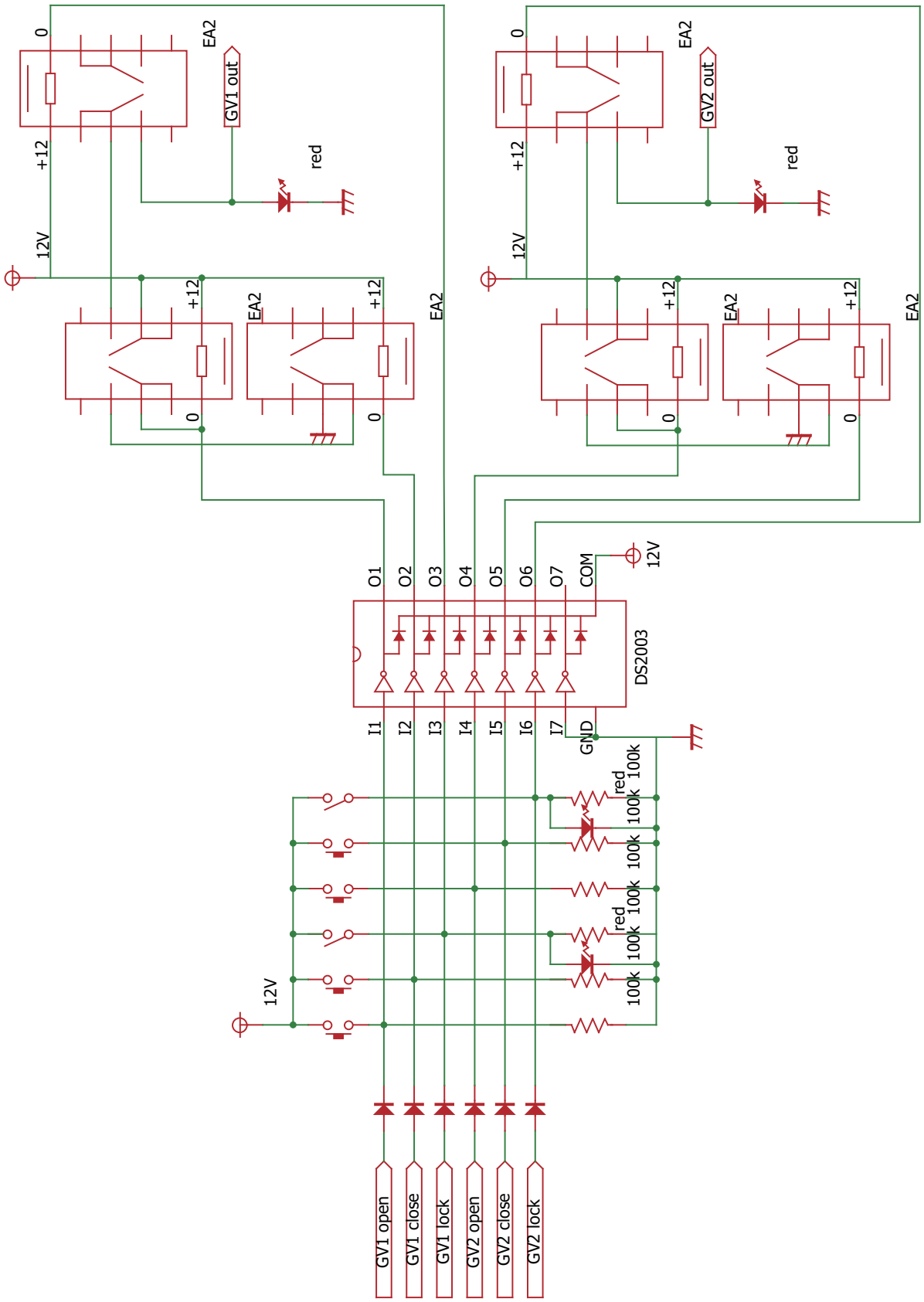

Figure D.9: A circuit drawing of the vacuum valve controller.

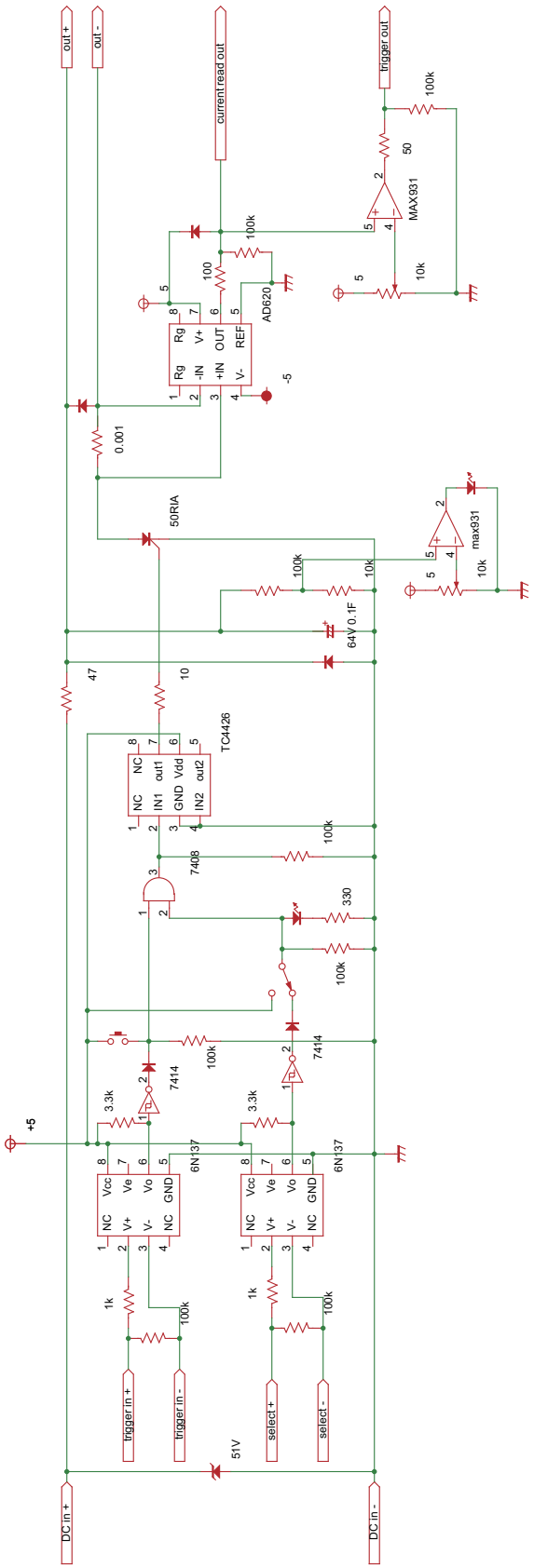

Figure D.10: A circuit drawing of the extraction coil controller.

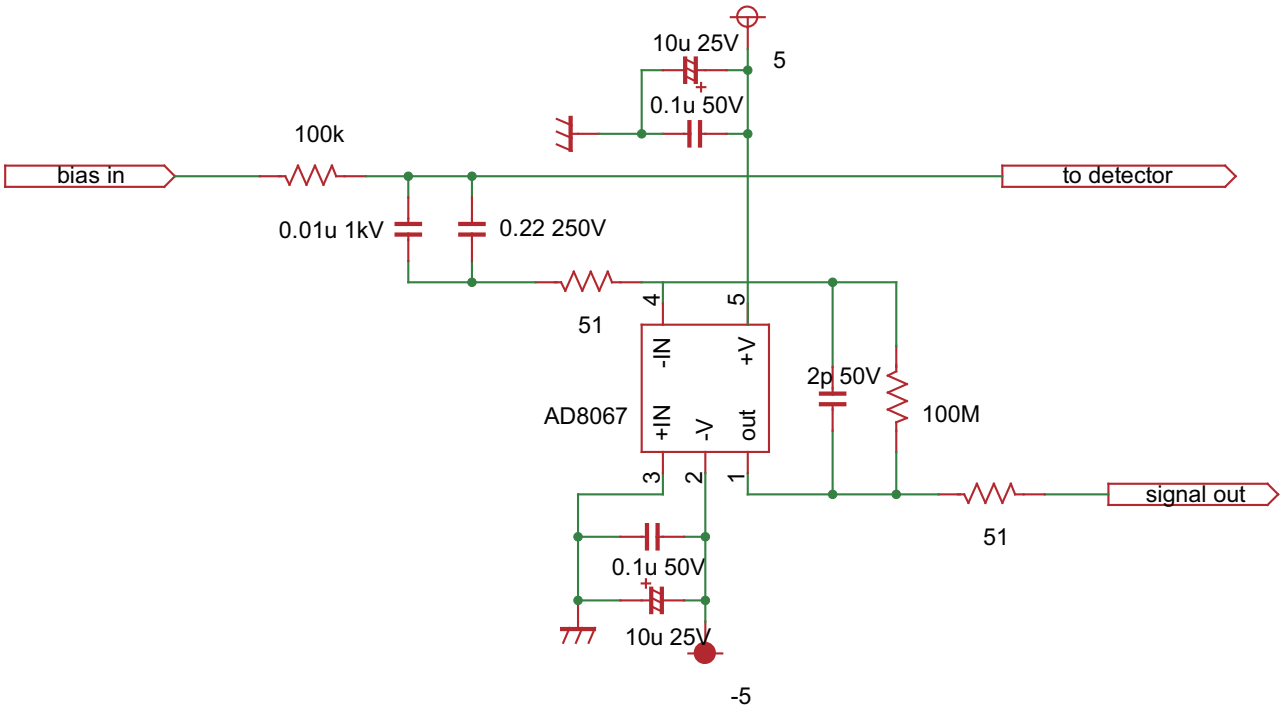

Figure D.11: A circuit drawing of the charge amplifier used to measure the number of positrons.

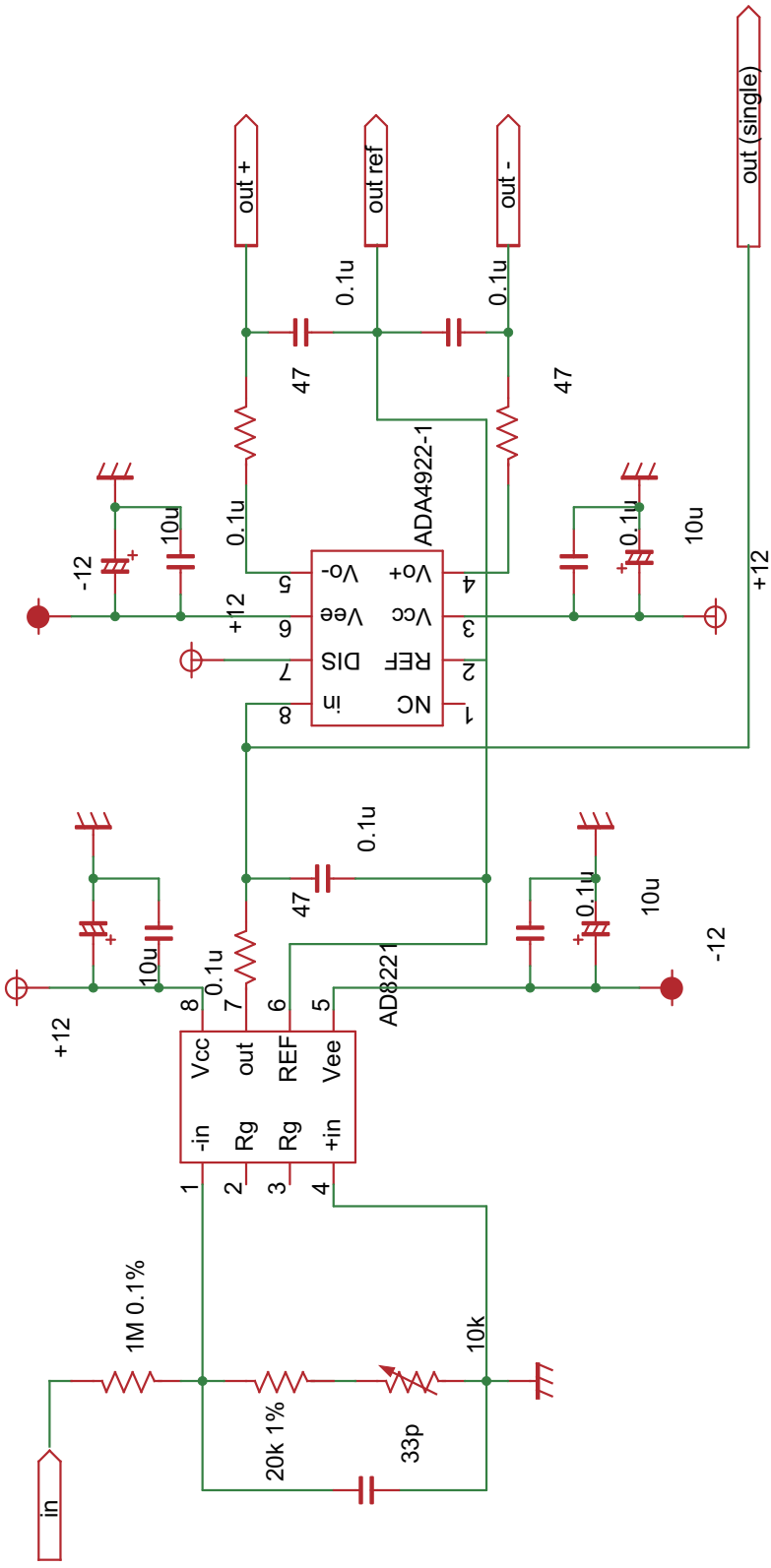

Figure D.12: A circuit drawing of the buffer amplifier used to drive ADC of the PXI express DAQ module (PXIe-6224) (Buffer amp 1).

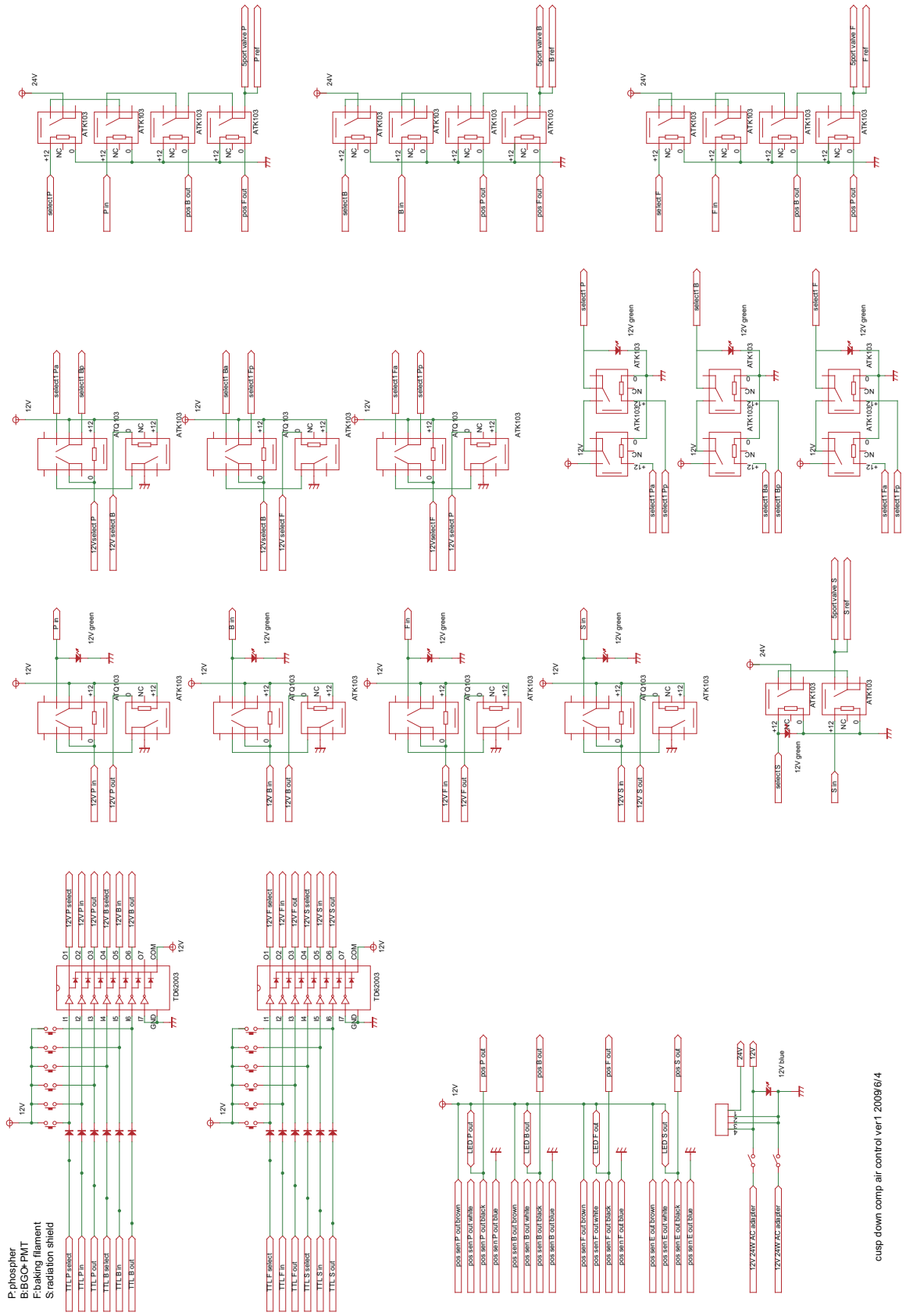

Figure D.13: A circuit drawing of the controller of the compressed air used in the cusp trap (for the UV light source and downstream thermal shield actuator).

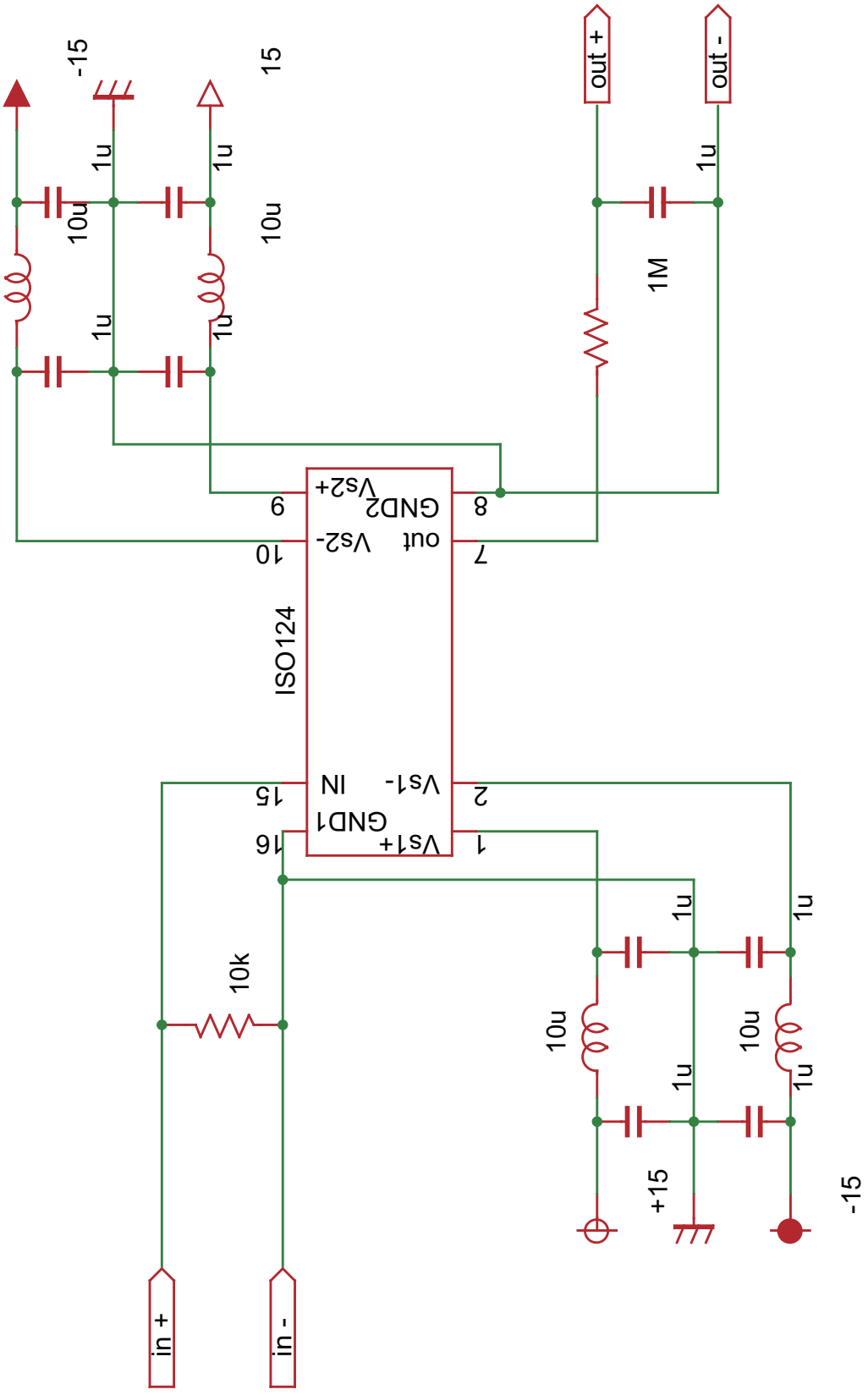

Figure D.14: A circuit drawing of the isolation amplifier between the DAC and DC power supplies (isolation amp 1).

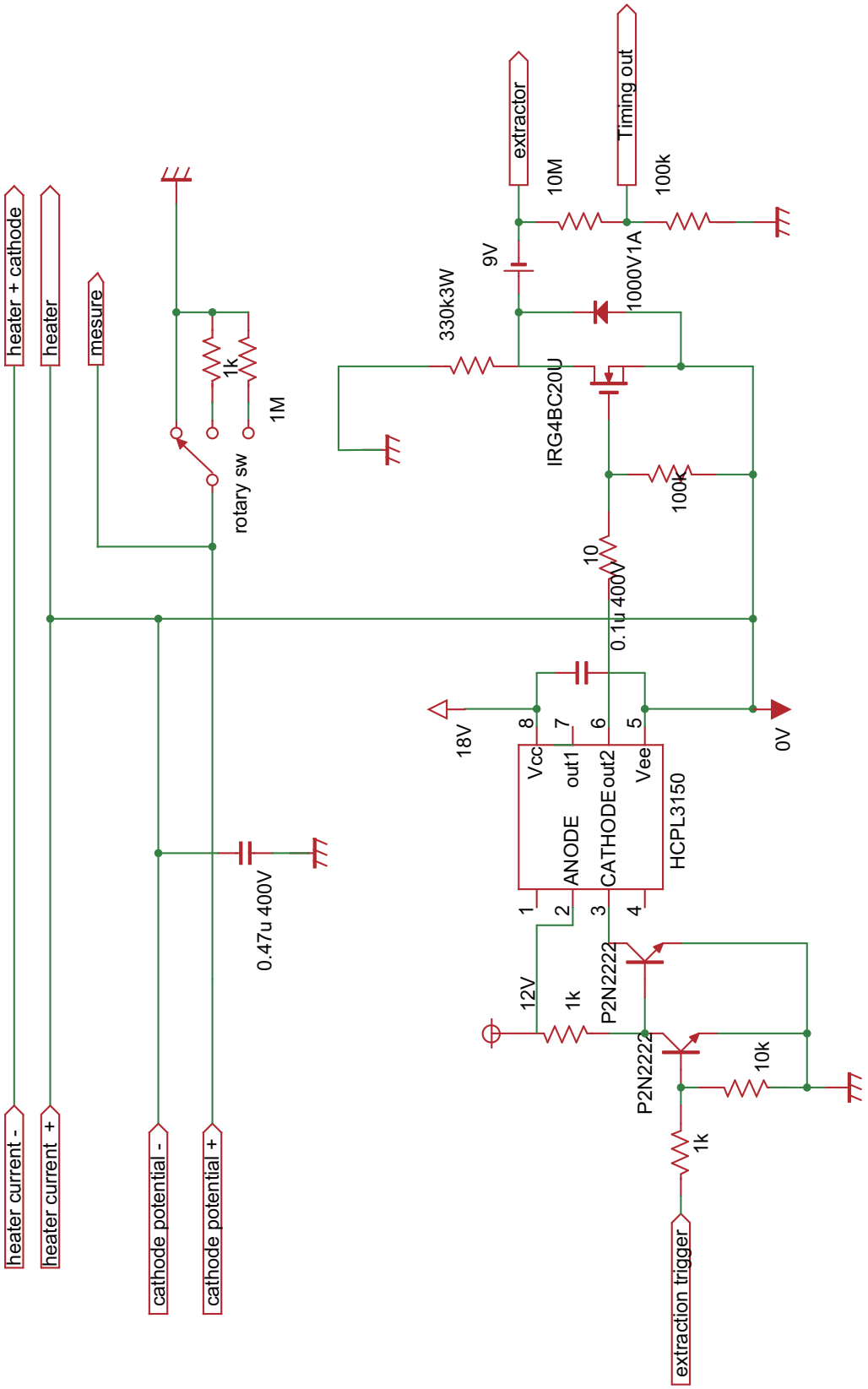

Figure D.15: A circuit drawing of the controller of the electron gun used in the cusp trap (electron gun controller).

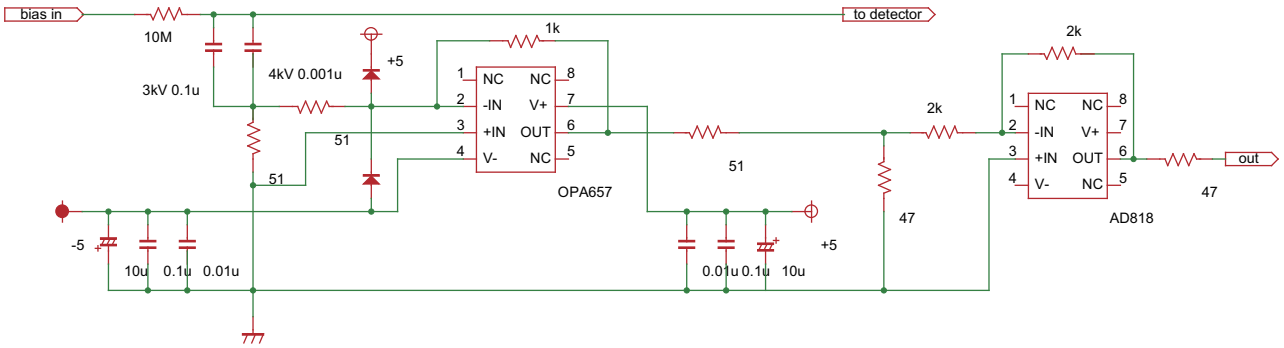

Figure D.16: A circuit drawing of the fast voltage amplifier used to count the number of positrons (pre amp 1).

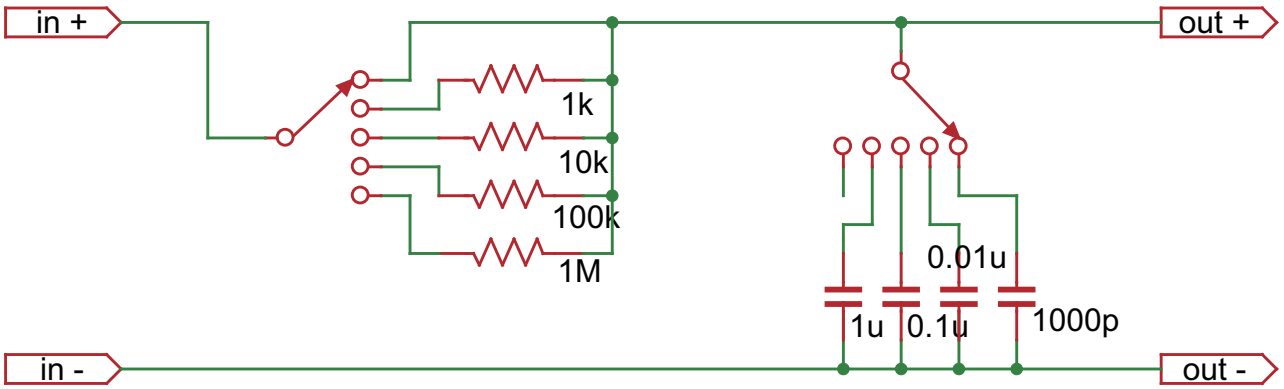

Figure D.17: A circuit drawing of the variable constant RC row pass filter used in the cusp trap voltage control system (RC LPF 1).

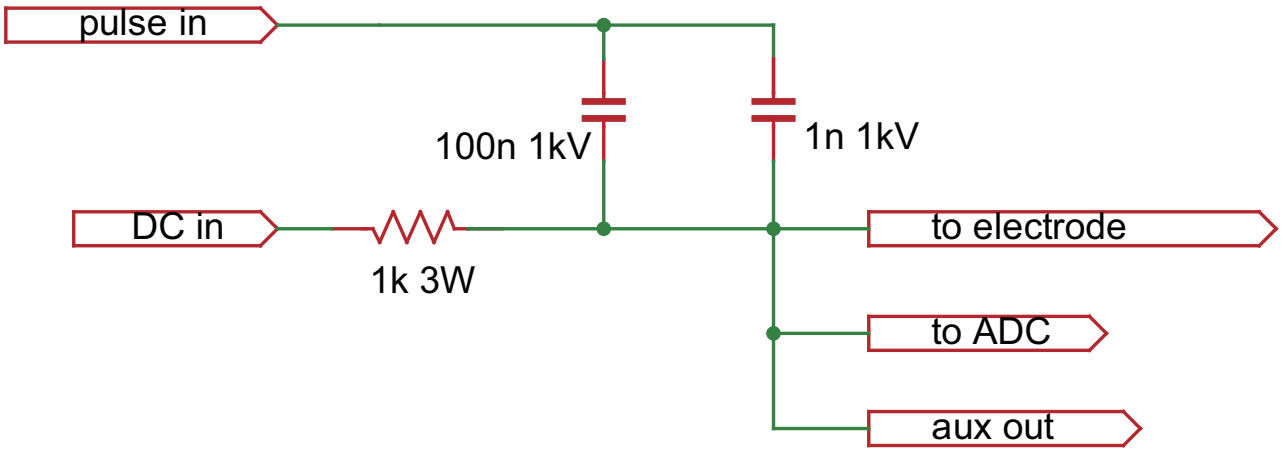

Figure D.18: A circuit drawing of the RC mixer used to superimpose pules signal on the DC voltage used in the cusp trap (RC mix 1).

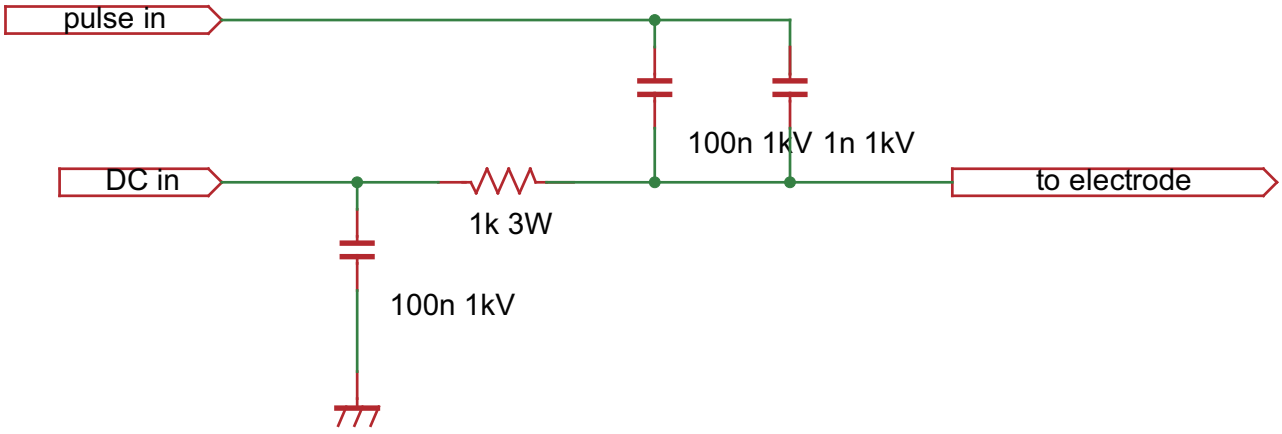

Figure D.19: A circuit drawing of the RC mixer used to superimpose pules signal on the DC voltage used in the positron accumulator (RC mix 2).

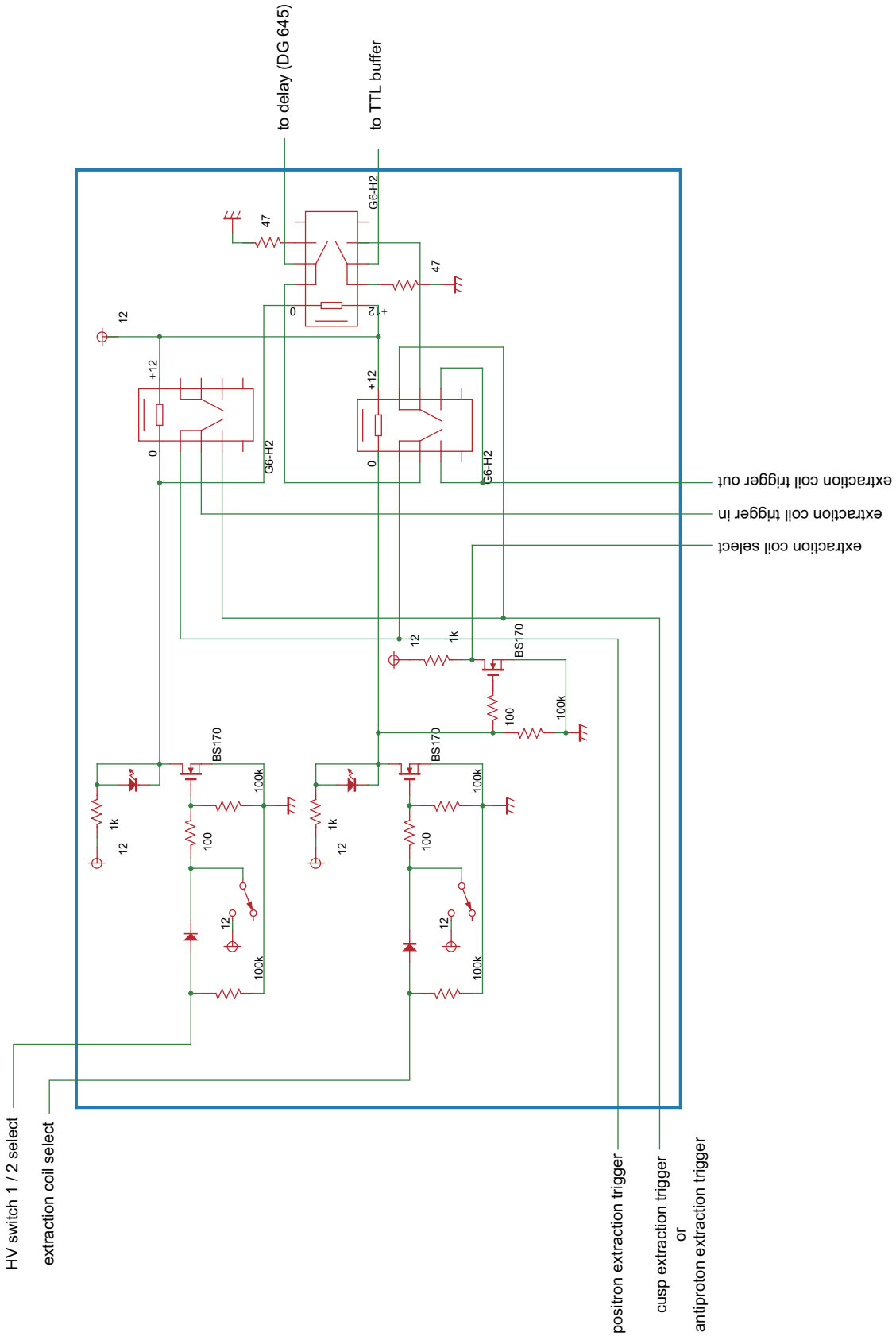

Figure D.20: A circuit drawing of the trigger controller (Trig controller 1).

Appendix E

Safety interlock of the positron source

The activity of the radio isotope used in the positron accumulator(1.97GBq) is high enough to cause serious contamination to the environment in case of leakage. In addition unexpected opening of the source shield can damage those who is in front of the accumulator. Therefore safety interlock system is installed.

The outlet of the scroll pump connected to the positron accumulator and the buffer gas chamber chamber are monitored by a NaI scintillator and PMT. The peak hight of the signal from the scintillator is analysed by the Single channel analyser(SCA) and only the signal which considered to be corresponding to positron annihilation is counted by the DAQ system(National Instruments , USB-6008) connected to a PC by USB(see figure E.1).

As long as the count rate is below the pre-set value, the DAQ output reset signal every 10s to the timer(omron, H5CX) which continuously counting down from 15s until receiving reset signal. If the timer count down to 0 without receiving reset signal, vacuum valve controller close all gate valve and angle valve of the positron accumulator and it is isolated from other vacuum lines and atmosphere.

The holder of the positron source which also works as a radiation shield has another safety interlock system. A 5 port solenoid valve is inserted in between the compressed air line for the air cylinder which actuates the cover in front of the holder. The valve connect the air to the cylinder only when the vacuum inside the accumulator is below the pre-set value. Thus the cover can be opened only the system is under vacuum. This is to avoid unexpected opening of the source shield especially during the bore is open and someone is working in front of the accumulator. since under that situation, there is nothing to shield the positron or γ ray from the source.

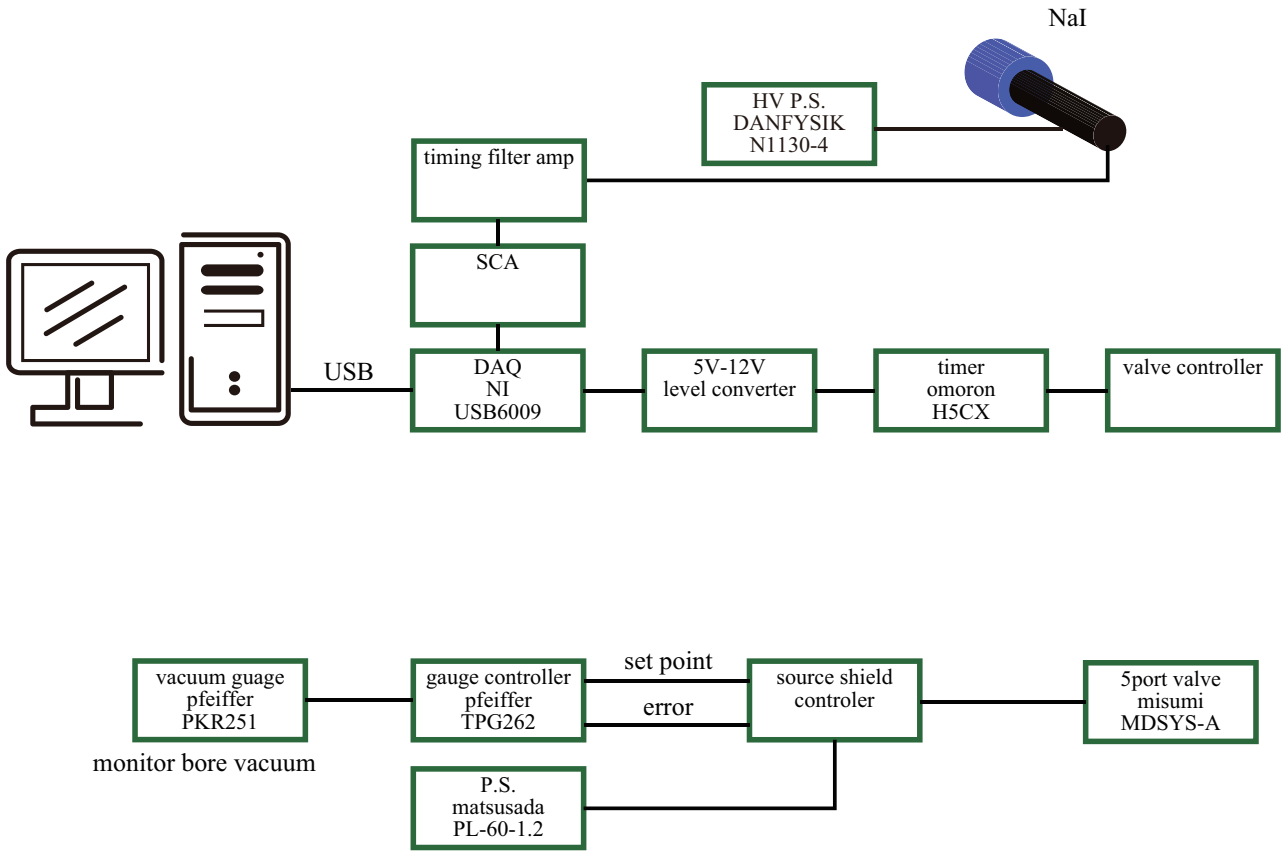

Figure E.1: A connection diagram of the safety interlock system

Appendix F

Compressed air system

Because the experimental area is not allowed to enter while antiproton beam is coming due to high radiation level, remote motion control of several apparatus like electron gun which is inserted only electron injection and must be extracted to avoid conflict with antiproton and positron beam is required.

Thus air cylinders are used to actuate several apparatus; electron gun, MCPPS detector, downstream thermal shield and UV light source in addition to all vacuum valves Control of their motion is done by changing direction of the air with 5 port solenoid valves which is located in the compressed air controller and controlled by external TTL signal (see figure F.1 for details of the connection).

Since pressure drop of the air line and wrong or unexpected operation of the actuators or vacuum valve can cause serious damage to the system, several safety measures are taken.

1. A lockup valve(MDC,IL201-02) is connected at the entrance of the air. This valve can disconnect output from input in case the pressure of the input drops below the pre-set value. Therefore the pressure of the air after this valve can be kept in case of pressure drop of supply side.

2. A pressure sensor(misumi, MDPSA) is installed to monitor the pressure of the air. This sensor can output a signal when the measured pressure value go down the pre-set value. The signal is connected to a warning lamp.

3. The electron gun and MCPPS detector has a position sensor and the controller of them send insert signal to them only when the other one is in extracted position to avoid

conflict[1].

4. The air cylinder used in the electron gun(koganei, CCDAK40x150HL) is end keep cylinder which can keep the position even if the air pressure is lost as long as it was in extracted position before the air pressure is lost.

Figure F.2 is a connection diagram of the acmpressed air in the positron accumulator. A source shield, reflection moderator, MCPPS detector and electron gun is acutuated by compressed air. The system is more or less same as the one used in the cusp trap(see sectiorn 3.4.6 for more details).

[1]Due to the geometrical restriction, the electron gun and MCPPS detector are mounted same plane perpendicular to the axis thus if they inserted at the same time, they will collide with each other(see figure 3.37).

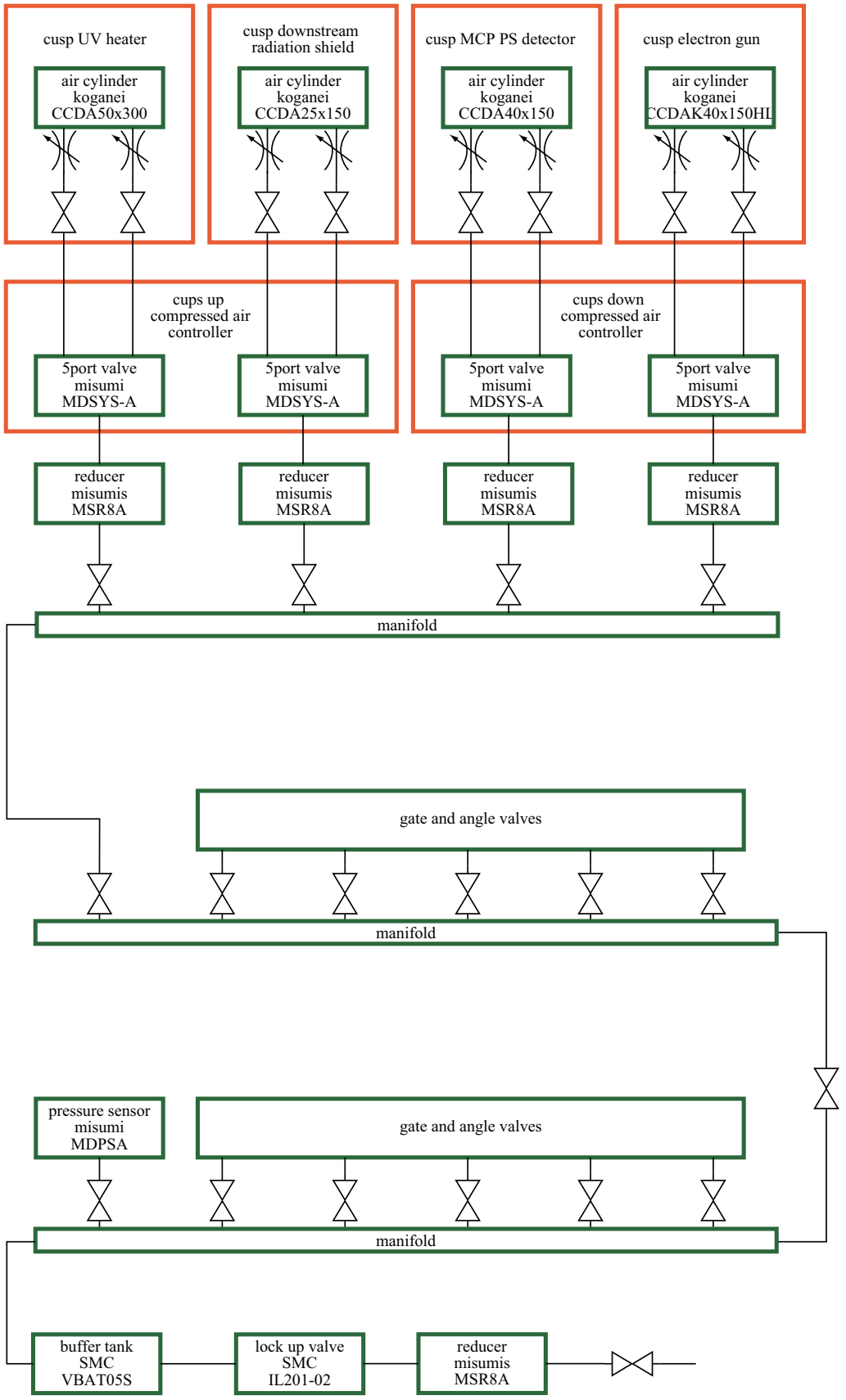

Figure F.1: Connection diagram of compressed air in the cusp trap

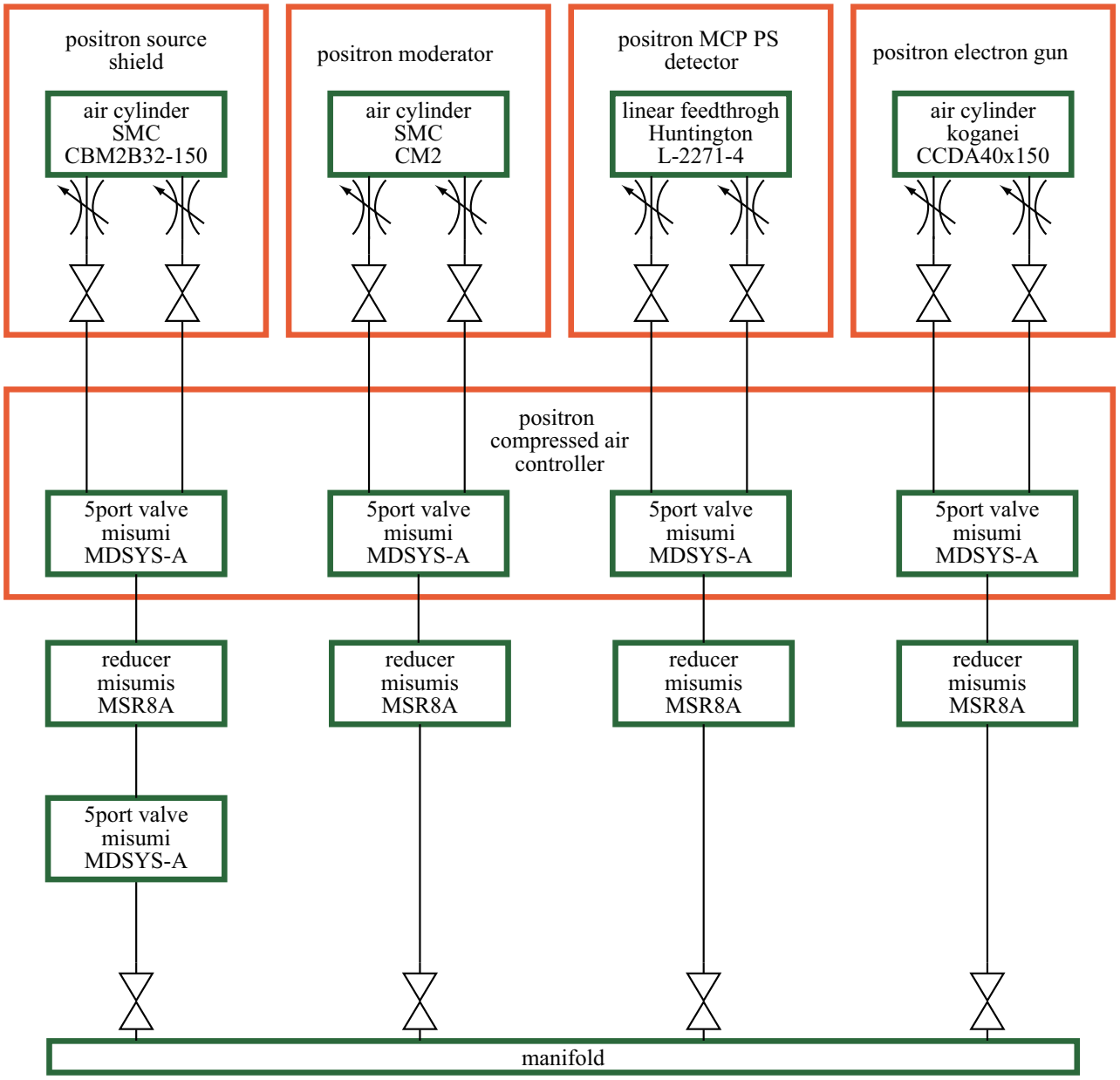

Figure F.2: Connection diagram of compressed air in positron accumulator

Appendix G

Useful formulae

Common notations

- $m_p = 9.11 \times 10^{-31}$ (kg) : antiproton mass.
- $m_e = 1.67 \times 10^{-27}$ (kg) : positron mass.
- $\epsilon_0 = 8.85 \times 10^{-12}$ (F/m) : permittivity of free space.
- $c = 3.00 \times 10^{8}$ (m/s) : speed of light.
- $e = 1.60 \times 10^{-19}$ (C) : unit charge.
- $C_0 = 1.60 \times 10^{-19}$ (J/eV) :conversion coefficient between J and eV
- B (T) : magnetic field.

1. speed of antiproton

$$v = \sqrt{\frac{2C_0E_{kp}}{m_p}} = 14\sqrt{E_{kp}} \text{ mm}/\mu\text{s} \tag{G.1}$$

   where E_{kp} (eV) is kinetic energy of antiproton.

2. speed of positron

$$v = \sqrt{\frac{2C_0E_{ke}}{m_e}} = 590\sqrt{E_{ke}} \text{ mm}/\mu\text{s} \tag{G.2}$$

   where E_{kp} (eV) is kinetic energy of positron.

3. cyclotron frequency of antiproton

$$f_c = \frac{1}{2\pi}\omega_c = \frac{1}{2\pi}\frac{eB}{m_p} = 15B \text{ MHz} \tag{G.3}$$

4. cyclotron frequency of positron

$$f_c = \frac{1}{2\pi}\omega_c = \frac{1}{2\pi}\frac{eB}{m_e} = 28B \text{ GHz} \tag{G.4}$$

5. cyclotron radius of antiproton

$$r_c = \frac{v}{\omega_c} = \frac{\sqrt{2C_0E_{kp}/m_p}}{eB/m_p} = 144\frac{\sqrt{E_{kp}}}{B} \ \mu\text{m} \tag{G.5}$$

6. cyclotron radius of positron

$$r_c = \frac{v}{\omega_c} = \frac{\sqrt{2C_0E_{ke}/m_e}}{eB/m_e} = 3.37\frac{\sqrt{E_{ke}}}{B} \ \mu\text{m} \tag{G.6}$$

7. bounce frequency of antiproton in a potential well

$$f_b = \frac{1}{2\pi}\omega_b = \frac{1}{2\pi}\sqrt{\frac{8V_0e}{(10^{-2}W)^2m_p}} = 441\frac{\sqrt{V_0}}{W} \text{ kHz} \tag{G.7}$$

where V_0 (V) is depth of potential well, W (cm) is full width of potential well.

8. bounce frequency of positron in a potential well

$$f_b = \frac{1}{2\pi}\omega_b = \frac{1}{2\pi}\sqrt{\frac{8V_0e}{(10^{-2}W)^2m_e}} = 18.9\frac{\sqrt{V_0}}{W} \text{ MHz} \tag{G.8}$$

where V_0 (V) is depth of potential well, W (cm) is full width of potential well.

9. plasma frequency of antiproton cloud

$$f_p = \frac{1}{2\pi}\omega_p = \frac{1}{2\pi}\sqrt{\frac{10^6\rho_pe^2}{m_e\epsilon_0}} = 0.21\sqrt{\rho_p} \text{ kHz} \tag{G.9}$$

where ρ_p (cm^3) is density of antiprotons

10. plasma frequency of positron cloud

$$f_p = \frac{1}{2\pi}\omega_p = \frac{1}{2\pi}\sqrt{\frac{10^6\rho_ee^2}{m_e\epsilon_0}} = 8.8\sqrt{\rho_e} \text{ kHz} \tag{G.10}$$

where ρ_e (cm^3) is density of positron.

11. cooling constant of positrons by synchrotron radiation

$$\tau_{rad} = \frac{3\pi\epsilon_0m_e^3c^3}{e^4B^2} = \frac{2.6}{B^2} \text{ s} \tag{G.11}$$

12. kinetic energy of antiproton associated with rotational motion

$$E_{rp} = \frac{1}{2C_0} m_p (r\omega_r)^2 = 5.2 \times 10^{-15} (r\omega_r)^2 \text{ eV} \tag{G.12}$$

where r (mm) is radial distance from the axis, ω_r (Hz) angular rotational frequency.

When the rigid rotor angular frequency of antiproton cloud (ω_r) is 100 kHz, the kinetic energy of an antiproton, whose r is 1 mm, is 5.2×10^{-5} eV

13. kinetic energy of positron associated with rotational motion

$$E_{re} = \frac{1}{2C_0} m_e (r\omega_r)^2 = 2.8 \times 10^{-18} (r\omega_r)^2 \text{ eV} \tag{G.13}$$

where r (mm) is radial distance from the axis.

When the rigid rotor angular frequency of positron cloud (ω_r) is 100 kHz, the kinetic energy of a positron, whose r is 1 mm, is 2.8×10^{-8} eV

14. Field strength required to ionize antihydrogen atom whose principle quantum number is n

$$F = \frac{\pi \epsilon_0 E_{Ry}^2}{e^3 n^4} = 3.2 \times 10^8 n^{-4} \text{ V/cm} \tag{G.14}$$

where E_{Ry} (eV) is Rydberg energy.

15. black body radiation power

$$I(T) = \sigma T^4 A = 5.67 \times 10^{-9} T^4 A \text{ mW} \tag{G.15}$$

$$I(300) = 46A \text{ mW} \tag{G.16}$$

where T (K) is temperature, A (cm^2) area.

16. conversion between Pressure and number density of residual gas molecules

$$\rho = 0.96 \times 10^{19} \frac{P}{T} \text{ cm}^{-3} \tag{G.17}$$

where P (Torr) is pressure of residual gas.

Bibliography

[1] C.D. Anderson. The positive electron. *Physical Review*, 43(6):491, 1933.

[2] P.A.M. Dirac. The quantum theory of the electron. *Proceedings of the Royal Society of London. Series A*, 117(778):610, 1928.

[3] P.A.M. Dirac. Quantised singularities in the electromagnetic field. *Proceedings of the Royal Society of London. Series A*, 133(821):60, 1931.

[4] O. Chamberlain, E. Segre, C. Wiegand, and T. Ypsilantis. Observation of Antiprotons. *Physical Review*, 100(3):947, 1955.

[5] W.M. Yao, C. Amsler, D. Asner, R.M. Barnett, J. Beringer, P.R. Burchat, C.D. Carone, C. Caso, O. Dahl, G. D'Ambrosio, et al. Review of Particle Physics. *Journal of Physics G*, 33(1):1, 2006.

[6] M.S. Fee, S. Chu, A.P. Mills Jr., R.J. Chichester, D.M. Zuckerman, E.D. Shaw, and K. Danzmann. Measurement of the positronium 1^3S_1 - 2^3S_1 interval by continuous-wave two-photon excitation. *Physical Review A*, 48(1):192, 1993.

[7] M. Hori, A. Dax, J. Eades, K. Gomikawa, R.S. Hayano, N. Ono, W. Pirkl, E. Widmann, H.A. Torii, B. Juhász, et al. Determination of the Antiproton-to-Electron Mass Ratio by Precision Laser Spectroscopy of $\bar{p}He^+$. *Physical Review Letters*, 96(24):243401, 2006.

[8] G. Gabrielse, A. Khabbaz, D.S. Hall, C. Heimann, H. Kalinowsky, and W. Jhe. Precision Mass Spectroscopy of the Antiproton and Proton Using Simultaneously Trapped Particles. *Physical Review Letters*, 82(16):3198, 1999.

[9] A. Kreissl, A.D. Hancock, H. Koch, T. Köhler, H. Poth, U. Raich, D. Rohmann, Wolf, L. Tauscher, A. Nilsson, et al. Remeasurement of the magnetic moment of the antiproton. *Zeitschrift für Physik C*, 37(4):557, 1988.

[10] M. Amoretti, C. Amsler, G. Bonomi, A. Bouchta, P.D. Bowe, C. Carraro, C.L. Cesar, M. Charlton, M.J.T. Collier, M. Doser, et al. Production and detection of cold antihydrogen atoms. *Nature*, 419(6906):456, 2002.

[11] G. Gabrielse, N.S. Bowden, P. Oxley, A. Speck, C.H. Storry, J.N. Tan, M. Wessels, D. Grzonka, W. Oelert, G. Schepers, et al. Background-Free Observation of Cold Antihydrogen with Field-Ionization Analysis of Its States. *Physical Review Letters*, 89(21):213401, 2002.

[12] G. Gabrielse, N.S. Bowden, P. Oxley, A. Speck, C.H. Storry, J.N. Tan, M. Wessels, D. Grzonka, W. Oelert, G. Schepers, et al. Driven Production of Cold Antihydrogen and the First Measured Distribution of Antihydrogen States. *Physical Review Letters*, 89(23):233401, 2002.

[13] G. Baur, G. Boero, S. Brauksiepe, A. Buzzo, W. Eyrich, R. Geyer, D. Grzonka, J. Hauffe, K. Kilian, M. LoVetere, et al. Production of antihydrogen. *Physics Letters B*, 368(3):251, 1996.

[14] G. Gabrielse, P. Larochelle, D. Le Sage, B. Levitt, W.S. Kolthammer, R. McConnell, P. Richerme, J. Wrubel, A. Speck, M.C. George, et al. Antihydrogen production within a Penning-Ioffe trap. *Physical Review Letters*, 100(11):113001, 2008.

[15] G.B. Andresen, W. Bertsche, P.D. Bowe, C. Bray, E. Butler, C.L. Cesar, S. Chapman, M. Charlton, J. Fajans, M.C. Fujiwara, et al. Antihydrogen formation dynamics in a multipolar neutral anti-atom trap. *Physics Letters B*, 685(2-3):141, 2010.

[16] Y. Enomoto, N. Kuroda, K. Michishio, C.H. Kim, H. Higaki, Y. Nagata, Y. Kanai, H. Torii, M. Corradini, M. Leali, et al. Synthesis of Cold Antihydrogen in a Cusp Trap. *Physical Review Letters*, 105(24):243401, 2010.

[17] G.B. Andresen, M.D. Ashkezari, M. Baquero-Ruiz, W. Bertsche, P.D. Bowe, E. Butler, C.L. Cesar, S. Chapman, M. Charlton, A. Deller, et al. Trapped antihydrogen. *Nature*, 468(7324):673, 2010.

[18] H. Hellwig, R.F.C. Vessot, M.W. Levine, P.W. Zitzewitz, D.W. Allan, and D.J. Glaze. Measurement of the unperturbed hydrogen hyperfine transition frequency. In *IEEE Transactions on Instrumentation and Measurement*, volume 19, page 200, 1970.

[19] N.F. Ramsey. Experiments with trapped hydrogen atoms and neutrons. *Physica Scripta*, 1995(T59):323, 1995.

[20] S.G. Karshenboim. Nuclear Structure-Dependent Radiative Corrections to the Hydrogen Hyperfine Splitting. *Physics Letters A*, 225(1-3):97, 1997.

[21] M. Niering, R. Holzwarth, J. Reichert, P. Pokasov, T. Udem, M. Weitz, T.W. Hänsch, P. Lemonde, G. Santarelli, M. Abgrall, et al. Measurement of the Hydrogen 1S-2S Transition Frequency by Phase Coherent Comparison with a Microwave Cesium Fountain Clock. *Physical Review Letters*, 84(24):5496, 2000.

[22] M. Fischer, N. Kolachevsky, M. Zimmermann, R. Holzwarth, T. Udem, T.W. Hänsch, M. Abgrall, J. Grünert, I. Maksimovic, S. Bize, et al. New limits on the drift of fundamental constants from laboratory measurements. *Physical Review Letters*, 92(23):230802, 2004.

[23] F. Biraben. Spectroscopy of atomic hydrogen. *The European Physical Journal-Special Topics*, 172(1):109, 2009.

[24] ASACUSA collaboration. Atomic Spectroscopy and Collisions Using Slow Antiprotons. Technical report, CERN-SPSC 2005-002, 2005.

[25] J. Eades and F.J. Hartmann. Forty years of antiprotons. *Reviews of Modern Physics*, 71(1):373, 1999.

[26] R. Landua. Antihydrogen at CERN. *Physics Reports*, 403-404:323, 2004.

[27] M.H. Holzscheiter, M. Charlton, and M.M. Nieto. The route to ultra-low energy antihydrogen. *Physics Reports*, 402(1-2):1, 2004.

[28] R.G. Greaves and C.M. Surko. Antimatter plasmas and antihydrogen. *Physics of Plasmas*, 4(5):1528, 1997.

[29] G. Gabrielse, X. Fei, K. Helmerson, S.L. Rolston, R. Tjoelker, T.A. Trainor, H. Kalinowsky, J. Haas, and W. Kells. First capture of antiprotons in a Penning trap: A kiloelectronvolt source. *Physical Review Letters*, 57(20):2504, 1986.

[30] G. Gabrielse, X. Fei, L.A. Orozco, R.L. Tjoelker, J. Haas, H. Kalinowsky, T.A. Trainor, and W. Kells. Cooling and slowing of trapped antiprotons below 100 meV. *Physical Review Letters*, 63(13):1360, 1989.

[31] D.S. Hall and G. Gabrielse. Electron Cooling of Protons in a Nested Penning Trap. *Physical Review Letters*, 77(10):1962, 1996.

[32] C.M. Surko, M. Leventhal, and A. Passner. Positron Plasma in the Laboratory. *Physical Review Letters*, 62(8):901, 1989.

[33] M.E. Glinsky and T.M. O'Neil. Guiding center atoms: Three-body recombination in a strongly magnetized plasma. *Physics of Fluids B*, 3(5):1279, 1991.

[34] M. Pajek and R. Schuch. Three-body recombination of ions with electrons in cooler-storage rings. *Hyperfine Interactions*, 108(1):185, 1997.

[35] A. Müller and A. Wolf. Production of antihydrogen by recombination of $\bar{p}$ with e^+: What can we learn from electron–ion collision studies. *Hyperfine Interactions*, 109(1):233, 1997.

[36] M. Amoretti, C. Amsler, G. Bazzano, G. Bonomi, A. Bouchta, P.D. Bowe, C. Carraro, C.L. Cesar, M. Charlton, M. Doser, et al. High rate production of antihydrogen. *Physics Letters B*, 578(1-2):23, 2004.

[37] T.W. Hänsch and C. Zimmermann. Laser spectroscopy of hydrogen and antihydrogen. *Hyperfine Interactions*, 76(1):47, 1993.

[38] R. Bluhm, V.A. Kostelecký, and N. Russell. CPT and Lorentz Tests in Hydrogen and Antihydrogen. *Physical Review Letters*, 82(11):2254, 1999.

[39] I.I. Rabi, J.M.B. Kellogg, and J.R. Zacharias. The Magnetic Moment of the Proton. *Physical Review*, 46(3):157, 1934.

[40] A.G. Prodell and P. Kusch. The Hyperfine Structure of Hydrogen and Deuterium. *Physical Review*, 88(2):184, 1952.

[41] J.E. Nafe and E.B. Nelson. The Hyperfine Structure of Hydrogen and Deuterium. *Physical Review*, 73(7):718, 1948.

[42] P. Kusch. Redetermination of the Hyperfine Splittings of Hydrogen and Deuterium in the Ground State. *Physical Review*, 100(4):1188, 1955.

[43] D.H.E. Dubin and T.M. O'Neil. Trapped nonneutral plasmas, liquids, and crystals (the thermal equilibrium states). *Reviews of Modern Physics*, 71(1):87, 1999.

[44] A. Mohri, Y. Kanai, Y. Nakai, and Y. Yamazaki. Non-Neutral Plasma Confinement In A Cusp-Trap And Possible Application To Anti-Hydrogen Beam Generation. *AIP Conference Proceedings*, 793(1):147, 2005.

[45] F. Robicheaux. Simulations of antihydrogen formation. *Physical Review A*, 70(2):22510, 2004.

[46] F. Robicheaux and J.D. Hanson. Three-body recombination for protons moving in a strong magnetic field. *Physical Review A*, 69(1):10701, 2004.

[47] T. Pohl and T. Pattard. Electron–ion recombination in strongly coupled cold plasmas under nonequilibrium conditions. *Journal of Physics A*, 39(17):4571, 2006.

[48] F. Robicheaux. Three-body recombination for electrons in a strong magnetic field: Magnetic moment. *Physical Review A*, 73(3):33401, 2006.

[49] F. Robicheaux. Atomic processes in antihydrogen experiments: a theoretical and computational perspective. *Journal of Physics B*, 41(19):192001, 2008.

[50] S. Jonsell, D.P. Werf, M. Charlton, and F. Robicheaux. Simulation of the formation of antihydrogen in a nested Penning trap: effect of positron density. *Journal of Physics B*, 42(21):215002, 2009.

[51] E.M. Bass and D.H.E. Dubin. Antihydrogen formation from antiprotons in a pure positron plasma. *Physics of Plasmas*, 16(1):012101, 2009.

[52] M. Bell and J.S. Bell. Capture of cooling electrons by cool protons. *Particle Accelerators*, 12:49, 1982.

[53] M.C. Fujiwara, M. Amoretti, C. Amsler, G. Bonomi, A. Bouchta, P.D. Bowe, C. Canali, C. Carraro, C.L. Cesar, M. Charlton, et al. Temporally Controlled Modulation of Antihydrogen Production and the Temperature Scaling of Antiproton-Positron Recombination. *Physical Review Letters*, 101(5):53401, 2008.

[54] J.J. Sakurai and San Fu Tuan. *Modern quantum mechanics*. Addison-Wesley, 1994.

[55] Y. Nagata. *Manipulation of ultraslow antiprotons and first application to atomic collisions*. PhD thesis, The university of Tokyo, 2008.

[56] N. Kuroda. *Accumulation of a large number of antiprotons and production of an ultra-slow antiproton beam*. PhD thesis, The university of Tokyo, 2004.

[57] N. Kuroda, H.A. Torii, M. Shibata, Y. Nagata, D. Barna, M. Hori, D. Horváth, A. Mohri, J. Eades, K. Komaki, et al. Radial Compression of an Antiproton Cloud for Production of Intense Antiproton Beams. *Physical Review Letters*, 100(20):203402, 2008.

[58] T. Ichioka. *Development of intense beam of ultracold antiprotons*. PhD thesis, The university of Tokyo, 2000.

[59] H. Imao, M. Tarek, K. Michishio, Y. Enomoto, T. Shimoyama, Y. Kanai, N. Kuroda, A. Mohri, H. Higaki, H. Saitoh, et al. ASACUSA MUSASHI: New progress with intense ultra slow antiproton beam. *Hyperfine Interactions*, 194(1):71, 2009.

[60] H. Imao, K. Michishio, Y. Kanai, N. Kuroda, Y. Enomoto, H. Higaki, K. Kira, A. Mohri, H.A. Torii, Y. Nagata, et al. Positron accumulation and manipulation for antihydrogen synthesis. *Journal of Physics: Conference Series*, 225(1):012018, 2010.

[61] 下山拓也. 反水素合成に向けた陽電子の蓄積および輸送. Master's thesis, 東京大学, 2009.

[62] R. Ley. Positron production using accelerators. *Hyperfine Interactions*, 109(1):167, 1997.

[63] E.H. Chao, R.C. Davidson, S.F. Paul, and K.A. Morrison. Effects of background gas pressure on the dynamics of a nonneutral electron plasma confined in a Malmberg–Penning trap. *Physics of Plasmas*, 7(3):831, 2000.

[64] A. Mohri, H. Saitoh, Y. Enomoto, Y. Kanai, and Y. Yamazaki. Nonneutral Plasma Confinement in a Spindle Cusp. In *Proceedings of the 33rd EPS conference on Plasma Physics*, volume 30I, page 4.067, 2006.

[65] http://www.allectra.com/index-e.htm.

[66] http://www.stahl-electronics.com/.

[67] J.S. Cohen. Molecular effects on antiproton capture by H_2 and the states of $p\bar{p}$ formed. *Physical Review A*, 56(5):3583, 1997.

[68] M. Shibata, A. Mohri, Y. Kanai, Y. Enomoto, and Y. Yamazaki. Compact cryogenic system with mechanical cryocoolers for antihydrogen synthesis. *Review of Scientific Instruments*, 79(1):015112, 2008.

[69] http://www.fieldp.com/tricomp.html.

[70] http://www.cst.com/.

[71] R.G. Greaves and C.M. Surko. Inward Transport and Compression of a Positron Plasma by a Rotating Electric Field. *Physical Review Letters*, 85(9):1883, 2000.

[72] J.R. Danielson and C.M. Surko. Radial compression and torque-balanced steady states of single-component plasmas in Penning-Malmberg traps. *Physics of Plasmas*, 13(5):55706, 2006.

[73] H. Saitoh, A. Mohri, Y. Enomoto, Y. Kanai, and Y. Yamazaki. Radial compression of a non-neutral plasma in a cusp trap for antihydrogen synthesis. *Physical Review A*, 77(5):51403, 2008.

[74] H. Saitoh, A. Mohri, Y. Enomoto, Y. Kanai, and Y. Yamazaki. Radial Compression of a Non-neutral Plasma in a Non-uniform Magnetic Field of a Cusp Trap. *AIP Conference Proceedings*, 1114(1):163, 2009.

[75] private communications.

[76] B.R. Beck, J. Fajans, and J.H. Malmberg. Temperature and anisotropic-temperature relaxation measurements in cold, pure-electron plasmas. *Physics of Plasmas*, 3(4):1250, 1996.

[77] D.L. Eggleston, C.F. Driscoll, B.R. Beck, A.W. Hyatt, and J.H. Malmberg. Parallel energy analyzer for pure electron plasma devices. *Physics of Fluids B*, 4(10):3432, 1992.

[78] B. Autin, S. Baird, D. Berlin, J. Boillot, J. Bosser, M. Brouet, F. Caspers, M. Chanel, V. Chohan, T. Eriksson, et al. THE ANTIPROTON DECELERATOR(AD), A SIMPLIFIED ANTIPROTON SOURCE (FEASIBILITY STUDY). Technical report, CERN 95-36, 1995.

[79] S. Baird, D. Berlin, J. Boillot, J. Bossen, M. Brouet, J. Buttkus, F. Caspers, V. Chohan, D. Dekkers, T. Eriksson, et al. DESIGN STUDY OF THE ANTIPROTON DECELERATOR: AD. Technical report, CERN 96-43, 1996.

[80] S. Maury. The antiproton decelerator: AD. *Hyperfine Interactions*, 109(1):43, 1997.

[81] G. Tranquille. Recent highlights from the CERN-AD. *Nuclear Instruments and Methods in Physics Research A*, 532(1-2):111, 2004.

[82] C. Carli and F. Caspers. STOCHASTIC COOLING AT THE CERN ANTIPROTON DECELERATOR. Technical report, CERN/PS 2000-024, 2000.

[83] A.M. Lombardi. Decelerating and Accelerating RFQs. In *Proceedings of the XIX International Linear Accelerator Conference*, page 377, 1998.

[84] W. Pirkl Y. Bylinsky, A.M. Lombardi. RFQD - A DECELERATING RADIO FREQUENCY QUADRUPOLE FOR THE CERN ANTIPROTON FACILITY. Technical report, CERN/PS 2000-61, 2000.

[85] P. Belochitskii, J. Bosser, J. Buttkus, C. Carli, F. Caspers, V. Chohan, D. Cornuet, T. Eriksson, A. Findlay, M. Giovannozzi, et al. Commissioning and first operation of the antiproton decelerator (AD). In *Proceedings of the 2001 Particle Accelerator Conference*, volume 1, page 580, 2002.

Acknowledements

カスプトラップを用いた反水素の合成という、魅力的な研究テーマを与えてくださった山崎泰規教授に感謝します。本研究では新しい装置の開発が重要な位置をしめましたが、それはまさに私の希望するところでもあり、終始充実した研究生活をおくることが出来ました。また、個々の装置の細かな設計から、物理的な結果の解釈にいたるまで、あらゆる点で助言を頂き、励まして頂きました。そうした先生のご支援がなければ、この論文を完成させることはできなかったでしょう。

毛利明博名誉教授には実験の進め方から回路の作り方にいたるまで、実験を進めていく上で重要なあらゆることを教えていただきました。松田恭幸准教授には、なかなか成果が出ずに落ち込んでいるときに、常に励ましていただきました。また本論文を丁寧に読んで頂き沢山のご指摘を頂きました。黒田直史助教には装置開発からデータの解析にいたるまで、様々な点でご支援頂きました。氏が中心となって開発された、反陽子トラップの経験がなければ、カスプトラップの完成にはもっと時間がかかったことでしょう。鳥居寛之助教にはCERNでの生活等についてサポートしていただきました。CERNでの生活が充実したものになったのは氏の様々な情報のおかげです。

カスプトラップの冷却機構を開発され、低温装置の設計方法を教えてくださった柴田政宏博士、電子を用いたテスト実験を精力的に進められ、非中性プラズマについて教えてくださった齋藤晴彦博士、陽電子蓄積器を開発された今尾浩士博士の３名ポスドクの方々には、良き先輩として、また目指すべき目標として色々な刺激を受けました。陽電子トラップの安定した運用と性能向上については満汐孝治君が大いに活躍してくださいました。また、氏の一生懸命に実験に取り組む姿を見て、自分も精進せねばとしばしば思わされました。金井保之博士には冷凍機のメンテナンスや陽電子蓄積器の放射線モニター等で、また毎回の装置の実験エリアへの搬入と接続等でお世話になりました。プラズマや荷電粒子トラップについては檜垣浩之准教授から多くを学びました。吉良健太郎君には電子を使ったテスト実験でたくさんのデータを取得してもらいました。最も近い世代の先輩として永田祐吾博士からは物理のことから、大学での手続きにいたるまで、色々な情報を頂きました。田中香津生には引き出しコイルの開発をして

いただき、陽電子画像の取得に大変役立ちました。また ASACUSA MUSASHI グループのメンバーとしてともに実験をすることができた、豊田寛君、下山拓也君、金燦鉉君、大塚未来さん、藤居甲基君に感謝します。さらに共同研究グループとして、本実験で重要な役割をはたした３ D 検出器を開発されたイタリアグループの方々、（Dr. M. Corradini, Dr. M. Leali, Dr. E. Lodi-Rizzini, Mr. V Mascagna, Dr. L. Venturelli, Dr. N. Zurlo）及び、様々な場面で進んで手伝って下っさた ASACUSA のメンバーの方々の支えがあってこそ、ここまで実験をすすめることができたのだと思います。

また本研究とは直接関係はありませんが、理化学研究所山崎原子物理研究室の方々、東京大学大学院総合文化研究科山崎松田研究室及びその前身である小牧山崎研究室の方々には様々な場面で助けていただきました。特に畠山温助手（現東京農工大准教授）には、４年生の時に卒業研究で大変お世話になりました。私がこの道へ進んだのは、氏が研究の面白さを伝えてくれたことが大きかったと思います。

最後に、海外での実験に伴う出張や荷物の輸送などの手続きにおいてだけでなく、常に励まし、支え、あらゆる相談に乗っていただいた、秘書の和田ひとみさんに、深い感謝の念を捧げます。